Identification of mine blast interaction pressure on excited plates

Using transient adjoint optimization for solving the inverse problems

R.J.W.E. van den Brink

Technische Universiteit Delft

TU Delft

Identification of mine blast interaction pressure on excited plates

Using transient adjoint optimization for solving the inverse problems

by

R.J.W.E. van den Brink

to obtain the degree of Master of Science
at the Delft University of Technology,
to be defended publicly on Wednesday October 9, 2019 at 12:45 AM.

Student number:	4278895	
Project duration:	26-09-18 – 09-09-19	
Thesis committee:	Dr. ir. S. Turteltaub,	TU Delft, supervisor
	Dr. B. Chen,	TU Delft
	Dr. Ir. R.C. Alderliesten,	TU Delft
	Ir. B.C. de Jong,	TNO, supervisor

An electronic version of this thesis is available at http://repository.tudelft.nl/.

TU Delft

Preface

Preface...

R.J.W.E. van den Brink
Delft, October 2019

For 12 months from 26-09-18 till 09-09-19 I worked on my thesis project at TNO (Nederlandse Organisatie voor toegepast-natuurwetenschappelijk onderzoek) English: (Dutch Organization for Applied Scientific Research). TNO is an independent research organization involved in a large variety of scientific research projects. This thesis is part of my master program in Aerospace Engineering at the TU Delft. One of TNO's units, is Buildings Infrastructure & Maritime (BIM) of which Structural Dynamics (SD) is the department where I did my project. One of the fields of expertise of this department is modeling the impact on vehicles caused by mine explosions. During my thesis I researched inverse measurement techniques utilizing Digital Image Correlation (DIC) data of plates excited by mine blasts to measure the interaction pressure.

Acknowledgement

Acknowledgement...

R.J.W.E. van den Brink
Delft, October 2019

I would like to express my sincere grate fullness to my main supervisor from TNO, Ir. Bart de Jong and my co-supervisor from TNO Ir. Wim van den Heuvel. Thank you for offering me the internship and thesis opportunity to work on advanced vehicle dynamics in the Structural Dynamics (SD) department. I am especially grate-full that the academic purpose of this assignment was realized and given great attention. I would like to thank my main supervisor for his support and patience during the weekly meetings, which have cost him a substantial amount of time. Furthermore his support to help me grow in my engineering profession is recognized. I would like to thank all other engineers, scientists and personnel from the structural dynamics department for their occasional help support and the creation of a great atmosphere. For this master thesis project Dr. Sergio Turteltaub accepted my request to be my academic supervisor. I would like to thank him for that. I would also like to thank Sergio for taking the time to meet with me and discuss the research in length, steering me in the right direction. Especially solving the optimization problem using the transient continuous adjoint was paramount to the project.

List of Symbols

A	Operator forward problem	[General]
A	Peak pressure parameter for benchmark pressure P_s	[Pa]
b_i	Coefficient basis function pressure	[-]
C_{imp}	Calibration factor for impulse	[-]
C_{press}	Calibration factor for pressure time profile	[-]
d	Vector with problem dimensions	[m]
$\boldsymbol{e}_g$	Unit vector direction of gravity force	[m]
E_t	Energy in explosives	[J]
E_y	Youngs modulus soil	[Pa]
f(t), F(ω)	Source function	[General]
f(**x**)	Initial displacement plate	[m]
F[u]	Convex Functional	[General]
F_g(t)	Force gravity	[N]
$\boldsymbol{F}_b$(t)	Force boundary test rig and plate	[N]
$\boldsymbol{F}_{ex}$(t)	Force externally applied on the test rig	[N]
g(**x**)	Initial velocity plate	$[\frac{m}{s}]$
g(t), G(ω)	Impulse response	[General]
g	Gravitational constant	$[\frac{kg}{ms^2}]$
h	Jump height	[m]
H	Approximate inverse of forward Operator A	[General]
h	Step in **x**	[m]
I(x,y)	Impulse used in simulations	$[\frac{kg}{ms}]$
$I_{Westine}(x, y)$	Impulse from original Westine model	$[\frac{kg}{ms}]$
J	Jacobi matrix $\frac{\partial r_i}{\partial x_i}$	[General]
L	size rectangular plate	[m]
L_p	Vector norm	[General]
M	Vehicle mass	[kg]
P(**x**,t)	Pressure distribution mine blast	[Pa]
P_s(**x**,t)	Pressure distribution mine blast bench mark simulation	[Pa]
$\hat{P}$(**x**,t)	Pressure distribution mine blast determined by IMP algorithm	[Pa]
r	radial distance center plate	[m]
R	Soil bubble radius	[m]
R	Largest length parameter for pressure front benchmark pressure	[m]
r, r_i	Least square residuals	[General]
t	Thickness plate	[m]
t	Time variable	[s]
t_d	Duration for a pressure wave to travel a certain distance	[m]
T	End time simulation	[s]
t	Traction	[Pa]
u(t),U(ω)	Time dependent solution of the forward problem	[General]
v	velocity parameter for pressure front benchmark pressure P_s	$[\frac{m}{s}]$
v(**x**,t)	Out of plane plate displacement measured	[m]
w	Width parameter for pressure front benchmark pressure P_s	$[\frac{1}{m}]$
w(**x**,t)	Out of plane plate displacement	[m]
w_{in}	displacement discrete measurements from DIC data	[m]
$\hat{w}$(**x**,t)	Out of plane plate displacement DIC measurements	[m]
x	Variable of interest (measurement problem)	[General]
x	Vector of variables for optimization problem	[General]

$\mathbf{x}$	Location vector	[m]
y	Measured variable (measurement problem)	[General]
$\epsilon_{1,2,3}$	Errors in benchmark test pressure	[General]
$\boldsymbol{\epsilon}$	Strain tensor	[-]
$\eta(\mathbf{x},t)$	Noise in displacement data (input for IMP algorithm) equivalent to Error in DIC output	[m]
$\pi_{0,1,2,3}$	pi-products	[-]
ρ	Density of Soil or steel	$[\frac{kg}{m^3}]$
σ_p	Standard measurement uncertainty in pressure	[m]
$\sigma_{w_{in}}$	Standard measurement uncertainty in displacement	[m]
$\boldsymbol{\sigma}$	Stress tensor	[Pa]
$\boldsymbol{\sigma_y}$	Soil failure parameters	[Pa]
$\boldsymbol{\tau}(t)$	Torque in center of gravity test rig	[Nm]
$\phi(\mathbf{x}, t)$	Adjoint variable	[General]
$\boldsymbol{\phi}(\mathbf{x}, t)$	Adjoint field	[General]
ψ_i	Basis function pressure	[Pa]
ω	Frequency parameter (for frequency domain)	$[\frac{1}{s}]$
Ω	Spatial domain	[m, m^2, m^3]

Acronyms

ALE	Arbitrary Lagrangian Eulerian
BIM	Buildings Infrastructure & Maritime
DIC	Digital Image Correlation
DMO	Defence Material Organization
DRI	Dynamic Response Index
FE	Finite Element
FE	Finite Element Method
FSI	Fluid Structure Interaction
HIC	Head Injury Criteria
HPB	Hopkinson Pressure Bar
IED	Improvised Explosive Device
IMA	Inverse Measurement Algorithm
IMP	Inverse Measurement Problem
ISF	Inverse Structural Filter
KKT	Karush Kuhn Tucker
KL	Kirchhoff-Love
MoD	Ministry of Defence
MMALE	Multi-Material Arbitrary Lagrangian Eulerian
PDE	Partial Differential Equation
RSM	Response Surface Method
SD	Structural Dynamics
SPH	Smoothed Particle Hydrodynamics
SWAT	Sum Weighted Acceleration Technique
TNO	Dutch Organization for Applied Scientific Research
TU	Technical University

Abstract

Mines and improvised explosive devices are the cause of many mortalities of vehicle occupants. Both experimental and numerical research in this field aims to improve the safety of military vehicles. TNO has advanced Finite Element (FE) models to simulate such events. The numerical research is done to better understand mine blasts. Another aim is to reduce experimental costs for Defence Material Organization (DMO).

For full vehicle simulations the empirical Westine model is the basis of the in-house TNO mine blast model. The model consists of a triangular pressure pulse consistent with the Westine impulse which is calibrated using the a test rig developed by TNO and DMO. Experiments are compared with numerical results using the TNO mine blast model and the jump height, representative for total impulse transferred, shows scattered results for different vehicle tests. A possible cause can be accuracy of the current mine blast model.

This research will study a new technique to validate mine blast models. When this new technique results in improvements in validation of mine blast models it can be used to study and improve the current TNO model.

The aim of the new validation method is to calculate the interaction pressure of an plate excited by a mine blast loading. The obtained pressure can be compared with existing mine blast models for validation of the mine blast model. The methodology is based on solving the inverse problem which requires transient Digital Image Correlation (DIC) measurements of the deforming plate for the duration of the mine blast loading. Such measurements are done with the state of the art test setup from TNO and DMO.

Several methods to solve the inverse problem will be studied. The proposed best way to solve the problem at hand is by solving the corresponding optimization problem using an iterative gradient of descent algorithm. The main difficulty in this approach will be the calculation of the gradient of the objective function. To do this the corresponding transient adjoint problem has to be solved.

First an algorithm to solve the inverse problem is implemented for a linear Kirchhoff Love plate model to study the behaviour of the inverse problem for a relatively simple test case. For this algorithm the transient adjoint problem is derived. The forward and adjoint problem are numerically solved. The implementation is verified using the method of manufactured solutions and a convergence study. The algorithm is verified using three different bench mark test pressures. It was found that without any exception the displacement of the algorithm converged with great accuracy to the applied displacement. The corresponding pressure converged good for smooth pressure distributions. Non smooth pressure distributions representative for mine blast interaction pressure did not converge. This shows the non-uniqueness of the solution of the inverse problem. It was realized after these tests that the forward problem acts as a low pass filter for time and spatial oscillations of the pressure distribution. This implies that the inverse problem in non-unique and that noise in the displacement data will be amplified in the obtained pressure from the inverse solution. The total force and radial position as function of time, obtained after integration over the spatial domain, for a localized load are accurately captured back. These parameters could be useful to validate a mine blast model such that research was continued for a continuum model.

A non-linear elastic material model is proposed to model the deforming plate assuming monotonically increasing strain. This model is used and calibrated against the Johnson-Cook plasticity model. One plate simulation excited by the TNO mine blast model verifies that the non-linear elastic and Johnson-Cook material model result in almost the same displacement.

The adjoint problem for a general continuum with elastic material model is derived. The same optimization algorithm is implemented for the continuum model using the calibrated non-linear elastic material model. The forward and adjoint problem are solved using the author's transient FEM implementation which is verfied using commercial software. From the benchmark tests it was verified that the displacement converged quite well however less compared to the linear problem studied earlier. The corresponding pressures behaved similar. It was concluded that the total force and centroid position of a localized load are not always in agreement for the benchmark and solved pressure.

This research shows that the limitations of the inverse problem shed light on the limitations in the validation methods employed by many researchers in the field.

Contents

1 Introduction

Mines and Improvised Explosive Devises (IED's) are the cause of fatality and serious injuries for the occupants of (military) vehicles [50]. Mine impact is a large threat for military vehicles during operations [45]. Figure 1.1 illustrates that almost half the fatalities are due to IED's. When a military vehicle is impacted by a mine explosion, one of the key requirements is that the occupants will not suffer too large injuries [1].

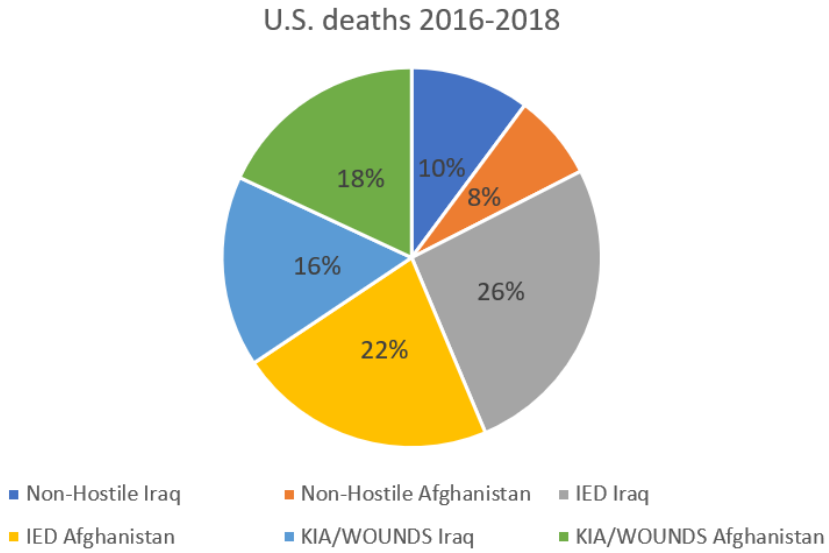

Figure 1.1: U.S. Military deaths during the period 2016 to 2018. This figure illustrates illustrates the large contribution of IED's to military deaths. *Source: data obtained from [12]*

1.1. Background information

The Ministry of Defence (MoD) is interested to know what types of mine blasts their vehicles can withstand, quantified by means of a STANAG 4569 protection level [37]. To determine these protection levels TNO does full scale experiments and Finite Element (FE) simulation work. The simulation is used to estimate the protection level of the vehicle such that less experiments are required. In Figure 1.2 a typical vehicle and corresponding FE mesh shown.

[1] Several criteria such as Head Injury Criteria (HIC) and Dynamic Response Index (DRI) quantify injuries. For design a quantification of 'not too large' must be defined. This implies that e.g. (depending on the criteria used) both HIC and DRI in experiments and simulations should be below a certain reference value.

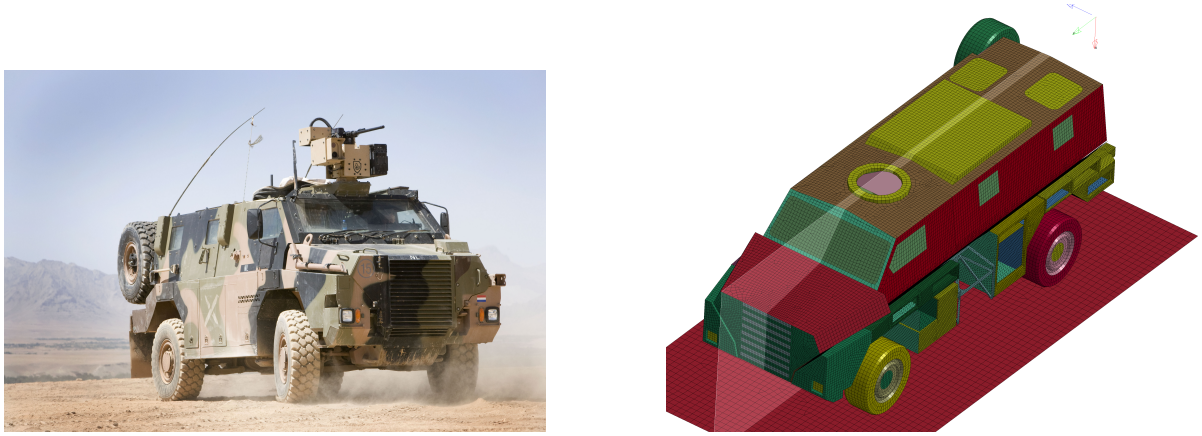

Figure 1.2: Left figure shows the bushmaster with a turret, a typical vehicle for which TNO does full scale experiments. The right figure shows the mesh of the Bushmaster (Military armoured vehicle) used by TNO for FE mine blast simulations.

The FE simulations require a mine blast model. Several methods exist, one can model the complete explosion process which is computational expensive, or one can use an empirical model which can have certain limitations. Independent of the model chosen there is a need to validate the model. Researchers validate their model by means of comparing simulations with experiments. In general the response of some rigid or flexible object excited by a mine blast is simulated and compared with experiments. Such an object could be a plate, a small structure or even a full vehicle. Most researchers compare either or both the trajectory and final deformation of such an object. TNO and DMO developed a test setup which measures a plate's deformation during the explosion using Digital Image Correlation (DIC) techniques together with high speed cameras. This allows TNO to validate their mine blast model more accurately compared to for example only using the final deformation. Figure 1.3 graphically illustrates the experimental setup.

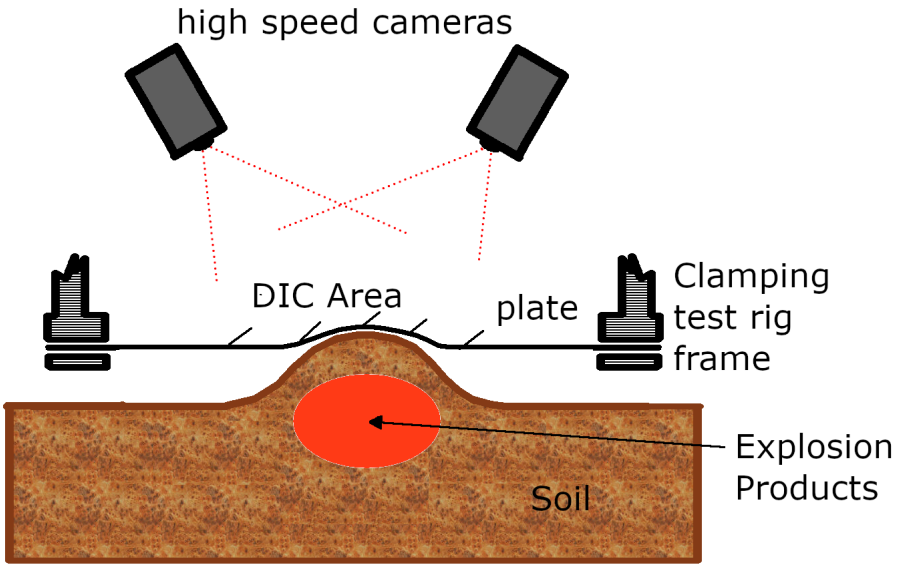

Figure 1.3: The figure illustrates a clamped plate located above a mine blast. Two high speed cameras captures the deformation of the plate. On the area captured by the camera DIC is be used to obtain out off plane displacement measurements. Two cameras are used such that 3D DIC is possible.

1.2. Research scope

This research studies a new validation techniques that can be used for mine blast models. The goal is to calculate the mine blast interaction pressure using the measured deformation over the plate's surface. This interaction pressure can be compared with existing models for validation purpose. The research question is: *Can displacement measurements obtained from DIC be used to calculate the interaction pressure to validate the current TNO mine blast model?*

Determining the interaction pressure from displacement data is an inverse problem. The corresponding forward problem, is finding the displacement for a given load/pressure. The standard forward problem in structural engineering is usually solved using FE simulations. For the inverse problem, several techniques exist. Both direct methods and iterative methods are often used. The direct methods are often limited in capability or bounded to linear problems. The non-linear behaviour of the current problem is the reason to use and study iterative methods. Figure 1.4 shows the final deformation of a plate after an experiment. The large plastic deformation shows the need for non-linear analysis.

Figure 1.4: The image shows a plate after an experiment. The top of the plate is marked with a somewhat random pattern necessary for the DIC measurements. The straight bar positioned on top emphasizes that the plate has a large final deformation. Non linear modeling due to material non-linearity will be required.

The iterative method is based on the minimization of the error (the objective function) between measurement and simulation displacements. Here the optimization variable is the pressure used for the simulation. The aim is thus to find a pressure such that the solution of the forward problem (the simulation) matches the measurements. Hence in this thesis the inverse problem is reduced to a minimization problem which will be iterative solved. This is a usual approach for non-linear inverse problems. Efficient optimization algorithms require the gradient of the objective function. This gradient is determined by solving the transient adjoint problem.

This research first studies the inverse problem for a linear Kirchhoff-Love (KL) plate model. Here the transient adjoint problem for a KL plate will be derived. Using the adjoint solution the gradient is obtained such that efficient gradient of descent algorithms can be used to minimize to objective function. Three benchmark pressures are used to study the behaviour of the Inverse Measurement Algorithm (IMA). The first is a smooth bench mark pressure, not related to the expected mine blast interaction pressure. The second is a more local pressure distribution, closer related to the expected mine blast interaction pressure. The final pressure distribution is based on measured pressure distributions.

After the IMA is studied for the linear KL plate the problem is researched for a general continuum. The transient adjoint problem is derived for an elastic material model for a general continuum. The IMA is researched for a continuum plate model using a non-linear elastic material model. The non-linear elastic model aims to approximate the plastic behaviour assuming monotonically increasing strain during the mine blast loading. This research does not consider 'real' plasticity which is left for future research.

Finally the developed IMA will be used to calculate the interaction pressure for a real experiment. The obtained pressure distribution will be analyzed in detail and be compared with the TNO model. In general it is observed that the displacement always converges quite accurately to the measurment data however the pressure distribution does not. This limitations of the IMA sheds light on the limitations of the validation process used by many researchers.

1.3. Report structure

This work is carried out at TNO hence some background information concerning their methods models and test setup is given in Chapter 2. A brief review of mine blast focused on experiments and modeling is included. Also a short review of current validation techniques is given in this Chapter. This should motivate the reader why this research is relevant. Before discussing any algorithm to solve the inverse problem one needs a way to check if such an algorithm works. For this purpose Chapter 3 discusses existing bench mark tests and proposes a new bench mark pressure model based on experimental results from the university of Sheffield [40]. Inverse problems are the discussion of Chapter 4. Here first a small review of force indentification techniques is given. It is argued that in this specific case reducing the inverse method to an optimization method is the best way to solve this problems. Some popular optimization methods are discussed in this chapter. The most suitable optimization method are argued to be the first order methods that require the gradient of the objective function. This gradient is determined using the adjoint method which is discussed in the next two chapters. In Chapter 5 a plate model for the forward problem and the corresponding adjoint problem will be discussed. Also the implementation and verification are discussed here. Chapter 6 is similar to Chapter 5 however the model is applicable for a general continuum. The implementation will use a non-linear elastic material model to represent plasticity under the assumption of monotonically increasing strain. Results of both plate models for several tests including the bench mark problem are discussed in Chapter 7. Finally the algorithm is applied on existing DIC data. These results are discussed in Chapter 9. Chapter 10 summarized the results found in this research and in Chapter 11 recommendations for further research are given.

2

Background

To introduce the current methods employed by TNO for modeling mine blast events some background to mine blast modeling is required. In this chapter a brief review of mine blast research focused on a variety of popular modeling techniques is given. Secondly a short discussion concerning popular validation methods in the field is given to support the current research. Finally the TNO mine blast model and calibration method is explained.

2.1. Mine blast

A mine blast, according to Bergeron, Walker and Coffey [13] consists of three phases, detonation products soil interaction, gas expansion and soil ejecta phase. Accurately modeling mine blasts is a difficult process. A variety of models to determine the mine blast loading for the simulations exist. An excellent review of several mine blast models and experiments is given by Anderson, Behner and Weiss [11]. They point out that research started with empirical models and trends continued to several simulation methods where the complete explosion process is modeled.

2.1.1. Empirical model: Initial impulse

Several experimental setups exist to determine the impulse transferred to a structure. The simplest experiment is the 'flying plate' experiment. Here a plate is placed on top of an explosive and during the mine blast its trajectory is measured using a camera. From the trajectory the initial velocity can be calculated. The impulse transferred can then be obtained when the mass of the plate is known. A sketch of such a setup is shown in Figure 2.1.

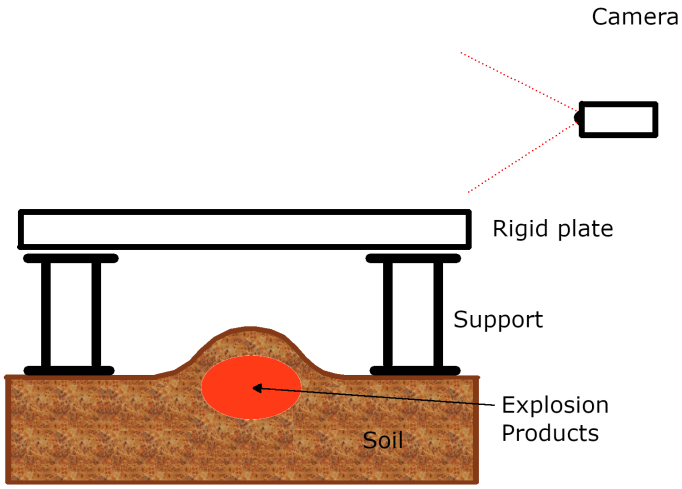

Figure 2.1: Illustration of the flying plate experiment. The plate is placed on top of supports which ensure the correct initial distance. The plate is not constrained and hence can fly away during the mine blast event. The actual initial velocity is zero, however the experiments aims to find $v(0)$ by assuming finite initial velocity as caused by instant impulse transferred from the mine blast event. This velocity is calculated from the height of flight and/or velocity measured using the camera.

Such an experiment only measures the integral impulse transferred to the plate. To measure more locally other setups exits. The experimental setup used by Westine [47] uses a rigid plate with impulse plugs inserted. The trajectory of the plugs is again measured to obtain the impulse transferred to the impulse plug. In this way the impulse is more locally measured such that a spatial impulse distribution can be obtained. The setup is sketched in Figure 2.2.

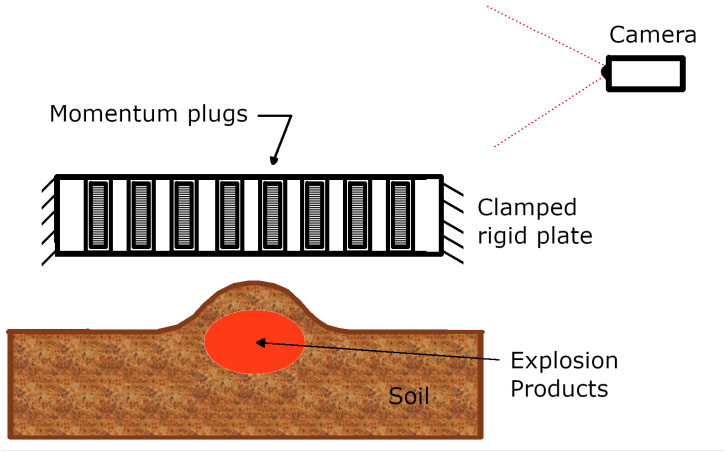

Figure 2.2: The illustration shows a thick rigid plate clamped along the edges. Several holes in the plate support insert plugs. These plugs are free to fly out the plate due to the mine blast loading. Camera measurements allow the determination of the initial velocity of the separate plugs similar as the flying plate experiment. This results in several spatial measurements of the impulse distribution.

The specific impulse (impulse per unit area) distribution of the Westine model is a function of several parameters of the experimental setup and geometry calibrated using several experiments. Several similar methods exist using e.g. momentum plates or momentum rings. From these methods no time dependent loading is known. Under the assumption that the loading occurs fast these models are often used by calculating an initial velocity of the excited structure from the specific impulse function. The mine blast event is then modeled as a structure with an initial impulse.

2.1.2. Empirical model: Pressure time

Research into the empirical Westine model, explained in [47], by Bouamoul, Fillion-Gourdea, Toussaint and Durocher [4] concluded that a purely impulsive model is inaccurate and will over estimate the structural deflection. They investigated several pressure time models however only state the final one that matched best with their experimental results. This model is a Friedlander waveform multiplied with a half sin function were only the positive duration of the Friedlander waveform is used [36]. This waveform has a rather slow rise time, compared to experimental pressure time results e.g. found by [42]. However they state that at the time of their experiments they were not aware of experimental pressure time measurements. The main relevance of their research for this paper is to support the need of an accurate pressure time model.

2.1.3. Model the complete explosion process

The research from Fourney, Leiste, Bonenberger and Goodings [52] concluded that Fluid Structure Interaction (FSI) [1] effects, neglected by empirical pressure time models, play an important role during mine blast loading. M. Saleh and L. Edwards [32] compare the empirical Conwep [20] and their ALE model to show that FSI plays an important role.

Models capable of FSI effects often simulate the complete explosion process. One method often used is the Multi Material Arbitrary Lagrangian Eulerian (MMALE) method. Fewer research is done in Smoothed Particle Hydrodynamics (SPH) simulations, which avoid difficulties of mesh deformation and coupling. Both methods

[1] In the current paper, FSI can both refer to the interaction between the detonation products with the soil, the structure or the surrounding air and also the interaction of the soil with the structure or surrounding air. This convention of the abbreviation 'FSI' will be used in this paper where the meaning is always clear from the context.

are computationally very expensive compared to the empirical models. A large study, done by A. Bouamoul [3], compares both methods for several experimentally validated simulations. The simulation domain used is shown in figure 2.3

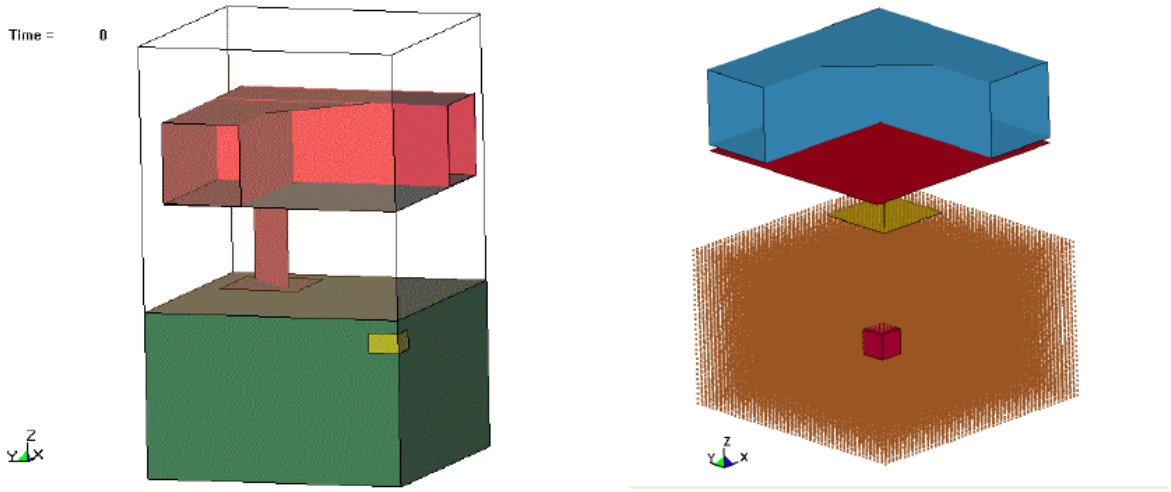

Figure 2.3: ALE and SPH simulation from A. Bouamoul [3], left shows the continuum ALE model and right the SPH model. In both models the complete explosion process; explosive, soil and structure is modeled.

2.2. Validation

Independent of the chosen model, validation is necessary. Several methods to validate mine blast models are discussed below. Often the experimental setups used for mine blast calibration are similar to the ones used for validation.

2.2.1. Deformation comparison

One popular method among mine blast researchers to validate their model by means of experiments which compare final structural deformation, e.g. [21]. TNO and DMO have a unique setup where DIC measurements are used during the mine blast event such that the deformation can be compared for multiple points in time. A description of the test setup is given in next section. Deformations never match the experiments exactly, none of the researches found mentioned the implications of the discrepancy in deformations for the accuracy of the mine blast model. This seems to be important and hence is a field that need to be studied.

2.2.2. Integral impulse measuring

The total impulse transferred to a rigid plate can be measured using e.g. a ballistic pendulum [5] or by means of capturing the global motion of a structural object [4] [16] [49] [11]. This object could be a flying plate as explained earlier or simple model of a vehicle bottom, and even a complete vehicle. The information gained by such an experiment is often only the integral impulse transferred since only global motion is obtained.

2.2.3. Local impulse measuring

Other researchers take validation one step further. The experimental set up using e.g. impulse plugs from which the empirical Westine model [47] was constructed, can be simulated as well to validate local impulse transferred. Similar methods are the use of momentum plates [19] or momentum rings [49], these methods however lack the pressure time information. Leiste [48] uses a punch gage test to verify peak pressures. This test consists of a steel target plate with counterbore holes in which brass inserts are placed. The applied pressure resulting in shear failure of the brass insert, which is then pushed through the counterbore hole, can be calculated. The thickness of the insert is varied to anticipate on different maximum pressure values. For this test the forward problem, calculation of the shear failure, is static and simplified for which no justification is given. Brass specimens that

were partially sheared are the expected cause of the short time dependent loading however no analysis method for these specimens is mentioned.

2.2.4. State-of-the-art: time dependent measurements

The importance of correctly modeling the pressure time loading was the basis for Leiste [48] from the university of Maryland and Rigby, Clarke, Tyas, Reay, Warren, Gant and Elgy [42] from the university of Sheffield to create their experimental setup. Their experimental setup made it possible to include spatial pressure distributions using multiple Hopkinson Pressure Bars (HPB's). Schwer and Rigby [28] showed that their MMALE model is in good agreement with the experimental impulse transfer however have poor accuracy in the corresponding pressure time loading.

To the author's best of knowledge the experimental setup employed by Rigby et al. [42] is the current State-of-the-art to measure spatial distributed pressure time loading and can indeed be used for model validation. There are however some limitations. The current configuration of their experimental setup is not capable of measuring the interaction pressure for deformable structures such that FSI effects cannot be taken into account. The author of this paper is of the opinion that extending their setup to measure deformable structures is most likely hard or not possible. For such an experiment the HPB's need to follow the deformation of the plate, they should not be clamped in the plate also not due to deformation of the plate and at the same time measurements need to be taken. Furthermore the duration of the measurement for a moving HPB implies multiple waves are present inside the HPB due to reflections, which makes measurements harder. Another issue Rigby et al. [41] states is that the soil used in agreement with STANdardization AGreement (STANAG) 4569 certification [37] gives large spread due to presence of large grain size.

There is a need for measuring the spatial distributed pressure time loading for structures subjected to mine blast loading for a large variety of soil types including STANAG 4569 soil [37]. Ideally one would measure deformable structures, representative for actual structures to be modeled such that numerical models can be validated in their range of interest. Exactly that is possible with the test rig and inverse measurement techniques.

2.3. TNO mine blast model and calibration

The thesis assignment is done at Structural Dynamics (SD) department of TNO, hence some background information concerning the methods employed by TNO is needed. The cost of full-scale testing of military vehicles for the Defence Material Organization (DMO) are reduced by the use of simulations made by the SD department of TNO. TNO has done research in modeling structures excited by buried mine explosions and developed a test rig to calibrate their models for structures of the same scale as the vehicles to be modeled.

2.3.1. The test rig

The test rig positions a plate, clamped along the edges, with a variable standoff distance from the ground. Above the plate a camera is mounted such the deformation of the plate can be computed using Digital Image Correlation (DIC) techniques. The test rig is free to jump upwards, only restricted by its own weight. A sketch of the test rig is given in Figure 2.4a and the actual test rig is shown in Figure 2.4b.

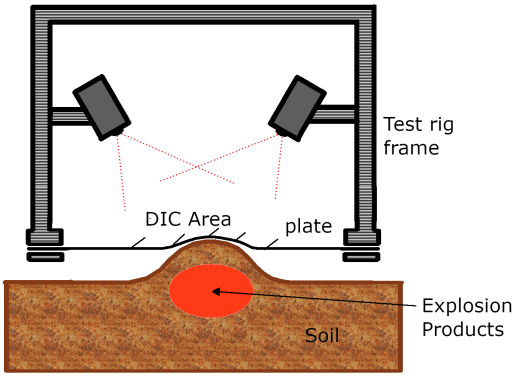

(a) The test rig used by TNO to calibrate empirical models. The plate deflection is measured using the DIC with two cameras as shown.

(b) The test rig during an experiment, one can see the soil ejecta and the ignition of detonation products. It can be seen that the test rig jumps upwards.

TNO has done several tests for sandy-gravel soil and charge mass in accordance with STANAG 4569 [37]. The parameters varied are the charge mass and the burial depth. The impulse obtained from experiments is quantified by the jump height of the test rig such that

$$I_{experiment} = M\sqrt{2gh} \tag{2.1}$$

here M is the test rig mass, g the gravitational constant and h the jump height. The impulse obtained from Westine model [47] is scaled using C_{imp} such that the experimental jump height and modeled jump height are the same, that is

$$I(x, y, z) = I_{westine}(x, y, z) * C_{imp} \tag{2.2}$$

here $I_{westine}(x, y, z)$ is the impulse per unit surface area on spatial location (x,y,z) obtained from Westine model. I(x,y,z) is the impulse distribution used by TNO.

TNO does not just use an initial impulse model, instead a time dependent pressure load consistent with the previously explained impulse distribution is used. The second calibration factor, C_{press}, is used to calibrate a simplified pressure time loading model of the explosion. The pressure model over time used is a simple triangular pulse, Figure 2.5. The duration of the triangular pulse has a large influence on the deformation of the plate, hence this deformation is used to calibrate the triangular pressure model.

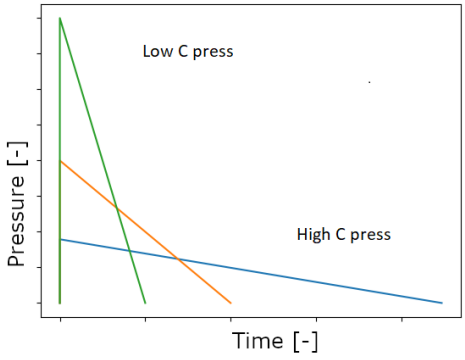

(a) Pressure versus time loading for constant impulse, the aspect ratio is varied

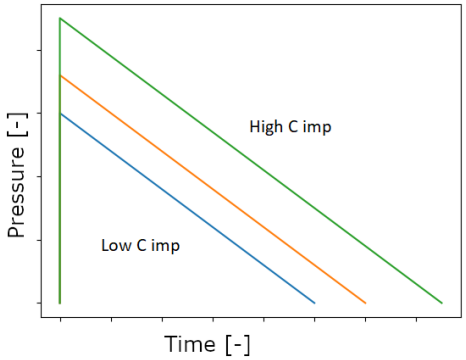

(b) Pressure versus time loading for constant aspect ratio, the impulse is varied

Figure 2.5: Pressure versus time model for Westine impulse. The slope of the decaying phase (aspect ratio) and the total impulse of the triangular pulse are adjustable.

There are some limitations to the current model, some of which are expected to be the cause of discrepancies in global motion for the full vehicle FE simulations. Calibration factors C_{press} and C_{imp} are not a function of

spatial position. For C_{imp} this implies the assumption that the spatial impulse distribution of Westine model is accurate. For C_{press} this implies the same decaying slope for pressure time loading at all locations. To study these assumptions a pressure distribution is required. The aim of this research is to find such a distribution from existing DIC test data.

3

Benchmark test

The focus of this research is to solve an Inverse Measurement Problem (IMP). To solve this problem an algorithm will be developed. In order to verify whether the algorithm works a benchmark problem is required. The assumption is that if the algorithm performs well on the benchmark problem then it will work on similar mine blast problems. Hence if the IMP algorithm is able to calculate pressure data from displacement data for the benchmark test then it is assumed that the same algorithm is capable of measuring the interaction pressure from actual mine blast DIC measurements. The difference between the benchmark test and the actual experiment is that for the benchmark test the applied pressure is known hence comparison of the actual pressure and the solved pressure is possible, such that the algorithm performance can be verified.

The benchmark test is constructed by simulation of the forward problem using a known pressure distribution $P_s(x,t)$. From this simulation the deflections on the surface at discrete locations, that could be obtained using DIC, are extracted and noise representing measurement error is added. This data is input for the developed IMP algorithm from which an pressure distribution is the output. This pressure distribution is compared with the simulated pressure distribution to verify the model. Using the benchmark test it can be determined which IMP algorithm performs best for several noise levels. A flow chart of this process is given in Figure 3.1

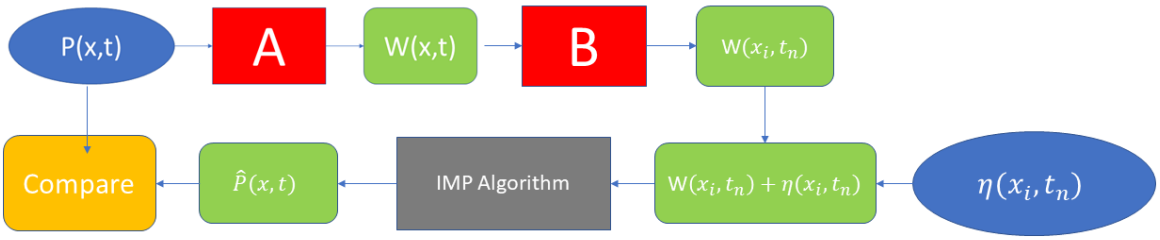

Figure 3.1: From the simulation pressure 'P(x,t)' the operator 'A' determines the displacement which operator 'B' samples to represent DIC data. Noise is added '$\eta(x_i, t_n)$' to simulate measurement noise. The IMP algorithm solves for the pressure '$\hat{P}(x,t)$' which is compared to the simulated pressure.

3.1. Existing bench mark tests

This research is not the first that aims to find the spatial distributed pressure time loading caused by an explosion using DIC measurements by solving the IMP. The researchers Shaowen Xu, Xiaomin Deng, Vikrant Tiwari, Michael A. Sutton, William L. Fourney and Damien Bretall [44] have the the exact same approach, however their function space for the pressure is spatially quite limited. In [44] they have spatial constant pressure and in [39] they assume an exponential distribution see Figure 3.2.

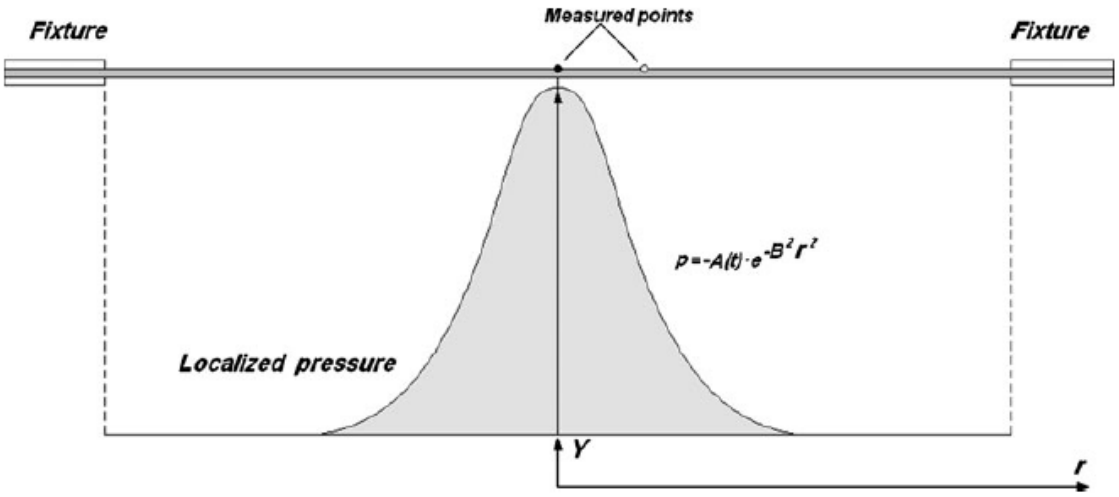

Figure 3.2: The exponential pressure distribution from [39] is shown. The model has only two time dependent variables and is a global distributed pressure. For the experimental setup from TNO one expects a more local pressure distribution moving over time.

These simulation pressure models for their bench mark test are to limited to validate the current model. No recent developments of [44], [39] are found. Their bench mark problem uses a circular plate, however to stay consistent with the TNO test rig this research will use a rectangular plate.

3.2. Model and simplifications

The benchmark problem should be similar to the test setup however a complete model of the test setup is too computationally expensive. For this reason some simplifications are made. The main difficulty arises with the boundary conditions of the plate. Two different boundary conditions will be discussed in the next section, the main setup will be discussed here.

- The dimensions of the plate will be equal to the dimensions used in the test rig which are confidential. It can however be said that the plate is square of size 'L' and thickness 't'.
- The plate is modeled as rigidly clamped at the test rig boundary. In the actual experiment the plate is mechanically clamped to the test rig however such a connection is never perfectly clamped. The stiffness of this connection and possible slip of the plate can be of large influence to the global impulse transferred [14].
- The surface traction caused by the explosive is assumed only in normal direction, which is referred to as the pressure. Shear components are thus neglected
- The total impulse 'I' of the applied load P(x,t) is chosen to cause similar jump height as test rig experiments, which is confidential.

3.3. Dynamic boundary conditions

The plate is fixed to a test rig that is allowed to jump upwards. Assuming that the test rig can be modeled as rigid implies that the plate boundary does not move w.r.t the test rig. Note however that the rigid body motion of the test rig will cause the plate and the boundary to move. Two different model domains are distinguished, the plate Ω_p and the rigid test rig Ω_{TR}. The external force applied on the test rig '$\boldsymbol{F}_{ex}(t)$' 3.1 is assumed to be only caused by gravity '$\boldsymbol{F}_g(t)$' 3.2 and the plate test rig boundary force '$\boldsymbol{F}_b(t)$', Equation 3.3. The torque acting in the center of gravity of the test rig is assumed only due to the plate test rig boundary force. Here '$r(x)$' is the distance from the test rig center of gravity and location 'x'.

$$\boldsymbol{F}_{ex}(t) = \boldsymbol{F}_g(t) + \boldsymbol{F}_b(t) \tag{3.1}$$

$$\boldsymbol{F}_g(t) = gM_{testrig}\boldsymbol{e_g} \tag{3.2}$$

$$\boldsymbol{F}_b(t) = \int_{\partial\Omega_{TR}\cap\partial\Omega_p} \boldsymbol{t}(x)\mathrm{d}\partial\Omega \tag{3.3}$$

$$\boldsymbol{\tau}(t) = \int_{\partial\Omega_{TR}\cap\partial\Omega_p} \boldsymbol{r(x)} \times \boldsymbol{t}(x)\mathrm{d}\partial\Omega \tag{3.4}$$

These equations link the rigid body motion of the test rig and the plate deformation and hence need to be solved concurrently.

3.4. Static boundary conditions

The dynamic boundary conditions discussed above are simplified. It is assumed that the loading takes place in a very short time such that the test rig has not yet moved after the loading. The plate boundary conditions are assumed non moving during the loading, such that the plate deformation during loading can be considered separately. Furthermore the center of gravity of the combined plate and test rig is assumed to be not influenced by the plate's deformation, such that the rigid body motion of the test rig can be analyzed separate as well. The test rig rigid motion will then be determined from initial linear and angular velocity only, which can be determined from the load applied on the plate. The test rig angular velocity is quite small, since the loading and test setup is symmetric. Hence this research only uses the jump height.

3.5. Simulation pressure

The pressure used for the simulations should be similar to the actual pressure. It was found for the static Kirchhoff Love plate that very localized pressure distributions, which have large spatial pressure gradients are more difficult to solve for using an IMP algorithm. More global distributed pressure with small gradients, such as the exponential distribution used by [39] are easier to solve for. In [40] it is shown that the distribution is more localized. The simulation pressure will be chosen similar to [40]. It can be seen in their paper that the pressure can be approximated with a radially outward moving pressure. Note that pressure distribution can be localized or global depending on the geometry of the setup. For most of the TNO experiments an localized load is expected, hence the benchmark problem will be designed as such.

The pressure model proposed here is a bit arbitrarily however its purpose is to test the IMP algorithm, not to accurately represent a mine blast. The proposed model still has similar characteristics of a mine blast loading. For that reason it is expected to be a good benchmark test pressure to verify IMP algorithms.

The pressure model is radial symmetric. For the pressure model it is assumed that the velocity of this moving localized pressure distribution is constant (v), and the amplitude decreases quadratic being zero for $r = R$ where 'R' is the largest dimension of the plate. Spatially the pressure increase with a jump discontinuity and decreasing exponentially given by

$$P(r,t) = \begin{Bmatrix} Ae^{-(vt-r)w}(1-(\frac{r}{R})^2), & vt-r>0 \,\mathrm{AND}\, r<R \\ 0, & \text{otherwise} \end{Bmatrix} \tag{3.5}$$

here 'A' scales the total size of the impulse and 'r' is the radial location on the plate measured from the center. A normalized plot shows the pressure distribution for several point in time in Figure 3.3. The coefficients A, w, v, that determine the mine blast model are chosen to accurately represent the test rig case and are for that reason confidential. The method used to determine these parameters are discussed in Appendix B.

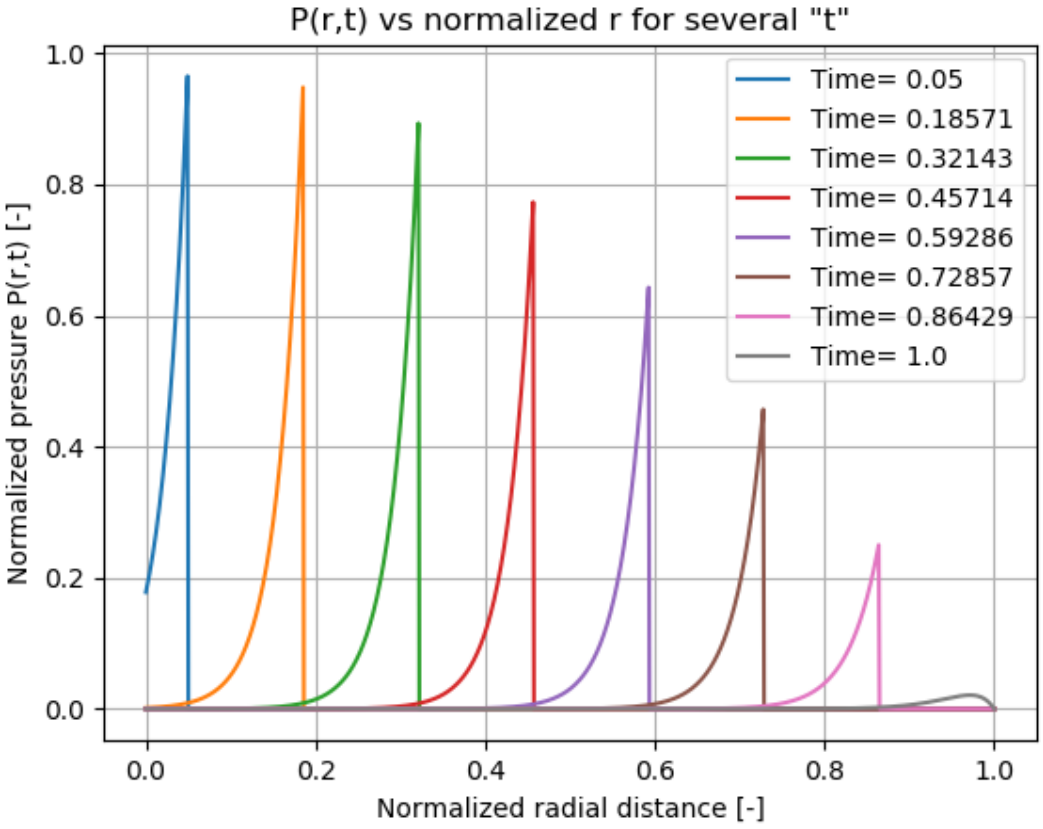

Figure 3.3: Simulation pressure 'P(r,t)' plotted along the normalized radial distance of the plate for several points in time. Note the large spatial gradients and a very localized pressure distribution.

4

Inverse measurement problem algorithm

This chapter discusses the algorithm used to solve the inverse measurement problem in general. First it is explained why some common direct methods are not used. Then the optimization method used for this research is explained. Several popular optimization algorithms are reviewed. It is explained why for this research gradient of descent among the reviewed algorithms is chosen. Finally a flow chart for of the optimization algorithm is given.

4.1. The inverse problem

Solving for the pressure when the displacement is known is an Inverse Measurement Problem (IMP). These type of problems often occur in measurement devices, hence the name. Here the aim is indeed to measure the pressure using the DIC displacement measurements. In mechanics this problem is often named force identification problem. The normal or forward problem here is solving displacement for a known pressure distribution. For linear and some non-linear problems several direct methods exists, that is without the need for iteration. The advantage of such methods is that they are much faster.

4.1.1. SWAT

T.J. Kreittinger [46] gives an excellent review of force identification techniques and studies the Sum of Weighted Acceleration Technique (SWAT). This method is studied in time and frequency domain. The SWAT method assumes a lumped mass system and determines the weights of these masses 'w_i' from response measurements. When these weights are known the force can be determined from acceleration measurements, Equation 4.1. The limitation is that SWAT can only determine the total external force and not the separate external forces. This makes SWAT too limited for the current research.

$$F_r(t) = \sum w_i a_i(t) \tag{4.1}$$

4.1.2. ISF

Another technique developed by A.D. Stelzner and D.C. Kammer is the Inverse Structural Filter (ISF) technique [7]. This technique considers a discrete state space representation of the system which is identified by means of vibration tests. The method is capable of measuring multiple input forces (as many as there are sensors). J.F. Doyle [25] uses deconvolution techniques for force identification. The deconvolution method is based on the assumption that the response can be written as the convolution of the force with an known function representing the structure 4.2. This method thus requires the system 'g' to be known. The usual way to solve this system is by transformation to the frequency domain 4.3 and solving 4.4.

$$u(t) = \int_0^t g(t-\tau) f(\tau) \mathrm{d}\tau \tag{4.2}$$

$$U(\omega) = G(\omega) F(\omega) \tag{4.3}$$

$$F(\omega) = \frac{U(\omega)}{G(\omega)} \tag{4.4}$$

The discrete form is similar and often used since measurement data is discrete. One problem mentioned by J.F. Doyle [25] is that G can be zero for some frequencies depending on the problem. Another problem for exact solutions is that they are sensitive to noise. From static Kirchhoff love experiments it was found that the sensitivity to noise is too large. A similar direct solution in combination with regularization might solve this problem. This method seems however only applicable for linear systems for which 'g' can be determined. This research will focus on techniques that are applicable for non linear systems such that material non linearity can be taken into account. In the introduction of this report Figure 1.4 shows the large final deformation of the plate supporting the need for a non-linear material model.

4.1.3. Optimization method

One method often employed for inverse problems which can be used for a large variety of problems is by means of reformulating the problem into an optimization problem. The minimization problem is to reduce the error between measurement and model. The error is often taken as the sum or integral of the square of the difference that is,

$$J[w] = \int_0^T \int_\Omega (w(x,t) - v(x,t))^2 \mathrm{d}\Omega \mathrm{d}t \tag{4.5}$$

here w(x,t) is the model and v(x,t) is the measurement data. One of the difficulties is that w(x,t) is linked to P(x,t) by means of solving the forward problem. Hence J has to be minimized for some P, that is J[w(x,t;P)]. Note that here P is still a continuous function. Discretizing P(x,t) using e.g. shape function gives

$$P(x,t) = \sum_i \psi_i(x,t) a_i. \tag{4.6}$$

The problem now reduces to finding coefficients a_i which define a pressure P(x,t) which causes a displacement w(x,t) that has error J which should be minimized. Thus minimize $J[a_i]$ for some a_i. The disadvantage is that most optimization problems need to be solved by means of itterative methods, which is often a slow procedure. A major advantange however is the possibility to steer the function P(x,t) in some direction based on prior knowledge. Since IMP are non-unique the possibility to use prior knowledge of the solution is a major benefit. Often for example the solution is known to have some smoothness properties, which could be enforced by adding a penalty to the functional J for non-smooth functions P. This is called regularization, in statistical regression Tikhonov regularization is well known [15]. Other regularization methods are discussed by M. Gong, X. Jiang, H. Li [31]. For this specific problem one expects, based on the geometry of the problem, that P(x,t) is radial symmetric. Hence by only considering a radial symmetric function space one reduces the amount of variables and makes the problem less sensitive to noise. One could also constrain P to only positive values ($P > 0$) adding an inequality constrained to the optimization problem. This reduces oscillations which are else often observed. For this problem negative pressure values are not expected based on prior knowledge.

4.2. Optimization algorithms

A large variety of methods to solve optimization problems exists. The optimization problem can be written as Equation 4.7. In the current problem the variables '$\boldsymbol{x}$' would determine the pressure.

$$\boldsymbol{x} = \arg\min_{\exists \boldsymbol{x}} f(\boldsymbol{x}) \tag{4.7}$$

That is the vector $\boldsymbol{x}$ has to be found that minimizes the objective function 'f'. The design space of vector $\boldsymbol{x}$ can be constrained by a relational constrained Equation 4.8 or an inequality constrained Equation 4.9.

$$g(\boldsymbol{x}) = 0 \tag{4.8}$$

$$h(\boldsymbol{x}) \leq 0 \tag{4.9}$$

The constrained optimization problem with only equality constraints can be changed to an unconstrained different problem using Lagrange multipliers [17]. The Karush-Kuhn-Tucker condition (KKT) generalizes this approach for inequality constraints [35].

Several optimization algorithms exists. G. Venter [22] gives an basic overview of several optimization techniques. His review gives a good introduction into the topic. The Response Surface Method (RSM) is reviewed by A.I. Khuri, S. Mukhopadhyay [9]. This method requires a large amount of objective function evaluations for a large number of design parameters and is for that reason not feasible for the current research. W. Hare, J. Nutini, S. Tesfamariam [51] give a more detailed review of other non-gradient based methods. Pseudo code for a variety of algorithms is shown. According to them, however gradient methods are preferred when possible. The follow up research aims to use gradient based methods such that non-gradient based methods are not studied.

4.2.1. Gradient based methods

In the book written by A. Antoniou, W.S Lu [2] optimization methods are thoroughly discussed. In most methods an initial design point '$\boldsymbol{x_0}$' is either chosen random or based on prior knowledge. The objective function is evaluated for this point and a new design point has to be chosen. The update is often done in the direction of the gradient, Equation 4.10. This method is called gradient of descent, the negative sign causes the next design point to move in the direction where the objective is decreasing.

$$\boldsymbol{x}_{n+1} = \boldsymbol{x}_n - \alpha_n \nabla f(\boldsymbol{x}_n) \tag{4.10}$$

The parameter 'α', the step size, varies for different algorithms. Too large step size will cause the method to overshoot, too small step size will have slow convergence. One can use constant step size or adaptive step size. In [6] A. Kozma, C. Conte, M. Diehl give an overview and compare several classical methods. Line search algorithms [35] perform multiple iterations along the gradient direction to find the optimum along that line. At the new found optimum the gradient is computed in which direction the new step is taken. Often algorithms do not compute the exact optimum along that line, since that is computationally expensive and not the optimum of interest, continuing with the next step before the optimum is found is often the approach. One particular interesting line search method is the use of one newton step in the line search direction. Consider the taylor expansion of the objective function along the gradient direction, Equation 4.11. The optimal step size 'α' is such that this quadratic is optimal 4.12. Solving for 'α' gives Equation 4.13. The first derivative, Equation 4.14 is obtained from the gradient alone and the second derivative, Equation 4.15 can be approximated with finite difference.

$$f(\boldsymbol{x}_n + \alpha \nabla f(\boldsymbol{x}_n)) = f(\boldsymbol{x}_n) + \alpha \frac{\mathrm{d}}{\mathrm{d}\alpha}|_{\alpha=0} f(\boldsymbol{x}_n + \alpha \nabla f(\boldsymbol{x}_n)) + \frac{1}{2}\alpha^2 \frac{\mathrm{d}^2}{\mathrm{d}\alpha^2}|_{\alpha=0} f(\boldsymbol{x}_n + \alpha \nabla f(\boldsymbol{x}_n)) \tag{4.11}$$

$$0 = \frac{\mathrm{d}}{\mathrm{d}\alpha} f(\boldsymbol{x}_n + \alpha \nabla f(\boldsymbol{x}_n)) = \frac{\mathrm{d}}{\mathrm{d}\alpha}|_{\alpha=0} f(\boldsymbol{x}_n + \alpha \nabla f(\boldsymbol{x}_n)) + \alpha \frac{\mathrm{d}^2}{\mathrm{d}\alpha^2}|_{\alpha=0} f(\boldsymbol{x}_n + \alpha \nabla f(\boldsymbol{x}_n)) \tag{4.12}$$

$$\alpha = \frac{\frac{\mathrm{d}}{\mathrm{d}\alpha}|_{\alpha=0} f(\boldsymbol{x}_n + \alpha \nabla f(\boldsymbol{x}_n))}{\frac{\mathrm{d}^2}{\mathrm{d}\alpha^2}|_{\alpha=0} f(\boldsymbol{x}_n + \alpha \nabla f(\boldsymbol{x}_n))} \tag{4.13}$$

$$\frac{\mathrm{d}}{\mathrm{d}\alpha}|_{\alpha=0} f(\boldsymbol{x}_n + \alpha \nabla f(\boldsymbol{x}_n)) = \nabla f(\boldsymbol{x}_n) \cdot \nabla f(\boldsymbol{x}_n) \tag{4.14}$$

$$\frac{\mathrm{d}^2}{\mathrm{d}\alpha^2}|_{\alpha=0} f(\boldsymbol{x}_n + \alpha \nabla f(\boldsymbol{x}_n)) \approx \frac{\nabla f(\boldsymbol{x}_n + \Delta\alpha \nabla f(\boldsymbol{x}_n)) - \nabla f(\boldsymbol{x}_n)}{\Delta\alpha} \tag{4.15}$$

When the gradient can be efficiently calculated the second derivative along the gradient direction can be computed, which can be used to calculate a Newton step size along the gradient direction. This method allows an efficient step size to be determined at the cost of one extra gradient calculation.

4.2.2. Conjugate gradient method

The method of conjugate gradients was initially designed to solve a system of linear equations in the form $A\boldsymbol{x} = \boldsymbol{y}$ [34]. Here the method relies on minimizing the quadratic $f(\boldsymbol{x}) = \frac{1}{2}\boldsymbol{x}^T A\boldsymbol{x} - \boldsymbol{y} \cdot \boldsymbol{x}$. For such quadratic functions it can be proven that the method converges in 'n' steps, where 'n' is the dimension of $\boldsymbol{x}$. The optimization method initializes in gradient of descent direction and then takes steps in conjugate directions w.r.t. matrix A. The conjugate-gradient method requires the hessian matrix. A popular method described in [2] based on the conjugate gradient method is the 'Fletcher-Reeves' method [38]. This method does not require the hessian matrix at the expense of requiring a line search for each step. Which can be useful when the hessian is not known or expensive to compute. An introduction to the topic with help full intuitive insight is given in [26]. Several similar algorithms were invented later, a generalization is given by Y. Liu, C. Storey [53].

4.2.3. Newtons method

Newtons method is a well known method in optimization. Consider the Taylor expansion of the objective function Equation 4.16. The aim is to make a step $\boldsymbol{h}$ such that the Taylor approximation of the objective is optimum, thus in accordance with Equation 4.17. Rewriting gives the step to take Equation 4.18 which leads to the iterative algorithm Equation 4.19.

$$f(\boldsymbol{x}+\boldsymbol{h}) = f(\boldsymbol{x}) + \nabla f(\boldsymbol{x})\boldsymbol{h} + \frac{1}{2}\boldsymbol{h}^T \boldsymbol{H}\boldsymbol{h} \tag{4.16}$$

$$\frac{\partial f(\boldsymbol{x}+\boldsymbol{h})}{\partial \boldsymbol{h}} = \nabla f(\boldsymbol{x}) + \boldsymbol{H}\boldsymbol{h} = 0 \tag{4.17}$$

$$\boldsymbol{h} = -\boldsymbol{H}^{-1}\nabla f(\boldsymbol{x}) \tag{4.18}$$

$$\boldsymbol{x}_{n+1} = \boldsymbol{x}_n - \boldsymbol{H}^{-1}\nabla f(\boldsymbol{x}) \tag{4.19}$$

Note that here the step size is known, due to the assumption of a quadratic error surface (linearization of the gradient). It is however also possible to do a line search along the hessian gradient product direction. The method requires the Hessian matrix which is often expensive to compute or not possible to obtain. Researchers have, for this reason, developed so called quasi-Newton methods that approximate the hessian matrix. A good survey of these methods is provided by C. Xu, J. Zhang [10]. Multi-step quasi-Newton methods use the information of the previous step. J.A. Ford, I.A. Moghrabi [24] discuss these methods for optimization. To illustrate such a method, consider the linearization of the gradient, Equation 4.20

$$\nabla f(\boldsymbol{x}_n + \boldsymbol{h}) \approx \nabla f(\boldsymbol{x}_n) + \boldsymbol{H}\boldsymbol{h} \tag{4.20}$$

$$\boldsymbol{H}\boldsymbol{h} \approx \nabla f(\boldsymbol{x}_n + \boldsymbol{h}) - \nabla f(\boldsymbol{x}_n) \tag{4.21}$$

Assuming a quadratic error surface $f(\boldsymbol{x})$ the hessian matrix is constant. Equation 4.21 can be used where gradient at 'n' and 'n+1' are used together with '$\boldsymbol{h} = \boldsymbol{x}_{n+1} - \boldsymbol{x}_n$'. when enough linear independent steps $\boldsymbol{h}$ are made the system for the hessian matrix can be solved. Often far less steps are used to approximate the hessian. Ofcourse for non quadratic error surfaces this approach leads to an estimation of the hessian matrix. Other algorithms compute the hessian only once and use this one for all iterations, which works well for error surfaces that are close to quadratic.

For the current problem the amount of variables is so large (N) that the size of the hessian N^2 becomes problematic for storage. For that reason Newton or quasi-newton methods for optimization are not used.

4.2.4. Convergence criteria

The algorithms discussed so far are all designed to approach the optimum in an iterative manner. For such algorithms it is important to have an convergence criteria which determines weather the current solution is close enough to the optimum. Several convergence criteria exists, popular ones are

$$\begin{cases} \left|f(\boldsymbol{x}_{n+1}) - f(\boldsymbol{x}_n)\right| < \epsilon_1 \ or \\ \alpha < \epsilon_2 \ or \\ \nabla f \cdot \nabla f < \epsilon_3. \end{cases}$$

When the algorithm converges to a design point where gradients are small too large convergence settings for ϵ can cause premature convergence. On the other hand too small will cause unnecessary extra iterations. The value for ϵ will depend on the problem.

4.2.5. Global optimization

The algorithms discussed so far will only converge to local minimum. For Global optimization a more global search through the design space is required. In general there are several local minimums in the design space, one of which is the global minimum. J.S. Arora, O.A. Elwakeil, A.I. Chahande [27] discuss several algorithms that are designed to find a global minimum. One particular interesting method to research is tunneling, which uses the current minimum to change the problem to a root finding problem instead of an optimization problem. The aim is to find other design points where the cost function is equal or less then the current design point. For root finding problems the gradient alone determines the required step size alpha in newtons method for root finding. The aim is start optimization again at the new found roots.

4.2.6. Summary of methods chosen

Several methods exists for solving IMP. Direct methods are not applicable due to the non-linear nature of the problem, instead iterative methods are required. The measurements and simulation are compared by means of an objective functional which has to be minimized for some P(x,t). Several minimization algorithms exists, gradient of descent is chosen. The step size for the gradient of descent algorithm is determined by using one newton optimization step along the gradient line. The required second derivative is obtained using a finite difference step along the line and compute the gradient there.

4.3. The algorithm

In this section the algorithm used is explained in more detail. In Figure 4.1 a flow chart of the algorithm is given.

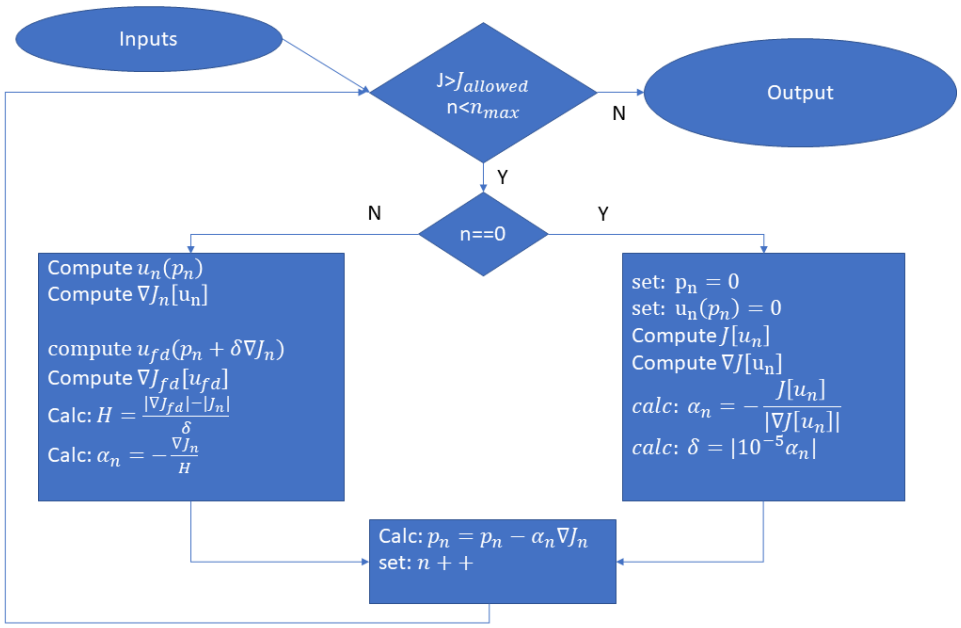

Figure 4.1: Flow chart of the gradient of descent optimization algorithm using Newton method for line search and Newton root finding step for the first iteration.

4.3.1. First step

The input of the algorithm is the displacement field obtained from DIC measurements. The output is the pressure distribution. In the first step the pressure in initialized with P=0. The solution of the forward problem in that case is trivially zero hence u=0. The objective function is calculated for that displacement. The adjoint problem is computed to obtain the gradient of the objective function. For the first step α is computed using a Newton root-finding step. Finally δ is computed. The step size for the finite difference computation of the second derivative along the gradient direction is δ. The size of δ is rather arbitrary. The value chosen was found to work for the current problem. In this block the most computational expensive procedure is the computation of the adjoint field to determine the gradient.

4.3.2. Successive steps

For n>0 first the displacements are computed by solving the forward problem. Secondly the gradient is computed by solving the adjoint problem. Again both the displacement and gradient is computed at a small step δ in the gradient direction. The step size of the gradient of descent method for n>0 are done using Newton optimization method along the gradient direction by approximation the second derivative using the finite difference method. In this block the most computational expensive procedures are the computation of the two forward problems and two adjoint fields.

5

Kirchhoff Love plate model

In this chapter the plate will be modeled as a Kirchhoff Love (KL) plate. The dynamic KL plate will be used to analyse the performance of the IMP algorithm. This chapter will discuss and derive the adjoint problem starting from the forward problem. This problem is self adjoint such that the same solver for the adjoint problem with only little adjustment can be used. The solution of both the forward and adjoint problem are both done numerical. The spatial discretization and time integration scheme are presented in this chapter. The chapter ends with the method of manufactured solutions used to check the numerical solution and a convergence test on the benchmark pressure model.

5.1. Forward problem

A Dynamic KL plate is modeled by the PDE 5.1. The boundary conditions may differ for each problem, for the current problem clamped boundary conditions are given by Equation 5.2. Since this is a second order time dependent problem there are two initial conditions given by Equation 5.3.

$$\nabla^4 w(\boldsymbol{x},t) + \frac{q(\boldsymbol{x},t)}{D} + \frac{2\rho h}{D}\ddot{w}(\boldsymbol{x},t) = 0 \ \boldsymbol{x} \in \Omega \, \forall \, t \tag{5.1}$$

$$w(\boldsymbol{x},t) = \nabla w(x,t) \cdot \boldsymbol{n} = 0, \ \boldsymbol{x} \in \partial\Omega \, \forall \, t \tag{5.2}$$

$$w(\boldsymbol{x},t) = f(\boldsymbol{x}), \ \dot{w}(\boldsymbol{x},t) = g(\boldsymbol{x}) \ \boldsymbol{x} \in \Omega \ t = 0 \tag{5.3}$$

5.2. Adjoint problem and the gradient

In this section the adjoint method is derived for a Kirchhoff Love plate model. The problem is given by the Partial Differential Equation (PDE) 5.1 with clamped boundary conditions 5.2 and initial conditions 5.3.

The solution of this problem '$w(\boldsymbol{x},t)$' is compared with the measurements '$v(\boldsymbol{x},t)$'. For the objective functional the L_2 norm is used, Equation 5.4. Adding the PDE multiplied with an yet unknown function ϕ gives $J[w]$, Equation 5.5. Since the PDE is zero $J[w] = F[w]$. The dependency notation is dropped to make the equations more readable 5.6.

$$F[w] = \int_0^T \int_\Omega \frac{1}{2}(w(\boldsymbol{x},t) - v(\boldsymbol{x},t))^2 \mathrm{d}\Omega \mathrm{d}t \tag{5.4}$$

$$J[w] = \int_0^T \int_\Omega \frac{1}{2}(w(\boldsymbol{x},t) - v(\boldsymbol{x},t))^2 + \phi(\boldsymbol{x},t)(\nabla^4 w(\boldsymbol{x},t) + \frac{q(\boldsymbol{x},t)}{D} + \frac{2\rho h}{D}\ddot{w}(\boldsymbol{x},t))\mathrm{d}\Omega \mathrm{d}t \tag{5.5}$$

$$= \int_0^T \int_\Omega \frac{1}{2}(w - v)^2 + \phi(\nabla^4 w + \frac{q}{D} + \frac{2\rho h}{D}\ddot{w})\mathrm{d}\Omega \mathrm{d}t \tag{5.6}$$

For this functional $J[w]$ the variation is given by Equation 5.7. The integral I_1 can be integrated by part four times giving Equation 5.8. Here the fact that the boundary is clamped, hence no variation is allowed together with conviniently chosen boundary conditions for ϕ are used, $\nabla\delta w \cdot \boldsymbol{n} = 0, \ w = 0, \ \nabla\phi \cdot \boldsymbol{n} = 0, \ \phi = 0 \ \boldsymbol{x} \in \partial\Omega \, \forall \, t$. Similar for integral I_2 integration by parts two times one obtains Equation 5.9. Here the fact that no variation in

initial conditions is allowed $\delta\dot{w} = 0,\ \delta w = 0\ \boldsymbol{x} \in \Omega\ t = 0$. Also the end conditions for ϕ are conveniently chosen $\phi = 0,\ \dot{\phi} = 0\ \boldsymbol{x} \in \Omega\ t = T$.

$$\delta J[w] = \int_0^T \int_\Omega (w - v)\delta w + \phi(\nabla^4(\delta w) + \frac{\delta q}{D} + \frac{2\rho h}{D}\delta\ddot{w})\mathrm{d}\Omega\mathrm{d}t \tag{5.7}$$

$$I_1 = \int_\Omega \phi\nabla^4(\delta w)\mathrm{d}\Omega = \int_\Omega \nabla^4(\phi)\delta w\mathrm{d}\Omega \tag{5.8}$$

$$I_2 = \int_0^T \phi\delta\ddot{w}\mathrm{d}t = \int_0^T \delta w\ddot{\phi}\mathrm{d}t \tag{5.9}$$

Now $J[w]$ can be rewritten into Equation 5.10. Choosing $(w - v + \nabla^4\phi + \frac{2\rho h}{D}\ddot{\phi}) = 0\ \boldsymbol{x} \in \Omega\ \forall\, t$ gives 5.11. One could now discretize 'q' using basis functions ψ_i such that $q = \sum_i \psi_i b_i$. The variation of q is then $\delta q = \sum_i \psi_i \delta b_i$. Substitution gives the gradient of J w.r.t b_i, Equation 5.12.

$$\delta J[w] = \int_0^T \int_\Omega (w - v + \nabla^4\phi + \frac{2\rho h}{D}\ddot{\phi})\delta w + \frac{\phi}{D}\delta q)\mathrm{d}\Omega\mathrm{d}t \tag{5.10}$$

$$\delta J[w] = \int_0^T \int_\Omega \frac{\phi}{D}\delta q\mathrm{d}\Omega\mathrm{d}t \tag{5.11}$$

$$\frac{\partial J}{\partial b_i} = \int_0^T \int_\Omega \frac{\phi}{D}\psi_i\mathrm{d}\Omega\mathrm{d}t \tag{5.12}$$

Sumarizing the gradient can be obtained by solving the adjoint problem for ϕ, which should be consistent with PDE 5.13, the boundary conditions 5.14 and the end conditions 5.15. Here ϕ should be solve backwards in time, since the end conditions instead of the initial condition is given. Note that the function 'w' is known from solving the direct problem. The gradient is then found by evaluation of the Integral 5.12 for each ψ_i. Usually this integration is less computationally expensive compared to solving the PDE for ϕ. Solving for ϕ only has to be done once, for this reason the adjoint method is computationally cheap compared to finite difference method, especially for for large amount of basis functions ψ_i.

$$(w - v + \nabla^4\phi + \frac{2\rho h}{D}\ddot{\phi}) = 0\ \boldsymbol{x} \in \Omega\ \forall\, t \tag{5.13}$$

$$\nabla\phi \cdot \boldsymbol{n} = 0,\ \phi = 0\ \boldsymbol{x} \in \partial\Omega\ \forall\, t \tag{5.14}$$

$$\phi = 0,\ \dot{\phi} = 0\ \boldsymbol{x} \in \Omega\ t = T \tag{5.15}$$

5.3. Numerical solution

This section discusses the numerical solution used for the kirchhoff love plate. First the weak formulation is used to then obtain the spatial discretization using trial and test functions. Then the Newmark time integration scheme used, will be explained.

5.3.1. Weak formulation

The weak formulation is used for the spatial FE discretization of the PDE. Accoding to Dubois and Reymond lemma [33] if the following holds 5.16.

$$\int_\Omega f(\boldsymbol{x})h(\boldsymbol{x})\mathrm{d}\Omega = 0\ \forall h(\boldsymbol{x}) \in \mathbb{C}_0^1(\Omega) \tag{5.16}$$

And $f(\boldsymbol{x}) \in \mathbb{C}(\Omega)$ then $f(\boldsymbol{x}) = 0$. This lemma is the basis of the weak formulation derived here. The current problem will be reformulated in this 5.16 exact format. First multiplying the PDE 5.36 with a test function 'h' and integration over the spatial domain gives 5.17. According to [33] this 'weak' form implies the strong form, when true for all $h(\boldsymbol{x}) \in \mathbb{C}_0^1(\Omega)$

$$\int_\Omega (\nabla^4 w + \alpha\ddot{w} - f)h\mathrm{d}\Omega = 0 \tag{5.17}$$

Using homogeneous Neumann boundary conditions for h the biharmonic operator may be integrated by part twice such that the boundary integrals vanish obtaining Equation 5.18.

$$\int_\Omega \nabla^2 w \nabla^2 h + \alpha \ddot{w} h - f h \mathrm{d}\Omega = 0 \tag{5.18}$$

The derived result is the weak formulation with reduced order of derivatives and will be used for the spatial discretization.

5.3.2. Spatial discretization

The weak formulation still implies the strong formulation in Equation 5.18. The function space for both the solution and the test functions w and h respectively are chosen according to Equations 5.19, 5.20.

$$w = \sum_i \gamma_i(x,y) w_i(t) \tag{5.19}$$

$$h = \sum_j \lambda_j(x,y) h_j \tag{5.20}$$

Requiring the weak formulation to hold only for the these function spaces implies the weak formulation holds approximately. Substitution gives Equation 5.21

$$\int_\Omega (\sum_i \nabla^2 \gamma_i(x,y) w_i(t))(\sum_j \nabla^2 \lambda_j(x,y) h_j) + \alpha(\sum_i \gamma_i(x,y) \ddot{w}_i(t))(\sum_j \lambda_j(x,y) h_j) - f \sum_j \lambda_j(x,y) h_j \mathrm{d}\Omega = 0 \tag{5.21}$$

Changing the order of summation and integration and dropping dependencies gives Equation 5.22. This should hold for any function 'h' which implies it should hold for any 'h_j'. Hence the relation reduces to Equation 5.23 and rewriting gives Equation 5.24. This set of equations can be written in matrix format Equation 5.25.

$$\sum_j h_j \left(\int_\Omega (\sum_i \nabla^2 \gamma_i w_i)(\nabla^2 \lambda_j) + \alpha(\sum_i \gamma_i \ddot{w}_i)(\lambda_j) - f \lambda_j h_j \mathrm{d}\Omega \right) = 0 \ \forall h_j \tag{5.22}$$

$$\int_\Omega (\sum_i \nabla^2 \gamma_i w_i)(\nabla^2 \lambda_j) + \alpha(\sum_i \gamma_i \ddot{w}_i)(\lambda_j) - f \lambda_j \mathrm{d}\Omega = 0 \ \forall j \tag{5.23}$$

$$\sum_i \int_\Omega \nabla^2 \gamma_i \nabla^2 \lambda_j \mathrm{d}\Omega w_i + \sum_i \int_\Omega \alpha \gamma_i \lambda_j \mathrm{d}\Omega \ddot{w}_i = \int_\Omega f \lambda_j \mathrm{d}\Omega \ \forall j \tag{5.24}$$

$$K\boldsymbol{w} + M\ddot{\boldsymbol{w}} = \boldsymbol{f} \tag{5.25}$$

$$K = \int_\Omega \nabla^2 \gamma_i \nabla^2 \lambda_j \mathrm{d}\Omega$$

$$M = \int_\Omega \alpha \gamma_i \lambda_j \mathrm{d}\Omega$$

$$\boldsymbol{f} = \int_\Omega f \lambda_j \mathrm{d}\Omega$$

5.4. Function space 1D

For both the trial and test functions the same function space is used, that is $\gamma_i = \lambda_i \forall i$. The functions should be chosen such that the Laplacian is non-zero, else the '**K**' matrix would be zero. Linear hat functions, often used in Finite Element Method (FEM), are thus not applicable. Instead the higher order local supported cubic Hermitian shape functions are used. The equations 5.26, 5.27 and corresponding plot in 1d 5.1 for these shape functions is given below.

$$\phi_i(x) = \begin{cases} \frac{1}{4}(1+\xi)^2(2-\xi) & \xi = \frac{2(x-x_{i-1})}{\Delta x} - 1 & x_{i-1} \le x \le x_i \\ \frac{1}{4}(1-\xi)^2(2+\xi) & \xi = \frac{2(x-x_i)}{\Delta x} - 1 & x_{i-1} \le x \le x_i \\ 0, & & otherwise \end{cases} \tag{5.26}$$

Here ϕ should not be confused with the adjoint variable, however the difference is always clear from the context.

$$\psi_i(x) = \begin{Bmatrix} \frac{\Delta x}{8}(1+\xi)^2(\xi-1) & \xi = \frac{2(x-x_{i-1})}{\Delta x} - 1 & x_{i-1} \le x \le x_i \\ \frac{\Delta x}{8}(1-\xi)^2(2+\xi) & \xi = \frac{2(x-x_i)}{\Delta x} - 1 & x_{i-1} \le x \le x_i \\ 0 & & otherwise \end{Bmatrix} \tag{5.27}$$

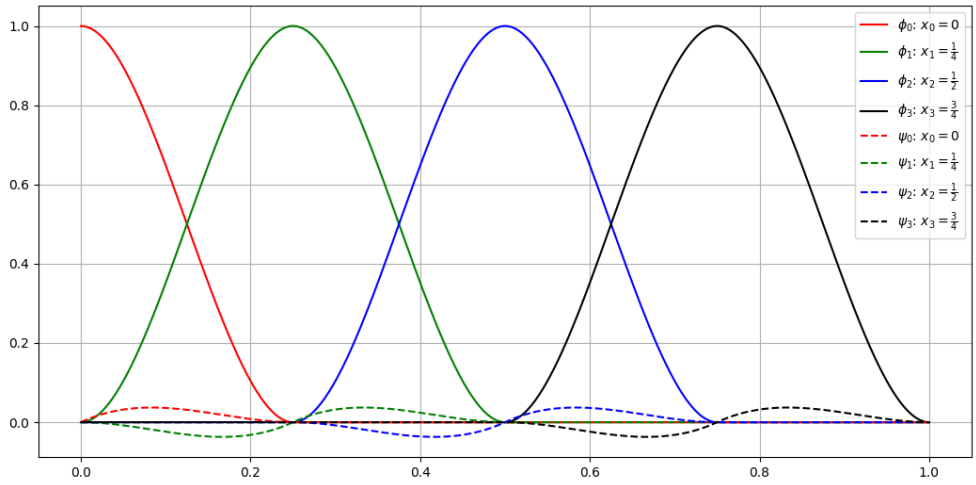

Figure 5.1: Four Hermitian shape functions interpolating displacement and four interpolating the slope on nodes $x \in \{0, \frac{1}{4}, \frac{1}{2}, \frac{3}{4}\}$.

Both the shape functions correspond to a node in x_i in the domain. They are locally non-zero for the previous and next adjacent nodes. The shape functions ϕ_i are such that their value and slope is zero at each node except at the i'th node, where the value unity and slope is also zero. Similar for ψ_i the value and slope is zero on all nodes except for the i'th node where the slope is unity and the value is zero. As can be seen in Figure 5.1.

These Hermitian shape function poses the required condition of a non zero laplacian. Linear combinations of these shape functions form a good FEM basis as given in equation 5.28.

$$w(x) = \sum_{i=1}^{n} a_i \phi_i(x) + \sum_{i=1}^{n} b_i \psi_i(x) = \sum_{i=1}^{2n} r_i R_i(x) \tag{5.28}$$

Here the last summation combines both ϕ_i and ψ_i into R_i such that the corresponding vector r_i relates the displacement and then the slope for all nodes. The ordering is arbitrary but often chosen such that: r_1 relates the displacement of node 1 r_2 the slope on node 1 r_3 the displacement of node 2 r_4 the slope of node 2 and so on.

5.5. Function space 2D

The KL plate PDE has a 2d spatial domain, hence basis functions of x and y are required. Combinations of the Hermitian shape functions that interpolate displacement and slope can be used to obtain these shape functions for 2D. The following combinations are made 5.33.

$$Q_1(x,y) = \phi(x)\phi(y) \sim w(x_i) \tag{5.29}$$

$$Q_2(x,y) = \phi(x)\psi(y) \sim \frac{\partial w}{\partial y}(x_i) \tag{5.30}$$

$$Q_3(x,y) = \psi(x)\phi(y) \sim \frac{\partial w}{\partial x}(x_i) \tag{5.31}$$

$$Q_4(x,y) = \psi(x)\psi(y) \sim \frac{\partial^2 w}{\partial x \partial y}(x_i) \tag{5.32}$$

$$\tag{5.33}$$

Each node will now correspond to four shape functions relating displacement and slopes that is $w(x_i)$, $\frac{\partial w}{\partial x}(x_i)$, $\frac{\partial w}{\partial y}(x_i)$, $\frac{\partial^2 w}{\partial x \partial y}(x_i)$. The 2d function space used 5.35 consists of Linear combinations of the functions shown in 5.33.

$$w(x,y) = \sum_{i=1}^{n} a_i Q_1(x,y)_i + \sum_{i=1}^{n} b_i Q_2(x,y)_i + \sum_{i=1}^{n} c_i Q_3(x,y)_i + \sum_{i=1}^{n} d_i Q_4(x,y)_i \tag{5.34}$$

$$= \sum_{i=1}^{4n} r_i \Pi_i(x,y) \tag{5.35}$$

Here the last sum is again combines the shape functions into function Π_i. The combination is arbitrary but the ordering explained for the 1d case is used, that is r_i corresponds to <node 1 shape function 1, node 1 shape function 2, node 1 shape function 3 node 1 shape function 4, node 2 shape function 1 ...,node n, shape function 4>.

5.5.1. Time integration

There are several time integration methods all with advantages and disadvantages. This research is not focused on optimal time discretization and time marching methods. For that reason a simple scheme capable of solving the PDE is used. The method of choice is the Newmark time integration method. The pseudo code for a Newmark time integration scheme is given in the pseudo Code below 1.

Algorithm 1: Newmark time integration

n=0;
$\gamma = \frac{1}{2}$;
$\beta = \frac{1}{4}$;
$\Delta t = ...$;
$N = ...$;

$\boldsymbol{a}_n = \boldsymbol{M}^{-1}(\boldsymbol{f}_n - \boldsymbol{K}\boldsymbol{x}_n)$;
$\boldsymbol{B} = \boldsymbol{M} + \beta \Delta t^2 \boldsymbol{K}$;
$\tilde{\boldsymbol{x}} = \boldsymbol{x}_n + \Delta t \boldsymbol{v}_n + \frac{\Delta t}{2}(1-2\beta)\boldsymbol{a}_n$;
$\boldsymbol{b} = \boldsymbol{f} + \boldsymbol{K}\tilde{\boldsymbol{x}}$;
$\boldsymbol{a}_{n+1} = \boldsymbol{B}^{-1}\boldsymbol{b}$;
$\boldsymbol{x}_{n+1} = \boldsymbol{x}_n + \Delta t \boldsymbol{v}_n + \frac{\Delta t^2}{2}((1-\gamma) + \gamma \boldsymbol{a}_{n+1})$;
$\boldsymbol{a}_n = \boldsymbol{a}_{n+1}$;
n++;

while $n<N$ **do**
  $\tilde{\boldsymbol{x}} = \boldsymbol{x}_n + \Delta t \boldsymbol{v}_n + \frac{\Delta t}{2}(1-2\beta)\boldsymbol{a}_n$;
  $\boldsymbol{b} = \boldsymbol{f} + \boldsymbol{K}\tilde{\boldsymbol{x}}$;
  $\boldsymbol{a}_{n+1} = \boldsymbol{B}^{-1}\boldsymbol{b}$;
  $\boldsymbol{x}_{n+1} = \boldsymbol{x}_n + \Delta t \boldsymbol{v}_n + \frac{\Delta t^2}{2}((1-\gamma) + \gamma \boldsymbol{a}_{n+1})$;
  $\boldsymbol{a}_n = \boldsymbol{a}_{n+1}$;
  n++;
end

First note that the matrix $\boldsymbol{B}$ is only computed once since the system here is linear. The required vectors, e.g $\boldsymbol{x}$ computed in the 'while' loop are of course stored. The parameters β and γ can be chosen between zero and one. For this research $\gamma = \frac{1}{2}$ and $\beta = \frac{1}{4}$ is used. Further more Δt should be chosen such that the simulation is known to converge and N such that the required simulation time is reached. The convergence is discussed later in this chapter.

5.6. Method of manufactured solutions

The problem discussed above and the later following adjoint problems are solved using the weak formulation. To verify that the numerical solution is a good approximation of the PDE ideally an analytic solution of the problem is known, which can be used to validate the numerical method. The analytic solution for the bench mark problem is however beyond the scope of this research. Instead an analytic solution for a different force function $f(\boldsymbol{x}, t)$ is manufactured. First rewriting the PDE 5.1 to 5.36

$$L(w) = \nabla^4 w(\boldsymbol{x}, t) + \alpha \ddot{w}(\boldsymbol{x}, t) = f \ \boldsymbol{x} \in \Omega \, \forall \, t \tag{5.36}$$
$$\alpha = \frac{2\rho h}{D}$$

A function for displacement, '$\tilde{w}$' consistent with the boundary and initial conditions is assumed and substituted into operator L(). From this result the function '$\tilde{f}$' is obtained. In this way an analytic solution for forcing function '$\tilde{f}$' is known namely '$\tilde{w}$'. This manufactured solution can be used to check the numerical model. Implementing the manufactured forcing function '$\tilde{f}$' and solving for 'w' is done and compared with the analytic solution '$\tilde{w}$'.

The function consistent with the boundary and zero initial conditions used for the method of manufactured solutions is given by Equation 5.37.

$$\tilde{w} = \sum_{n=1}^{N} \sum_{m=1}^{M} [cos(\frac{2\pi n x}{a}) - 1][cos(\frac{2\pi m y}{b}) - 1] w_{nm}(t) \tag{5.37}$$
$$w_{nm}(0) = 0$$
$$\ddot{w}_{nm}(0) = 0$$

Substitution in the differential operator L(w) gives, Equation 5.38.

$$\begin{aligned} \tilde{f} = \sum_{n=1}^{N} \sum_{m=1}^{M} \Big(& \Big((\frac{2\pi n}{a})^4 w_{nm} + (\frac{2\pi m}{b})^4 w_{nm} + (\frac{2\pi n}{a})^2 (\frac{2\pi m}{b})^2 w_{nm} + \alpha \ddot{w}_{nm} \Big) cos(\frac{2\pi n x}{a}) cos(\frac{2\pi m y}{b}) \Big) \\ & - \Big((\frac{2\pi n}{a})^4 w_{nm} + \alpha \ddot{w}_{nm} \Big) cos(\frac{2\pi n x}{a}) \\ & - \Big((\frac{2\pi m}{b})^4 w_{nm} + \alpha \ddot{w}_{nm} \Big) cos(\frac{2\pi m y}{b}) \\ & + \alpha \ddot{w}_{nm} \Big) \end{aligned} \tag{5.38}$$

5.7. Convergence numerical solution

This section discusses the convergence of the numerical solution first for the manufactured solution and secondly for the bench mark problem both for the discretization in space and time. It will be shown that the order of convergence for time integration is $\mathcal{O}(\Delta t^2)$ which is consistent with the expected behaviour of the Newmark time integration method.

5.7.1. Convergence for manufactured solution

In the previous section an exact solution was derived using the method of manufactured solutions. The numerical solution can be compared with this exact solution for increasing number of nodes (smaller Δx thus a larger function space for the spatial discretization. Similar simulations for an increasing number of time steps (smaller Δt) can be performed to increase the time integration accuracy. For the manufactured solution derived above one has the

freedom to chose the functions $w_{nm}(t)$ while still consistent with the boundary conditions. Obviously for large n,m a large amount of waves is present in the plate deformation requiring a larger function space to be captured by the numerical approximation. The expected deformation of the plate under mine blast loading is rather smooth such that a small function space could already model the deformation. For the manufactured solution the results for n=m=4 will be presented. It was found that for smaller values of n,m the numerical solution converged faster and for larger values slower. This is to be expected since more waves in one plate are harder to describe by the same function space. The results are shown in the Figure below 5.2. To prevent the spatial error to be of large influence in the time convergence test the manufactured solution is simplified by using n=m=1. The actual function used are four sine waves quadratic increasing over time given by Equation 5.39 for the spatial convergence and Equation 5.40 for the time convergence test.

$$w_{nm}(x) = \begin{Bmatrix} t^2 cos(\frac{8\pi t}{T}) & n = m = 4 \\ 0 & Otherwise \end{Bmatrix} \tag{5.39}$$

$$w_{nm}(x) = \begin{Bmatrix} t^2 cos(\frac{8\pi t}{T}) & n = m = 1 \\ 0 & Otherwise \end{Bmatrix} \tag{5.40}$$

5.7.2. Convergence of the bench mark problem

In previous section it was proven that the numerical solution will converge to the exact solution for several applied loads. It is therefore assumed that the numerical solution will also converge for other applied loads such as the bench mark problem. The remaining question is what solver settings will yield acceptable convergence for the bench mark pressure model. Since no exact solution is known simulations with increasing number of nodes (decreasing Δx) and increasing number of time steps (decreasing Δt) are performed until almost no change in the new simulations is found. At that point convergence is assumed to be occurred. Using the the solution with the finest discretization the L_2 error can be calculated for the other discretizations w.r.t. that solution. The results are shown in Figures 5.3.

5.8. Chapter summary

In this chapter the transient adjoint problem for a clamped KL plate was derived. The implemented numerical solution to solve the forward and adjoint problem is explained. First the weak formulation was derived. Secondly the spatial discretization using two dimensional hermitian shape functions was explained. Finally pseudo code for the used Newmark the time integration scheme is given. To test the numerical solution the method of manufactured solutions is used. It was found the the implementation convergence to the exact solution for the manufactured solution. Lastly it was shown that the nummerical solution also converges for the benchmark problem. The forward problem can be used to calculate the response of a plate for a mine blast problem. The adjoint problem can be used to calculate the gradient of the objective required for efficient optimization algorithms.

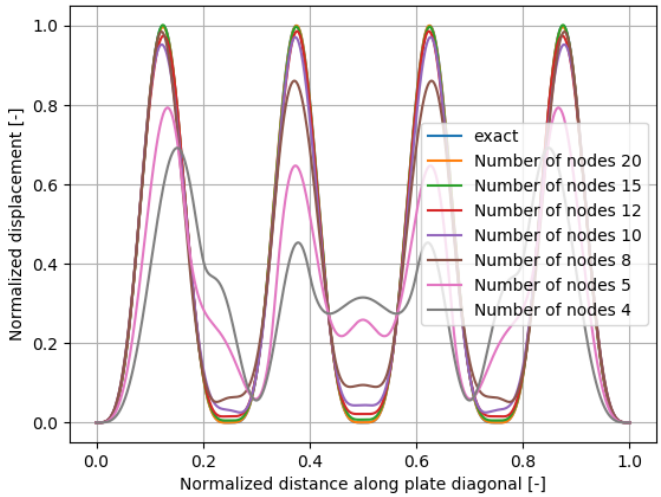

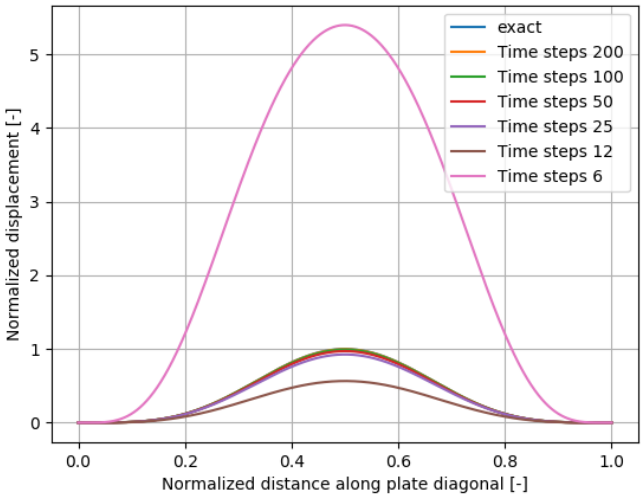

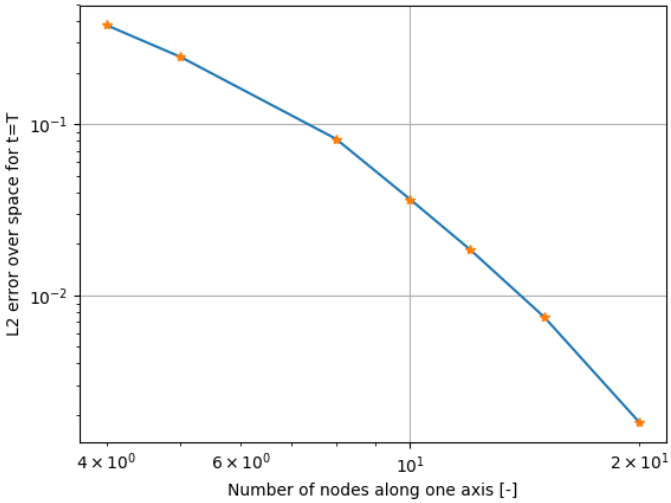

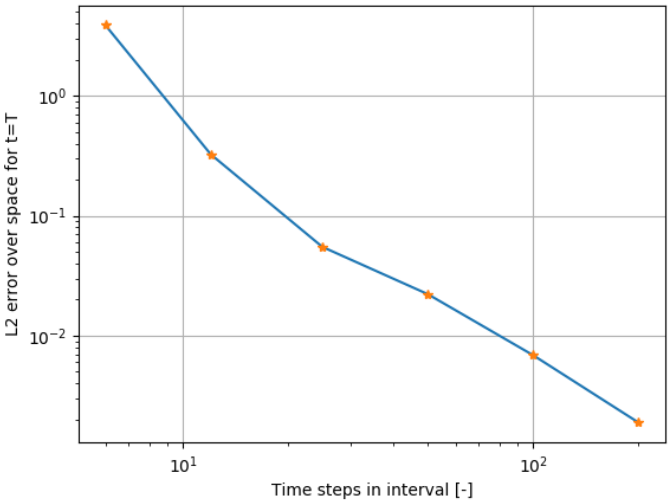

Figure 5.2: The plots on the top shows the displacement for t=T for increasing number of nodes along one axis left and increasing time steps right. In the left plot it is clear that the function space for 4 and 5 nodes is too small. Increasing number of nodes increases the function space such that the estimation converges to the exact solution. The right plot has a simpler function space to see the time convergence better. The L_2 error between the exact curve and the other curves is plotted below, left against the number of nodes and right for the time steps. It can be seen that the order of convergence for amount of nodes is approximately $\mathcal{O}(N^{3.3})$ and for amount of time steps is $\mathcal{O}(\Delta t^{2.2})$.

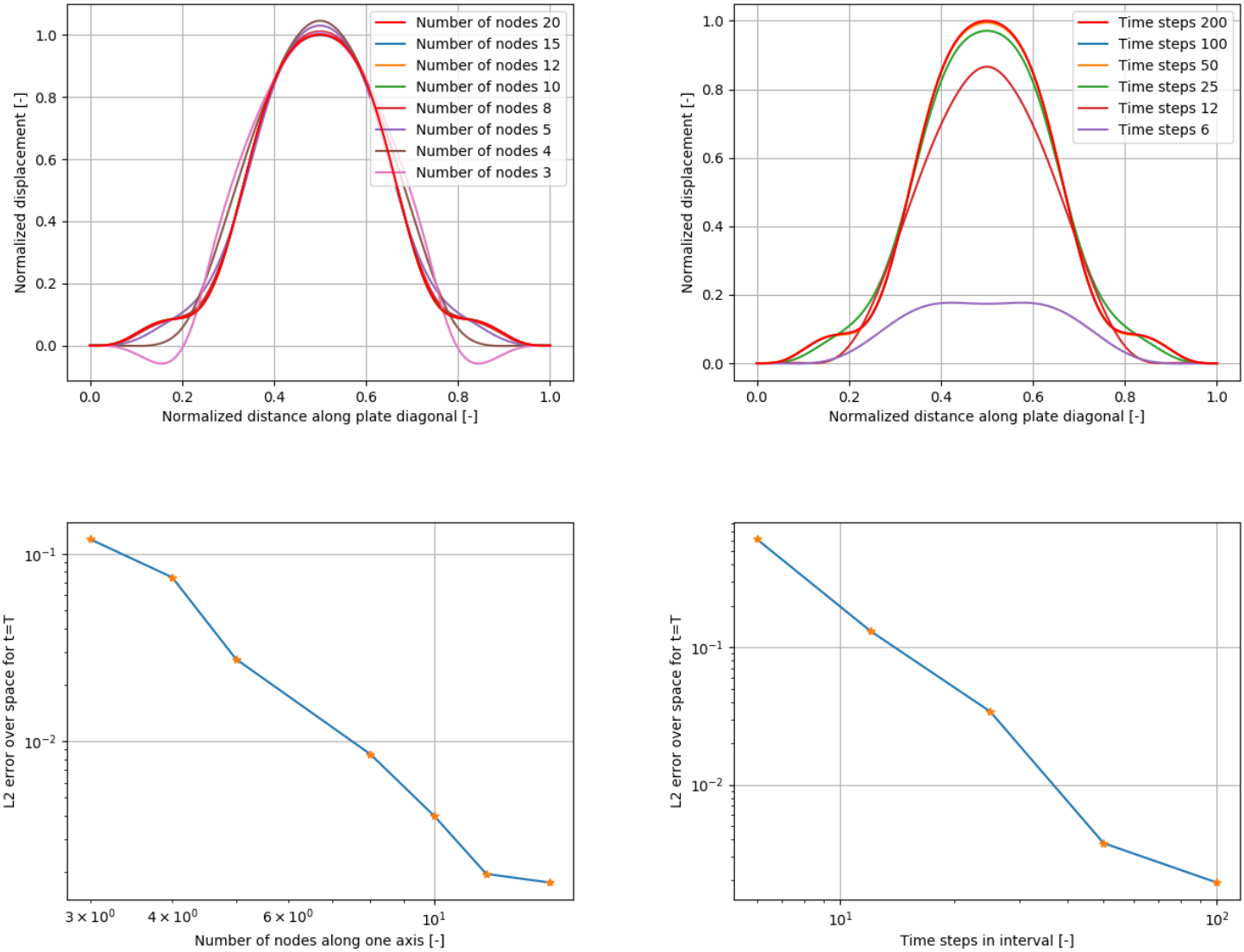

Figure 5.3: The plots on the top shows the displacement for t=T for increasing number of nodes along one axis left and increasing time steps right. At more than 8 nodes and more than 50 time steps the results are converged to almost the same displacement. The L_2 error between the best curve and the other curves is plotted below, left against the number of nodes and right for the time steps. It can be seen that the order of convergence for amount of nodes is approximately $\mathcal{O}(N^{2.5})$ and for amount of time steps is $\mathcal{O}(\Delta t^2)$.

6

Continuum with non-linear elastic constitutive material model

The plate deformation during the mine blast loading is large hence the plate will plastically deform as shown in the introduction in Figure 1.4. The forward problem has to be modeled accurately in order for the IMP algorithm to work. This chapter will discuss a non-linear elastic material model used to approximate the plastic behaviour during mine blast loading.

Furthermore the derivation of the adjoint problem corresponding a general continuum with elastic material model is given. From the adjoint field the gradient of the objective function can be calculated, which is required for the optimization algorithm. The implemented transient FEM solver is compared against commercial LS-Dyna software [30]. The gradient obtained from the adjoint for linear and non-linear material model is verified using finite difference techniques for several variations in pressure.

6.1. Constitutive model

To model the effect of plasticity in metals a constitutive model was created. The model does not actually represent plasticity, since it is an elastic model. That implies stress during loading and unloading follow the same path. The stress is then given as a function of the deformation gradient

$$\boldsymbol{\sigma} = \boldsymbol{\sigma}(\nabla \boldsymbol{u}(\boldsymbol{x})). \tag{6.1}$$

An elastic material model has the advantage of being more simple to implement. The disadvantage is that unloading is not correctly modeled. It is assumed that the material will strain monotonically during the explosion (and thus the simulation time) such that unloading does not occur.

The material model created is a linear elastic model until the equivalent stress reaches a limiting value after which the linear elastic model will be scaled using a power law relation. The constitutive model is given below

$$\sigma_{ij}(\epsilon_{kl}) = \begin{Bmatrix} C_{ijkl}\epsilon_{kl} & \epsilon_{eq} \leq \sigma_y \\ C_{ijkl}\epsilon_{kl}(\frac{\sigma_{eq}}{\sigma_y})^m & \sigma_{eq} > \epsilon_y \end{Bmatrix}. \tag{6.2}$$

To model the strain tensor ϵ_{kl} the following small strain relation is used

$$\epsilon_{kl} = \frac{1}{2}\left(\nabla \boldsymbol{u}(\boldsymbol{x}) + \nabla \boldsymbol{u}(\boldsymbol{x})^T\right). \tag{6.3}$$

Here the yield stress is σ_y, m is a hardening parameter and σ_{eq} is given by, Equation

$$\sigma_{eq} = \sqrt{\frac{3}{2}\hat{S}_{ij}\hat{S}_{ij}}. \tag{6.4}$$

Here $\hat{S}_{ij}$ is the stress tensor given by Equation

$$\hat{S}_{ij} = \hat{\sigma}_{ij} - \delta_{ij}\frac{1}{3}\hat{\sigma}_{kk}. \tag{6.5}$$

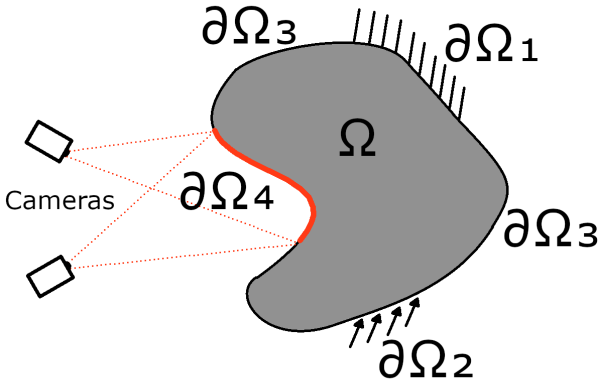

Figure 6.1: The figure illustrates the domain and boundary conditions used for this derivation for a general continuum. On $\partial\Omega_1$ the displacement field is zero. On $\partial\Omega_2$ the traction is prescribed that is the load due to the mine blast. On $\partial\Omega_3$ and $\partial\Omega_4$ the traction is zero i.e. a free boundary. In addition on $\partial\Omega_4$ the DIC measurements are obtained.

Here $\hat{\sigma}_{ij}$ is the stress as if the material was linear, given by $\hat{\sigma}_{ij} = C_{ijkl}\epsilon_{kl}$, to be distinguished from the actual stress in the material σ_{ij}. The performance of this material model is compared with the Johnson-Cook model by simulating the plate response caused by a mine blast loading using the TNO mine blast model in Appendix C.

6.2. Forward Problem

A sketch of a general continuum is given in Figure 6.1. The boundary conditions are itemized below:

- $\boldsymbol{x} \in \partial\Omega_1$: $\boldsymbol{u}(\boldsymbol{x}) = \boldsymbol{0}$,
- $\boldsymbol{x} \in \partial\Omega_2$: $\boldsymbol{t}(\boldsymbol{x}) = \boldsymbol{f}(\boldsymbol{x})$,
- $\boldsymbol{x} \in \partial\Omega_3$: $\boldsymbol{t}(\boldsymbol{x}) = \boldsymbol{0}$,
- $\boldsymbol{x} \in \partial\Omega_4$: $\boldsymbol{t}(\boldsymbol{x}) = \boldsymbol{0}$ on this boundary displacement data from DIC is obtained.

Balance of linear momentum is given by Equation 6.6. Here the second notation uses Einstein summation convention over double indexes and the last equation includes comma notation to denote partial derivatives with respect to the spatial coordinate. The last notation is mainly used in the derivation below to reduce the algebra.

$$\begin{aligned} \nabla \cdot \boldsymbol{\sigma} &= \rho \ddot{\boldsymbol{u}} \\ \frac{\partial \sigma_{ij}}{\partial x_j} &= \rho \ddot{u}_i \\ \sigma_{ij,j} &= \rho \ddot{u}_i \end{aligned} \tag{6.6}$$

Together with the material model given in the previous section the forward problem is complete. In the next section this will be used to derive the adjoint problem.

6.3. Derivation of the Adjoint problem

In this section the adjoint problem for a general continuum will be derived. Starting from the objective function and the added PDE constrained the variation of J will be derived. Large part of the effort is the integration by parts, hence this will be done in separate subsections for the time and spatial integrations. Finally the adjoint will be rewritten as continuum problem and compared to the forward continuum problem.

6.3.1. The objective function

Starting with the objective function which compares model displacement u_i and measured displacement v_i, Equation 6.7. This objective function is to be minimized. Note that the spatial integration is done over $\partial\Omega_4$ which is the boundary where the displacement is measured. The matrix H_{ij} can be simply the identity matrix such that measurement and model are compared directly. However H_{ij} can for example also filter certain components. For example when only z-displacement is known. The objective functional J can be written as

$$J[\boldsymbol{u}] = \int_0^T \int_{\partial\Omega_4} \frac{1}{2}(H_{ij}u_j - v_i)(H_{ij}u_j - v_i)\mathrm{d}\partial\Omega\mathrm{d}t. \tag{6.7}$$

Adding the forward problem PDE constrained to the objective function one obtains the augmented functional

$$\tilde{J}[\boldsymbol{u}] = \int_0^T \int_{\partial\Omega_4} \frac{1}{2}(H_{ij}u_j - v_i)(H_{ij}u_j - v_i)\mathrm{d}\partial\Omega\mathrm{d}t + \int_0^T \int_\Omega \phi_i(\sigma_{ij,j} - \rho\ddot{u}_i)\mathrm{d}\Omega\mathrm{d}t. \tag{6.8}$$

Here ϕ_i is the adjoint variable. For deformations consistent with the forward problem the PDE should be zero such that the objective and augmented objective functional are equal, i.e. $J = \tilde{J}$. For the optimization algorithm the gradient of the objective function is required. The continuous analog to the gradient is the variational derivative of the objective function. The variation is given by

$$\delta\tilde{J} = \int_0^T \int_{\partial\Omega_4} (H_{ij}u_j - v_i)H_{ij}\delta u_j\mathrm{d}\partial\Omega\mathrm{d}t + \int_0^T \int_\Omega \phi_i(\delta\sigma_{ij,j} - \rho\delta\ddot{u}_i)\mathrm{d}\Omega\mathrm{d}t. \tag{6.9}$$

In the second double integral on the right hand side the variation in divergence of stress and acceleration are unknown. In this form the variation cannot be directly computed. Using integration by parts this equation has to be rewritten to obtain the adjoint problem. The next two sections will discuss the integration by parts of the time and spatial derivatives respectively.

6.3.2. Partial integration time derivatives

The time derivatives in the second integral on the right hand side of Equation 6.9 need to be integrated by parts. To do this the first step is to switch the order of integration given in

$$\int_0^T \int_\Omega \phi_i(\rho\delta\ddot{u}_i)\mathrm{d}\Omega\mathrm{d}t = \int_\Omega \int_0^T \phi_i(\rho\delta\ddot{u}_i)\mathrm{d}t\mathrm{d}\Omega. \tag{6.10}$$

Now the focus will be on the inner integral, which needs to be integrated by parts twice. The first integration by parts gives

$$\int_0^T \phi_i(\rho\delta\ddot{u}_i)\mathrm{d}t = [\phi_i(\rho\delta\dot{u}_i)]_0^T - \int_0^T \dot{\phi}_i(\rho\delta\dot{u}_i)\mathrm{d}t. \tag{6.11}$$

There is no variation in initial conditions such that $\delta\dot{u}_i(\boldsymbol{x}, t = 0)$=0. Since ϕ_i is free to chose, the end conditions are chosen such that $\phi_i(\boldsymbol{x}, t = T) = 0$. In that case the boundary term from the integration by parts becomes zero $[\phi_i(\rho\delta\dot{u}_i)]_0^T = 0$. Note that the choice for $\phi_i(\boldsymbol{x}, t = T) = 0$ is not merely a convenience, since the variation $\delta\dot{u}_i(\boldsymbol{x}, t = T)$ is not known. Any other choice for $\phi_i(\boldsymbol{x}, t = T)$ would later require $\delta\dot{u}_i(\boldsymbol{x}, t = T)$ to be known when δJ is to be determined.

Again integrating by parts the remaining integral on the right hand side in 6.11 yields

$$\int_0^T \dot{\phi}_i(\rho\delta\dot{u}_i)\mathrm{d}t = [\dot{\phi}_i(\rho\delta u_i)]_0^T - \int_0^T \ddot{\phi}_i(\rho\delta u_i)\mathrm{d}t. \tag{6.12}$$

Similar as for the first integration by parts the following must hold $\delta u_i(\boldsymbol{x}, t = 0)$=0.Also since $\delta u_i(\boldsymbol{x}, t = T)$ is not known it is required that $\dot{\phi}_i(\boldsymbol{x}, t = T) = 0$. Both conditions cause the boundary term of the integration by parts to vanish. Substitution of the derived result into 6.10 yields

$$\int_0^T \int_\Omega \phi_i(\rho\ddot{u}_i)\mathrm{d}\Omega\mathrm{d}t = \int_0^T \int_\Omega \ddot{\phi}_i(\rho\delta u_i)\mathrm{d}\Omega\mathrm{d}t. \tag{6.13}$$

under the following constrains:

$$\phi_i(\boldsymbol{x}, t = T) = 0 \tag{6.14}$$

$$\dot{\phi}_i(\boldsymbol{x}, t = T) = 0 \tag{6.15}$$

It is worth pointing out that δu_i is not known a priori, further analysis is required to take care of this term, for which the integration by parts shown above will be used.

6.3.3. Partial integration space derivatives

For the spatial integration by parts the divergence theorem is used to obtain boundary integrals from volume integrals, i.e. [43],

$$\int_\Omega \frac{\partial}{\partial x_{i_k}} A_{i_1\, i_2 \ldots i_k \ldots i_n} \mathrm{d}\Omega = \int_{\partial\Omega} A_{i_1\, i_2 \ldots i_k \ldots i_n} n_{i_k} \mathrm{d}\partial\Omega. \tag{6.16}$$

Here $A_{i_1\, i_2 \ldots i_k \ldots i_n}$ refers to the Cartesian components of tensor $\boldsymbol{A}$ may be any tensor and '$\boldsymbol{n}$' is the normal vector on the boundary.

Similar as the integration by parts over time, the spatial derivatives in Equation 6.9 have to be integrated by parts. Using the divergence theorem Equation 6.16 to integrate by parts the first term of the second integral of the right hand side of Equation 6.9 yields

$$\int_\Omega \phi_i \delta\sigma_{ij,j} \mathrm{d}\Omega = \int_{\partial\Omega} \delta\sigma_{ij} \phi_i n_j \mathrm{d}\partial\Omega - \int_\Omega \delta\sigma_{ij} \phi_{i,j} \mathrm{d}\Omega. \tag{6.17}$$

The boundary term in Equation 6.17 can be rewritten as

$$\int_{\partial\Omega} \delta\sigma_{ij} \phi_i n_j \mathrm{d}\partial\Omega = \int_{\partial\Omega} \delta t_i \phi_i \mathrm{d}\partial\Omega. \tag{6.18}$$

Here $\delta t_i = (\delta\sigma_{ij}) n_j$ is the variation in the traction vector. In parts of the boundary where the traction is prescribed, the variation of t_i is known a priori. However for now the result is not simplified but instead kept as is.

For the second integration by part of Equation 6.17 the term $\delta\sigma_{ij}$ has to be further evaluated. Here the assumption $\sigma_{ij}(u_{p,l})$ plays an important role. The variation in stress is then further evaluated to give

$$\delta\sigma_{ij} = \frac{\partial\sigma_{ij}}{\partial u_{p,l}} \delta u_{p,l}. \tag{6.19}$$

Integration by parts a second time of the second integral on the right hight side of Equation 6.17 is less trivial. Consider the following Identity obtained by the differentiation using the chain rule:

$$\frac{\partial}{\partial x_l}\left(\frac{\partial\sigma_{ij}}{\partial u_{p,l}} \delta u_p \phi_{i,j}\right) = \frac{\partial}{\partial x_l}\left(\frac{\partial\sigma_{ij}}{\partial u_{p,l}} \phi_{i,j}\right) \delta u_p + \frac{\partial\sigma_{ij}}{\partial u_{p,l}} \phi_{i,j} \delta u_{p,l} \tag{6.20}$$

and using Equation 6.20 for the integration by parts of the right hand side of Equation 6.17 yields

$$\int_\Omega \delta\sigma_{ij} \phi_{i,j} \mathrm{d}\Omega = \int_\Omega \frac{\partial\sigma_{ij}}{\partial u_{p,l}} \delta u_{p,l} \phi_{i,j} \mathrm{d}\Omega = \int_{\partial\Omega} \frac{\partial\sigma_{ij}}{\partial u_{p,l}} \phi_{i,j} \delta u_p n_l \mathrm{d}\partial\Omega - \int_\Omega \frac{\partial}{\partial x_l}\left(\frac{\partial\sigma_{ij}}{\partial u_{p,l}} \phi_{i,j}\right) \delta u_p \mathrm{d}\Omega. \tag{6.21}$$

6.3.4. Variation of $\tilde{J}$

As previously indicated, Equation 6.9 requires further analysis to obtain an expression that can be computed directly. To this end the integration by part derived in subsections 6.3.2 and 6.3.3 can now be substituted back into Equation 6.9 to obtain

$$\delta \tilde{J} = \int_0^T \int_{\partial\Omega_4} (H_{ij}u_j - v_i) H_{ij} \delta u_j \mathrm{d}\partial\Omega \mathrm{d}t \tag{6.22}$$

$$+ \int_0^T \int_\Omega -\ddot{\phi}_i \rho \delta u_i + \frac{\partial}{\partial x_l}\left(\frac{\partial \sigma_{ij}}{\partial u_{p,l}} \phi_{i,j}\right) \delta u_p \mathrm{d}\Omega \mathrm{d}t \tag{6.23}$$

$$+ \int_0^T \int_{\partial\Omega} \delta t_i \phi_i - \frac{\partial \sigma_{ij}}{\partial u_{p,l}} \phi_{i,j} \delta u_p n_l \mathrm{d}\partial\Omega \mathrm{d}t. \tag{6.24}$$

$$\tag{6.25}$$

This equation for the variation of J is in a convenient form. The variation of δu_i can be taken outside bracket by first renaming the dummy index on the first contracted term in the second integral, i.e,

$$\begin{aligned}\delta \tilde{J} = &\int_0^T \int_{\partial\Omega_4} (H_{ij}u_j - v_i) H_{ij} \delta u_j \mathrm{d}\partial\Omega \mathrm{d}t \\ &+ \int_0^T \int_\Omega (-\ddot{\phi}_p \rho + \frac{\partial}{\partial x_l}\left(\frac{\partial \sigma_{ij}}{\partial u_{p,l}} \phi_{i,j}\right)) \delta u_p \mathrm{d}\Omega \mathrm{d}t \\ &+ \int_0^T \int_{\partial\Omega} \delta t_i \phi_i - \frac{\partial \sigma_{ij}}{\partial u_{p,l}} \phi_{i,j} \delta u_p n_l \mathrm{d}\partial\Omega \mathrm{d}t.\end{aligned} \tag{6.26}$$

Since the variation δu_p is not known a priori the adjoint variable is chosen to satisfy the following condition:

$$\ddot{\phi}_p \rho = \frac{\partial}{\partial x_l}\left(\frac{\partial \sigma_{ij}}{\partial u_{p,l}} \phi_{i,j}\right)) \; \forall \boldsymbol{x} \in \Omega \forall t \in [0, T]. \tag{6.27}$$

With this choice the second integral in Equation 6.26 becomes zero regardless of the value of δu_p. This condition for the adjoint variable is called the adjoint partial differential equation.

To further simplify 6.26, the boundary conditions are itemized:

- $\boldsymbol{x} \in \partial\Omega_1$: $\delta u_p = 0$. Since the variation in traction is not known on this boundary the boundary condition for the adjoint is $\phi_i = 0$. Hence the integrand of the third integral in Equation 6.26 is zero for $\boldsymbol{x} \in \partial\Omega_1$.
- $\boldsymbol{x} \in \partial\Omega_2$: Here the traction δt_i is known/controlled. The boundary condition for the adjoint is $\frac{\partial \sigma_{ij}}{\partial u_{p,l}} \phi_{i,j} n_l = 0$
- $\boldsymbol{x} \in \partial\Omega_3$: Similar to $\boldsymbol{x} \in \partial\Omega_2$, the variation in traction δt_i is known and in addition on this boundary Ω_3 it is zero. Thus again the boundary condition for the adjoint is $\frac{\partial \sigma_{ij}}{\partial u_{p,l}} \phi_{i,j} n_l = 0$
- $\boldsymbol{x} \in \partial\Omega_4$: On this boundary δu_p is not known. For this specific problem $\delta t_i = 0$. Combining the first and third integral the boundary condition becomes $(H_{ij}u_j - v_i) H_{ij} - \frac{\partial \sigma_{ij}}{\partial u_{p,l}} \phi_{i,j} n_l = 0$

An important consequence of the chosen adjoint PDE and these boundary conditions is that the variation $\tilde{J}$ can be computed from 6.26 without having to determine the variation δu_p. At this point the adjoint problem is completely specified. It consists of a PDE that has to be satisfied, end conditions at t=T and boundary conditions. Under these conditions the variation of J is given by

$$\delta \tilde{J} = \int_0^T \int_{\partial\Omega_2} \delta t_i \phi_i \mathrm{d}\partial\Omega \mathrm{d}t \tag{6.28}$$

This implies that the variation of J for any chosen variation of traction can be found by the given integral 6.28 for which the adjoint first needs to be computed. The adjoint only has to be determined once, which implies a computational cost similar to one forward problem.

6.4. Adjoint as continuum problem

The adjoint problem derived in previous section can be rewritten slightly such that the adjoint problem is very similar to the forward problem. This is not just convenient for interpretation of the problem but it also simplifies the implementation since the majority of the code written for the forward problem can be reused for the adjoint problem. First an adjoint stress tensor $\tilde{\sigma}_{pl}$ and traction $\tilde{t_p}$ are defined as follows:

$$\tilde{\sigma}_{pl} = \frac{\partial \sigma_{ij}}{\partial u_{p,l}} \phi_{i,j}, \tag{6.29}$$

$$\tilde{t_p} = \tilde{\sigma}_{pl} n_l. \tag{6.30}$$

Using these definitions the adjoint problem can be rewritten as in Table 6.1. Both the forward and adjoint problems are summarized using vector notation.

Table 6.1: Table summarizes forward and adjoint problem in vector notation

	Forward Problem	Adjoint Problem
PDE	$\rho \ddot{\boldsymbol{u}} = \nabla \cdot \sigma$	$\rho \ddot{\boldsymbol{\phi}} = \nabla \cdot \tilde{\sigma}$
Initial Condition 1 $\boldsymbol{x} \in \Omega$	$\boldsymbol{u}(\boldsymbol{x}, t) = \boldsymbol{0}$, t=0	$\boldsymbol{\phi}(\boldsymbol{x}, t) = \boldsymbol{0}$, t=T
Initial Condition 2 $\boldsymbol{x} \in \Omega$	$\dot{\boldsymbol{u}}(\boldsymbol{x}, t) = \boldsymbol{0}$, t=0	$\dot{\boldsymbol{\phi}}(\boldsymbol{x}, t) = \boldsymbol{0}$, t=T
$\boldsymbol{x} \in \partial\Omega_1$, t ∈ [0,T]	$\boldsymbol{u}(\boldsymbol{x}, t) = \boldsymbol{0}$	$\boldsymbol{\phi}(\boldsymbol{x}, t) = \boldsymbol{0}$
$\boldsymbol{x} \in \partial\Omega_2$, t ∈ [0,T]	$\boldsymbol{t} = \boldsymbol{f}(\boldsymbol{x}, t)$	$\tilde{\boldsymbol{t}} = \boldsymbol{0}$
$\boldsymbol{x} \in \partial\Omega_3$, t ∈ [0,T]	$\boldsymbol{t} = \boldsymbol{0}$	$\tilde{\boldsymbol{t}} = \boldsymbol{0}$
$\boldsymbol{x} \in \partial\Omega_4$, t ∈ [0,T]	$\boldsymbol{t} = \boldsymbol{0}$ & DIC	$\tilde{\boldsymbol{t}} = \boldsymbol{H}^T \boldsymbol{H}\boldsymbol{u} - \boldsymbol{H}^T \boldsymbol{v}$
Constitutive Equation	$\boldsymbol{\sigma}(\nabla \boldsymbol{u})$	$\tilde{\boldsymbol{\sigma}}(\nabla \boldsymbol{\phi})$

The tangent stiffness tensor $\frac{\partial \sigma_{ij}}{\partial u_{p,l}}$ may be interpreted as stiffness matrix for the adjoint problem. it may appear counter intuitive that this stiffness varies in both space and time, while being known beforehand. Of course the stiffness of the forward problem can also vary over space and time (for non-linear constitutive models) however this is determined by the response itself, and not known before hand.

The FEM implementation is discussed in Appendix D. The same FEM solver is used for the forward and adjoint problem.

6.5. FEM verification

The author implemented a transient explicit FEM solver to solve the forward and adjoint continuum problems. The implementation is discussed in more detail in Appendix D. To verify that FEM implementation works correctly the results of a simple simulation are compared with the commercially available verified FE software package LS-Dyna. This is an indirect verification under the assumption that LS-Dyna results are correct. The simple simulation is a plate clamped along the edges and subjected to a constant distributed load. The both initial conditions, that are displacement and velocity, are zero. The distributed load is chosen small such that the displacement is small and hence the analysis is geometrically linear. This is required for the Author's implementation. The plate's deflection is visually compared for a large amount of time frames, two are shown in the Figure 6.2 below. In the figure it is clear that the deformation follows the same trend.

In the graph below Figure 6.3 the displacement of the middle of the plate is plotted versus time. Here it is clear that both simulations are almost identical.

After these simulation results no further effort is made in the verification process of the FEM implementation. The FEM implementation is used as described for the remainder of this thesis, further verification is outside the scope of this research.

6.6. Adjoint verification

The adjoint problem uses the same Fem solver as the forward problem except for the material model. To test this part of the implementation and more general the methodology several variations are calculated using the adjoint and the finite difference method. The tests where done for arbitrarily chosen traction, variation in traction and measured displacement, $\boldsymbol{t}$, $\delta \boldsymbol{t}$ and $\boldsymbol{v}$ respectively. The variation using the finite difference method is given by

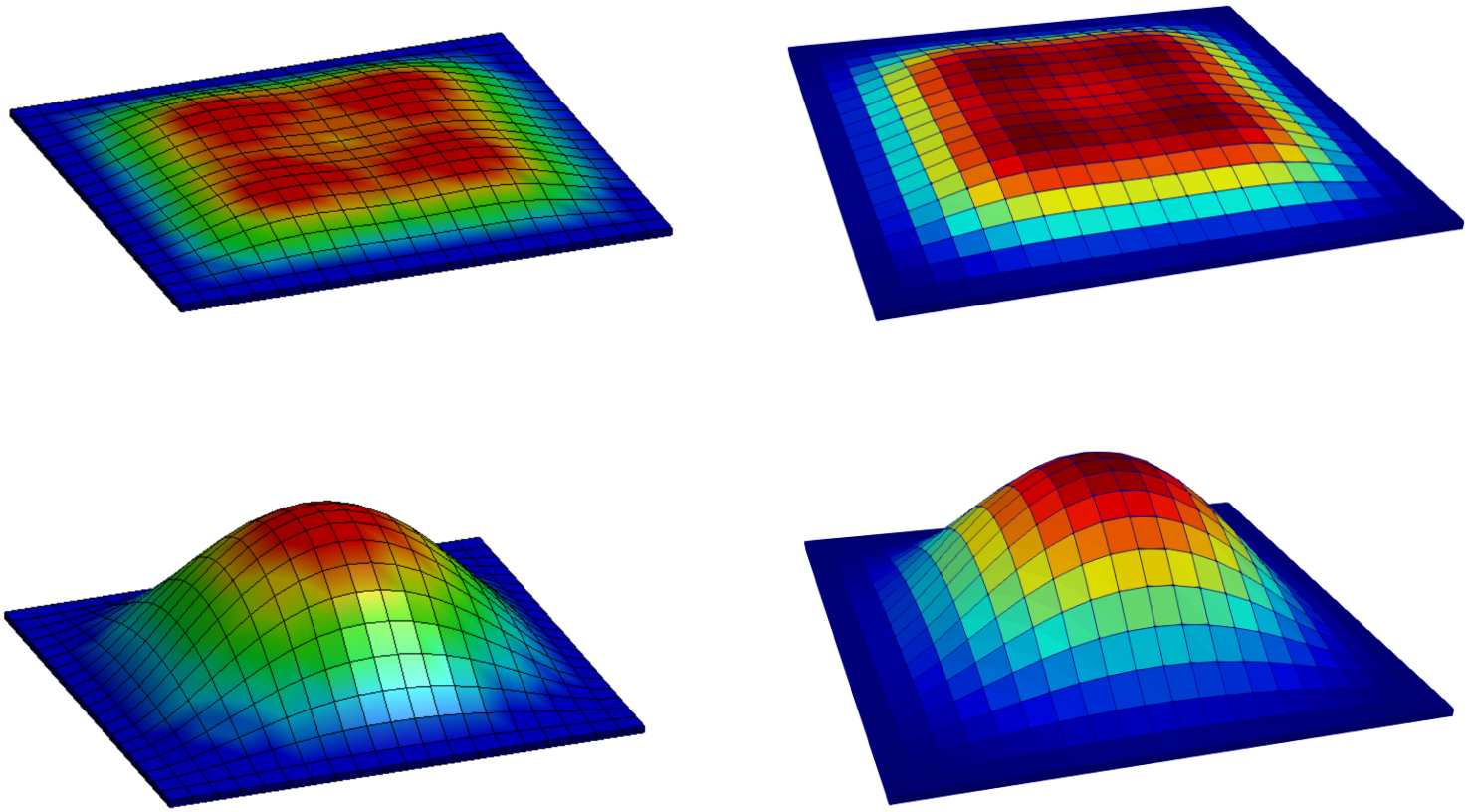

Figure 6.2: Left: LS-Dyna simulation results visualized using LS-PrePost [29], Right: visualization of the authors FEM implementation, using Paraview [8] First row are results at t=0.75ms and the second row at t=1.5ms. The simulations show excellent agreement.

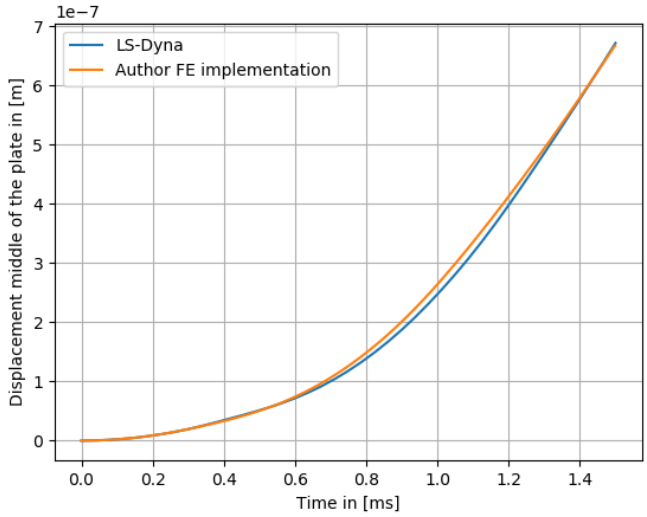

Figure 6.3: Displacement plotted of the middle of the plate plotted versus time for both the LS-Dyna and the authors FEM implementation. Both displacements show excellent agreement.

$$\delta J = J[\boldsymbol{u}(\boldsymbol{t} + \delta \boldsymbol{t})] - J[\boldsymbol{u}(\boldsymbol{t})]. \tag{6.31}$$

Here the objective function is evaluated for the displacement field $\boldsymbol{u}$ which is a function of the applied traction. The variation obtained using the adjoint solution was earlier derived, Equation 6.28 and repeated here

$$\delta \tilde{J} = \int_0^T \int_{\partial\Omega_2} \delta t_i \phi_i \mathrm{d}\partial\Omega \mathrm{d}t. \tag{6.32}$$

Note here that the objective function and the augmented objective function are the same since the field $\boldsymbol{u}$ is a solution of the forward problem.

The traction was first chosen small to obtain a linear response. Since the adjoint material model for linear response in equivalent to the forward problem this was expected to work. Secondly the traction amplitude was increased causing a non linear material response. The variation in traction had to increase as well such that the numerical precision would not become a problem. The amplitude of the measured solution was increased to the same order of magnitude as the forward problem. The used traction yielding linear response is

$$t_3 = \left(\frac{t}{T}\right) sin\left(\frac{\pi x}{a}\right) sin\left(\frac{\pi y}{b}\right). \tag{6.33}$$

The other components of the traction t_1 and t_2 are chosen zero.

The measured response is given by

$$v_3 = 10^{-9} \left(\frac{t}{T}\right)^2 sin\left(\frac{2\pi x}{a}\right) sin\left(\frac{2\pi y}{b}\right). \tag{6.34}$$

Finally the variation in traction is a given by

$$\delta t_3 = 10^{-7} \left(\frac{t}{T}\right)^i sin\left(\frac{n\pi x}{a}\right) sin\left(\frac{m\pi y}{b}\right) \tag{6.35}$$

here i,n and m are varied to obtain different variations in traction. The other components of the variation of the traction are again chosen zero. The results are shown in Table 6.2.

The traction used for the non-linear response is similar, just increased in amplitude, that is

$$t_3 = 10^9 \left(\frac{t}{T}\right) sin\left(\frac{\pi x}{a}\right) sin\left(\frac{\pi y}{b}\right). \tag{6.36}$$

The other components of the traction t_1 and t_2 are again chosen zero. The measured response is also simply increased in amplitude given by

$$v_3 = 0.3 \left(\frac{t}{T}\right)^2 sin\left(\frac{2\pi x}{a}\right) sin\left(\frac{2\pi y}{b}\right). \tag{6.37}$$

Finally the variation in traction is a given by

$$\delta t_3 = 100 \left(\frac{t}{T}\right)^i sin\left(\frac{n\pi x}{a}\right) sin\left(\frac{m\pi y}{b}\right) \tag{6.38}$$

The other components of the variation of the traction are again chosen zero. The results are shown in the same Table as before 6.2. In addition to the smooth variations in traction the following local supported functions, for linear and non linear response, were tested as well

$$\delta t_3 = \begin{Bmatrix} 10^{-7} & |x| < .3 \& |y| < .3 \& 0.5T < t < 0.55T \\ 0 & else \end{Bmatrix} \tag{6.39}$$

and

$$\delta t_3 = \begin{Bmatrix} 10^{-7} & |x| < .3 \& |y| < .3 \& 0.5T < t < 0.55T \\ 0 & else \end{Bmatrix}. \tag{6.40}$$

It can be seen that the variations in J are vary from largest to smallest value in 5 orders of magnitude for different variations in traction, yet the error between the variations obtained with the adjoint and the finite difference method are quite small.

Table 6.2: Adjoint and finite difference variations δJ_{ad} and δJ_{fd} respectively are compared for several variations in traction specified by variables i, n and m. There are approximately 5 orders of magnitude differences in the larger and smaller variations of J yet the error remains small between variations obtained from finite difference and the adjoint method.

			Linear				Non-linear		
i [-]	n [-]	m [-]	δJ_{ad} $[m^4 s]$	δJ_{fd} $[m^4 s]$	err %		δJ_{ad} $[m^4 s]$	δJ_{fd} $[m^4 s]$	Error [%]
0	1	1	2.18E-29	2.09E-29	3.71		2.41E-11	2.32E-11	3.73
0	1	2	9.04E-32	8.88E-32	1.70		1.52E-14	1.46E-14	3.95
0	1	3	-2.89E-30	-2.90E-30	-0.171		-9.00E-13	-9.76E-13	-8.44
0	2	1	-7.63E-32	-7.34E-32	3.77		-3.53E-14	-3.71E-14	-5.10
0	2	2	-2.50E-29	-2.43E-29	2.61		-1.11E-11	-1.08E-11	2.70
0	2	3	1.07E-32	1.10E-32	-3.02		-3.44E-15	-3.30E-15	4.07
0	3	1	-2.81E-30	-2.82E-30	-0.315		-8.53E-13	-9.24E-13	-8.32
0	3	2	2.02E-31	1.94E-31	3.87		4.19E-14	4.22E-14	-0.716
0	3	3	-3.71E-31	-3.86E-31	-4.1		-1.38E-13	-1.25E-13	9.42
1	1	1	6.30E-30	6.07E-30	3.65		6.87E-12	6.63E-12	3.49
1	1	2	2.14E-32	2.09E-32	2.02		2.88E-15	2.74E-15	4.86
1	1	3	-7.36E-31	-7.33E-31	0.28		-1.90E-13	-2.01E-13	-5.79
1	2	1	-1.94E-32	-1.87E-32	3.44		-8.45E-15	-8.91E-15	-5.44
1	2	2	-8.18E-30	-7.98E-30	2.52		-3.26E-12	-3.17E-12	2.76
1	2	3	2.03E-33	2.11E-33	-4.04		-1.19E-15	-1.18E-15	0.840
1	3	1	-7.13E-31	-7.12E-31	0.168		-1.78E-13	-1.89E-13	-6.18
1	3	2	5.25E-32	5.07E-32	3.29		7.92E-15	7.98E-15	-0.758
1	3	3	8.48E-32	8.74E-32	-3.13		-3.63E-14	-3.45E-14	4.96
2	1	1	2.76E-30	2.67E-30	3.56		2.98E-12	2.88E-12	3.36
2	1	2	7.95E-33	7.78E-33	2.17		9.43E-16	8.82E-16	6.47
2	1	3	-2.98E-31	-2.96E-31	0.65		-7.37E-14	-7.63E-14	-3.53
2	2	1	7.82E-33	7.58E-33	3.13		-3.47E-15	-3.61E-15	-4.03
2	2	2	-3.80E-30	-3.71E-30	2.45		-1.41E-12	-1.38E-12	2.13
2	2	3	5.99E-34	6.36E-34	-6.12		-5.42E-16	-5.44E-16	-0.369
2	3	1	-2.89E-31	-2.87E-31	0.569		-6.87E-14	-7.11E-14	-3.49
2	3	2	2.06E-32	2.00E-32	2.86		2.59E-15	2.58E-15	0.386
2	3	3	3.22E-32	3.29E-32	-2.25		-1.48E-14	-1.43E-14	3.38
local supported function:			-1.26E-31	-1.22E-31	3.55		1.64E-13	1.57E-13	4.12

7

Results

In this chapter several simulations for both the Kirchhoff Love (KL) plate model and the non-linear-elastic material model will be discussed. Three different pressure distributions are used to test the algorithm including the benchmark pressure model. Sensitivity tests are performed by varying the pressure distributions applied around a reference situation, e.g. increasing the plate thickness or adding noise. In general the displacement converges good however the pressure can be quite different. This shows that inverse problems are sensitive to input and not unique. For localized loads the total force and its centroid position versus time, 'F(t)' and 'r(t)' respectively, are obtained by integration of the pressure distributions found. These two quantities are found in good agreement even if the pressure models are off.

7.1. Kirchhoff Love model

In this section three tests to study the performance of the Inverse Measurement Problem (IMP) algorithm will be discussed. First a smooth distribution, then a localized smooth distribution and lastly the benchmark pressure which is localized and discontinuous. Each of these three pressure distributions are discussed separately in the following subsections. For each pressure distribution one reference configuration is chosen for which each time one parameter is changed to study the behaviour.

7.1.1. Smooth distribution

The smooth distribution is defined as a sine shape pressure distribution given by

$$P(x, y, t) = sin(\frac{n\pi x}{a}) sin(\frac{m\pi y}{b})(\frac{t}{T})^k. \tag{7.1}$$

In the reference situation: n=m=2, k=1 and the simulation time used T=2.5 ms. No noise is used in displacement data for the reference situation. The result for that case is given in the figure below 7.1. For this and all following plots in this chapter the blue curve is the 'Applied' pressure for which the forward problem is solved. For that forward problem displacement data at a set of points are stored at certain time intervals, noise is added to that data to simulate DIC measurements. This data is then used togheter with the IMP algorithm to find the pressure back, here the orange curve named 'Solved'. Ofcourse the solution obtained is P(x,y,t), i.e. a function of both x and y of the plate. However comparing the results in a 1d plot is far better, hence the pressure is plotted over the diagonal of the plate.

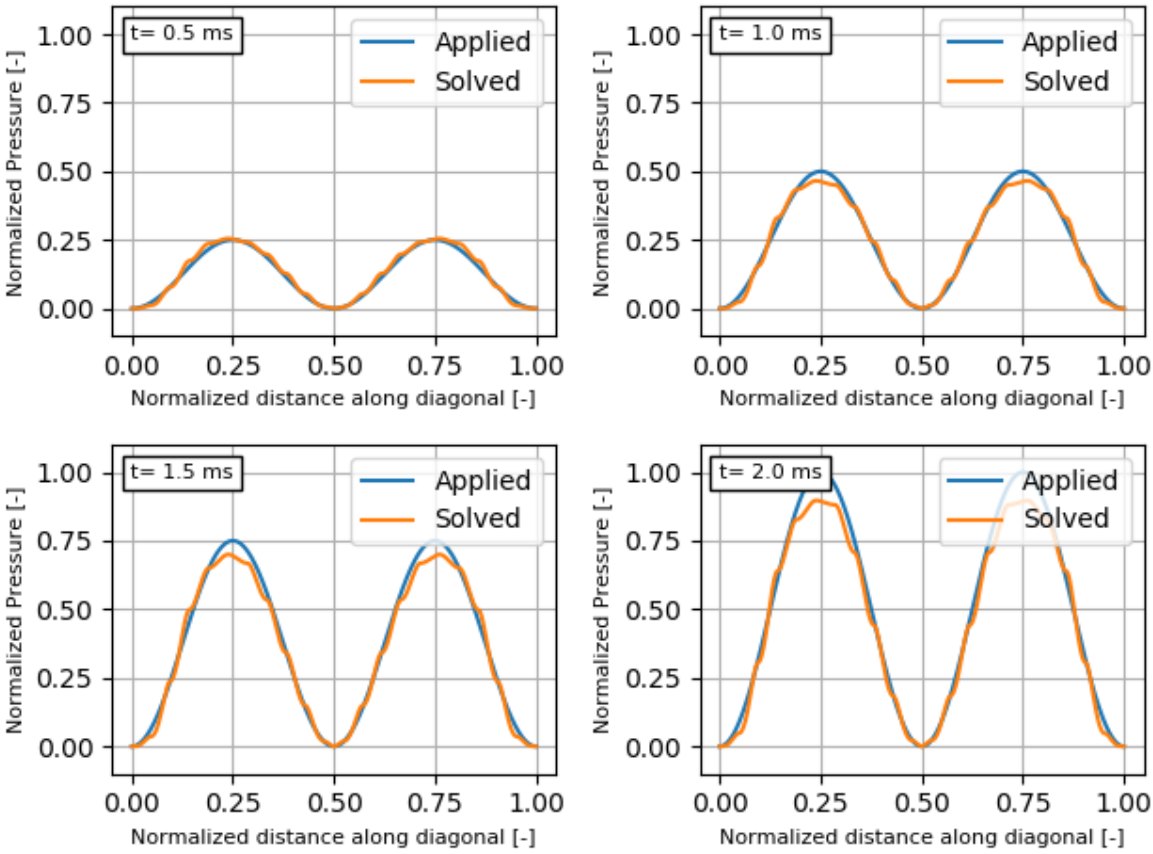

Figure 7.1: It can be seen that the smooth reference pressure distributions is captured back quite accurately. Note the linear increase in pressure over time.

First one sees that small oscillations around the correct pressure are observed. It is known from the static KL plate in Appendix F that spatially high frequency oscillations in pressure are filtered out in displacement. Hence such oscillations will not be seen in the displacement and its presence can thus not be determined from displacement data, this is a clear limitation of the IMP for plates.

Increasing the wave number

By increasing n,m the solution becomes less smooth, the plot below shows the results for n=m=3 to see the effect. From the static KL results in Appendix F it is expected that more waves is harder to capture back. In Figure 7.2 it can be seen that the pressure still captured back accurate. The results for n=m=4 are shown in the next Figure 7.3. The algorithm is still capable to capture the pressure profile back with reasonable accuracy.

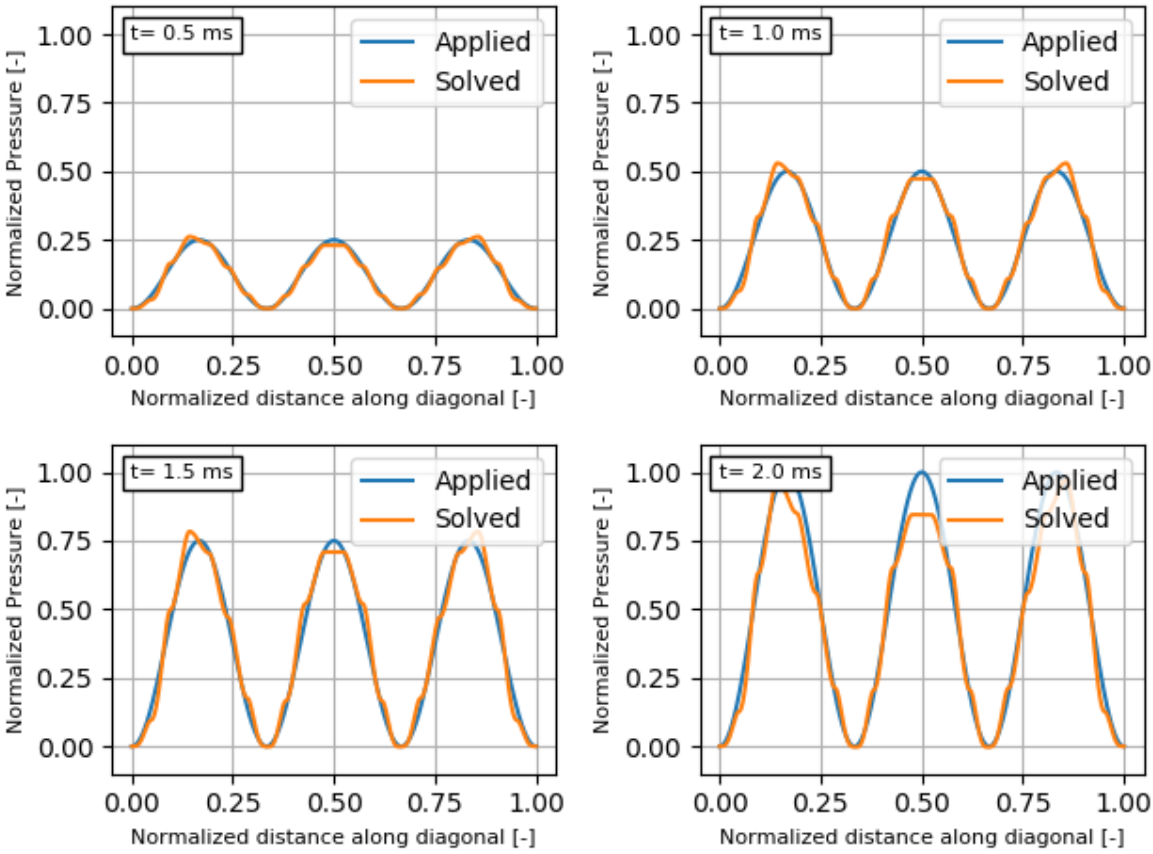

Figure 7.2: It can be seen that for n=m=3 the pressure distribution is still accurately captured.

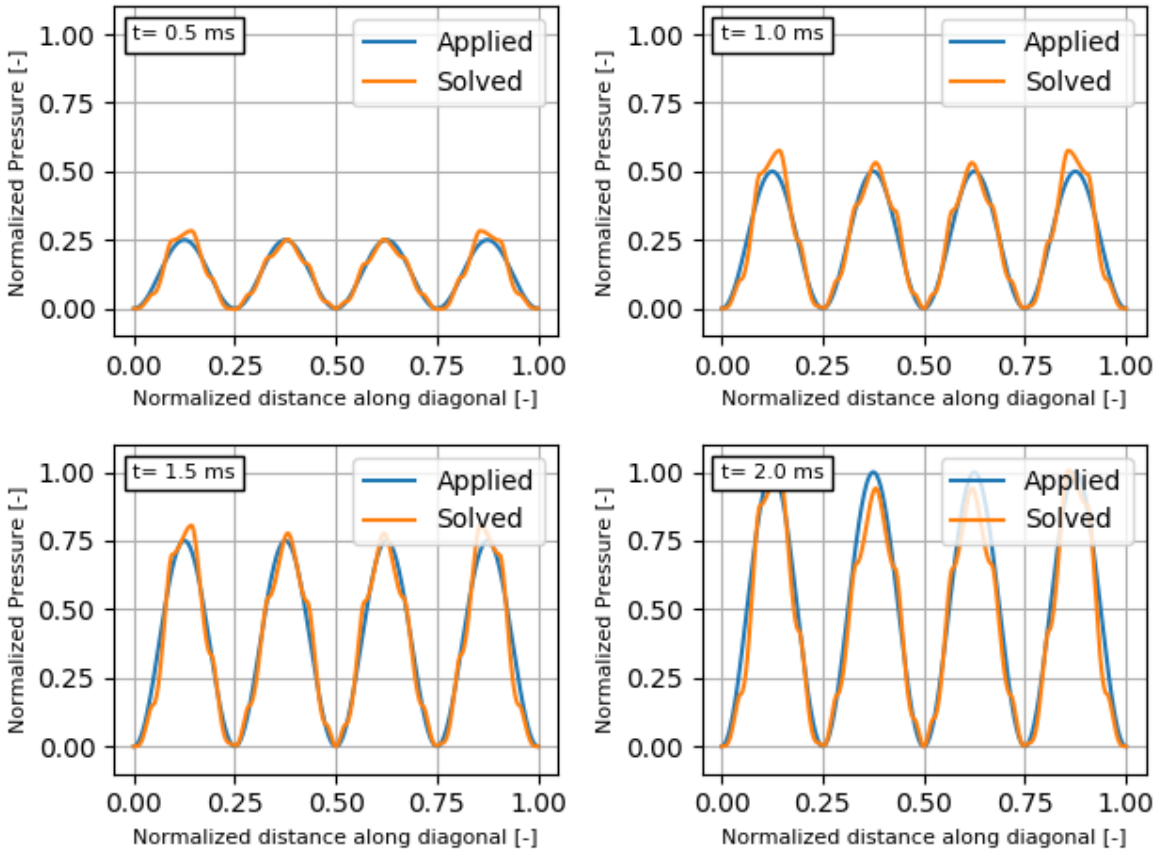

Figure 7.3: It can be seen that for n=m=4 the pressure distribution is still accurately captured.

Plate thickness

Again using the static KL result one can reason how the thickness would influence the result. For Navier solution it is seen that the deflection is inversely proportional to the bending stiffness. The thickness only influences the bending stiffness for the static KL plate. Since only scaling the input pressure and thereby the output displacement (linear problem) an gradient of descent algorithm will not perform any different. When the plate is thicker the bending stiffness will increase, decreasing the deflection. This will cause the noise to be relatively large for thicker plates. The direct influence of thickness for no noise situation is however expected to be small. Small and non zero because for the dynamic plate the thickness will also influences the mass matrix. The effect that thickness will have due to increase in relative noise will be similar to 'just' the effect of increasing relative noise discussed later. The results for a 2 times thinner and thicker plate are shown in Figures 7.4, 7.5 respectively.

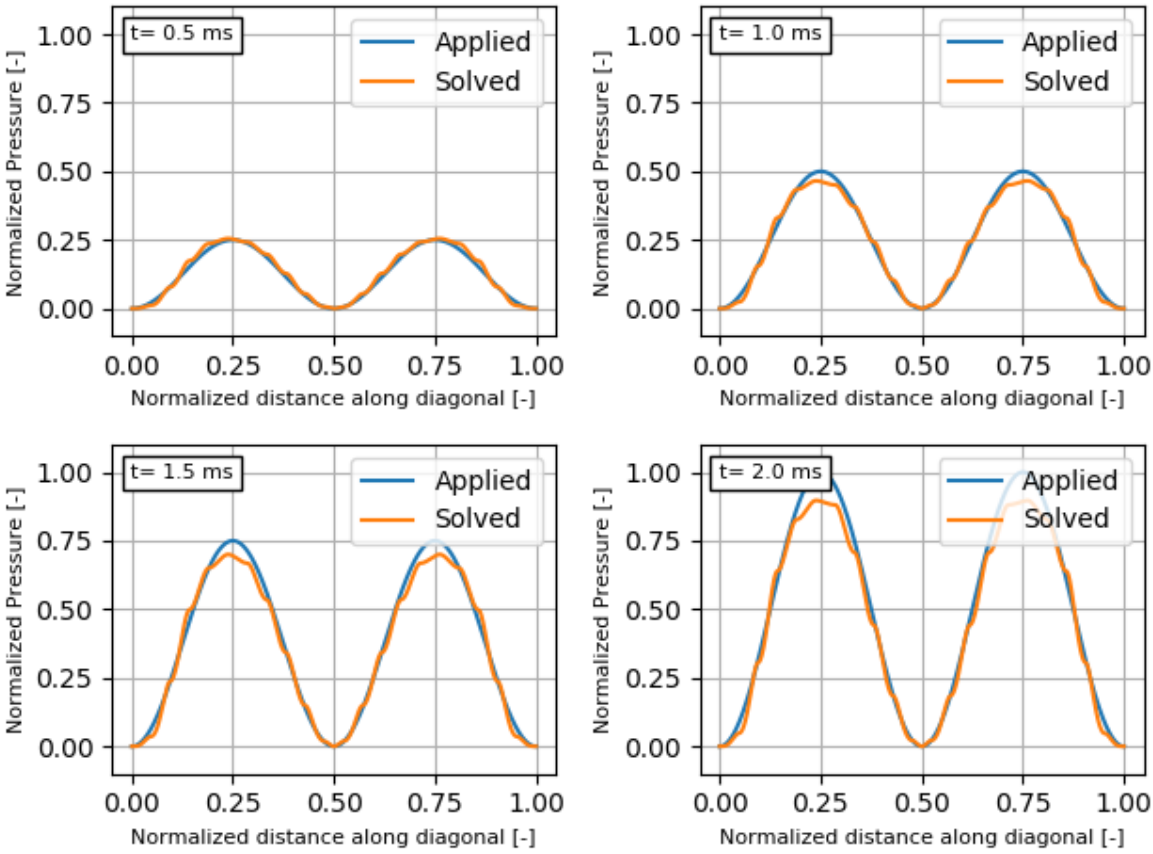

Figure 7.4: It can be seen that thickness only scaling barely influences the results, here the thickness is 0.5 times the reference thickness.

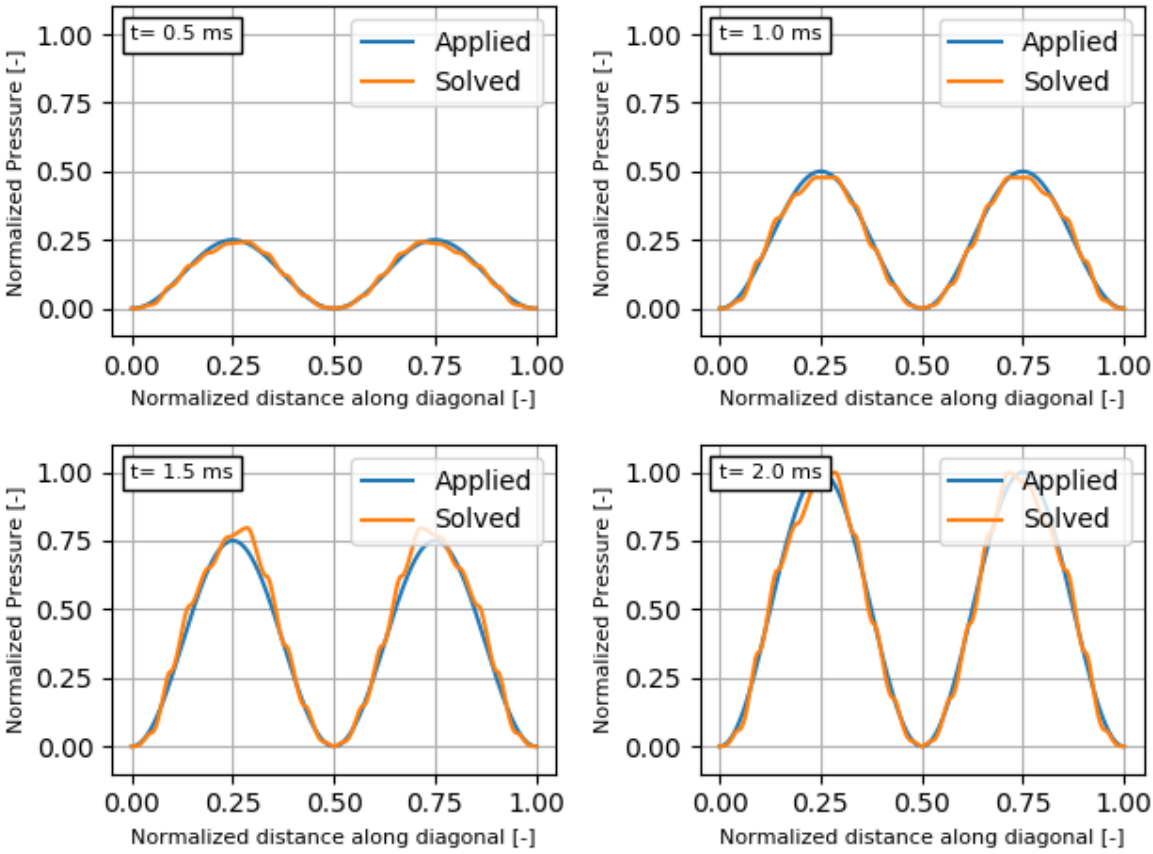

Figure 7.5: It can be seen that thickness only scaling barely influences the results, here the thickness is 2 times the reference thickness.

Amplitude change over time

In the reference situation the amplitude is increasing linearly over time (k=1). To study the effect of other time dependency k=3 is modeled. This implies that the pressure at $t = \frac{1}{2}T$ is $\frac{1}{8}$ of the maximum value at T. The pressure first increases slowly and near the end very rapidly. The results are shown in Figure 7.6.

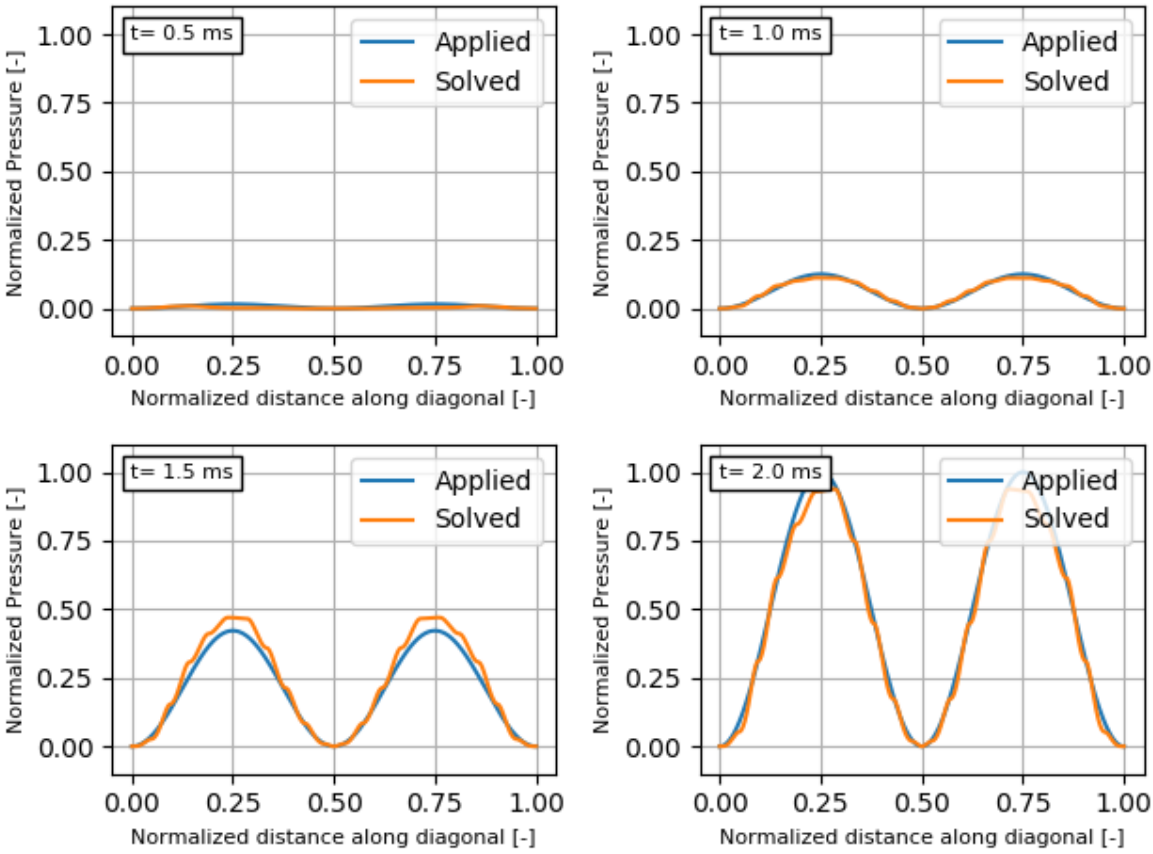

Figure 7.6: The pressure seems a bit less accurate for the cubic time increasing pressure amplitude i.e. k=3, however the algorithm is still accurate.

Simulation time T

The influence of simulation time is studied by simulations that take 10 times shorter and longer. No large differences are observed as seen in Figures 7.14,7.15. Currently no reason for any different behaviour is theorized. The main purpose of this test was to see if no strange behaviour is observed for different simulation times, covering most mine blast simulation times.

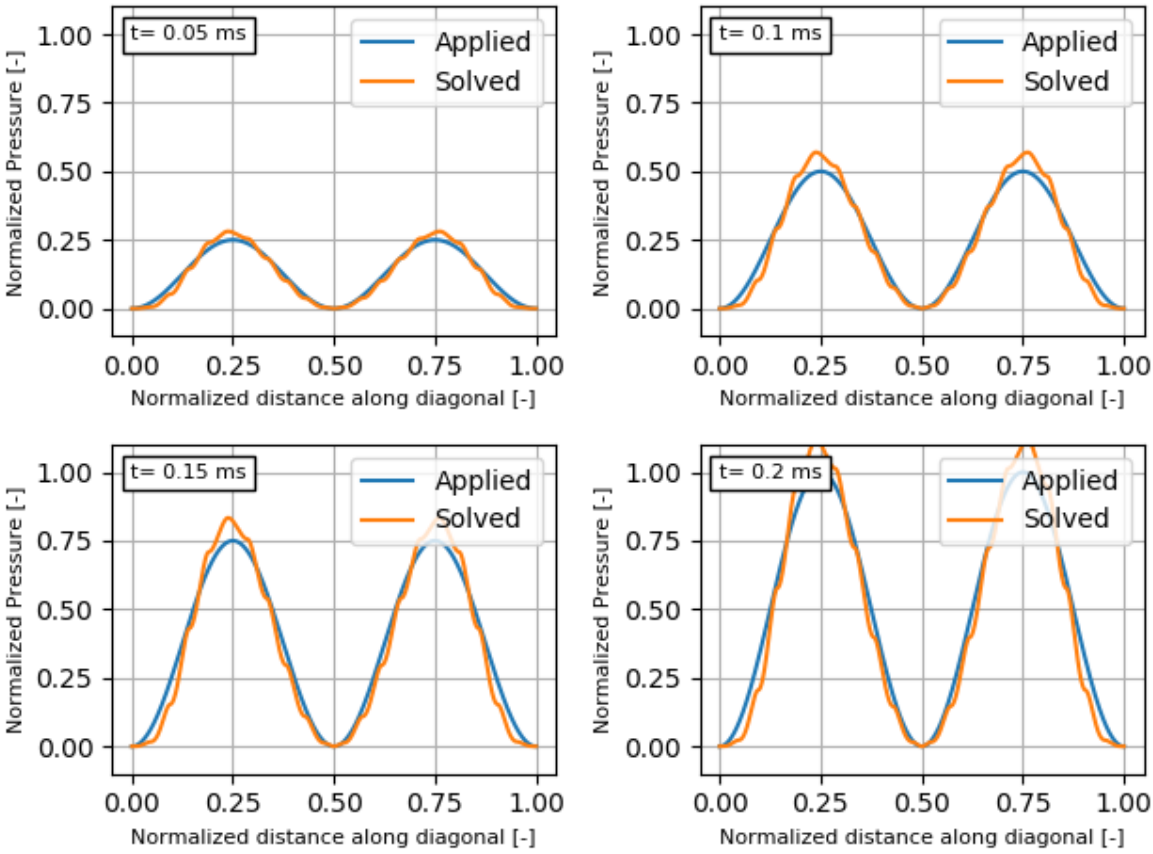

Figure 7.7: Simulations for T 10 times smaller than the reference situation, not much difference is observed w.r.t. the reference.

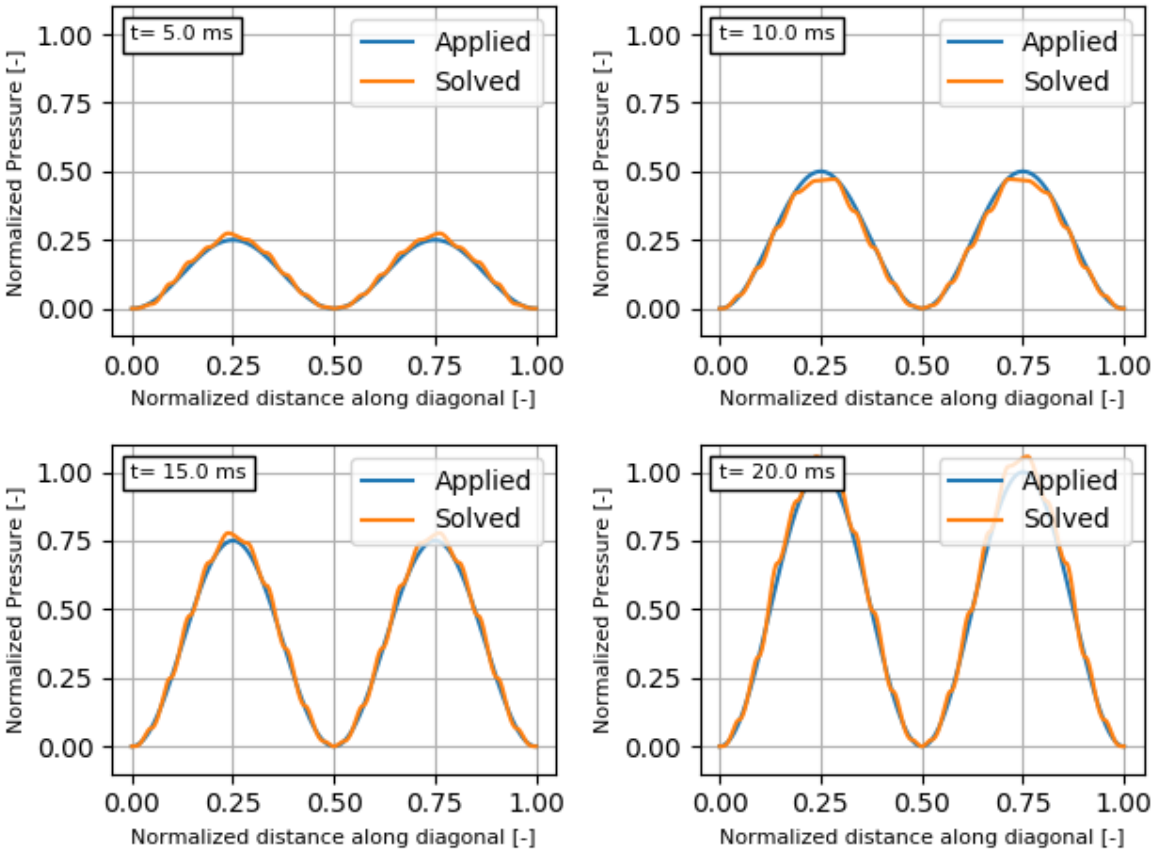

Figure 7.8: Simulations for T 10 times larger than the reference situation, not much difference is observed w.r.t. the reference.

Measurement Noise Untill now all previous simulations showed only little difference in behaviour for the variety of tests. It is well known that an IMP is very sensitive to noise. For this test 0.1% random Gaussian noise is added to the simulated data points. Here 0.1% is the percentage of the standard deviation of the Gaussian distribution w.r.t. the maximum deflection of the plate. The mean for the Gaussian distribution is chosen zero, here and for all other experiments. An error of 0.1% or less should be achievable by DIC techniques employed by TNO. The results are shown in Figure 7.9.

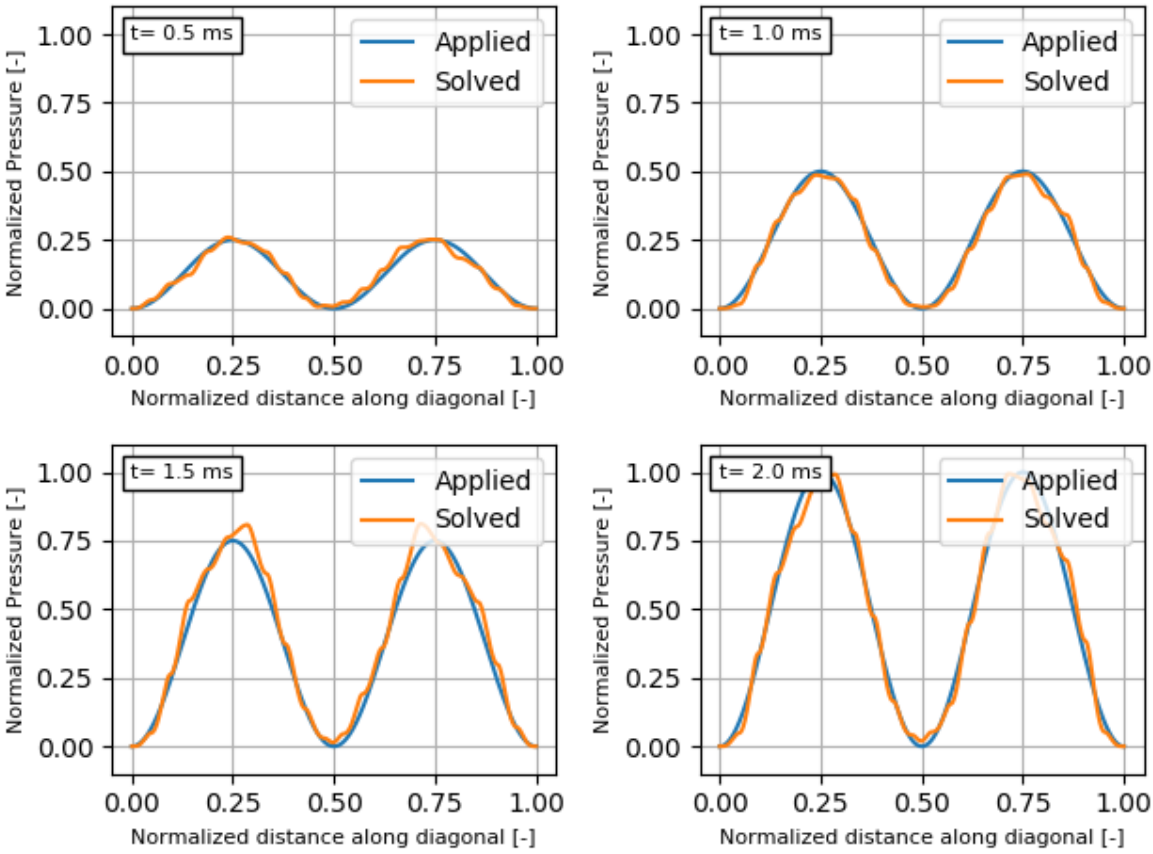

Figure 7.9: Adding 0.1% noise to simulate noise in DIC measurements. At this noise level the influence is still small.

By increasing the noise to 1% large errors are obtained. It can still be seen that the rough trend is followed, however high frequency oscillations around the correct solution are observed for the solved pressure. This demonstrates the need for very accurate measurements.

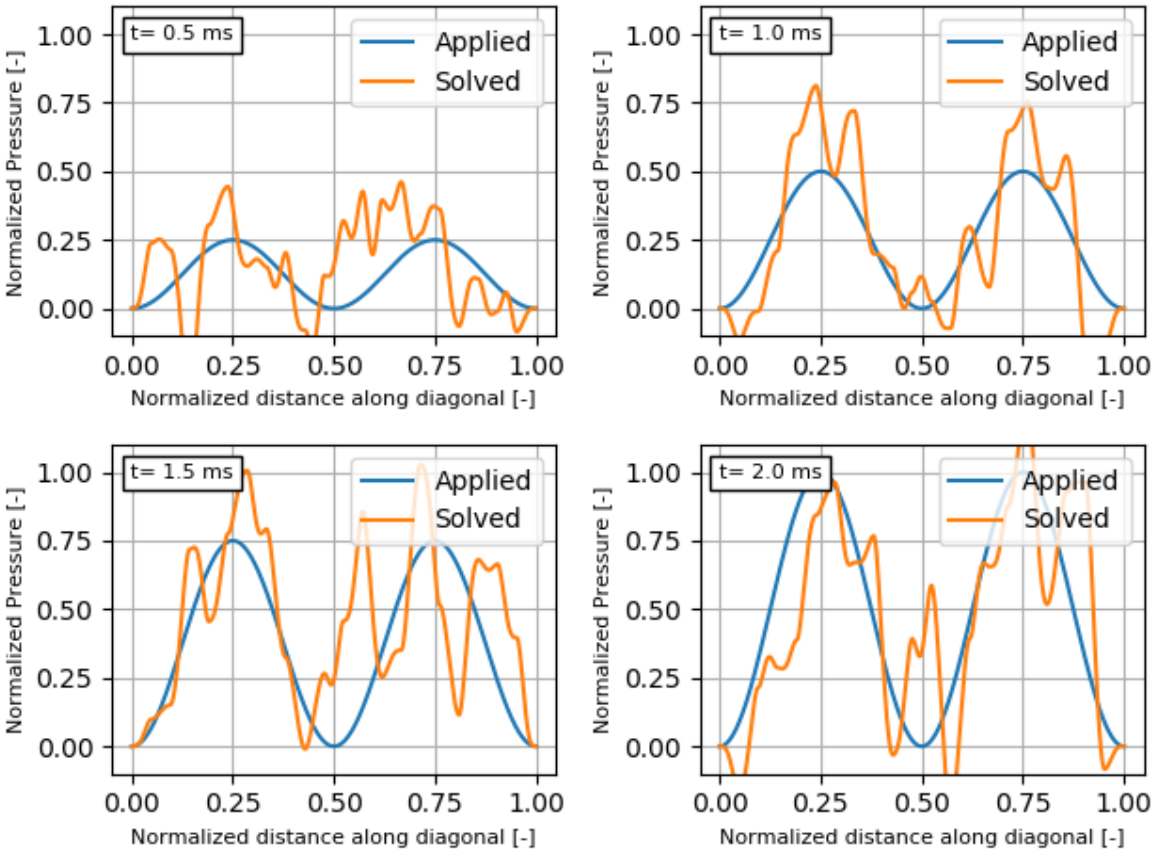

Figure 7.10: Adding 1% noise to simulate noise in DIC measurements. At this noise level the influence is rather large.

7.1.2. Localized distribution

The localized pressure distribution is similar to the benchmark pressure distribution. A radial symmetric moving exponential distribution is used, Equation 7.2. This distribution is localized but smooth.

$$P(r,t) = e^{-(B^2(r-vt)^2)} \tag{7.2}$$

Here 'v' is the velocity of the moving exponential and 'B' changes the width. For the reference simulation a velocity is used such that the wave moves from the middle to the edge of the plate in time 'T'. The width is chosen a bit arbitrarily and the influence of width will be studied below. The result for the reference situation is shown in Figure 7.11.

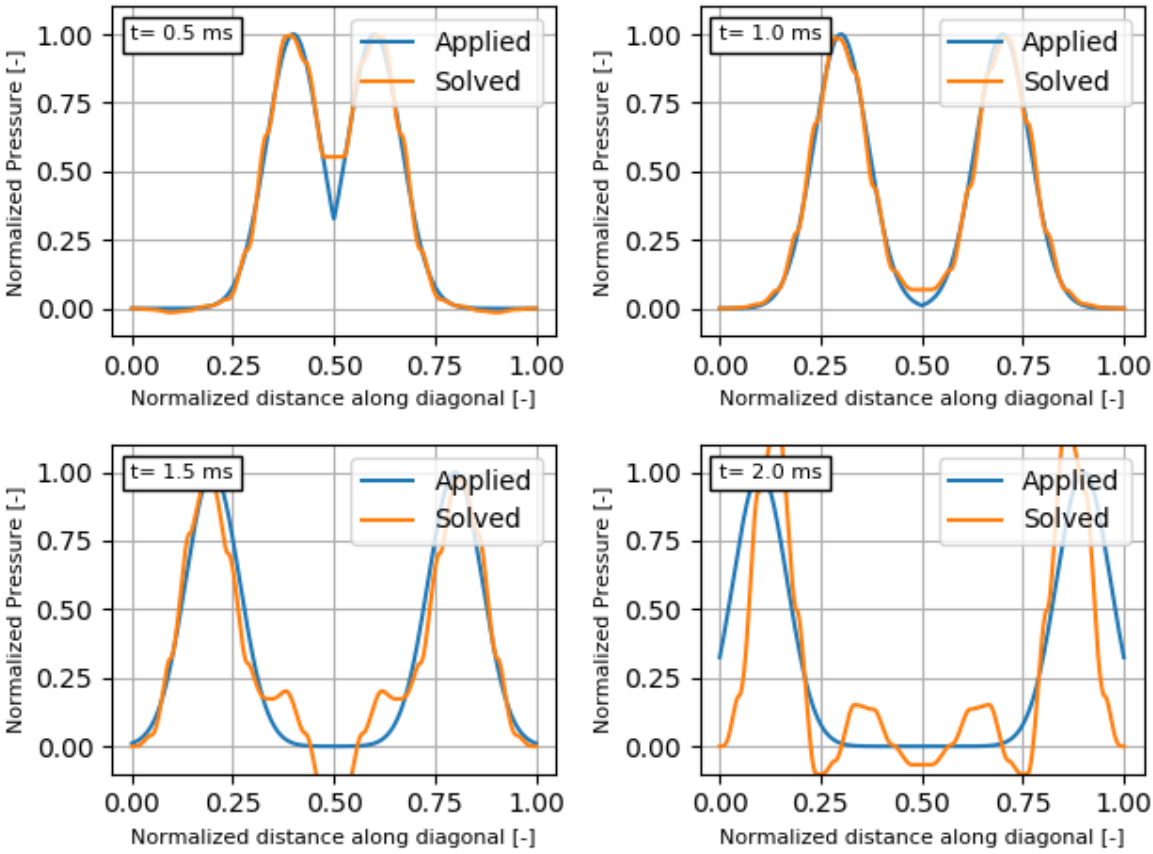

Figure 7.11: It can be seen that the smooth localized load is accurately captured, even for the slope discontinuity. Note that at t=1.5 ms and later oscillations are present.

Measurement Noise

Similar as before noise is studied for 0.1% and 1%. The results are shown in Figures 7.12 7.13.

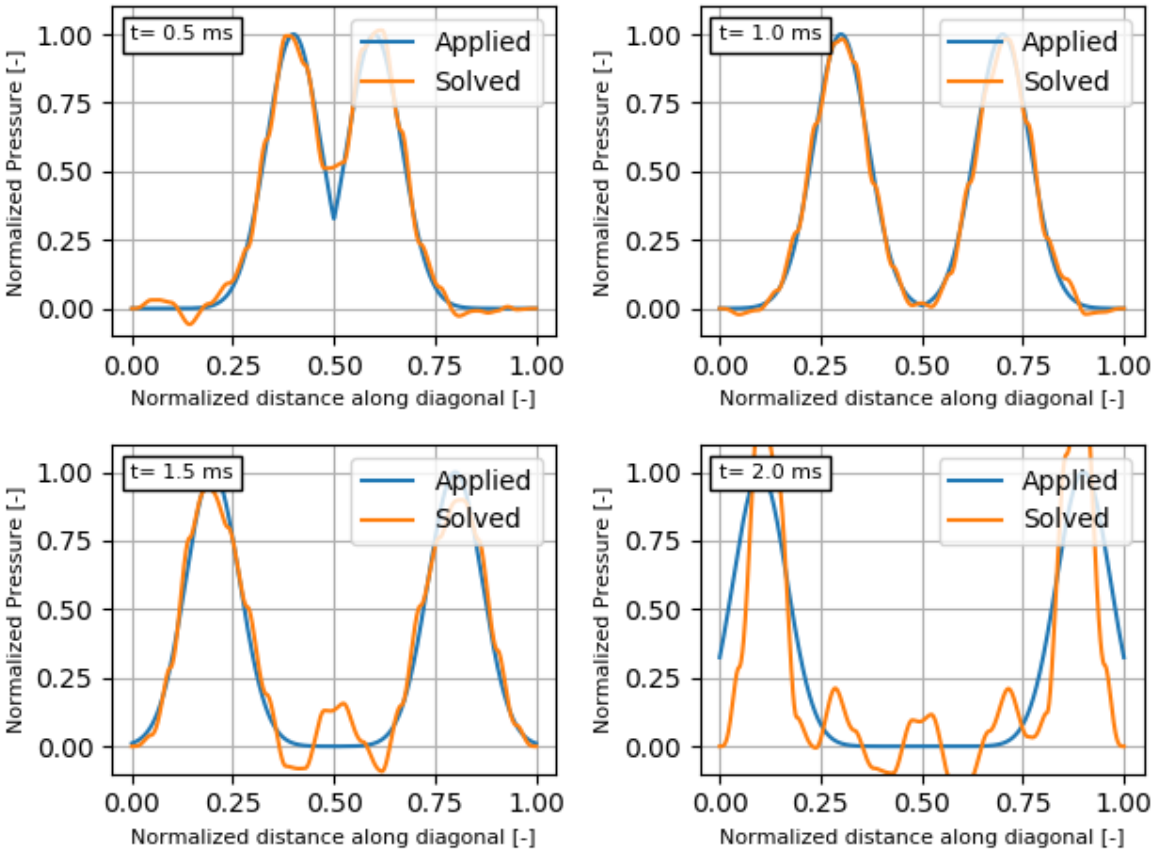

Figure 7.12: For noise level of 0.1% the observer error is not much different.

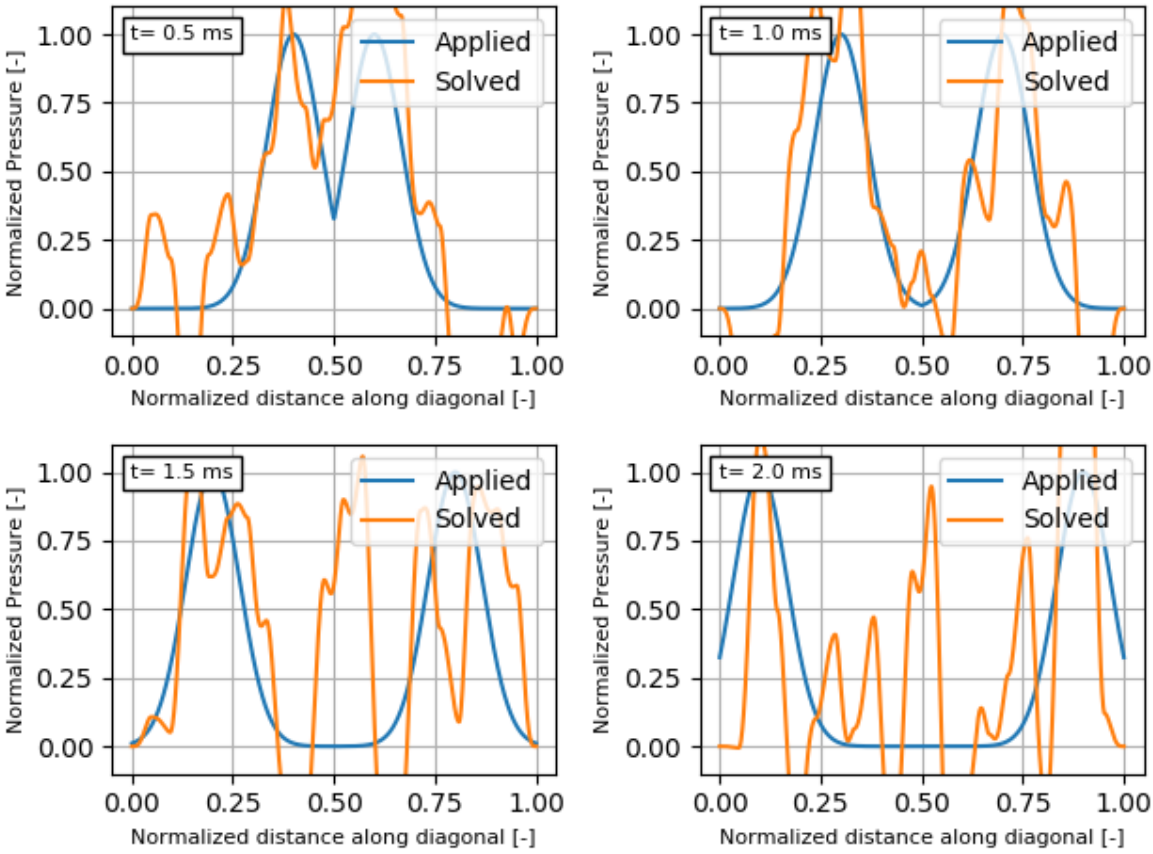

Figure 7.13: Noise level of 1% gives large amount of error as shown.

When 1% noise in the data present and the knowledge that the pressure distribution should be smooth one can use regularization. Since the actual pressure distribution of interest, a mine blast, is not smooth regularization is not used. Also errors near 0.1% are expected instead of the 1% where regularization seems required.

Simulation time T

Again the influence of simulation time is studied by simulations that take 10 times shorter and longer. The response in these cases is quite different, and for that reason the performance is of interest. The Figures below show the results 7.14, 7.15.

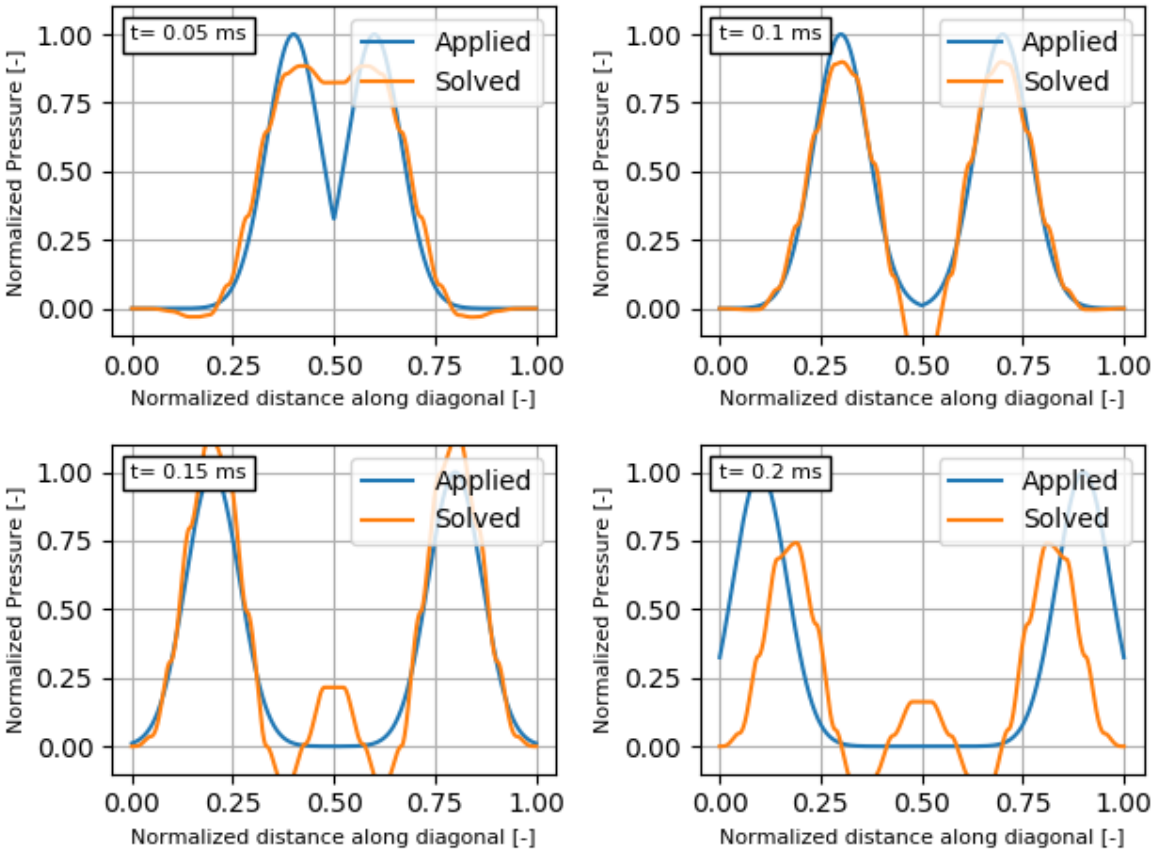

Figure 7.14: Simulations for T 10 times smaller than the reference situation, the results are slightly less good.

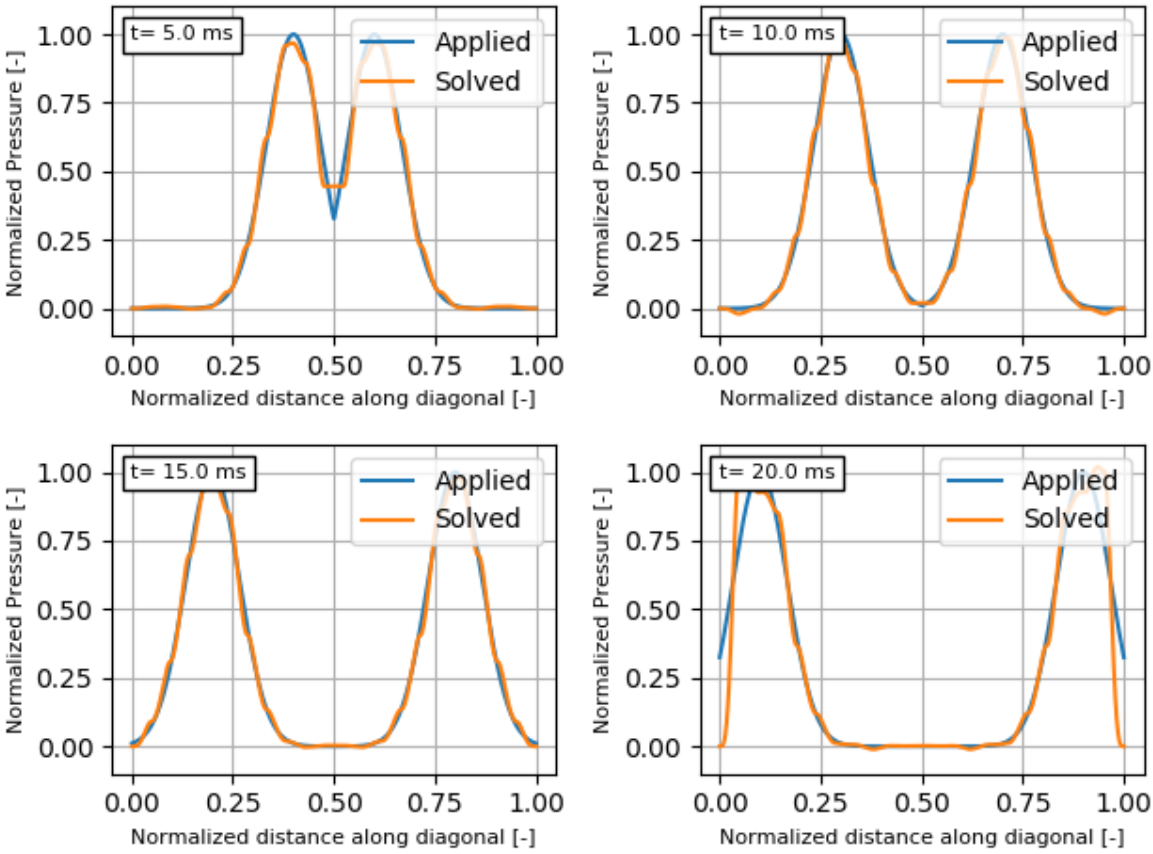

Figure 7.15: Simulations for T 10 times larger than the reference situation, the results are slightly better.

The results for shorter simulations is slightly less accurate. It should also be noted that the displacement for a shorter pulse is less, hence increasing the relative error, not taken into account here. Also the amount of data points in time will decrease when the duration is shorter which will decrease the accuracy. The results for longer duration are better.

Pressure pulse Width

It is expected that a larger pressure pulse width thus spatially smoother functions are easier to capture by the IMP algorithm. The pressure pulse width of a mine blast can vary for each situation, hence the performance is of interest. The simulation results are given in Figures 7.16, 7.17.

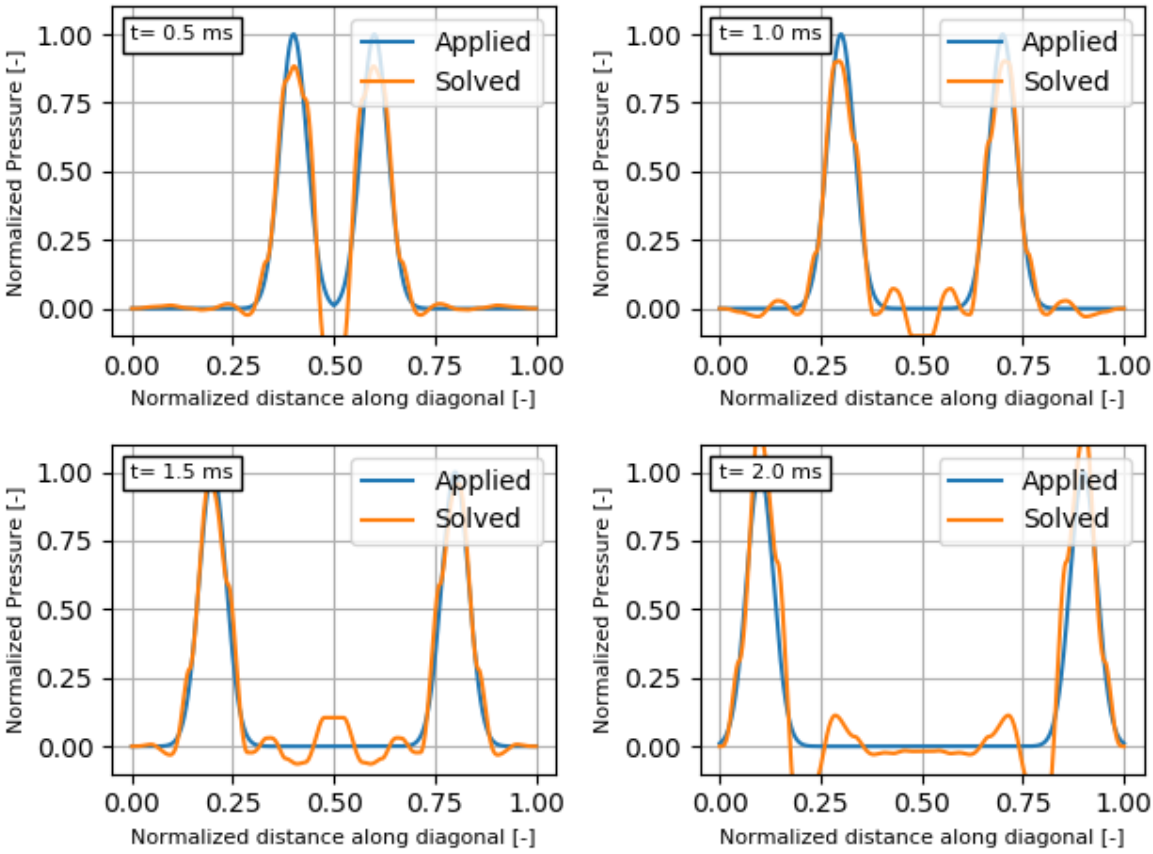

Figure 7.16: The figure shown is for a small pressure pulse width (B->2B) and is captured back accurately width the IMP algorithm, although there are some oscillations present.

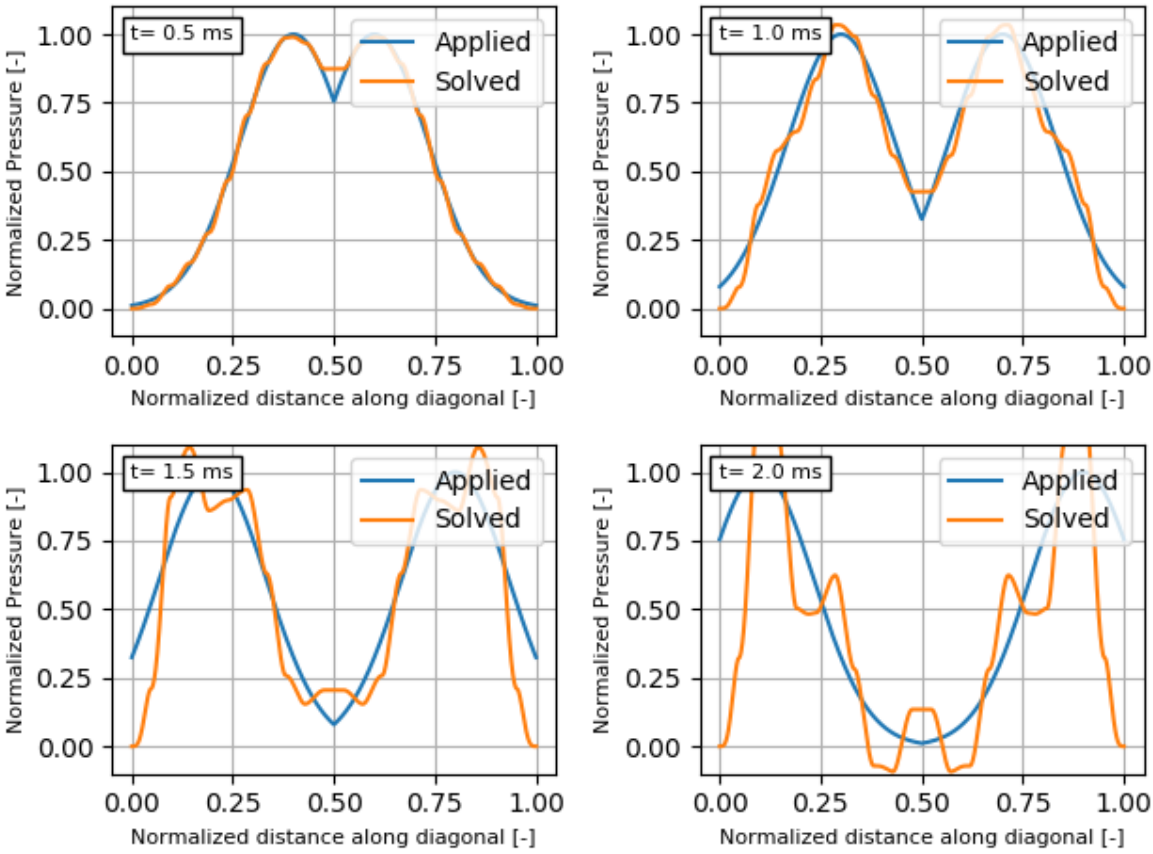

Figure 7.17: The figure shown is for large pressure pulse width (B->0.5B). Contrary the expected behaviour the algorithm shows quite some error. The cause is not known however expected due to the non-zero pressure values on the boundary.

It was expected that wider pressure pulses are easier to capture back, mainly based on the static KL derivation in Appendix F. The reason for poor performance of the wide pressure pulse might be due to non-zero pressure on the boundary.

7.1.3. Benchmark Pressure

The benchmark pressure itself, here repeated Equation 7.3 is localized and discontinues. As the results will show such a pressure distribution is found harder to capture back with the IMP algorithm.

$$P(r,t) = \begin{cases} Ae^{-(vt-r)w}(1-(\frac{r}{L})^2), & vt-r>0\ AND\ r<L \\ 0, & otherwise \end{cases} \tag{7.3}$$

The results for the reference situation are shown in Figure 7.18

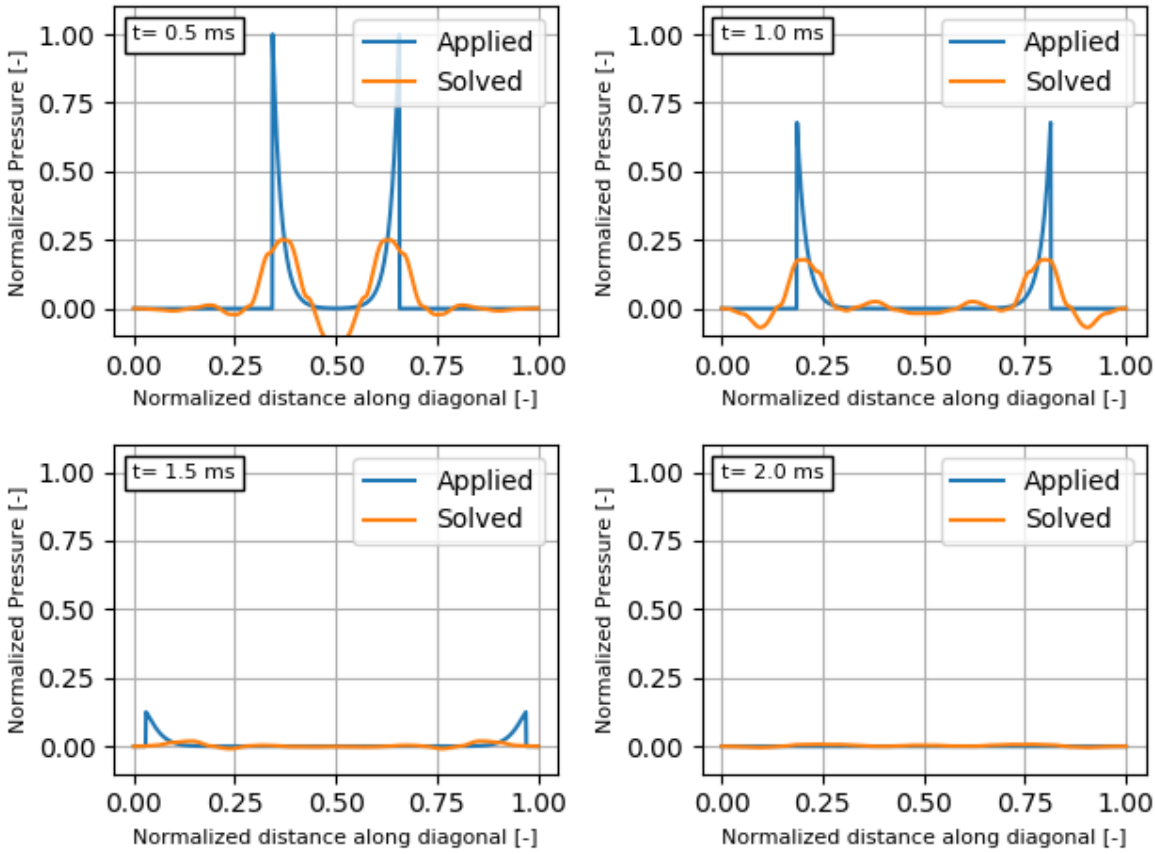

Figure 7.18: The reference situation for the Bench mark pressure. The highly localized and discontinues pressure distribution is captured back poorly. Yet the trend that is the movement of the largest peaks, is still clearly visible.

The reference benchmark pressure is localized and captured back poorly. Yet the trend of moving peaks is still observed. The benchmark pressure is clearly the limit of the IMP algorithms capability. It should be noted that the displacements for all test did converge well, as can be seen in Figure 7.19.

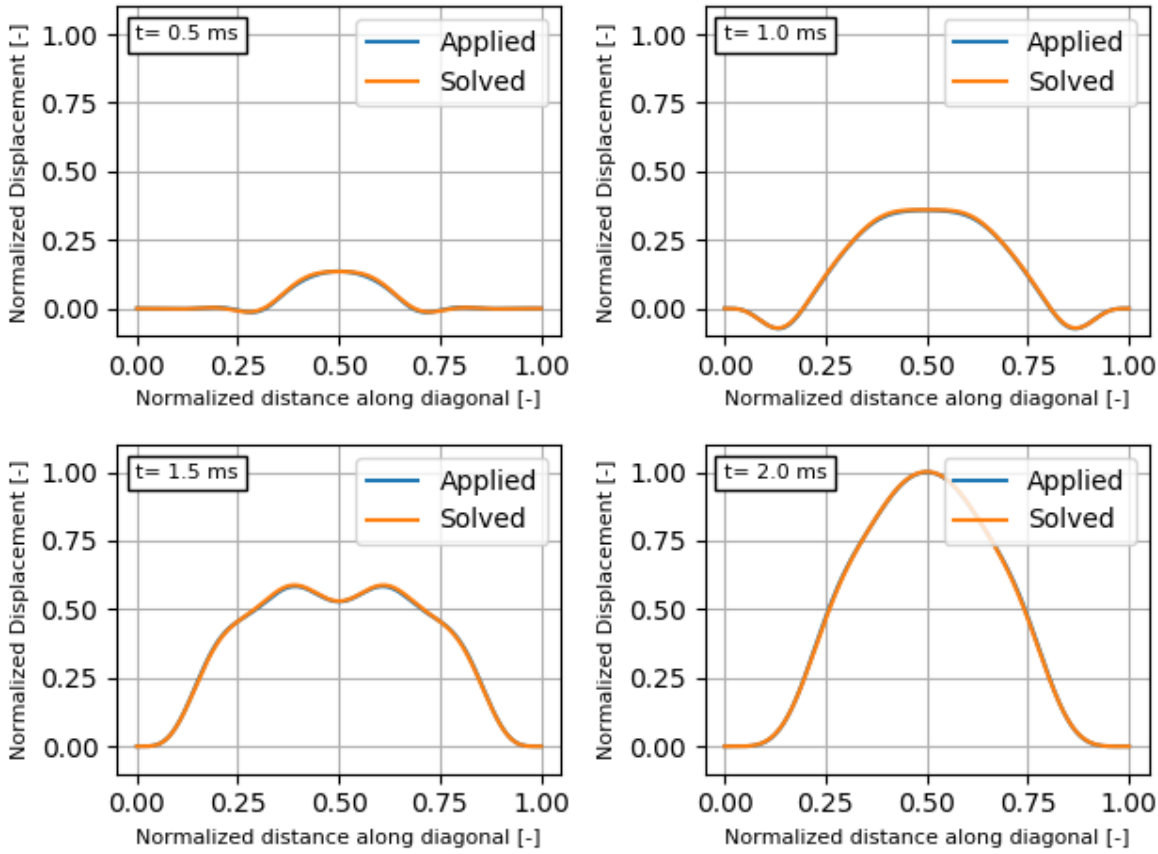

Figure 7.19: Displacement shown for the reference situation for the Bench mark pressure. The displacements are almost the same, and clearly converged to great accuracy.

Pressure pulse Width

The poor performance of the algorithm for the reference benchmark pressure is expected due to the very localized pressure distribution. For that reason the pressure pulse width is tested here, first 10 times smaller then 10 times wider, Figures 7.20, 7.21 respectively.

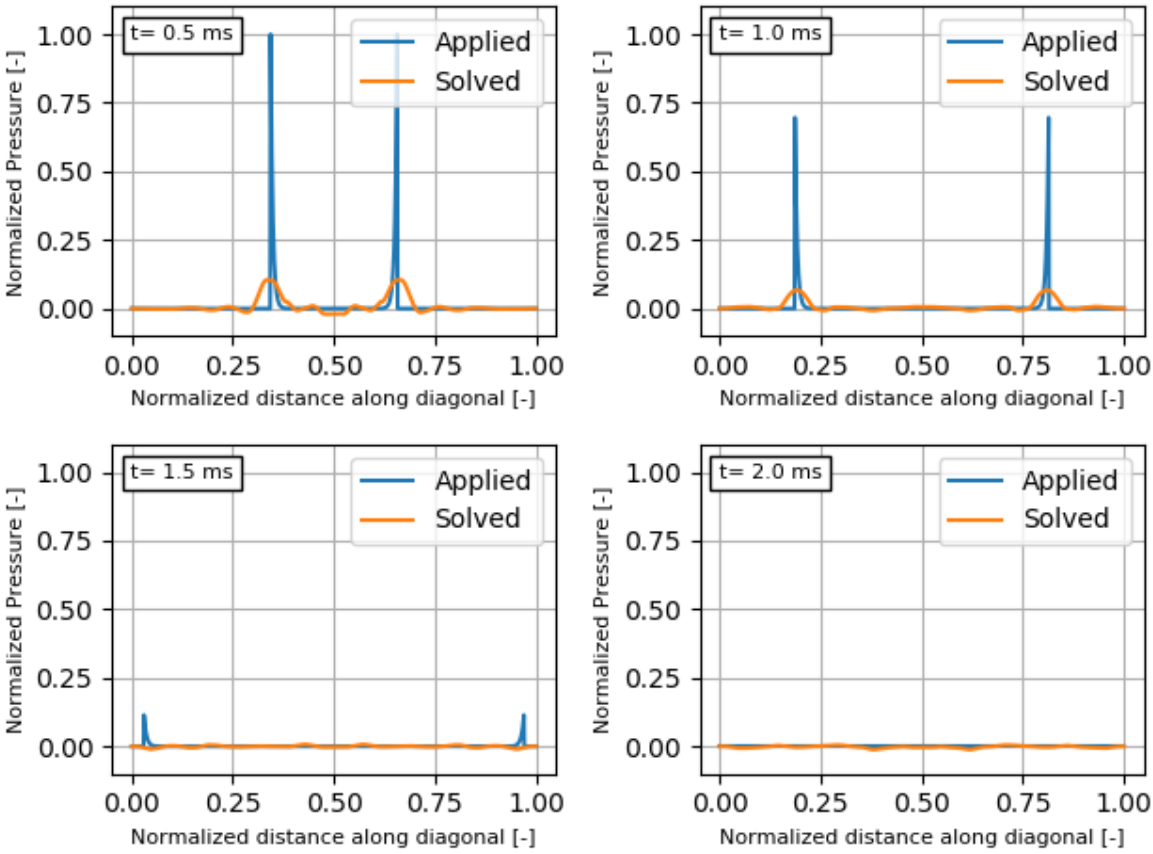

Figure 7.20: The figure shown is for a 10 times smaller pressure pulse width. The results are less compared to the reference.

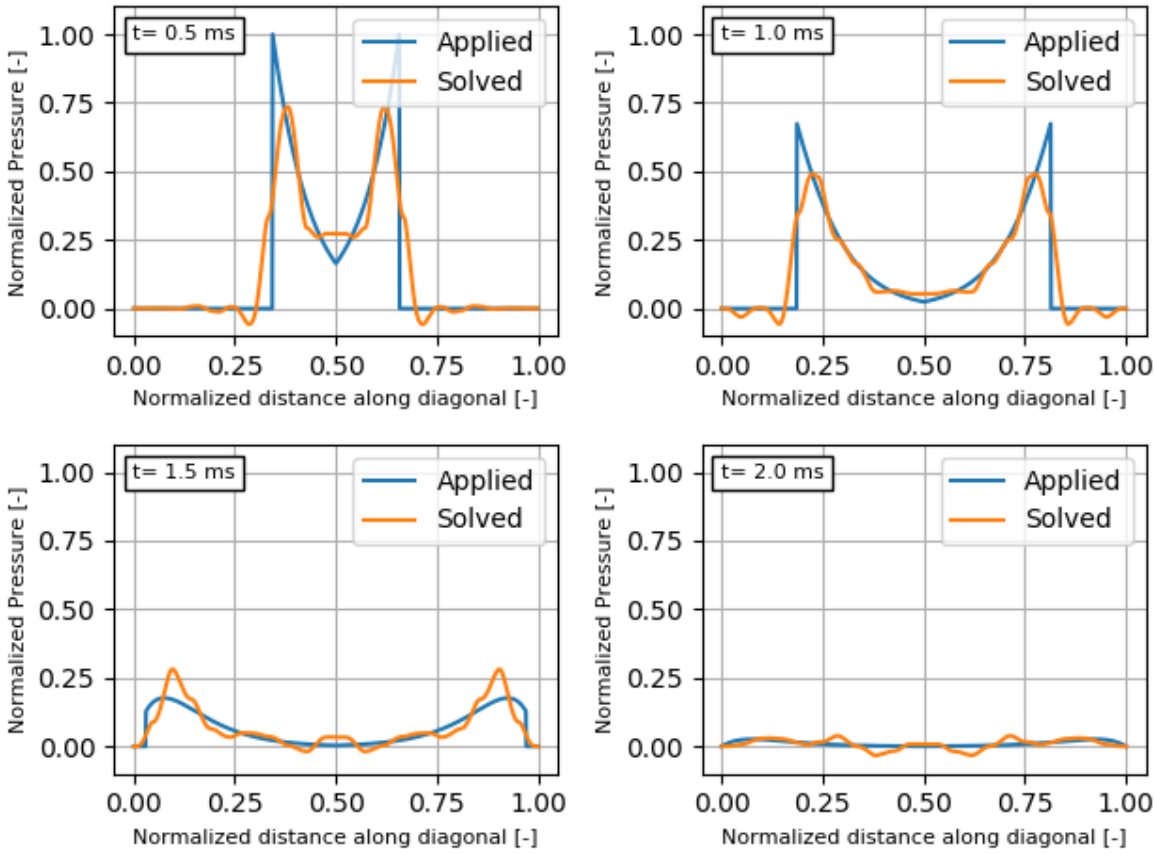

Figure 7.21: The figure shown is for a 10 times larger pressure pulse width. Clearly the results are much better as compared to the reference situation.

It is clear that the performance of the benchmark is poor. The displacements for all simulations (not shown) do however converge. This shows that this IMP is non-unique and thus several quite different pressures will give almost the same displacement. This is especially the case for very localized loads, the plate bending response will simply not measurably follow local pressure variations.

Measurement Noise

Again the influence of noise for 0.1% and 1% is tested, Figures 7.22 7.23. Since the error was already quite large for the reference situation not much can be said for the added noise situations.

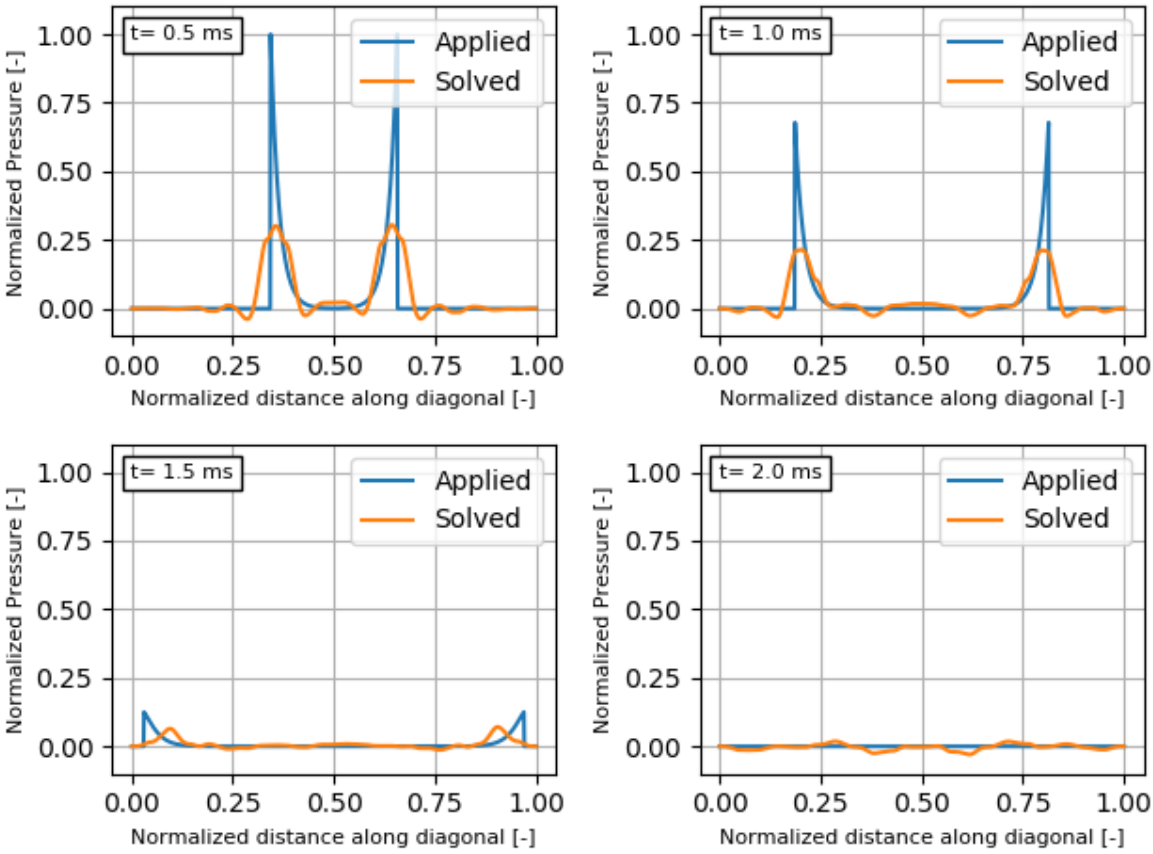

Figure 7.22: For noise level of 0.1% the observer error is not much different. Note that the main cause of error still seems to be caused by the very localized pressure distribution

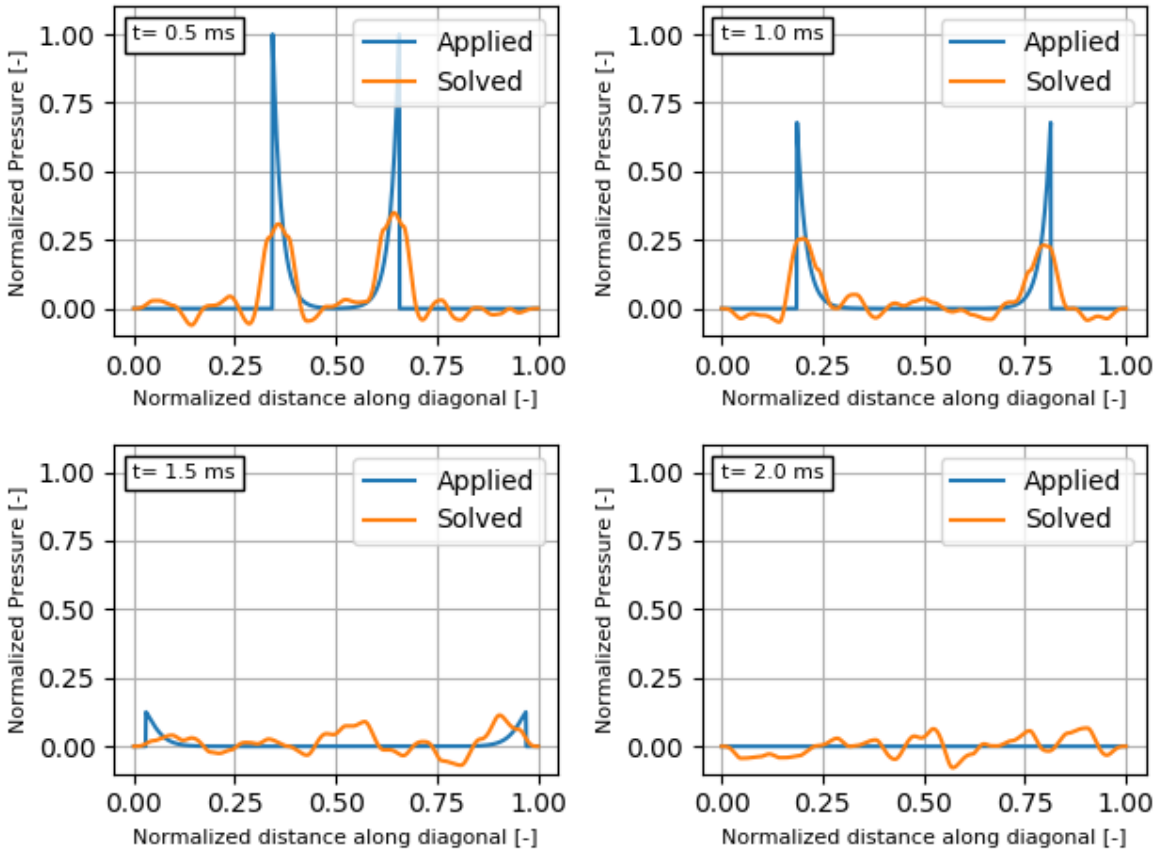

Figure 7.23: For noise level of 1% the difference is still surprisingly small. Mainly an increase in spatial pressure oscillations is observed. Note that the main cause of error still seems to be caused by the very localized pressure distribution.

7.1.4. Post processing pressure data: Determination of Invariants

In the previous section is became clear that capturing back the localized discontinues benchmark pressure is hard. The loading trend of the applied and solved is the same (two moving peaks), however the pressure distribution is different. It is known that both different pressure distributions give almost the same deformation. These effects illustrates the non-uniqueness and sensitivity of the IMP. Since the deformations match, the problem is not the algorithm used. One could force the pressure into a certain behaviour using e.g. a constrained function space, based on expected behaviour. This could lead to better pressure profiles when the expected behaviour is indeed correct. However instead of doing that the obtained pressure is post processed. The processing is done on the basis of one principal observed for localized loads. The pressure distribution of localized loads does not influence the response of the plate much, as long as the force and the centroid of the load remain the same. This statement is illustrated with a sketch for a cantiliver beam, Figure 7.24

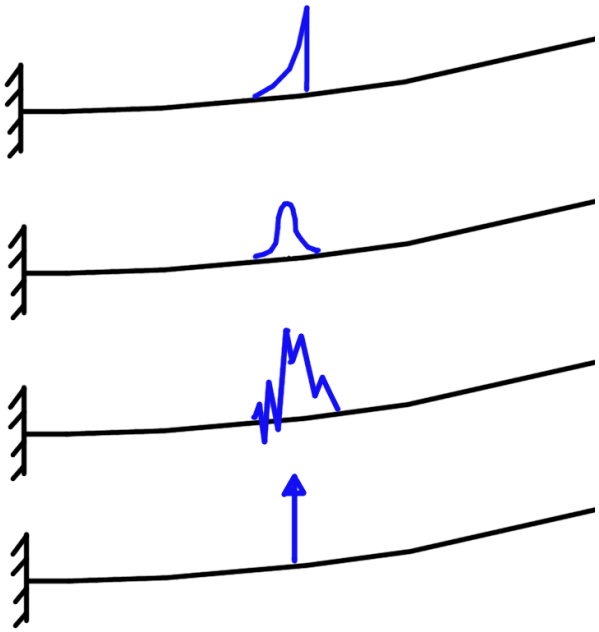

Figure 7.24: The sketch illustrates that localized pressure distributions of different shapes will give the almost the same response when the location of the load and the magnitude is equal.

The sketch shows a limitation of the IMP. No algorithm can determine the best pressure distribution among the four shown in the figure, since each will give almost the same deformation. This is an important conclusion as it illustrates the limitation of the validation process for mine blast models used by most researchers in the field. That is comparing experimental deformation of some test setup w.r.t. numerical or model results.

Two important parameters that can be determined from the deformation of a localized pressure distribution are the total force and the location where force is acting. First the total force as function of time is given by

$$F(t) = \int_{\Omega} P(\boldsymbol{x}, t) \mathrm{d}\Omega. \tag{7.4}$$

Assuming the pressure distribution is radial symmetric and localized, the centroid of the load can be determined. Here we define the centroid of the load as

$$\bar{r}(t) = \frac{\int_{\Omega} r P(\boldsymbol{x}, t) \mathrm{d}\Omega}{\int_{\Omega} P(\boldsymbol{x}, t) \mathrm{d}\Omega}. \tag{7.5}$$

The force and centroid location post processed in accordance with Equations 7.4 and 7.5 are in good agreement for the applied and solved pressure distribution for the numerical experiments. Particular poorly matching pressure distributions where obtained for the bench mark pressure distribution in reference situation, with 1% noise and for the 10 times smaller pressure pulse width. For that reason the post processed results for these situations are shown here. First the Benchmark pressure force and centroid position Figure 7.25.

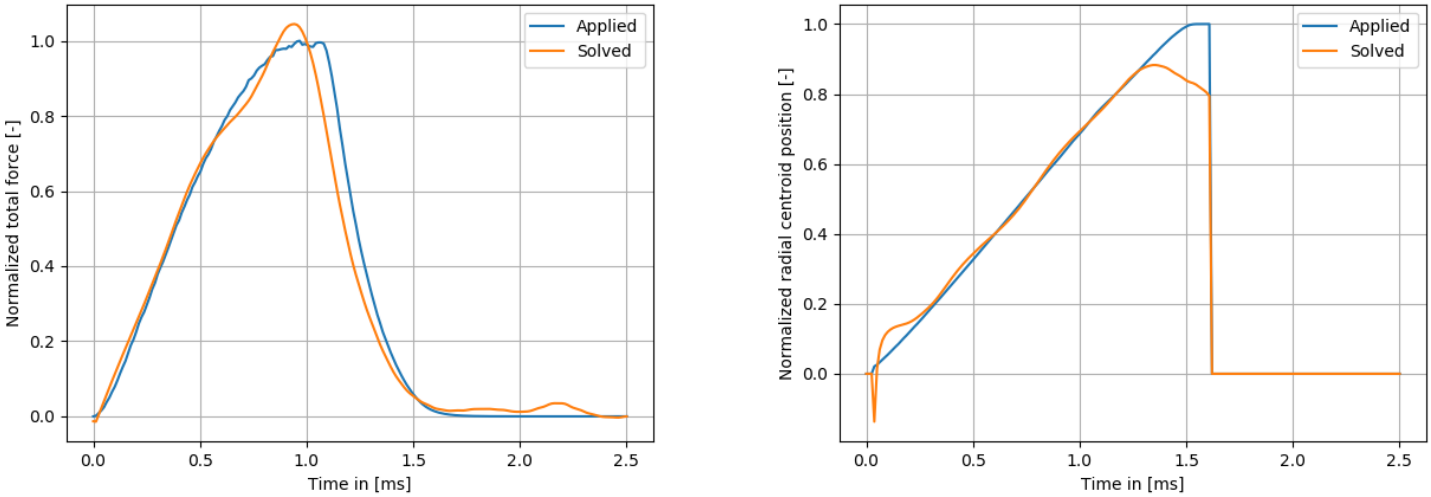

Figure 7.25: Left the the normalized total force vs time and right the normalized centroid location vs time. Both graphs are for the benchmark reference case and are in good agreement.

The post processed results for the Benchmark problem with 1% noise is given in Figures 7.26

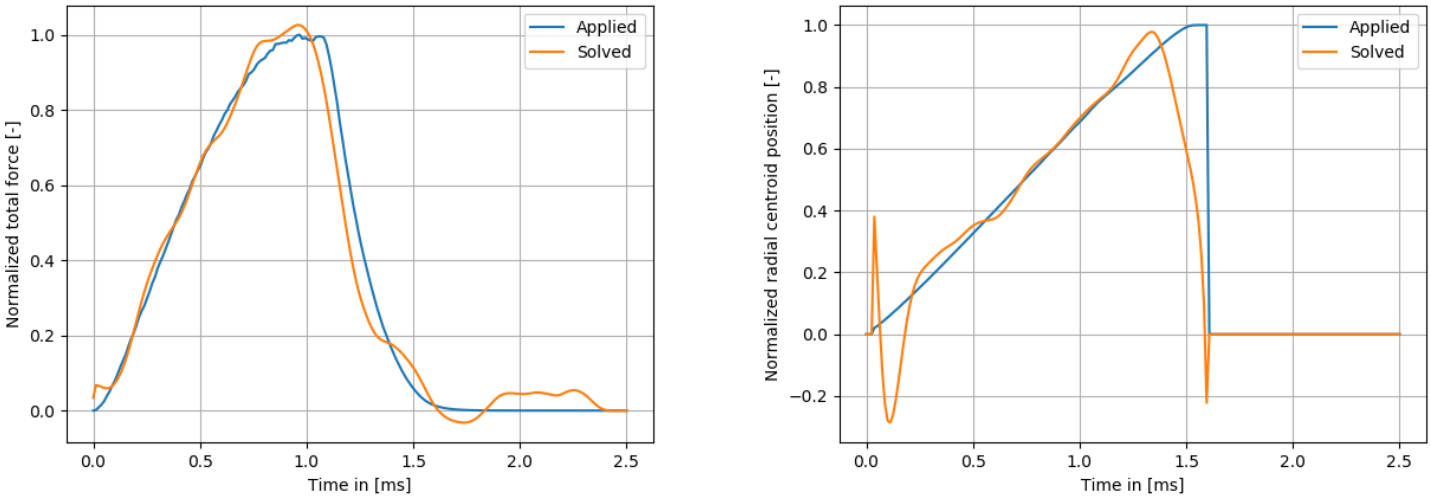

Figure 7.26: Left the the normalized total force vs time and right the normalized centroid location vs time. Both graphs are for the benchmark case with 1% noise. In contrast to the pressure profile the post processed results and are in good agreement.

The post processed results for the Benchmark problem with 10 times smaller pressure pulse width is given in Figures 7.27

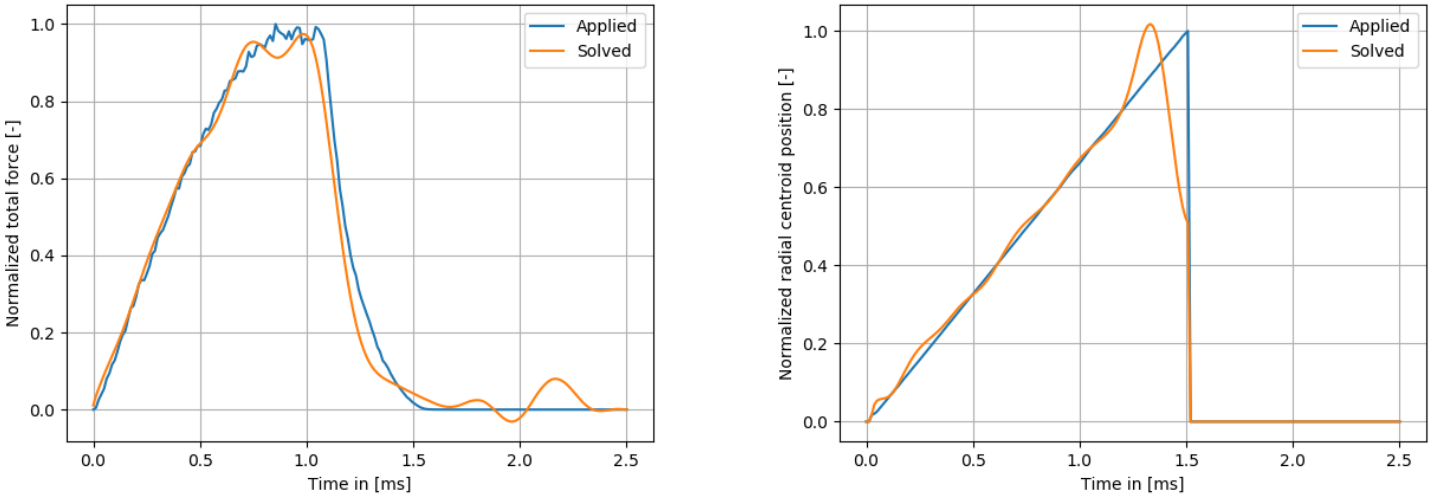

Figure 7.27: Left the the normalized total force vs time and right the normalized centroid location vs time. Both graphs are for the benchmark case with 10 times smaller pressure pulse width. Again in contrast to the pressure profile the post processed results and are in good agreement.

It can be seen that the results for the presented plots are accurate at locations where the force is not too small. Hence at the start and end of the loading the results are some times a bit off. When the force becomes to small the centroid position is set to zero as can be seen in the plots. This is done to prevent noisy data near zero division in the numerical results.

Invariants

The total force and the radial centroid position as function of time F(t) and r(t) respectively act as an invariant. That is for (vastly) different pressure distributions that give the same, or rather almost the same, deformation these parameters will be unchanged. The study of such invariants is important, and are per definition the only relevant parameters that can be determined from the experiment. It should be noted that the two proposed parameters seem invariant however this is not proven. Furthermore the existence of more invariants are expected. For example the width of a localized load will influence the response, which can vary without changing F(t) and r(t).

7.2. Non-linear elastic continuum

The results of the algorithm for a continuum plate model with described non-linear material model are discussed in this section. For this algorithm only three tests are performed since one simulation takes 4 days less tests were performed. The reference sine case, the reference case of the localized distribution and the reference benchmark case all with 0.1% noise are simulated. The amplitude of the pressure loading for the linear case was not important, scaling the input directly scaled the output. For the non-linear case the amplitude is chosen such that the deformation is approximately the same as the actual experiments. The displacements converged less accurate compared to the KL simulations hence the displacements are also shown in this section for the different simulations.

7.2.1. Smooth distribution

The final deformation of the plate is visualized using Paraview [8] see Figure 7.28. Both the applied and solved case are shown left and right respectively. The displacement are compared in Figure 7.29 where it can be seen that the algorithm is converged quite well. The match between the ‘applied’ and ‘solved’ case is good. The corresponding pressure loading is plotted in Figure 7.30. It can be seen that the pressure is similar however much larger differences are observed compared to the displacement. This shows that inverse problems are quite sensitive. That is small variations in the input (displacement) can result in large differences in output (pressure).

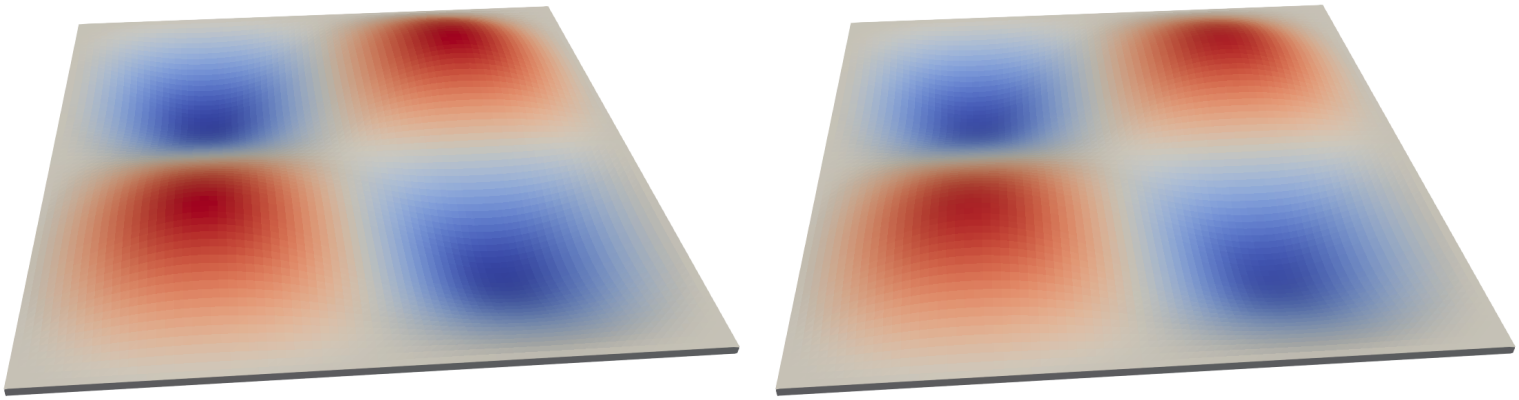

Figure 7.28: Both the Left and Right plot show the final deformation of the plate. The left for the 'applied' case and the right for the 'solved' case. Both deformations are a good match.

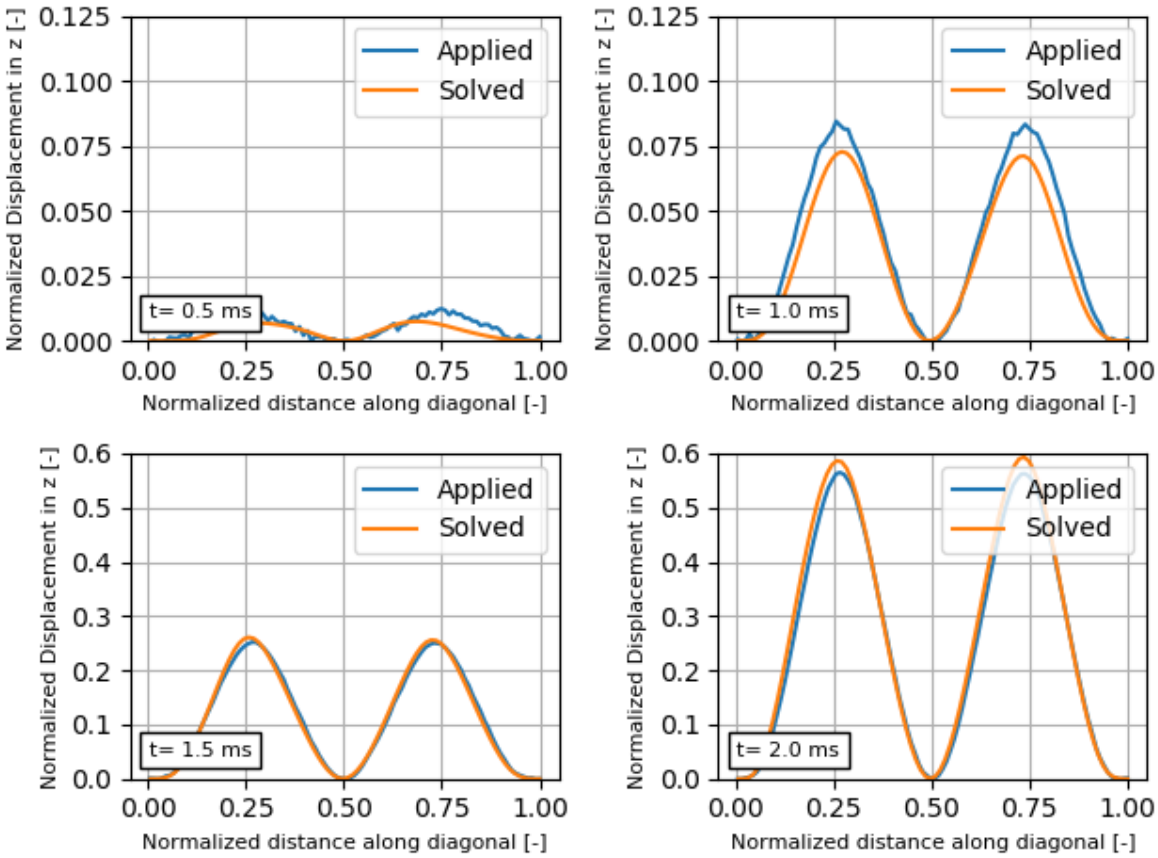

Figure 7.29: The displacement of the plate along the diagonal is plotted at four different time intervals. In the first and second plot some simulated noise in the 'applied' case can be seen. The algorithm has converged very well to the applied displacement.

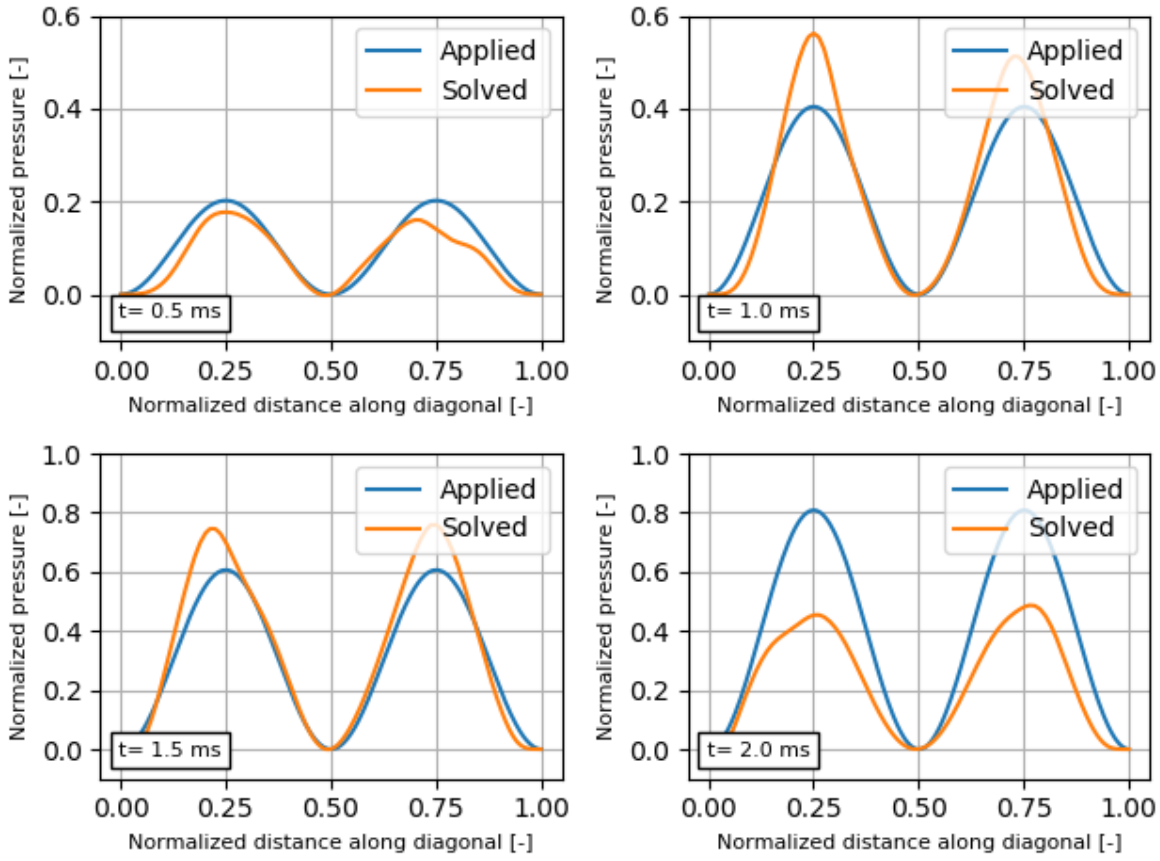

Figure 7.30: The pressure loading on the plate along the diagonal is plotted at four different time intervals. The 'solved' case has a similar pressure profile, however is sometimes quite off. This illustrates the sensitivity of an inverse problem.

7.2.2. Localized distribution

Similar as before the final deformation of the plate is shown in Figure 7.31 here the applied and solved case are shown left and right respectively. The displacements are compared in Figure 7.32 where it can be seen that the algorithm is converged quite well. The match between the 'applied' and 'solved' case is good. The corresponding pressure loading is plotted in Figure 7.33. It can be seen that the pressure is similar however again much larger differences are observed compared to the displacement.

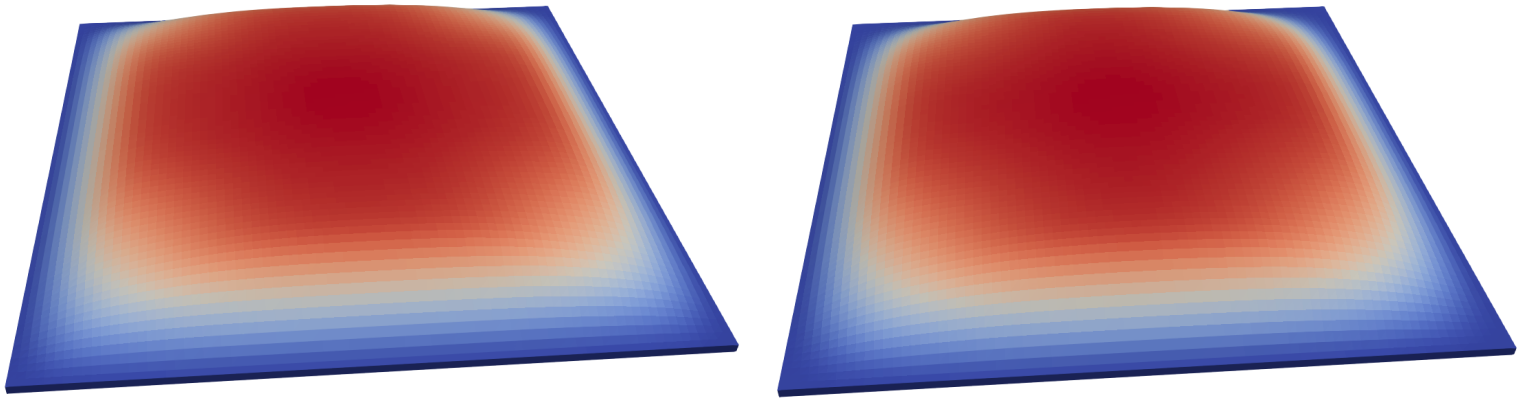

Figure 7.31: Both the Left and Right plot show the final deformation of the plate. The left for the 'applied' case and the right for the 'solved' case. Both deformations are a good match.

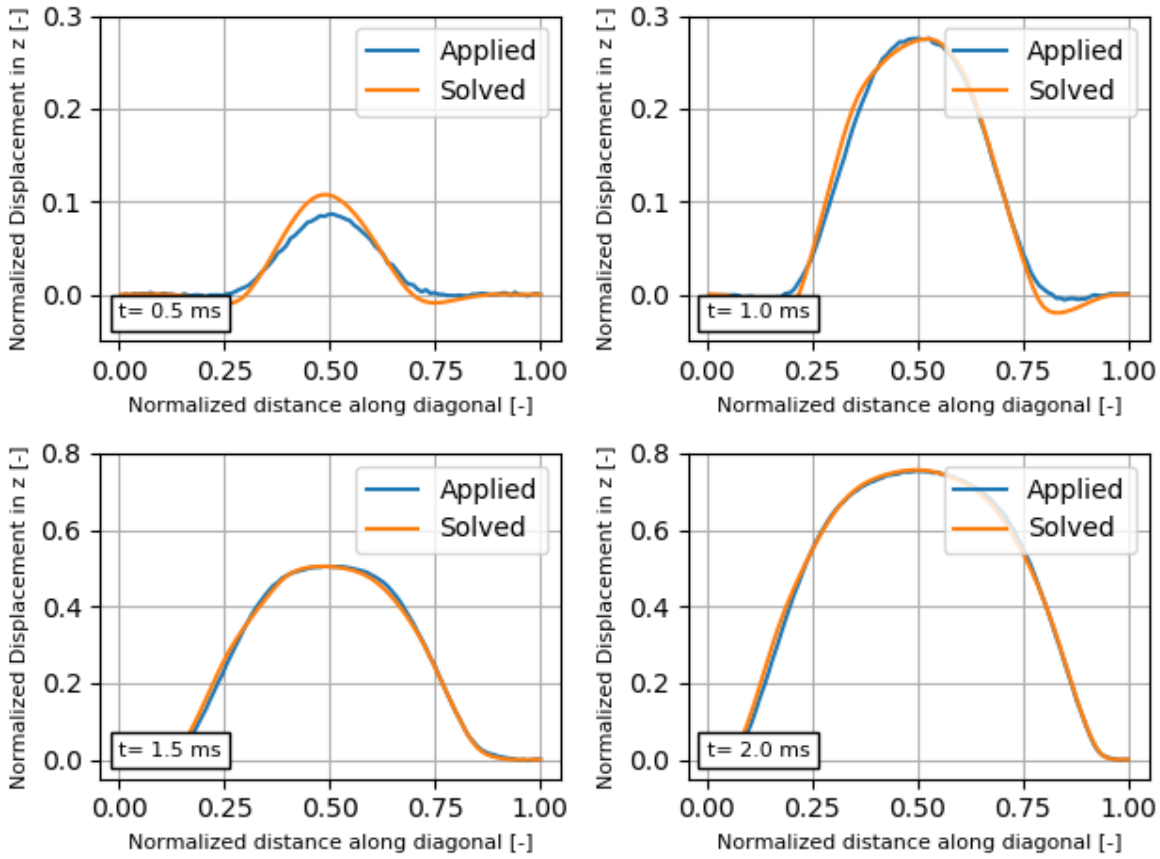

Figure 7.32: The displacement of the plate along the diagonal is plotted at four different time intervals. In the first and second plot some simulated noise in the 'applied' case can be seen. The algorithm has converged very well to the applied displacement.

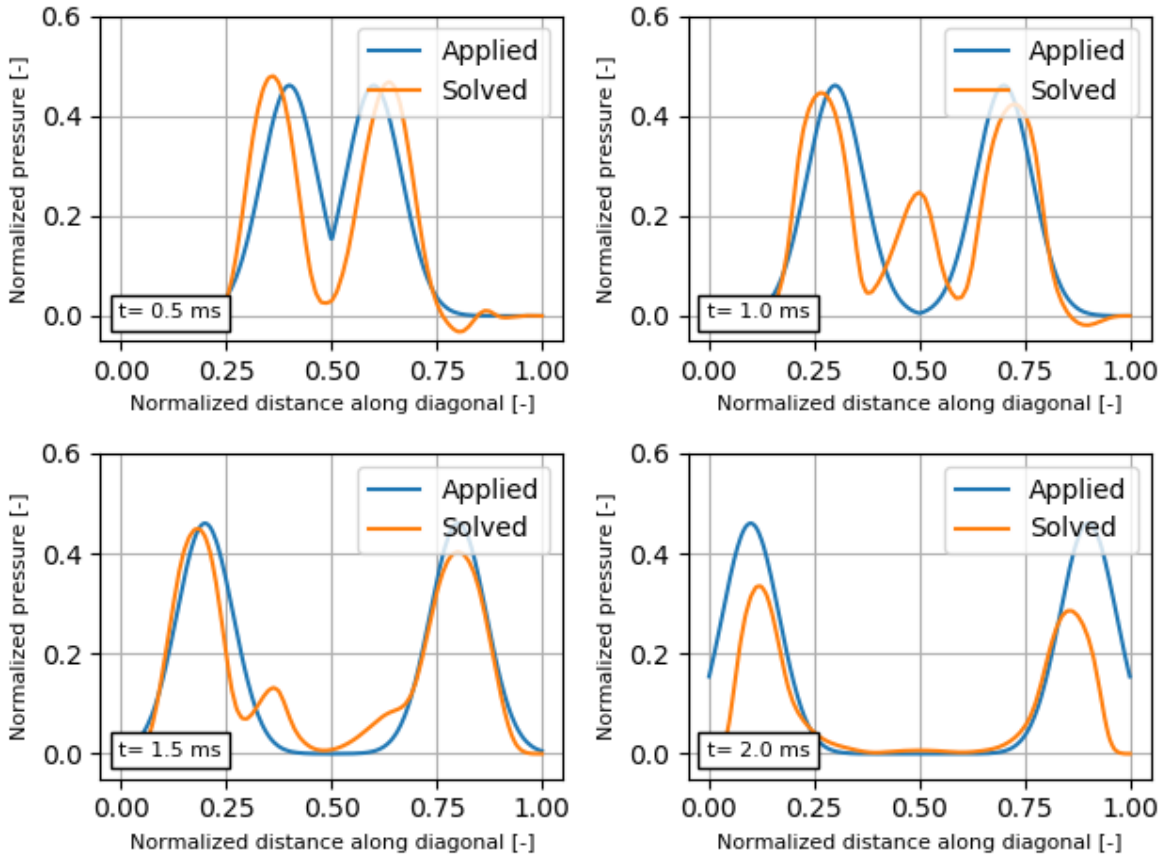

Figure 7.33: The pressure loading on the plate along the diagonal is plotted at four different time intervals. The 'solved' case has a similar pressure profile, however is sometimes quite off. This illustrates the sensitivity of an inverse problem.

The applied load has no negative pressure by design however the solved pressure does contain negative pressure. When negative interaction pressure is not expected one can use constrained optimization such that P>0. In Figure 7.34 the results for such an optimization are shown.

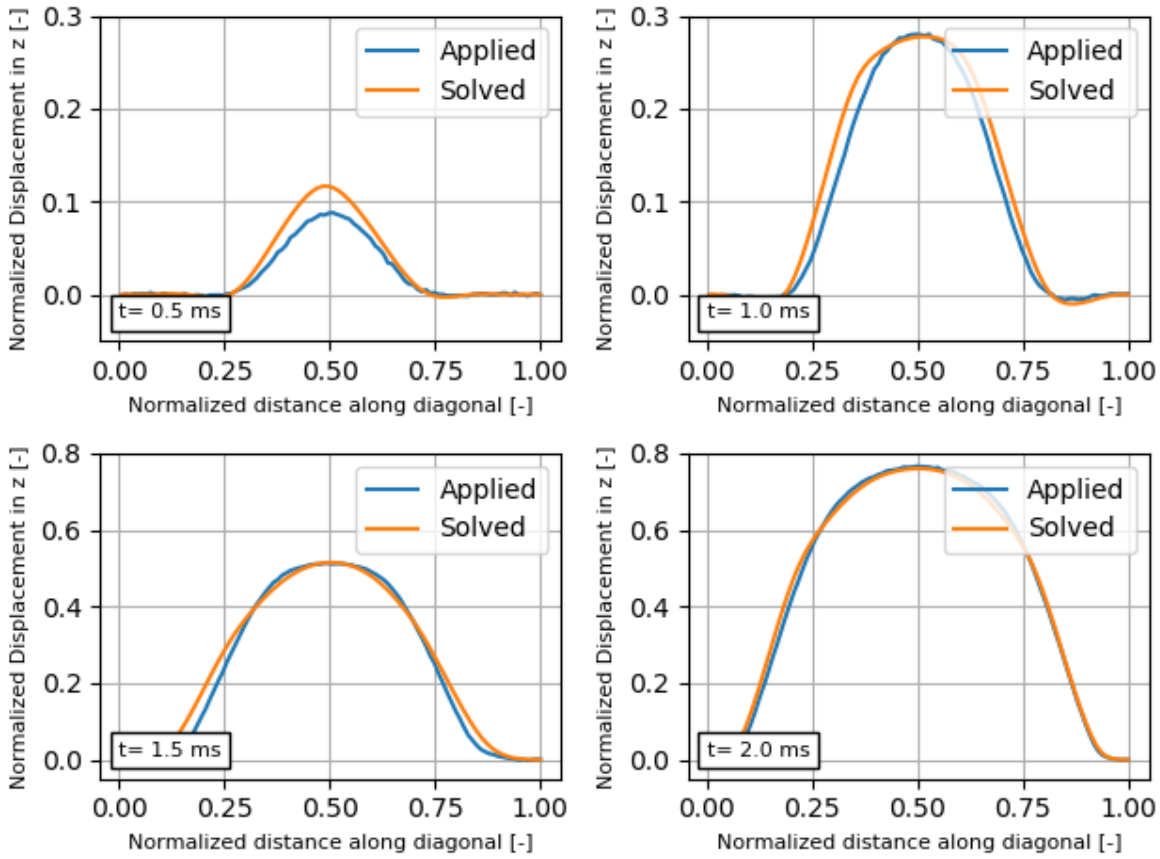

Figure 7.34: The displacement of the plate along the diagonal is plotted at four different time intervals for the constrained optimization problem P>0. In the first and second plot some simulated noise in the 'applied' case can be seen. The algorithm has converged very well to the applied displacement.

It can be seen that the displacements for the constrained optimization still converged well. The corresponding pressure is shown in Figure 7.35.

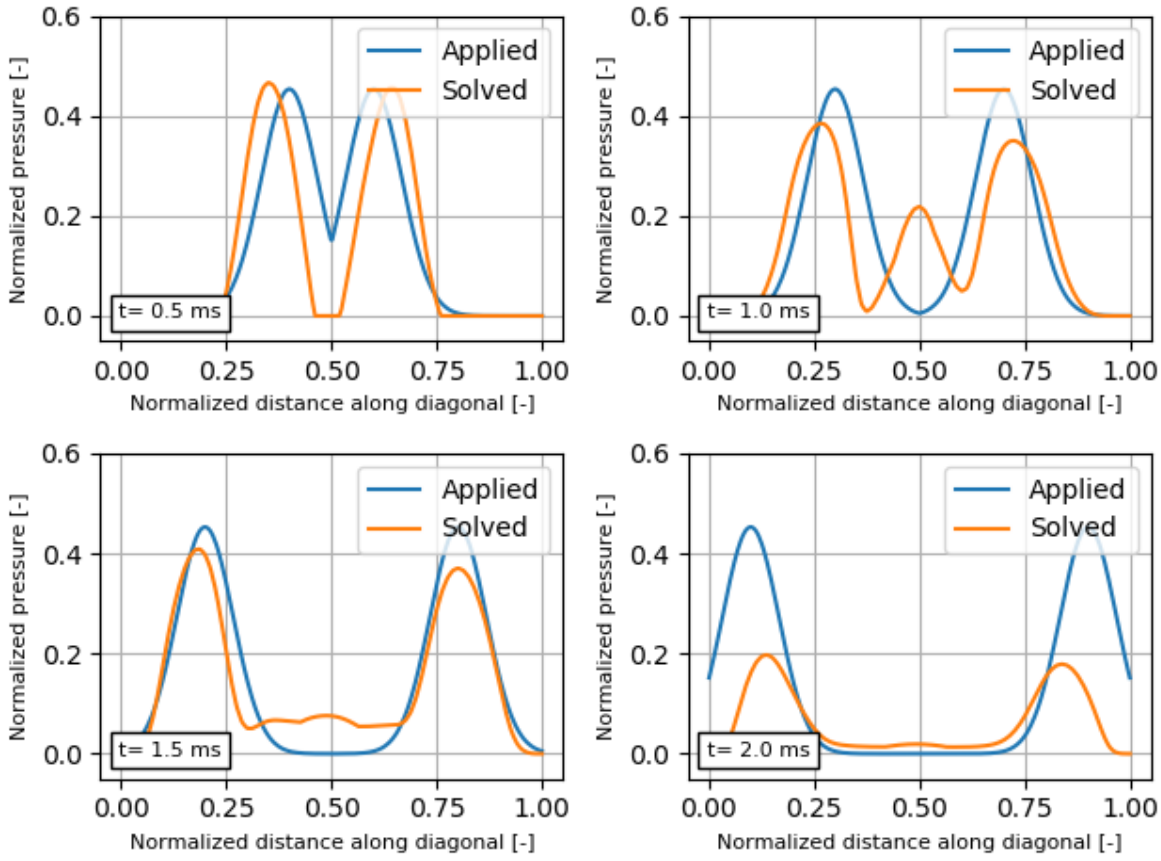

Figure 7.35: The pressure loading on the plate along the diagonal is plotted at four different time intervals for the constrained optimization problem P>0. The constrained solution is of similar accuracy.

7.2.3. Bench mark problem

The final deformation is shown in Figure 7.36 here the applied and solved case are shown left and right respectively. The displacements are compared in Figure 7.37 where it can be seen that the algorithm is converged quite well. The corresponding pressure loading is plotted in Figure 7.38. Similar to the linear results the pressures do not match. Especially the high peaks are not matched. When the integral of pressure and the radial centroid position are compared the results are in better agreement, Figure 7.39.

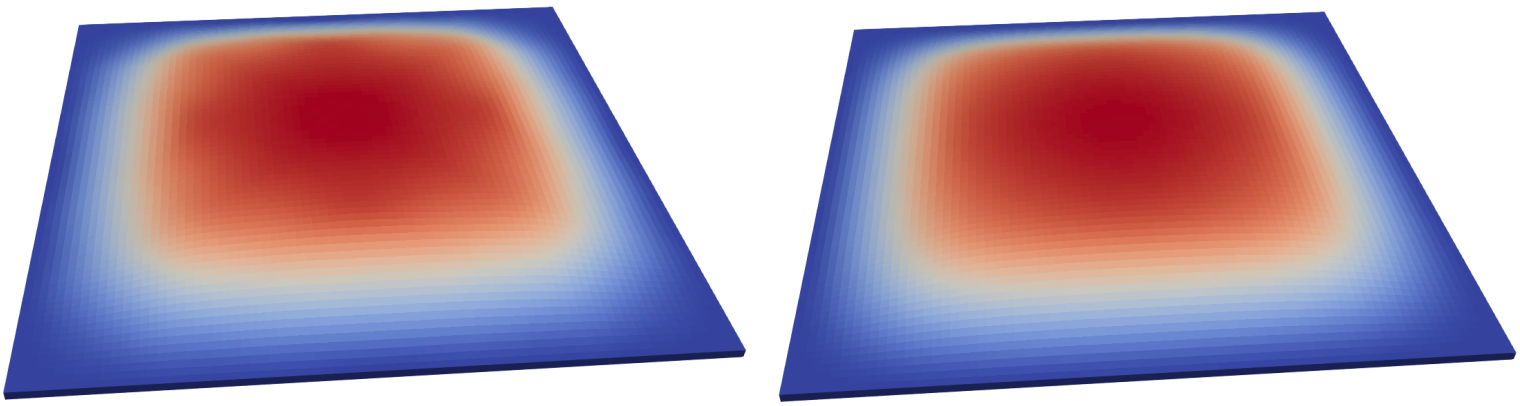

Figure 7.36: Both the Left and Right plot show the final deformation of the plate. The left for the 'applied' case and the right for the 'solved' case. Both deformations are a good match.

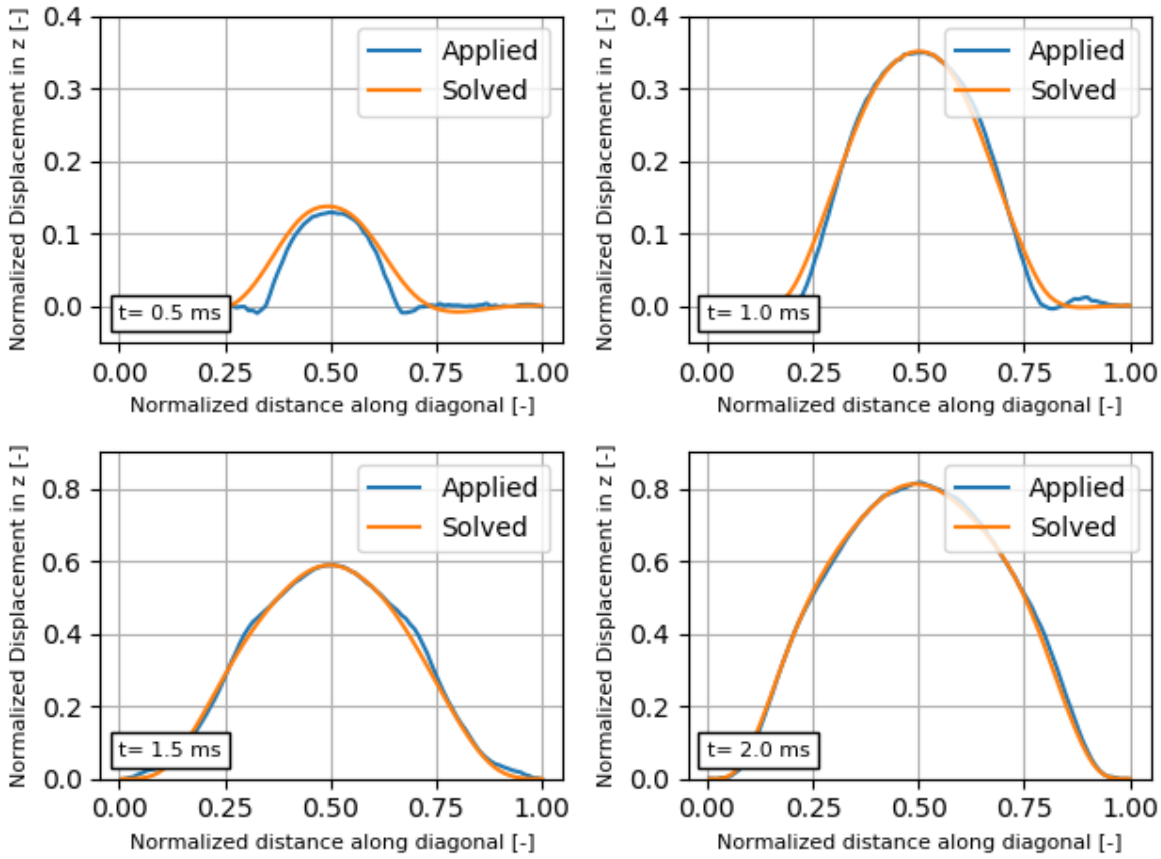

Figure 7.37: The displacement of the plate along the diagonal is plotted at four different time intervals. In the first and second plot some simulated noise in the 'applied' case can be seen. The algorithm has converged well to the applied displacement, however at t=0.5 ms and t=1.0 ms the sharp bending in the applied deformation is not captured. Further more at t=1.5 ms the applied curvature at a normalized distance along the diagonal of 0.25 and 0.75 is not captured. These discrepancies can be the cause of large pressure inaccuracies.

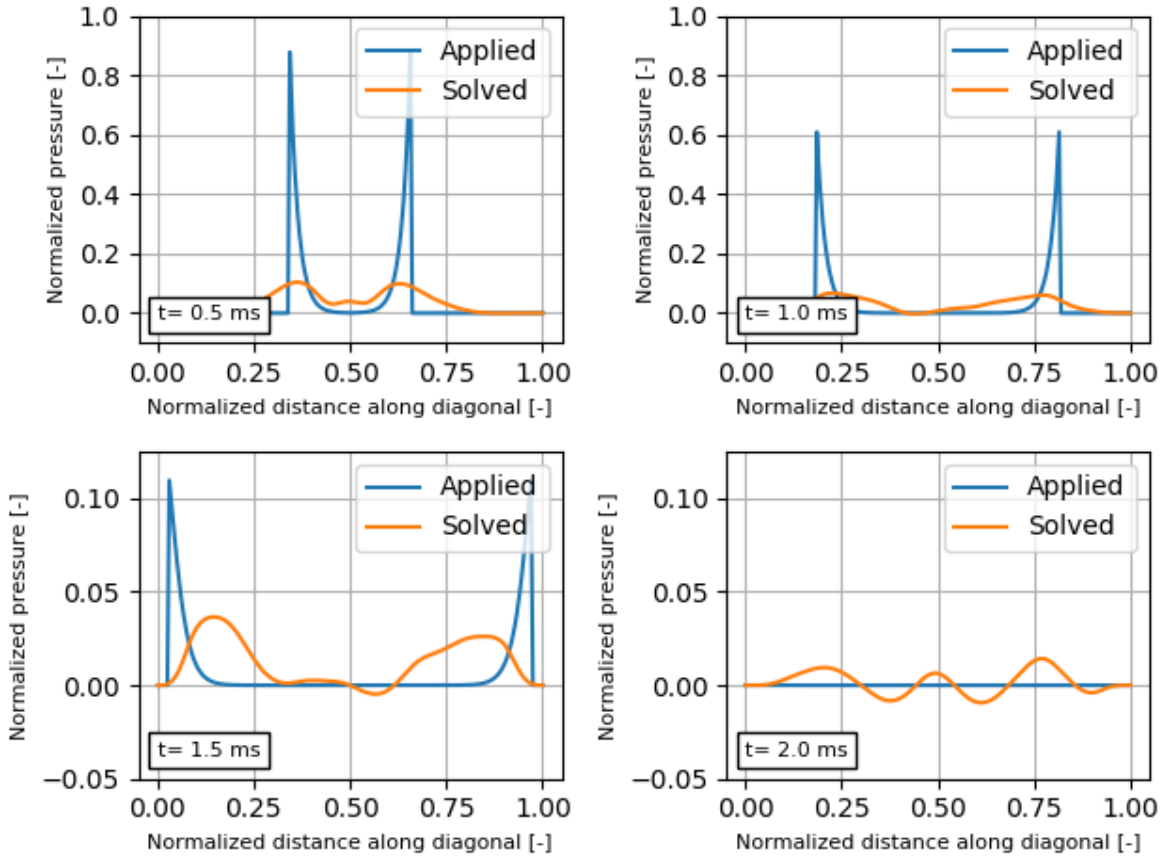

Figure 7.38: The pressure loading on the plate along the diagonal is plotted at four different time intervals. It is again seen that the benchmark problem is not captured back.

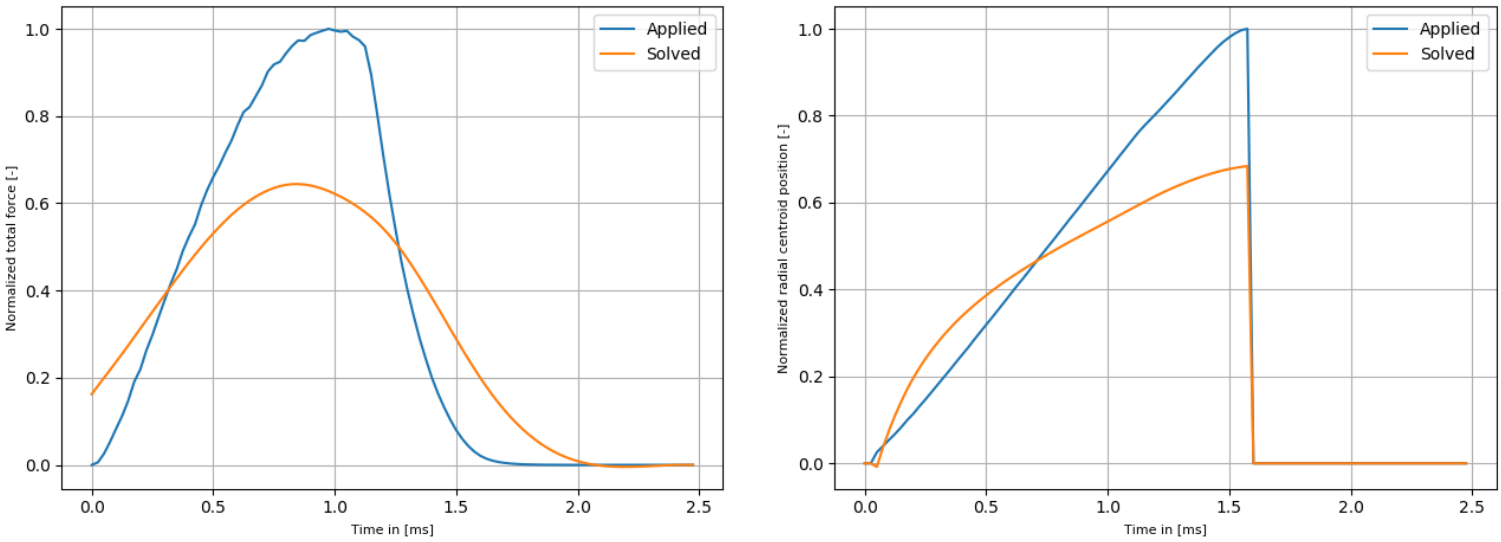

Figure 7.39: The solved pressure distribution follows the same trend however is off by quite a bit. Similar the centroid position on the right plot for both applied and solved are in reasonable agreement. The cause of the discrepany is expected to be the incomplete convergence of the displacement

Similar as before the applied load has no negative pressure by design however the solved pressure does contain

negative pressure. In Figure 7.40 the results for constrained optimization with P>0 are shown.

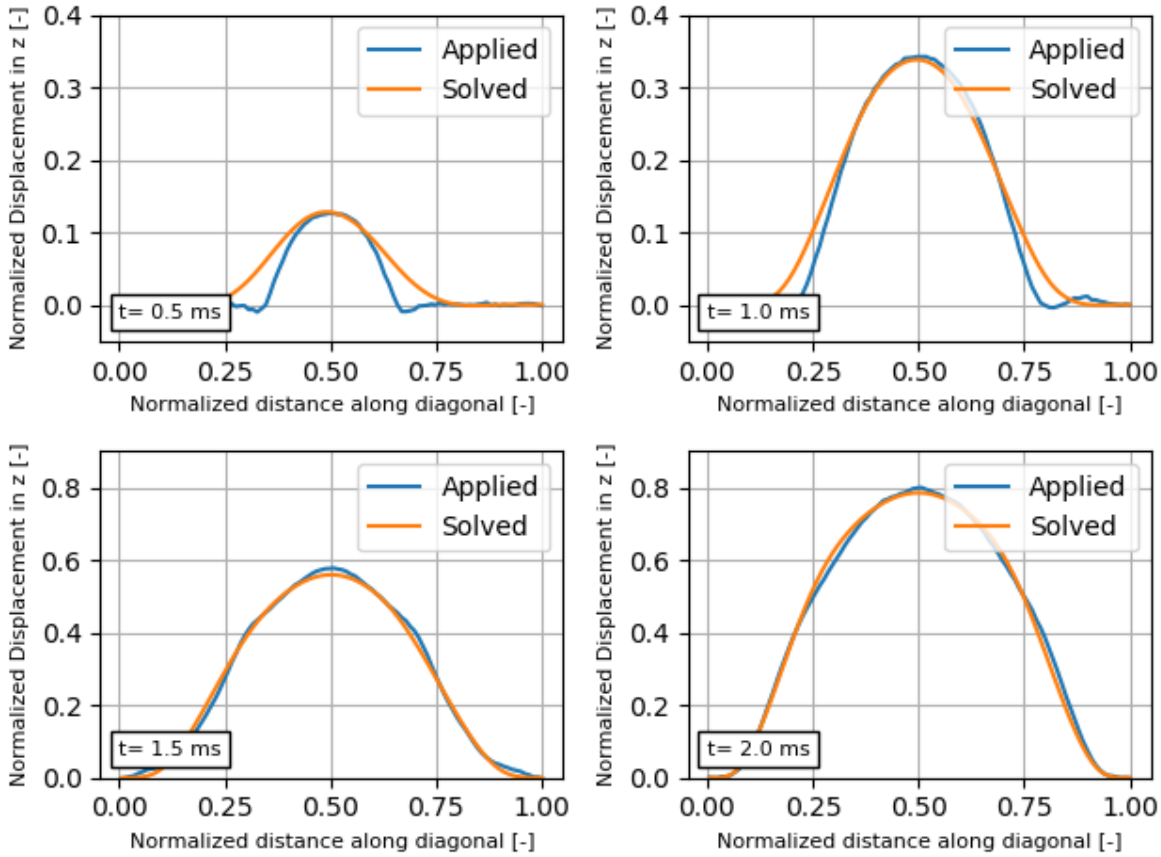

Figure 7.40: The displacement of the plate along the diagonal is plotted at four different time intervals for the constrained optimization problem P>0. The convergence is not not complete ans similar for the unconstrained situation

It can be seen that the displacements for the constrained optimization still converged well. The corresponding pressure is shown in Figure 7.41.

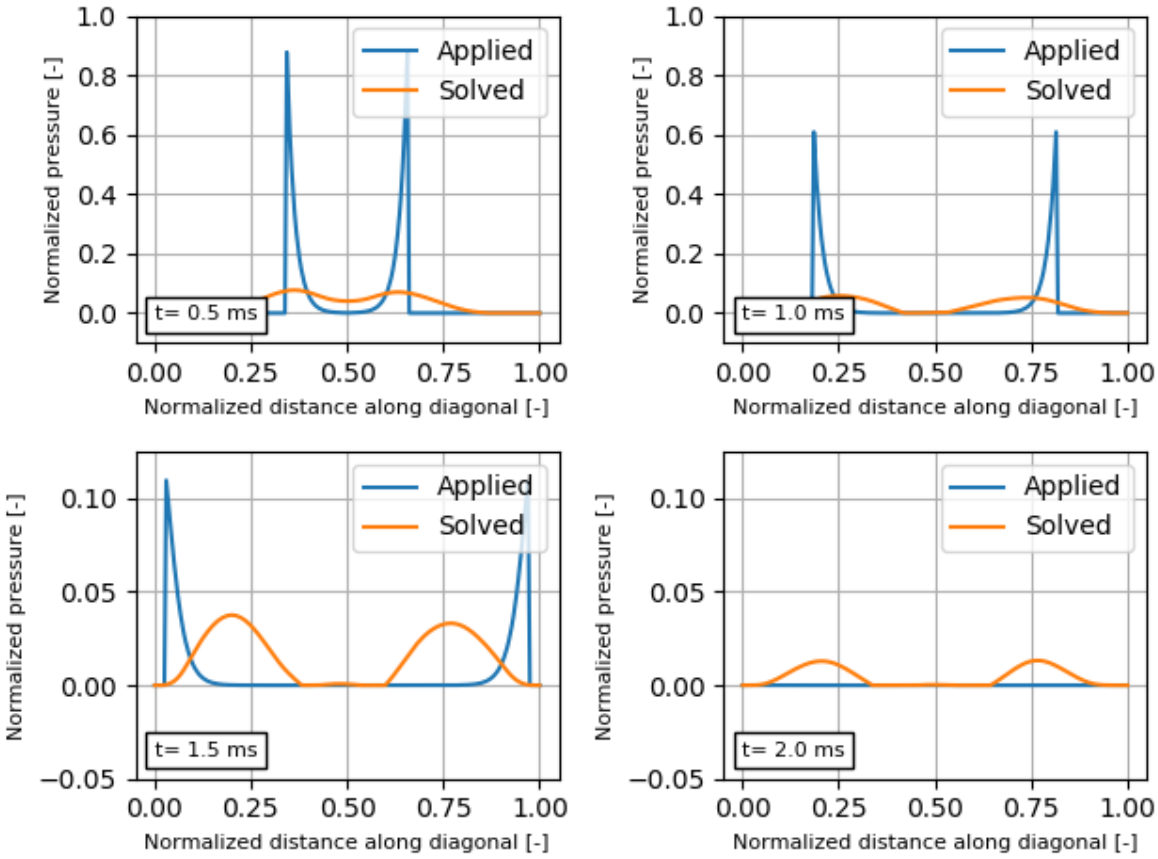

Figure 7.41: The pressure loading on the plate along the diagonal is plotted at four different time intervals for the constrained optimization problem P>0. The improvement compared unconstrained optimization is small.

7.2.4. Summary of results

Several important results are obtained from the KL plate experiments, are summarized and discussed in the list below. The test results showed no particular difference in IMP algorithm between the KL plate and the continuum model although the convergence of the displacement for the KL plate model was better. The less accurate convergence of the continuum problem showed that the pressure obtained is less accurate. Furthermore large inaccuracies in the total force and radial centroid position plotted over time are observed for the continuum results. This shows that these parameters require an very good convergence of the forward model.

Since the linear solver and thus algorithm is much faster more iterations were done. The continuum algorithm for all simulations was stopped earlier since this project was time constrained. It is expected that better convergence is possible when more iterations of the gradient of descent algorithm are done. Perhaps a finer mesh is required since the adjoint solution becomes more complex when near the optimum for which the mesh might be too coarse. This would slow the algorithm even more and is left for future research.

- Smooth pressure distributions are easier to capture back. Although some small oscillations are often present the IMP algorithm is quite accurate for smooth pressure distributions. In theory however much larger amplitude pressure oscillations could still result in almost the same deformation. The gradient of descent algorithm has some regularization properties such that this is not observed. The fact that smooth distributions are found back more accurately is thus partly artificially.
- The influence of plate thickness is indirect since the deflection for thicker plates is less such that the relative noise is higher. When relative noise remains the same no large influences for different thickness is observed.
- Large difference in loading amplitude over time causes the highest loading to be captured back the most accurately. The reason is that large magnitude loads have large influence on the deformation.

- The effect of duration time of the loading alone is quite small, although some simulations shown slightly better results for longer duration. The effect that displacement will be less for shorter duration loading such that the relative error will be bigger is not shown. This effect is expected to be big, however not taken into account since the reference situation with zero noise is chosen.
- The IMP is very sensitive to noise and thus measurement data should be as accurate as possible.
- Localized distributions are difficult to capture back. Also localized distributions are often not accurately captured back due to the non-uniqueness of the problem. In principle this is the case for any pressure profile, however its effect is mostly seen for the localized distributions. Similar effect for smooth distributions are the small oscillations around the correct pressure.
- The fact that quite different localized pressure distributions can have almost the same deformation clearly illustrates the limits of validation using this or similar methods. That is comparing by mine blast excited objects their response with a numerical model, employed by most researcher in the field. Deformations that are in good agreement do not guarantee a correct pressure model. Furthermore small errors in deformation, that might seem acceptable, can be the cause of large error in the mine blast models.
- Factors that do influence the response significantly for localized pressure distributions are the total force and the centroid location. Large differences in the total pressure and centroid position found for numerical and experimental results are a clear indication of an inaccurate pressure model. However Force and centroid plots that are in good agreement do not imply correctness in pressure model.
- Constrained optimization can force the pressure to behave a certain way. This was tested for P>0 constrained. For this constrained the displacement converges to similar accuracy and the pressure model had a slightly better fit compared to unconstrained optimization. When used one has to be certain that the constrained is valid.
- Non-zero pressure near the boundary and discontinuities in applied pressure seems to cause oscillations in the solution. This effect seems similar to Gibbs phenomena in Fourier series, however might be due to a completely different cause.

8

Grid stiffened panel

The IMA is only tested for a simple plate geometry, however the derived transient adjoint problem was for a general continuum. Hence the IMA is expected to work for a general continuum. In many structural engineering fields including the design of armoured vehicles the structure has to be light weight, yet remaining relatively stiff. One of the solution often used is the use of a grid stiffened structure. Remaining relatively close to the original problem this chapter discusses the results of the IMA for a grid stiffened rectangular panel as shown in Figure 8.1.

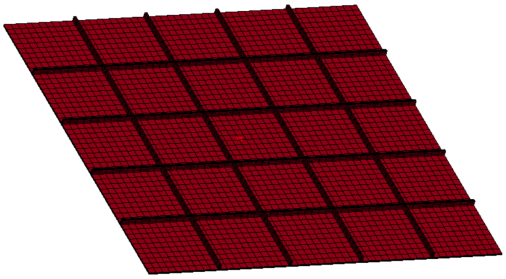

(a) Mesh of the grid stiffened panel

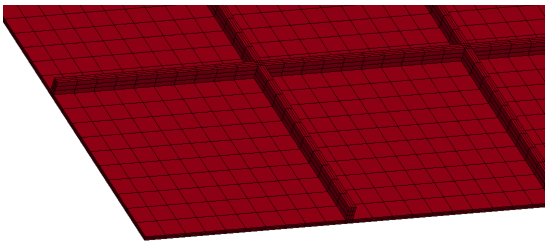

(b) Zoomed in on the bottom corner of the mesh to show the ribs of the grid stiffened panel

Figure 8.1: Grid stiffened panel used to test the general IMA for different geometry as compared to the plate problem studied in more detail earlier. Visualization obtained using LS-PrePost [29]

8.1. The domain

The interaction pressure due to the benchmark pressure model is applied on the entire flat bottom of the plate. The stiffeners facing upwards obstruct the camera's view. The plate displacement is thus not measured over the complete plate. The smaller area where measurements are obtained is shown in Figure 8.2. The error between simulation and experiment is computed on this area. Note that the ribs and a small part of the panel are not taken as measurement area.

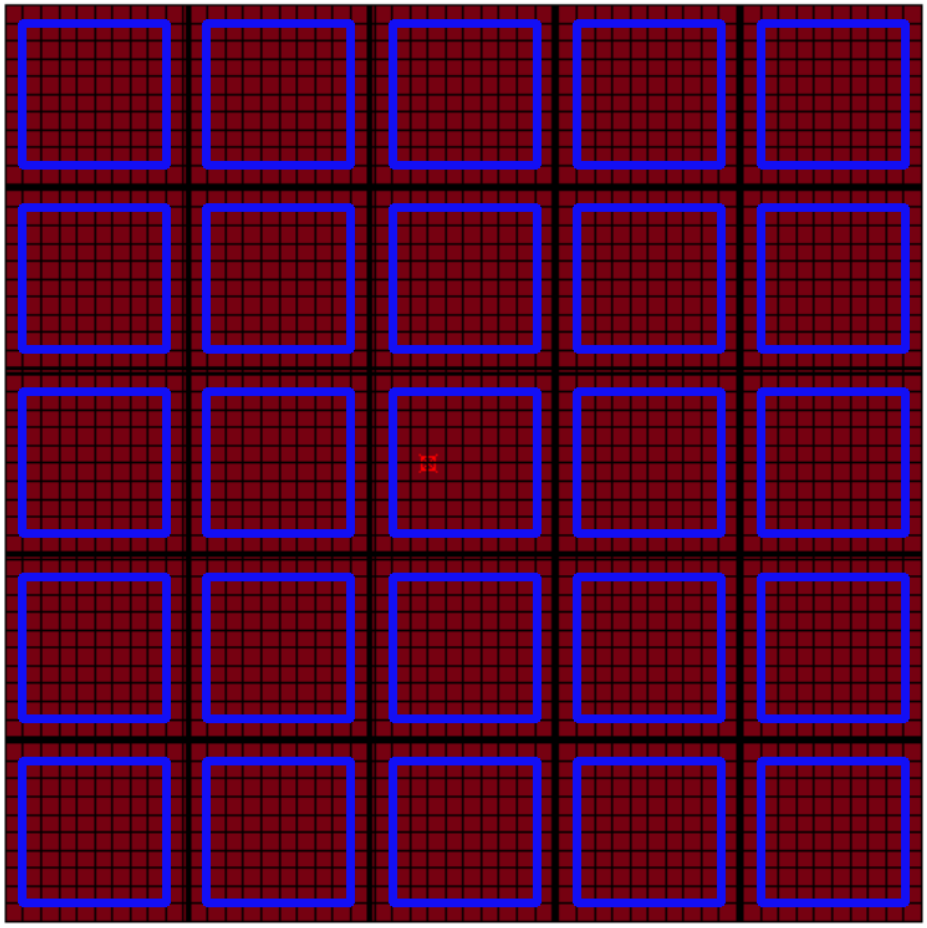

Figure 8.2: Top vieuw of the grid stiffened panel mesh, in side the blue area the displacement is known from measurements. This area is used to compute the error of the simulation w.r.t. the measurements.

8.2. The response

A similar response as for the plate problems is expected. In addition bell shaped deformation of the plate in between the stiffeners is seen, especially in the center of the plate Figure 8.3. The IMA converged quite well in displacement as can be seen in Figure 8.4. The bell shape deformation in between the stiffeners is a bit less compared to the applied displacement.

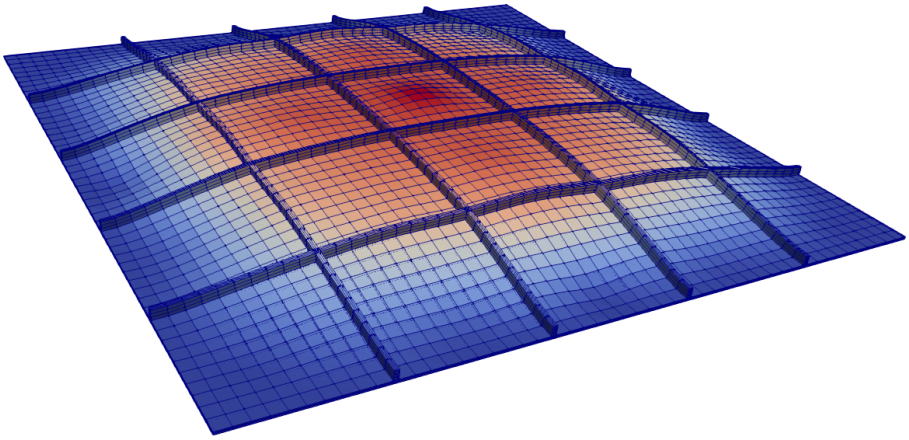

Figure 8.3: The response of the grid stiffened panel excited by the benchmark pressure model at t=2.0 ms. The color emphasizes the z-displacement. Visualization made using Paraview [8]

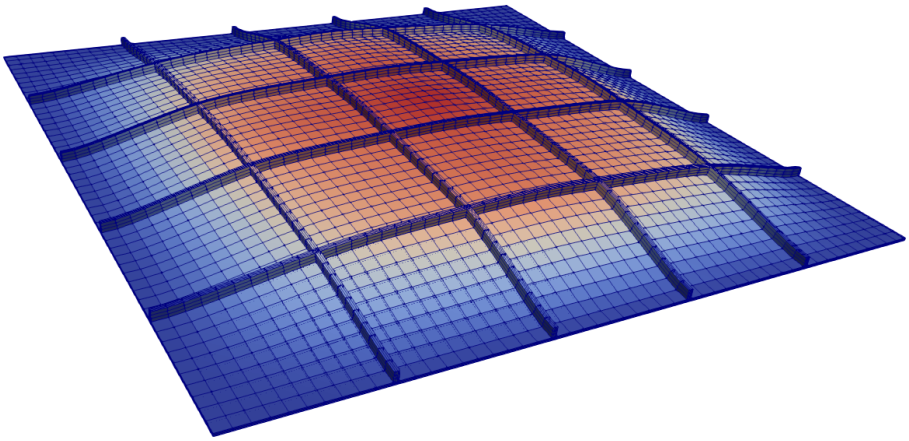

Figure 8.4: The iterative solved response of the panel at t=2.0 ms. The color emphasizes the z-displacement.

To better visually compare the applied and solved displacement both panels were clipped over the center of the plate. The panel in the background is the applied displacement and the panel in the foreground the solved displacement. In Figures 8.5, 8.6, 8.7, 8.8, 8.9 the panels are compared for several time steps.

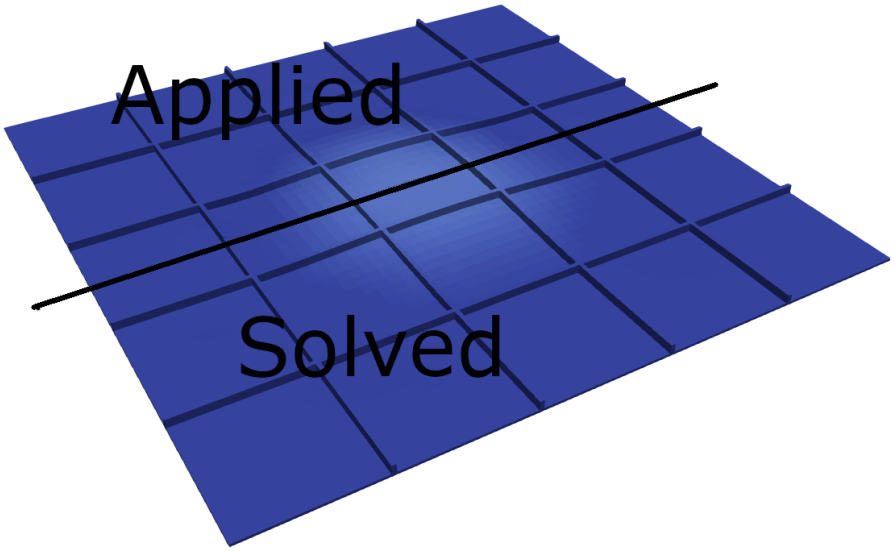

Figure 8.5: Comparison using clipped panels over the center y-axis of the plate for the applied displacement in the background and the solved displacement in the foreground at t=0.5 ms. The visualization is done using Paraview [8]

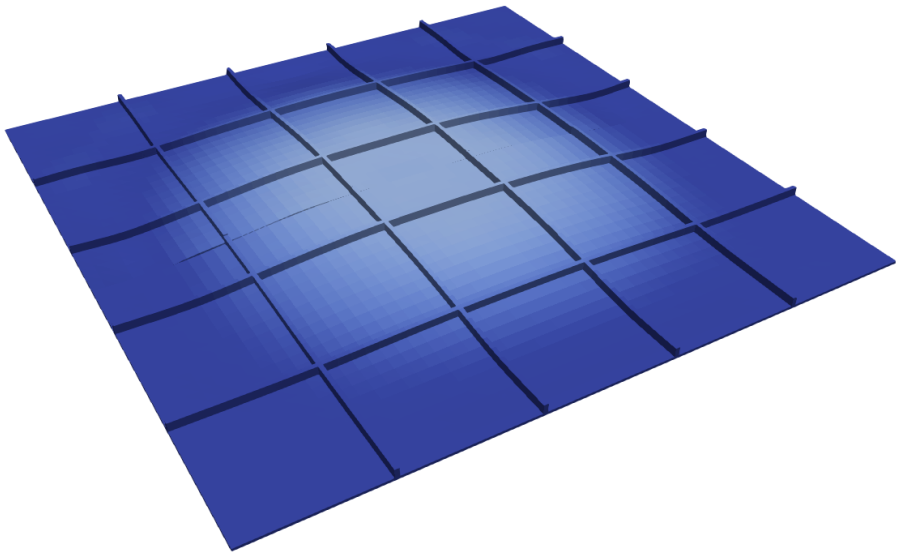

Figure 8.6: t=1.0 ms

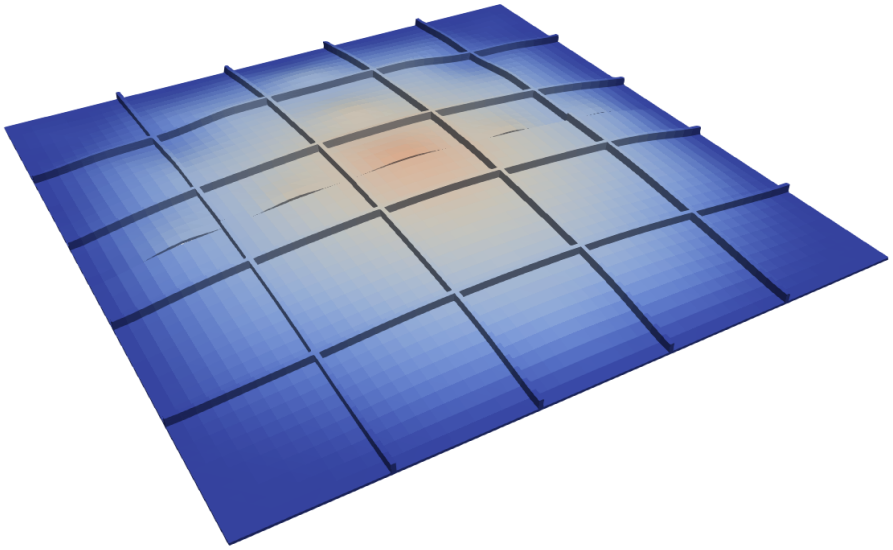

Figure 8.7: The bell shape deformation of the panel in between the stiffeners has larger amplitude for the applied loading at t=1.5 ms

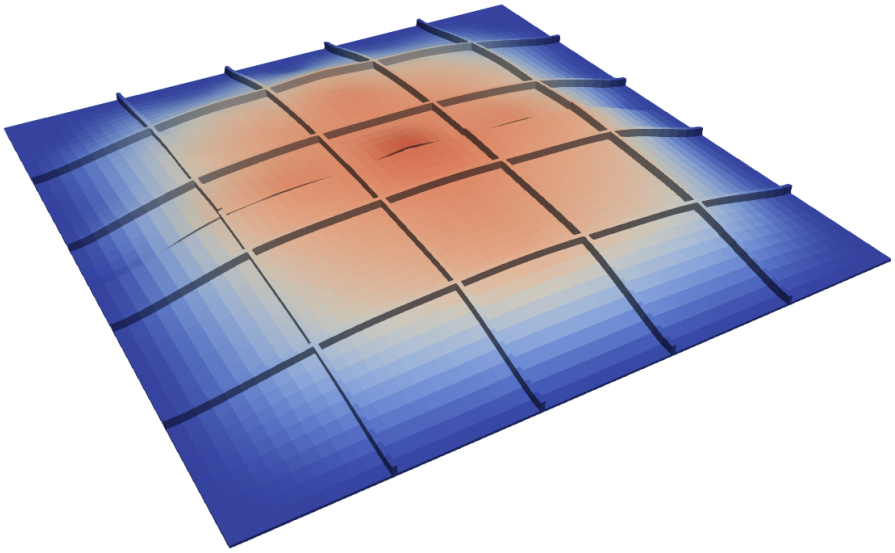

Figure 8.8: The bell shape deformation of the panel in between the stiffeners has larger amplitude for the applied loading at t=2.0 ms

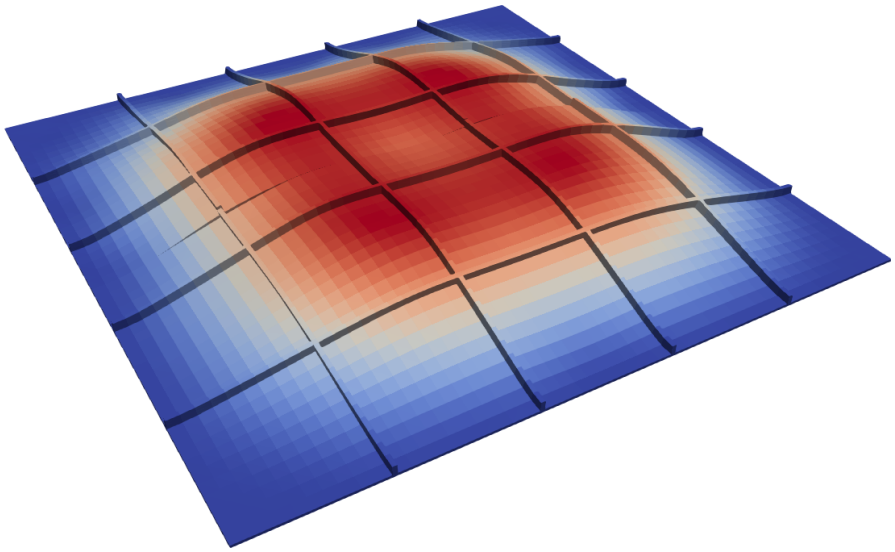

Figure 8.9: The final deformation (end of simulation) at t=2.5 ms shows a good agreement for the applied and solved response.

8.3. Comparison in 2D

In Figure 8.10 the displacements are compared along the diagonal of the grid stiffened panel. It can be seen that both displacements are a good match.

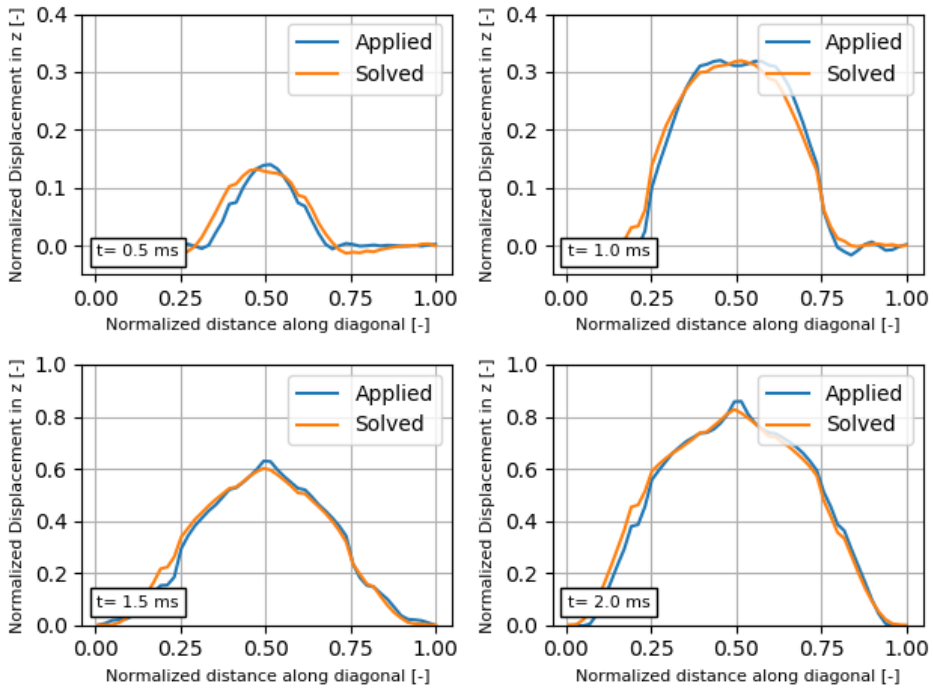

Figure 8.10: Comparison of the applied and solved displacement along the diagonal of the plate. both displacements are in good agreement

In Figure 8.11 the pressure of the applied and solved grid stiffened panels are compared. It can be seen that the pressure models are quite off, however the moving localized pressure is observed. Another observation is that the total force of the applied and solved is quite different, which can already be estimated by the area under the curves at t=1.0 ms. Figure 8.12 shows the comparison of the total force as function of time for the complete panel.

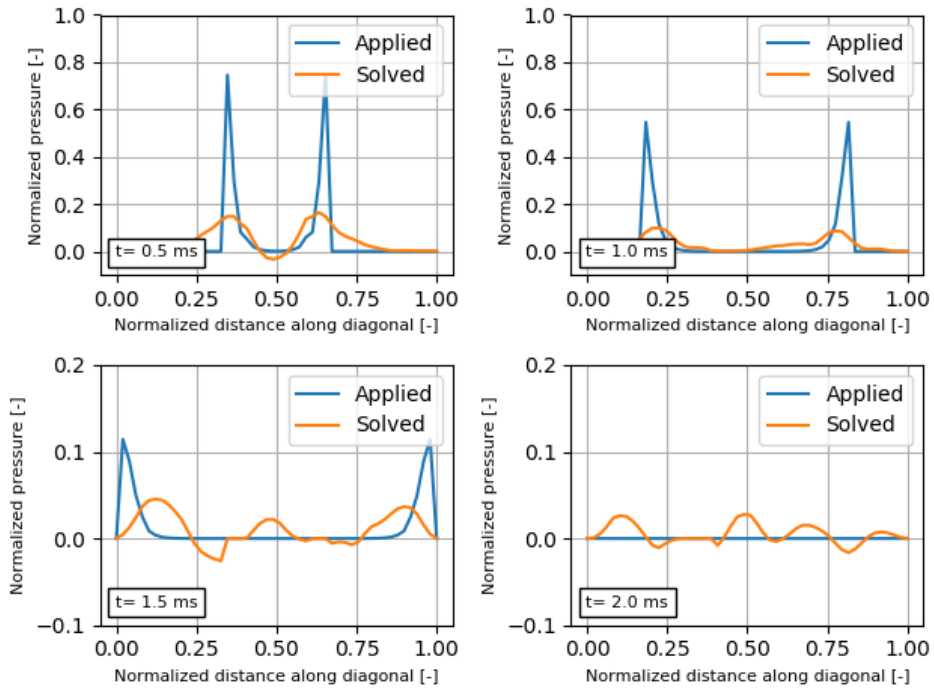

Figure 8.11: Comparison of the applied and solved pressure along the diagonal of the plate. Although the pressures are not in good agreement, the moving localized pressure for t=0.5 ms and t=1.0 ms is observed.

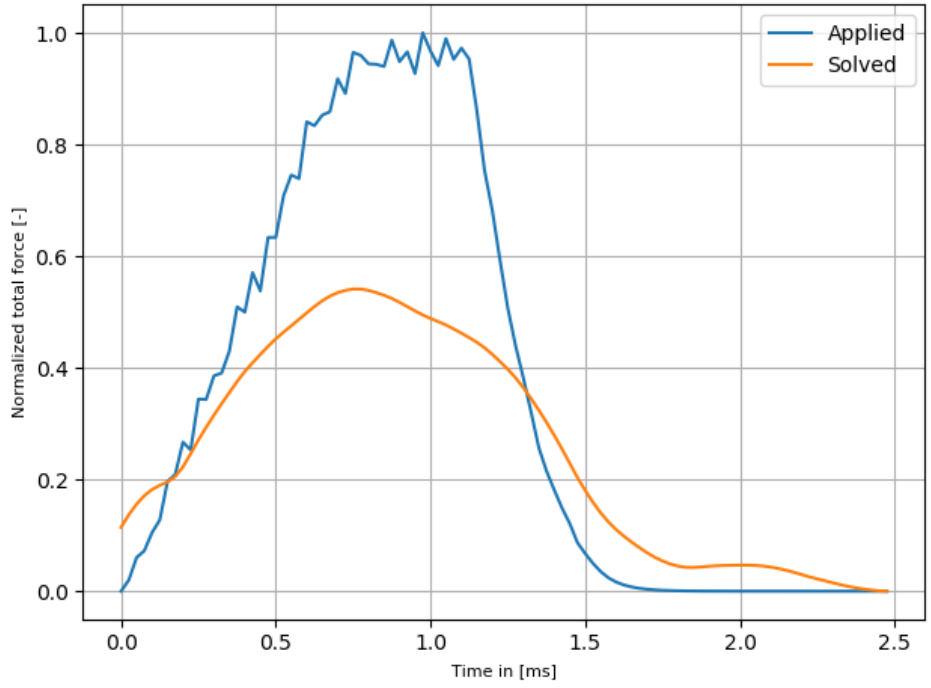

Figure 8.12: Comparison of the applied and solved total force versus time. It is clear that the solved pressure is much higher, which is unexpected since the response converged quite well.

Since a moving localized load is observed the centroid position can be computed and compared see Figure 8.13. Initially the centroid position is larger compared to the solved case, this is due to the less local more spread out pressure distribution of the solved pressure. Similar argument hold near the end of the plate.

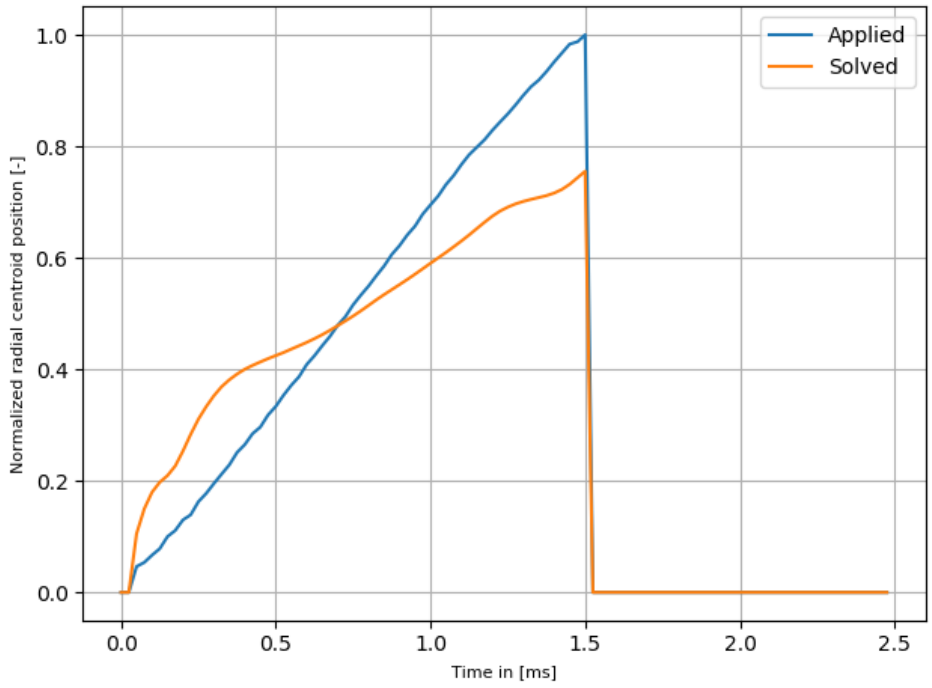

Figure 8.13: Comparison of the applied and solved centroid position versus time. Initially the solved centroid position is higher due to a wider pressure distribution. Similar near the ends of the plate the centroid position is less compared to the solved case.

8.4. Chapter conclusion

The IMA is capable of converging to the correct displacement quite accurately. The difference between the applied and solved displacement is however still larger then the precision of the measurement. Based on that fact alone better convergence is expected. When better convergence is possible the bell shape deformation in between the stiffeners should be captured better, since some error for t=1.5 ms and t=2.0 ms was observed. The small inaccuracy of the displacement again shows to be related to large inaccuracy in the applied pressure. The total force, was for previous plate simulations found to be in good agreement. For the grid stiffened panel is is observed that the total applied force is less for the solved case. The centroid position is in reasonable agreement, although near the beginning and end of the plate the position is a bit off.

9

Mine blast validation

In this chapter the IMP algorithm is applied on the DIC test data. First the processing of the test data is discussed. Then the results for a buried charge are discussed and compared with the current mine blast pressure model. Finally a second test is done for an explosive in a steel-pot.

9.1. Data interpolation

The displacement data is obtained using DIC techniques. The software from 'GOM-inspect' [1] was used as 'black box' to obtain the displacement data. The output were several '.stl' mesh files each corresponding to a different point in time. These '.stl' files had to be interpolated to a rectangular grid for which the described algorithm is designed. Furthermore at some locations on the plate data was missing. At these locations the data was interpolated using the neighbouring data. In Figure 9.1 a typical '.stl' data file is found at t=$\frac{T}{2}$ and in Figure 9.2 at t=T. Clearly the number of holes in the data file increases towards the end of the simulations.

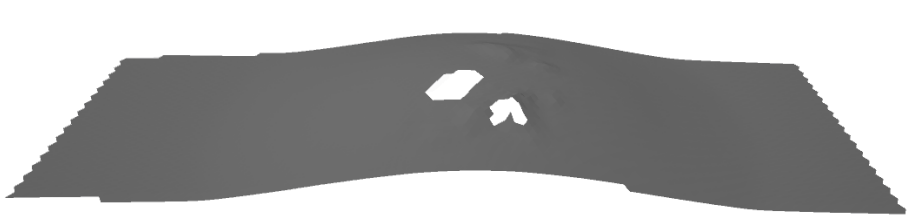

Figure 9.1: Output mesh of measured displacement from post processing the DIC data using 'Gom-inspect'. The mesh shows two holes in the data that need to be interpolated. The displacement is shown for t=$\frac{T}{2}$.

Figure 9.2: Output mesh of measured displacement from post processing the DIC data using 'Gom-inspect'. The displacement is shown for t=T and hence the quality is less since the mesh shows four holes in the data.

Dust clouds enter the test rig via the clamped boundary of the plate. These clouds obstruct the camera's view causing loss of DIC data. However these effect start at the boundary and move towards the middle of the plate for later time. These effects were small since the simulation time is short. The reason for the holes in the mesh files

(data missing) which start in the middle of the plate is different. This is caused by paint of the DIC pattern peeling off, see Figure 9.3

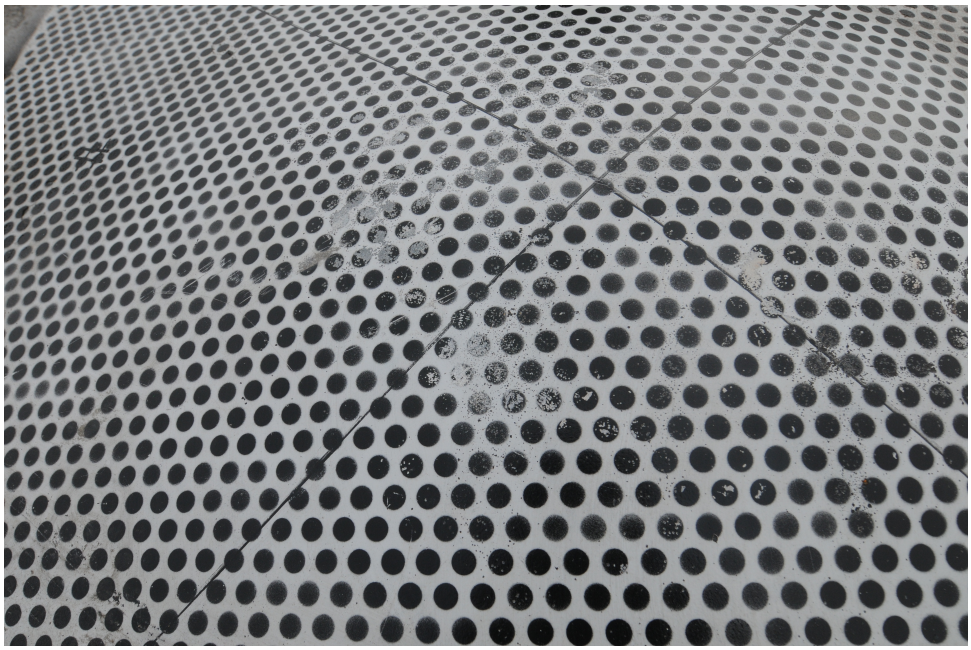

Figure 9.3: Zoomed in on the DIC pattern it is clear that paint is peeled off at certain locations causing the DIC measurement to miss some data which is observed as holes in the mes files.

In order to use the data as input for the developed program it has to be post-processed. The mesh is first interpolated to a rectangular grid see Figure 9.4a. As a last step the holes and edges are patched see Figure 9.4b.

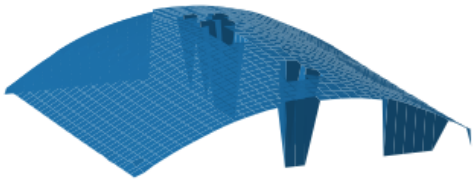

(a) DIC data directly interpolated from '.stl' mesh file to rectangular grid.

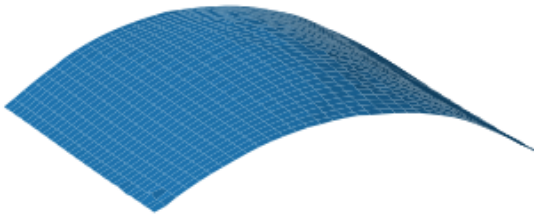

(b) Interpolation data from rectangular grid patched at the edges and holes.

Figure 9.4: Interpolated .stl data on a rectangular grid

The plate displacement is not measured over the complete plate. The smaller area where measurements are obtained is shown in Figure 9.5. The error between simulation and experiment is computed on this area.

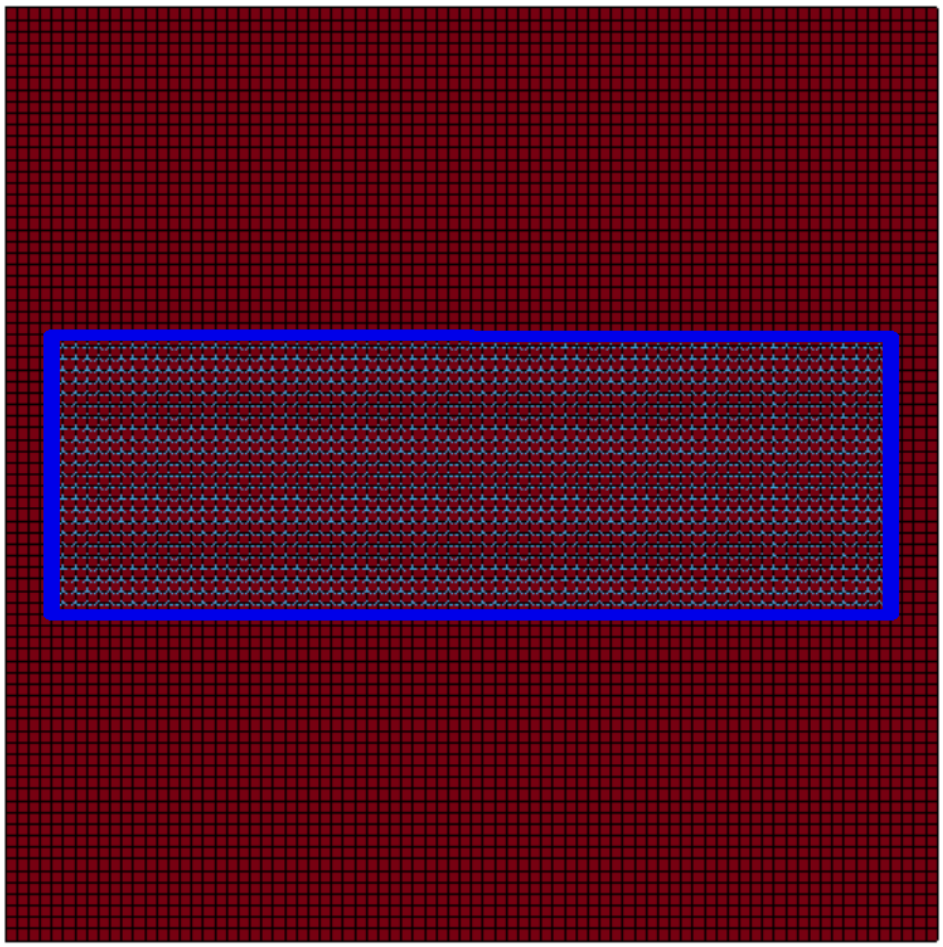

Figure 9.5: Top vieuw of the plate mesh (in LS-Prepost [29]), inside the blue area the displacement is known from measurements. This area is used to compute the error of the simulation w.r.t. the measurements.

9.2. Buried charge

From the geometry of the experiment it is expected to obtain a localized radial symmetric load that moves radially outwards over the plate. This is expected since the arrival time of the soil bubble will be longer for larger distances, as explained in Figure 9.6

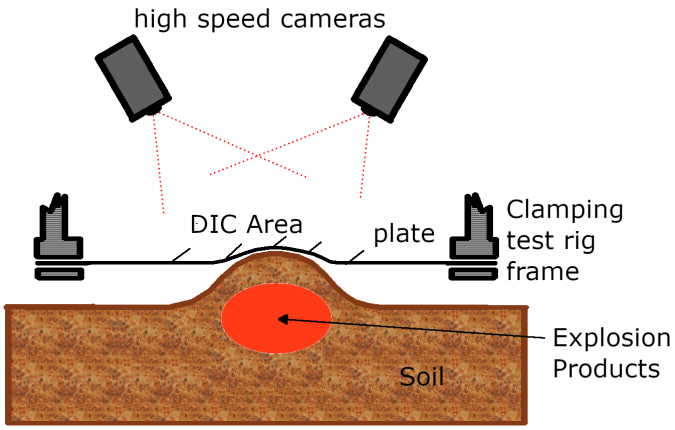

Figure 9.6: Illustration of the test setup for a buried charge. The arrival time of the soil bubble varies for different radial positions on the plate. For that reason a localized pressure distribution moving radially outwards is expected.

9.2.1. IMA displacement

The IMA is applied to the DIC data both constrained (such that P>0) and unconstrained. The displacement of the simulation is compared with the DIC measurements in Figure 9.7. The simulated displacement is in reasonable agreement with the measured DIC data, however the benchmark tests usually showed better convergence. The constrained and unconstrained results are very similar.

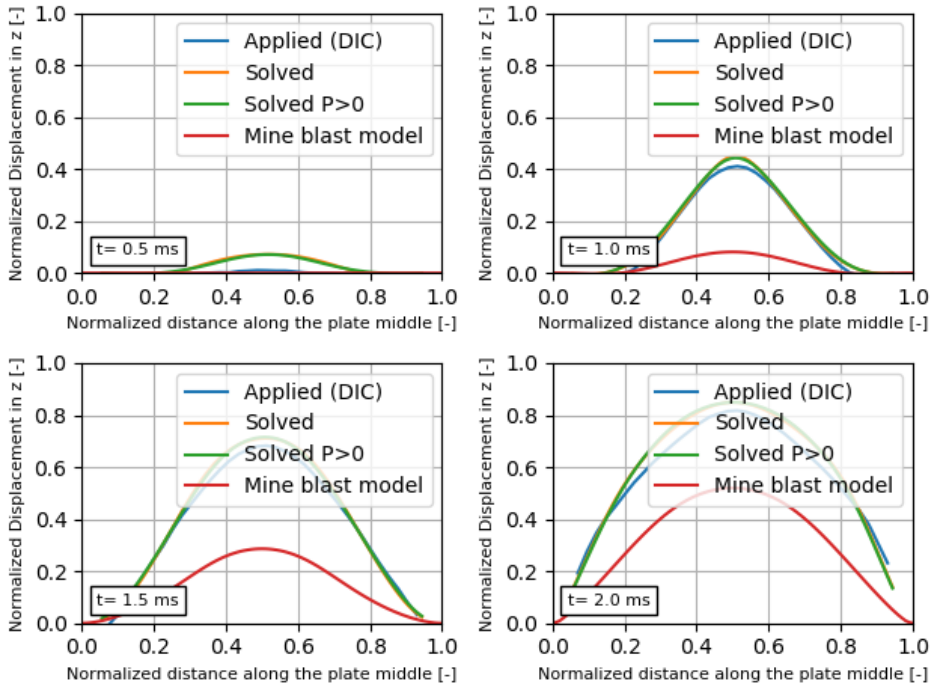

Figure 9.7: Here the displacements of the measurements 'applied' are compared to the simulation 'Solved'. The displacement is plotted over the middle of the plate, parallel to the long side of the DIC area. The plot starts at the beginning and ends at the end of the DIC area, hence the edges are excluded. The corresponding displacement of the mine blast model is plotted as well, the experiment is not done on a calibration point.

It was found that the DIC data for $t < 0.5$ ms are small and noisy and the data did not fit well, see Figure 9.8.

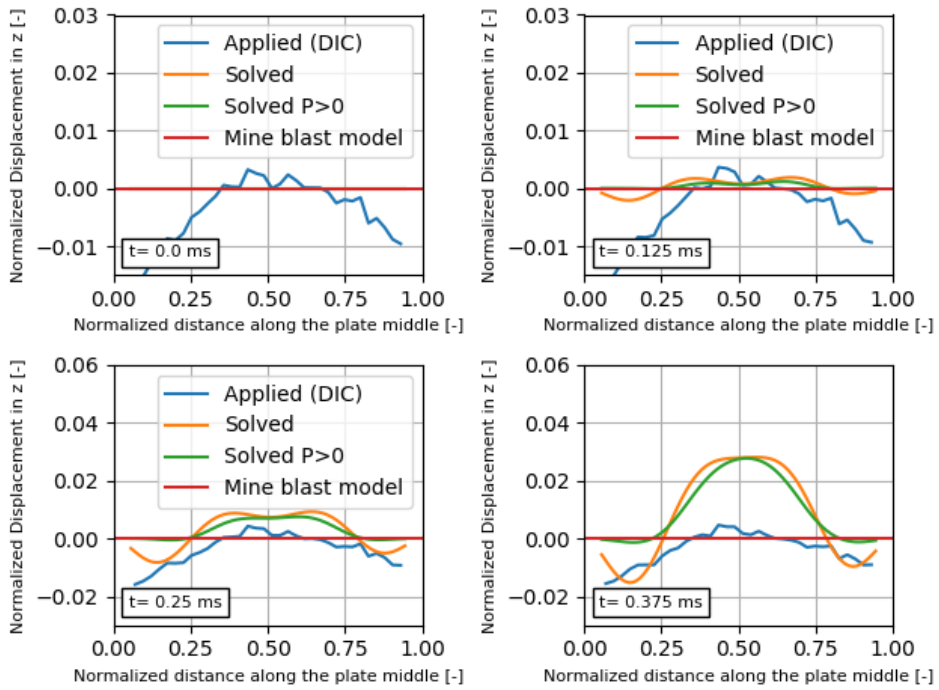

Figure 9.8: Small and noisy measured displacement at the beginning of the loading. The algorithm does not converge to the displacement, although discrepancies are small, note the displacement magnitude.

Furthermore at the center of the plate their is a small discrepancy between the the solved displacement applied displacement. From the convergence results and the verification benchmark tests it can be concluded that the error in the obtained pressure for these results can be large.

9.2.2. IMA Pressure

The solved pressure is shown in Figure 9.9. Contradictory to the expected behaviour no clear moving localized load is observed. Although at t=1.5 the signal seems to behave as such. As discussed in previous section the displacement did not converge well, such that large errors in pressure can be expected.

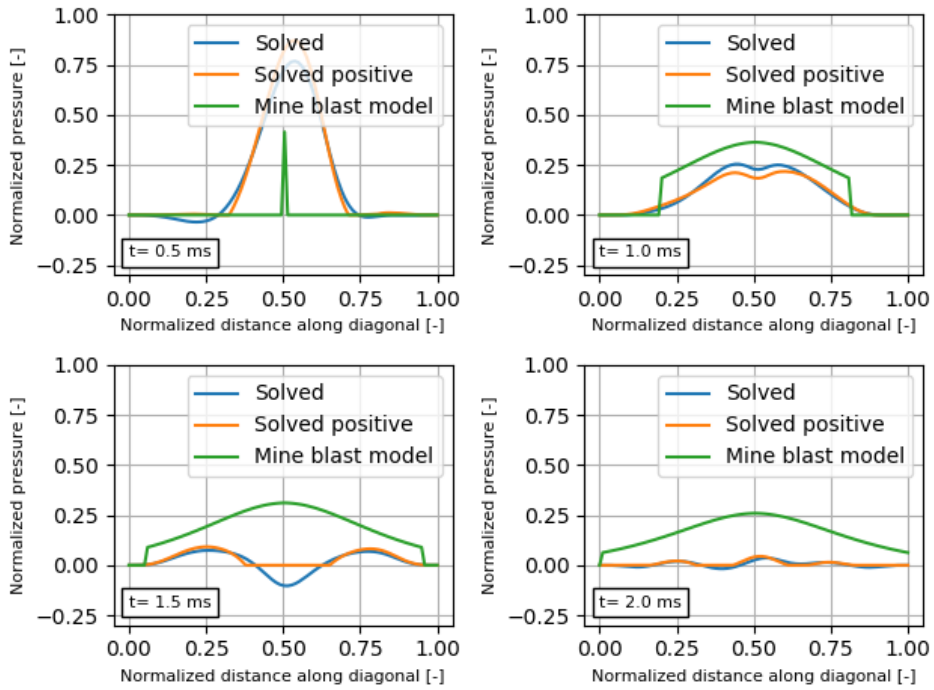

Figure 9.9: Pressure along the diagonal of the plate for different points in time. No clear localized (moving) load is observed. The Mine blast model lags behind in loading and also in displacement observed previously.

In Figure 9.10 the pressure distribution is shown for t<0.5 ms. It was observed that the displacement for t<0.5ms was not a good fit. The poor displacement fit in the beginning of the load is expected mainly due to the small amplitude of the noisy displacement, hence small contribution in error. The pressure found here is not expected to be correct.

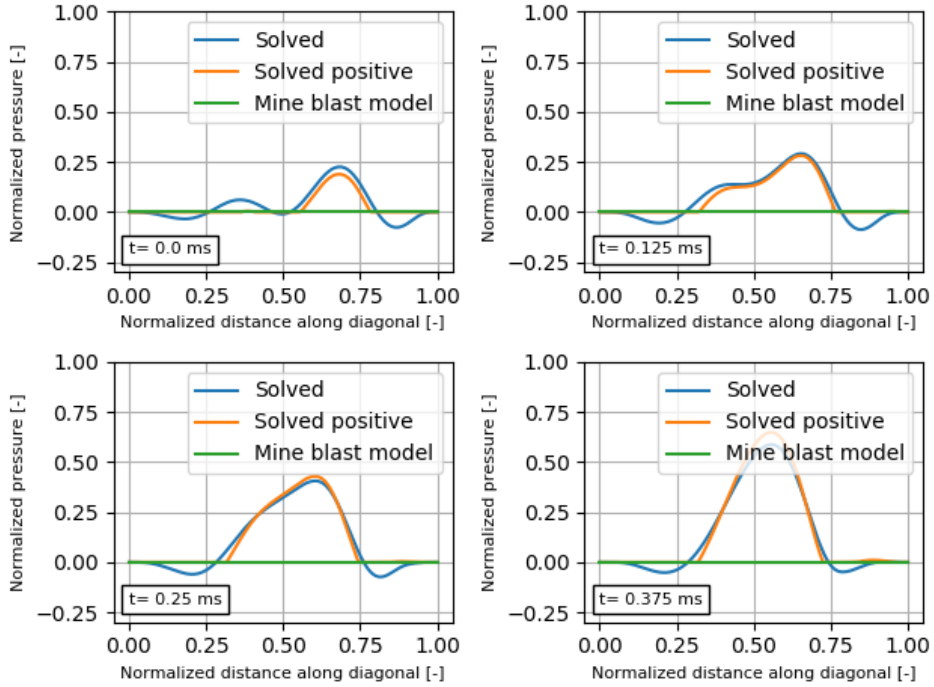

Figure 9.10: Pressure for different points in time. All points in time are for t<0.5ms for which the displacement was not converged. The obtained load is small, hence not too influential, however expected inaccurate.

9.2.3. Post processing pressure data

For the benchmark pressure it was found that the displacement was in very good agreement however the pressure distribution was not always accurately captured. Post processing the obtained pressure data showed that the total force and the centroid location of this force as function of time where parameters that closely matched for simulation and experiments (simulated experiment). Since for this simulation the pressure does not have the characteristic of a moving localized load computation of the centroid position is meaningless. The total force can however be computed versus time, results shown in Figure 9.11. From the verification tests in can be concluded that the convergence of the displacement is not accurate enough to expect an accurate total force. The mine blast model is not expected to be the correct one either however validation with this pressure is not yet possible.

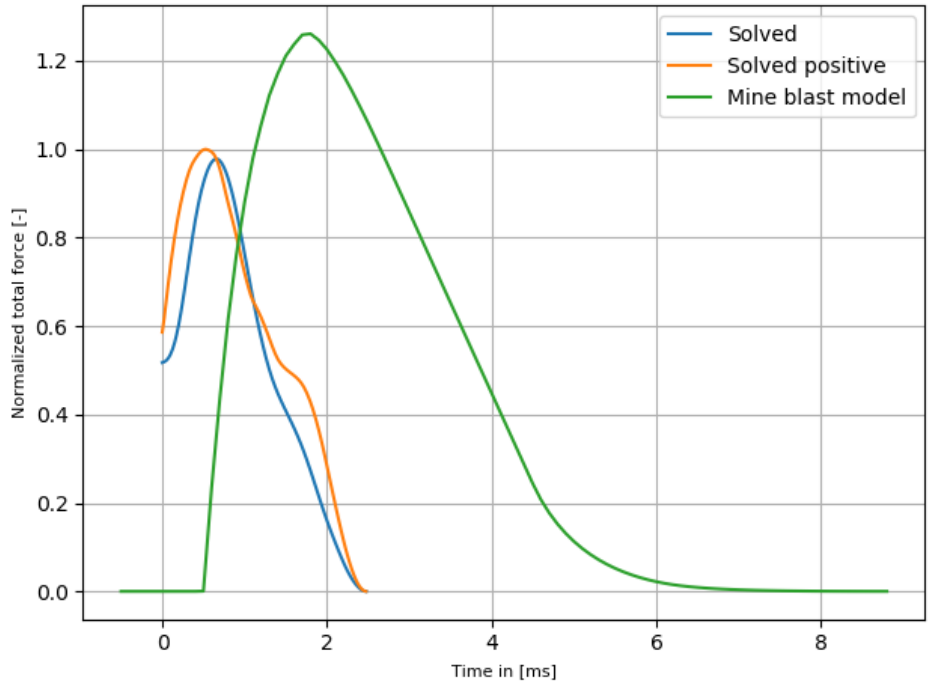

Figure 9.11: Total force obtained by integration of the pressure profile over the plate area remaining a function of time. The force is not expected to be correct since the displacement here is not converged hence validation with this parameter is not yet possible.

9.3. Steel-pot

In this section the IMA is applied to data obtained from a steel-pot experiment. For steel-pot explosions different (blast models) are required which are outside the scope of this work hence no comparison is done. The steel-pot has no soil layer on top such that only blast interaction pressure excites the plate.

The effect of arrival time is expected to be smaller, and a high peak load in the middle of the plate is expected. In Figure 9.12 the initial configuration of a steel-pot experiment is illustrated and in Figure 9.13 the focused blast loading is shown.

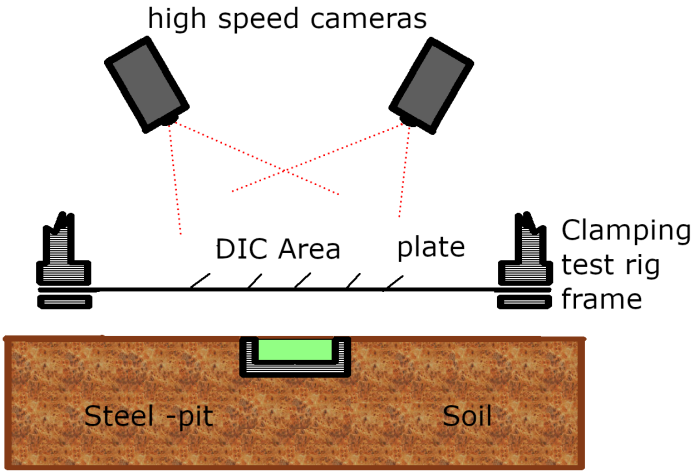

Figure 9.12: Illustration of the test setup for an explosive inside a steel-pot.

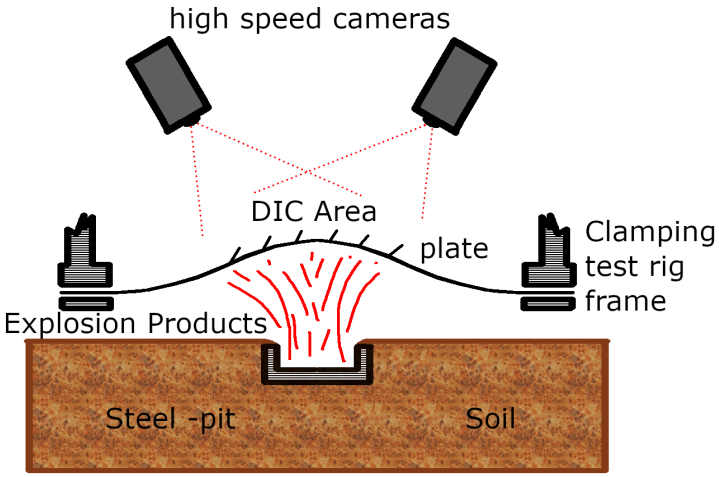

Figure 9.13: As the sketch illustrates there will be no soil bubble formation, instead the steel-pot will focus the explosion products upwards hence a completely different loading case. A focused localized pressure distribution in the center of the plate is expected.

9.3.1. IMA displacement

The displacement of the simulation is compared with the DIC measurements in Figure 9.14. It is can be seen that the simulated displacement is in agreement with the measured DIC data. The displacement in the beginning is a bit of and at the center of the plate at t=1.5 ms and t=2.0 ms the curvature of the DIC data seems larger, which will influence the accuracy of the found pressure.

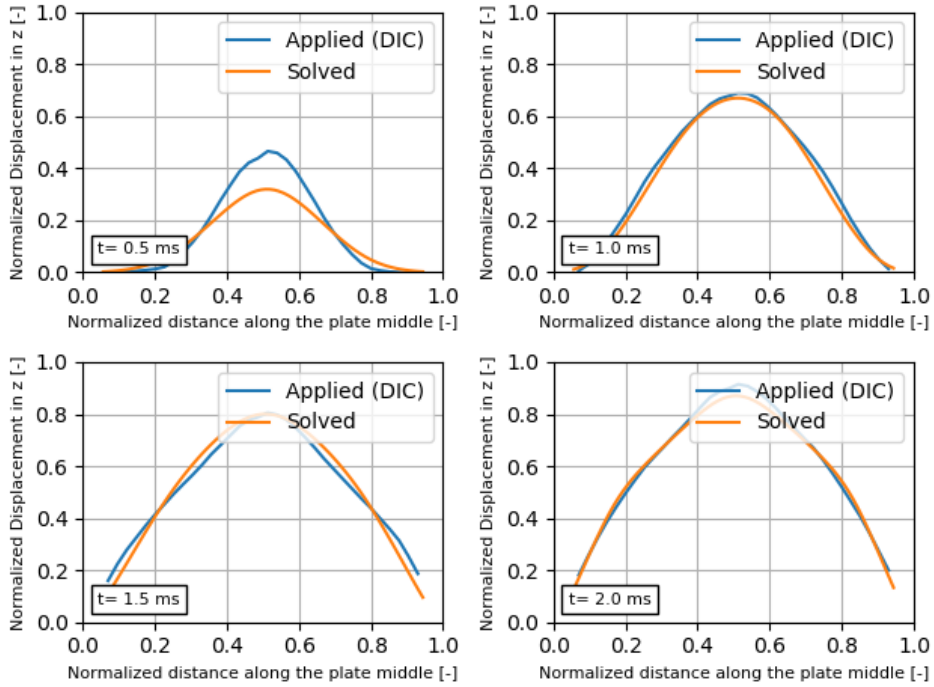

Figure 9.14: Here the displacements of the measurements 'applied' are compared to the simulation 'Solved'. The displacement is plotted over the middle of the plate, parallel to the long side of the DIC area. The plot starts at the beginning and ends at the end of the DIC area, hence the edges are excluded. The displacement is converged quite well except for the start of the loading t<0.5 ms.

9.3.2. IMA Pressure

The solved pressure is shown in Figure 9.15. For all pressures where t>=0.5 ms the pressures are quite small. Further analysis of the results showed that the larger pressures mainly occur only at t<0.5 ms.

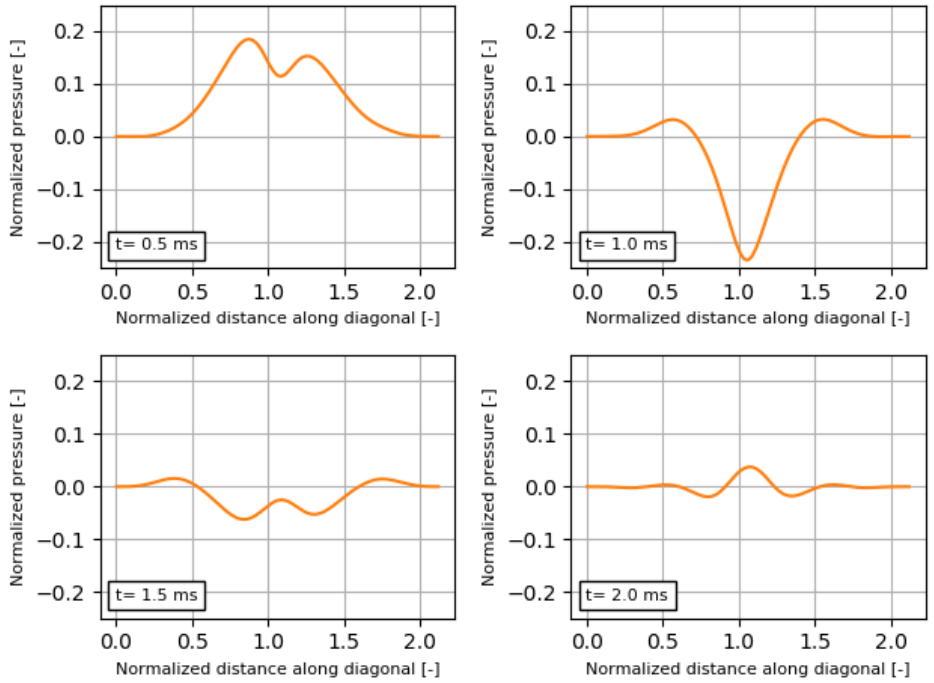

Figure 9.15: Pressure along the diagonal of the plate for different points in time. All points in time have a relatively small amplitude. The largest pressures are found to be between t=0 and t=0.5 ms (not shown here).

In Figure 9.16 the pressure distribution is shown for t<0.5 ms. The pressure found here does not show the moving localized load such as the benchmark problem. The pressure distribution is very similar to an exponential distribution, in accordance with the research of reviewed earlier [44] and [39].

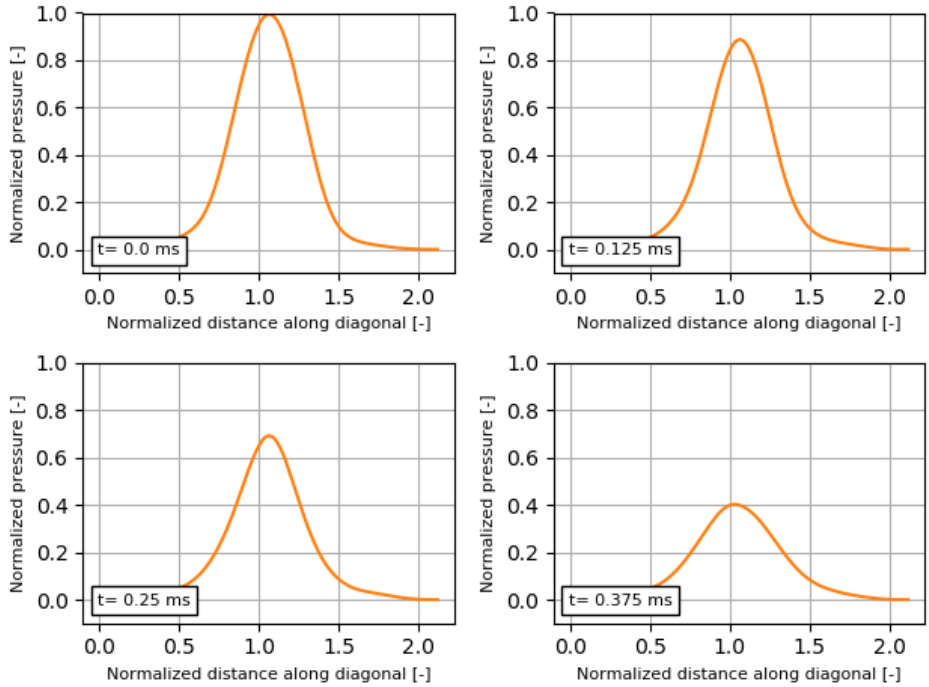

Figure 9.16: Pressure along the diagonal of the plate for different points in time. All points in time are for t<0.5ms where a relatively large amplitude is found. The distribution is close to an exponential distribution which is in agreement with the research of [44] and [39].

9.3.3. Post processing pressure data

The pressure found does not have the characteristic of a moving localized load computation of the centroid position is meaningless. The total force can however be computed versus time, results shown in Figure 9.17.

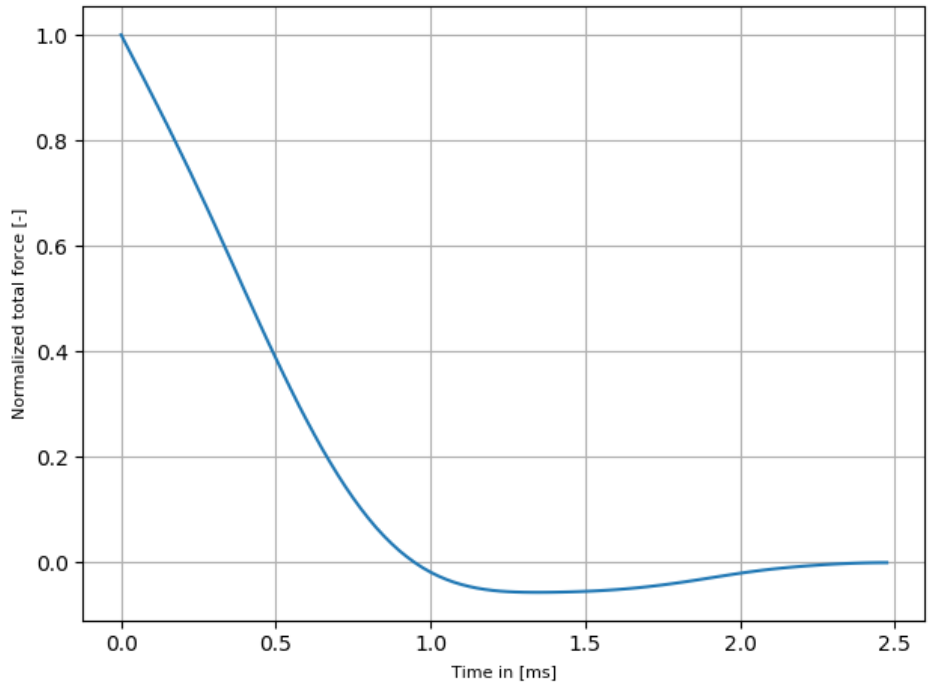

Figure 9.17: Total force obtained by integration of the pressure profile over the plate area remaining a function of time. The total force is largest for t<0.5ms peaking at t=0ms and decreases close to linearly. During a small section in time the total force is slightly negative. The shape reminds us of the classical Friedlander wave used for blast load modeling [36]. However the magnitude of the negative pressures is sometimes significantly higher then one atmosphere. No physical explanation is known, the not completely converged algorithm might be the cause.

The total force is largest for t<0.5 ms and peaks at t=0 ms. During a small part of the loading the total force is negative. This occurs when the displacement is still a good match and is in agreement with the Friedlander wave [36]. The negative pressures are however significantly higher then one atmosphere. No reasons for this is found. The cause can be the algorithm that has not completely converged.

9.4. Summary

The convergence of the displacement is of similar accuracy as the verification tests. From the verification it was determined that for this accuracy the discrepancies in pressure can be large. Furthermore the total force applied can be inaccurate when the convergence is not accurate. For this reason it has to be concluded that the current algorithm is not yet capable of validating mine blast models. From this research it can be concluded that any validation based on displacement measurements require the experiment and simulation results to be a very close match. If not the modeled mine blast interaction pressure and even applied total force as function of time can be far from the truth. This is an interesting conclusion since many researchers in the field show much larger discrepancies between their measurements and experiments. Furthermore many researchers only have measurements compared for one point in time, e.g. the maximum displacement or final deformation. This research proves that these validation methods are quite limited (a good fit for one point in time does not imply a correct pressure model).

10 Conclusion

The main conclusions of the research are discussed here for first the inverse measurement problem in general. Secondly the inverse problem specifically for mine blast pressure loading. Researching the inverse problem resulted in better understanding mine blast validation which is discussed next. Finally the validation of the mine blast model is discussed.

10.1. Inverse measurement problem

In this report an inverse problem to measure the interaction pressure using DIC displacement measurements is studied. Measurement and simulation are compared by means of an objective or error function. The aim is to find an interaction pressure that minimizes this error. The inverse problem is thus reduced to a minimization or optimization problem, for which many algorithms exists. The large design space of the interaction pressure as function of space and time P(x,y,t) requires gradient based optimization algorithms to prevent 'the curse of dimensionality' in optimization problems. The computation of the gradient of the objective function is done using the adjoint method, which proved to be very efficient having computational cost of the same order as one forward problem. The adjoint problem was first derived for a dynamic linear Kirchhoff Love plate. Secondly the adjoint was derived for a general continuum with an elastic material model.

A non-linear elastic material model was proposed to model plastic plate behaviour under the assumption of monotonically increasing strain.The continuum problem was studied for a plate using this material. This material model proved to be accurate for the beginning of the deformation of a plate exited by the TNO mine blast model as compared to Johnson-Cook material model.

For both the Kirchhoff love and continuum model both the forward and adjoint problem had to be solved. This was done using the Author's implemented dynamic FEM solver written using 'python' and 'c' programming language. The linear solver was verified using the method of manufactured solutions and the continuum solver by means of a comparison with LS-Dyna.

The algorithm to solve the inverse problem was benchmark tested using three different benchmark pressures. First one or more smooth sine waves over space increasing in amplitude with variable power of time (t^k). Secondly a radial symmetric exponential distribution over space was modeled to move radial outwards with constant velocity. This has the mine blast characteristic of a running localized load however is a relatively smooth distribution. Finally a pressure distribution was designed as benchmark load for inverse problems specifically for mine blasts based on research of [40]. This distribution is a discontinuous localized load moving radial outwards with constant velocity while decreasing in amplitude. The main idea is that when such a load can be captured back successfully using an inverse measurement algorithm then the correct algorithm will also work for mine blast for which the load is not initially known.

Without exceptions the designed algorithm was capable of finding a pressure such that the displacement is a very close match with the simulated or real experimental data. This implies that the optimization algorithm is success full in minimizing the objective function. From the tests for which the applied pressure is known it was

found that the pressure is not always captured back accurately. From these results it can be concluded that the solution of the inverse problem is unstable and non-unique. Stability here implies small deviations in displacement (input) can cause large deviation in pressure (output). The property that the inverse problem is non-unique is by no means mathematically proven, quite the contrary for the static Kichhoff Love plate it is shown that there is an exact solution for any displacement that can be written as 2d Fourier sine series see Appendix F. Instead here with non-uniqueness implies that vastly different pressure distributions can result in displacements that are very similar.

It was found that smooth distributions such as the sine and localized smooth distributions are captured back better. Especially the sine load was captured back accurately, except for very small spatial oscillations of the pressure distribution. The localized load did very well in most circumstances except for somewhat larger spatial oscillations in pressure. Finally for the benchmark pressure it was found that the high peaks, very localized and discontinuous load was not captured back accurately. Although the displacements are a very good match the pressure distribution found had smaller amplitude and a larger pulse width. For all three pressure distributions it was found that small noise levels of 0.1% had little influence in the solution while larger noise levels exceeding 1.0% did result in large oscillations in pressure distribution captured back.

10.2. Mine blast

The research question was; '*Can displacement measurements obtained from DIC be used to calculate the interaction pressure to validate the current TNO mine blast model?*' From this research it is concluded that smooth pressures are captured back accurately, however moving localized discontinuous pressure distributions are the expected shape of mine blast interaction pressures which are captured back poorly. Hence the interaction pressure for a mine blast cannot be captured back accurately thus direct comparison of a mine blast model interaction pressure with the inversely measured pressure is meaningless. The idea at the beginning of this project was based on the expectation that the pressure could be captured back with reasonable accuracy. After this research it is concluded that this is not possible due to the non-uniqueness of the inverse problem.

Two invariants are defined by post processing the pressure data. These invariants remain a good match, first the total force as function of time obtained after integration of the pressure. Secondly the location of the localized load, defined as the radial centroid position of the load. By visual inspection of the pressure load found it can be seen whether the latter has any physical meaning and should be computed or not. It should be noted that these invariants can be far off when displacement convergence is slightly inaccurate. Partial validation can be done by comparison of these parameters. These parameters are observed to act as invariant for different pressures which cause the same deformation. Whether this is true should however be researched more fundamentally.

10.2.1. Validation mine blast research

The usual way of validating a mine blast model is by means of comparing the deformation or trajectory of some object excited by a mine blast for both an experiment and simulation. When the deformation or trajectory match the model it is often said to be validated or calibrated for that range. Traditionally researcher in the field use this methodology to validate their mine blast simulations. Often only one measurement in time is compared being the maximum displacement or final deformation of a deformable object. For multiple time measurements a unique test setup such as the test rig is required, which is not seen in literature much.

The fact that the inverse problem is unstable implies that the deformations need to have a very good match in order to claim correctness of the mine blast model. The described IMP algorithm can be used to obtain a pressure distribution with a much better matching displacement which can be compared with models that have non-perfectly matching displacements. In general the non-uniqueness of the inverse problem implies that the interaction pressure cannot be found. Validation of interaction pressure by meas of traditional validation methods is thus not possible. Validation of the invariants of a pressure loading can be done and will be helpful in further understanding of the mine blast loading. Note that for such validation the experiment and simulation results need to be in almost perfect agreement. The study of this inverse problem has shed light on the limitations of current validation methods.

10.2.2. Validation mine blast model

The displacement of the mine blast model was compared to the experimental DIC data. The z-displacement of the center of the plate from the mine blast model increased slower compared to the experiment. The pressure from the

mine blast model starts localized in the center of the plate and rapidly moves outwards to a more global pressure distribution. The IMA pressure was more localized in the center for a longer time. The peak pressure of the IMA was also higher, both these affects are the expected reason for the faster increasing plate displacement in experiment compared to the mine blast model. However it should be noted that the convergence of the algorithm for the displacement was not accurate enough to use the pressure data to validate the mine blast model. Furthermore the IMA has to be further studied before it can be used to validate mine blast models. Recommendations for such follow up research is given in the next chapter.

11

Recommendations

Computing the interaction pressure from DIC measurements is a rather new field of studies. This work provided a methodology to find an interaction pressure such that the corresponding displacements are in close agreement with the measurements. It is however concluded that the solution in non-unique. This chapter will provide several aspects of the current research that require to be further studied. Furthermore interesting follow up research is proposed. The chapter is split in two sections focusing on general inverse measurement problem and specifically for the identification of mine blast interaction pressure.

11.1. Inverse measurement problem

A large and complex IMA was developed to solve the IMP. Several methods used for the algorithm are recommended to be studied in more detail. Furthermore the behaviour of the algorithm under a variety of circumstances should be studied in more detail. In this section recommendations for further research concerning the IMP are given.

11.1.1. DIC data

The derivation for the adjoint assumes a continuous measurement '$v(\boldsymbol{x}, t)$'. Post processing the DIC data gives discrete data points in space and time. These data points are interpolated to obtain the continuous measurement '$v(\boldsymbol{x}, t)$'. For the current algorithm trilinear interpolation was used. Since the simulation time is rather short the amount of DIC frames is small, bound by the camera's frame rate. The coarse interpolation over time might have a large influence on the solution. The performance of the IMP algorithm for different interpolation methods or varying number of frames in time should for that reason be studied.

The spatial interpolation is expected to be less of a problem since it is already quite smooth. Furthermore if the spatial discretization poses a problem the discretization of the plate would need to be improved first since the mesh discretization is of similar size as the DIC resolution.

Patching of missing DIC data (holes in the .stl mesh files) obtained from GOM-inspect [1] could be done with a variety of interpolation methods, which might be interesting to study. Further more the problem could be extended and studied for a dynamically changing DIC area such that patching of holes in not required.

The DIC data sometimes contains noise, this data could be smoothend to obtain a better displacement field. The effects of such data smoothing methods on the IMP algorithm are interesting to study.

The IMP has limitations on the precise spatial accuracy simply because a plate will not bend or deflect over very small distances, that is large spatial oscillations will not be recovered. This will depend on the thickness of the plate. It is interesting to research the maximum useful number of data points or minimum distance between two data points that will still give extra information for the inverse problem. This will depend on the noise level and the thickness of the plate. As a first step this could be studied for simulations without noise to obtain an lower bound for the best spatial DIC accuracy required. It is best to study this together with the recommendation on 'Fourier series interaction Pressure'.

One could also study an error function ‘J’ to be minimized as a discrete sum over measurement data instead of the integral over a continues signal, preventing the need of interpolation. Lastly the DIC measurements where obtained using GOM-inspect. Calculation of the displacement data from images is itself a measurement problem. The performance of the algorithm could increase when the two measurement problems are solved as one. Hence defining an objective function to be minimized directly from the measured images.

11.1.2. Mesh refinement adjoint

For both the KL plate and the continuum model the IMP algorithm was found capable of converging to the ‘applied’ displacement. The continuum model converged slightly less accurate. This might be due to the accuracy of the adjoint. As shown in Chapter 6 in Table 6.2 the variation obtained from the adjoint for some variations in traction is sometimes off by 8%. This can cause the optimization algorithm to stop converging when near the optimum. Often when the solved displacement is close to the applied displacement the difference of the displacements will oscillate a bit. This difference is the traction of the adjoint problem, hence oscillations over space and time of the adjoint field are expected causing complex adjoint fields. For such complex fields a finer mesh is required hence the influence of mesh refinement for the adjoint problem on the IMA should be studied. Since this effect is expected to be one of the main reasons for the algorithm to stop converging four frames of the adjoint field in z-direction are shown in Figures 11.1, 11.2, 11.3 and 11.4.

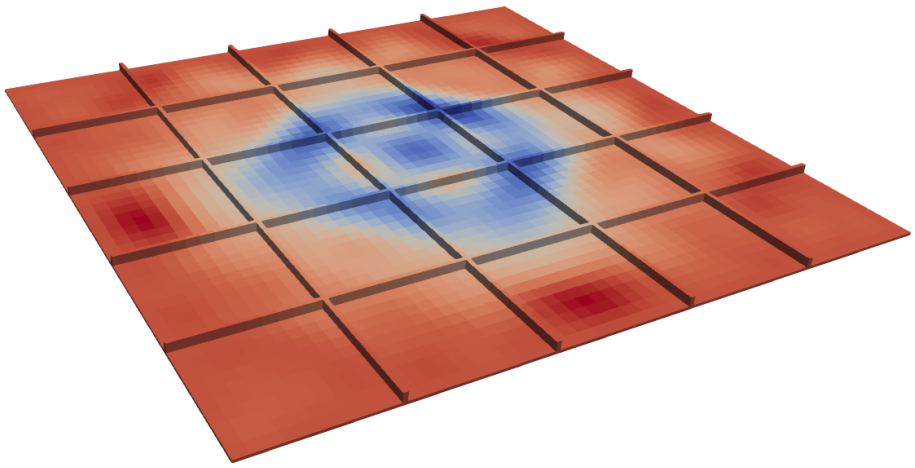

Figure 11.1: Adjoint field for the grid stiffened panel after IMA converged at t=0.5. The coloring emphasizes adjoint field in z-direction. The spatial and time oscillations (see next frames) can be the cause of non-converging adjoint problem such that gradient of descent algorithm fails to converge.

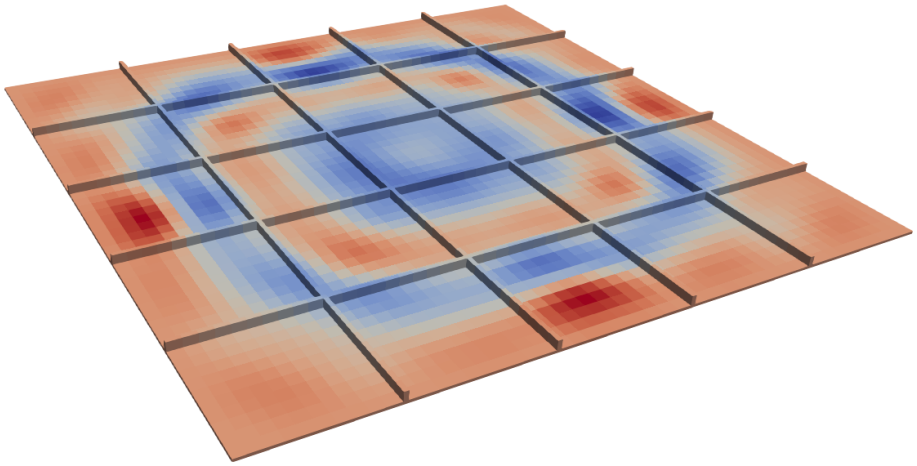

Figure 11.2: t=1.0 ms.

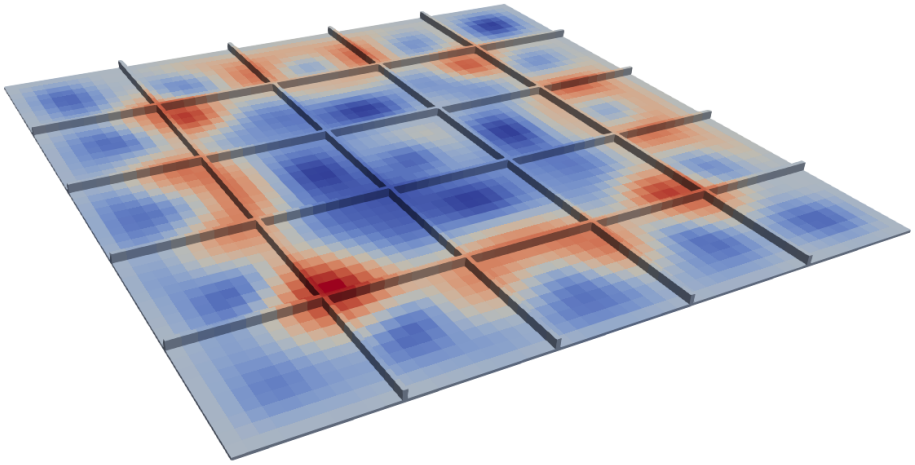

Figure 11.3: t=1.5 ms.

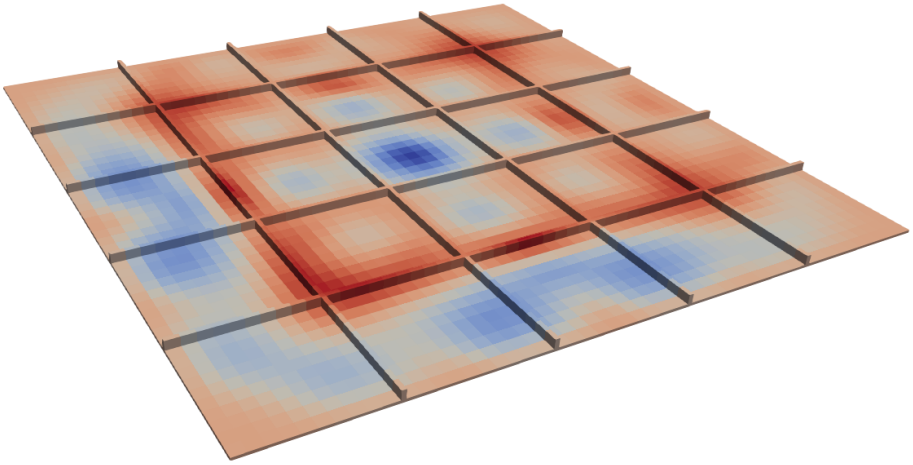

Figure 11.4: t=2.0 ms.

Similar behaviour was observed for the plate simulations. Due to computational cost simulations with finer mesh where not performed. When finer mesh algorithms are studied it is recommended to use an adaptive mesh refinement algorithm to decrease computational cost at the start of the simulation. In practice this will imply the need of a finer mesh when the algorithm is converged close to the optimum.

11.1.3. Regularization and constraints

The current algorithm used unconstrained optimization and one constrained optimization was tested as well (P>0). One could constrain the pressure, using prior knowledge of the solution, in an attempt to stabilize the inverse problem. Interesting examples would be radial symmetric pressure or strictly positive pressure. Instead of direct constrained on the pressure one could use regularization by adding penalty terms in the objective function. The observed oscillations in pressure can be decreased when non-smooth pressure distributions are penalized using e.g.

$$J_{regularization} = \int_0^T \int_\Omega (P_x)^2 + \left(P_y\right)^2 + 2 * \left(P_{xy}\right)^2 \mathrm{d}\Omega \mathrm{d}t \tag{11.1}$$

were P is the applied pressure. Regularization was briefly studied for the benchmark problem however the existence of a discontinuity in the solution will not be captured due to regularization hence defeating the purpose. One interesting idea to solve this problem is by splitting the pressure 'P' in two components

$$P = P_s + P_{d1} + P_{d2} \tag{11.2}$$

were P_s is a general smooth pressure distribution to be solved, P_{d1} is a discontinuous pressure distribution with a step function in pressure and P_{d2} is a discontinuous step function in the slope of the pressure distribution. For the discontinuous pressure functions the location and size of the step are to be found hence increasing the number of unknowns to optimize for. The potential of the method is shown in Appendix G.

11.1.4. Oscillations near discontinuities

The KL plate was discretized using hermitian basis functions. The same discretization was used for the pressure function space. This space does not allow non-zero values of displacement and slope near the boundary, consistent with the displacement boundary conditions. For pressure distributions that have non-zero pressures on the boundary oscillations were observed in the 'solved' solution. similar oscillations were observed near discontinuities in the pressure distribution or slope of the pressure distribution. These oscillations seem similar to the Gibbs phenomenon for Fourier series near discontinuities and are recommended to be studied further.

11.1.5. Benchmark test smaller DIC area

The Benchmark tests were performed using the complete area of the plate as measurement area. The real experiment did not have measurement over the complete area. The effects of a reduced measurement area are recommended for further research. Besides the size of the measurement area it is interesting to determine if the pressure can be captured back outside the measurement area of a plate and if the accuracy outside this area decreases.

Due to dust clouds and other problems a part of the data from the DIC measurements is lost. This is seen as holes in the measurement data. The size and amount of holes increases over time. These holes where patched using interpolation. It would be better if no assumption is made for the unknown area in such holes by defining the error function as an integral over a dynamically changing measurement area. It is recommended to research that if such improvements are possible and if so derive a new adjoint problem for such a case. The improvement of such a method is however not expected to be large since the size of the holes present and the resulting difference in the error function is small.

11.1.6. Benchmark different forward model

The benchmark tests performed used the same forward model to create the displacement data. It was found that the benchmark tests always converged accurate to the applied displacement. The convergence to the real measurement data was found less accurate. It is possible that the inaccuracy in the forward model compared to the real plate will will cause the convergence to be less accurate. The accuracy in the forward model will also influence the pressure found. Creating displacement data with a (slightly) different forward model can be done to benchmark test the sensitivity for differences in forward models.

11.1.7. Adjoint problem using shells

Often plates are modeled using shell elements. This reduces the computational costs and is known to be accurate. The assumption used in shell theory is often a displacement over the thickness as used in Kirchhoff-Love plates, i.e. planes remain planes. For the adjoint problem the material stiffness varies over the thickness of the plate, since this stiffness is the tangental stiffness of the forward problem. This could cause the planes to warp such that shell theory is invalid. For that reason no shell theory was used. It could be researched if this is indeed the case. When shell theory can be used, such that the described effect is non-existing or negligible, then the cost of solving the adjoint problem may be greatly reduced. Of course this should be studied while considering the used forward model. For a linear elastic material model as forward model the problem is self adjoint such that the adjoint stiffness matrix is constant. For this case it is known that shell theory will work fine.

11.1.8. Measurement near the boundary

The boundary condition at the clamped edges of the physical plate for the adjoint field is zero (similar to clamped). The final pressure obtained from the IMA is the sum of several scaled adjoint solutions

$$P(\boldsymbol{x}, t) = \sum_{n=1}^{N} -\alpha_n \phi_n(\boldsymbol{x}, t), \tag{11.3}$$

since the adjoint is the gradient. Hence at the boundary the pressure will always be zero. For this reason the accuracy of the algorithm near the boundary is expected to be less. It is recommended to further study this and determine the distance from the boundary where measurements are expected to be accurate.

11.1.9. Different shape and topology

The adjoint was derived for a general continuum however only used for plates and a grid stiffend panel. It is interesting to see if the methodology will work for vastly different shapes and typology. This is generally interesting for inverse load identification. For example a typical force identification problem is to model a bridge, measure the displacement on several locations and determine the loads applied on the bridge. In theory the derived method could be applied for such a complex geometry.

11.2. Mine blast

The developed IMP can be improved. In this section recommendations for further improvements are given specifically for mine blast loading.

11.2.1. Quantify allowable displacement deviation

From this research is was concluded that when displacements of experiment and simulation are in very good agreement the pressure interaction pressure can be quite off. Part of this problem is the non-uniqueness of the inverse problem, the other part is the sensitivity of the inverse problem. Slightly larger deviations can be the cause of significantly different pressure profiles. A large amount of researchers compare the displacement or deformation of experiment and simulations as validation method. Often quite large errors in displacement and different curvatures/deformation shapes are accepted. No research is found that studies the allowable difference in displacement in terms of an acceptable error in pressure. Of course this is a complex problem, the formulation alone would be difficult. It is expected that L^2 error relation between pressure and displacement errors is not enough for example errors in displacement near the boundary are the expected result of larger inaccuracies compared to the middle of the plate.

When no criteria exists for the accuracy in which displacement fields from experiment and simulation have to match then the amount in which the model is validated for the interaction pressure or more general the mine blast model remains unclear. This problem could be studied by studying several different deviations in displacement and using an IMA such as the one discussed here to find the corresponding pressures and their deviations. This has the advantage that different deviations observed can be directly studied. On the other hand the disadvantage is the need for an IMA which is complex and slow as compared to solving the forward problem. The other method to study the problem is by studying the response for deviations in pressure which has the advantage that only the forward problem has to be computed. The disadvantage is that displacements observed in experiments and simulations have to be matched with correctly chosen pressures, which itself is an inverse problem.

It is important to quantify the aforementioned problem for different geometry, e.g. different plate thickness or various grid stiffened structures. When a small deviation in displacement field between simulation and experiment for say ‘case X’ implies a large deviation in pressure the model might still be useful for experiments similar to ‘case X’ however when the model is now applied to say ‘case Y’ the accuracy in pressure could be paramount for the simulated response or the inaccuracy of the model in ‘case X’ could have large influences in ‘case Y’. Hence the allowable deviation in displacement should ideally be quantified for different geometries.

11.2.2. Pressure model

As described in previous section regularization and constraints may be applied to stabilize the inverse problem. Specifically for mine blast several assumptions on the pressure model can be made:

- Radial symmetric load;
- Strictly positive pressure;
- Localized load;
- Smooth load, including two discontinuities, one for pressure and one for pressure slope (Appendix G);
- No high frequency spatial and time oscillations in pressure.

Using constraints and regularization these characteristics can be enforced on the pressure model. In addition one could use any mine blast model together with the methodology described in Appendix E to find the functions or parameters that result in the best displacements.

11.2.3. In plane traction

The adjoint derived for a continuum uses a general traction. It was however assumed that the in plane components are negligible. This assumption can be checked by including the in plane components of the traction. Before this is done the sensitivity of the algorithm should be studied for in plane traction components. It is expected that in plane traction components will have little influence on the response (the deformation of the plate), which are measured with less accuracy. Different methods or test setups are in this case required to measure the in plane traction components. In general the inverse problem first has to be studied for the presence of in plate traction components to see if the assumption made is correct. Perhaps the match between the solved and applied displacement for the real DIC data is not as accurate as the benchmark tests due to the lack of in plane traction components that are present in the real experiment.

11.2.4. Boundary conditions

The plate is modeled as clamped along the edges. In reality the plate is mechanically clamped which is never perfectly clamped. It is known that the boundary conditions are important for the response of mine blast simulations [14]. The IMA should be studied for different boundary conditions. It is expected that modeling the plate slipping due to the mechanically clamped boundary conditions introduce some additional uncertainty. When inaccuracies in boundary conditions have large influence in the displacement of the plate this shows a large limitation of the test setup for validation and calibration purpose. Perhaps using a welded joint which is expected to introduce less uncertainty, is preferred however the cost aspect of such a setup is an obvious problem. Perhaps bolted plates are the best compromise between a cost effective solution and a reduction in uncertainty.

Furthermore for the test setup the plate was clamped to a test rig which is allowed to move. The boundary of the plate is modeled as clamped and static i.e. not moving. It is recommended to study the influence of that assumption. As a first step modeling the test rig as a rigid body attached to a plate with clamped edges that are allowed to move (dynamic boundary condition) seems a good approach.

11.2.5. Invariants

Invariants of a pressure distribution were defined as quantities that remain unchanged for different pressure distributions that result in close to the same deformation. Here 'close to the same' should be better defined. Two invariants for a localized radial symmetric moving load were defined namely the total force as function of time and the radial centroid position. It is recommended to study these invariant and determine whether there are no exceptions to the observed behaviour. A third invariant recommended to be studied is the width of the pressure distribution, which could be defined as standard deviation around the centroid position. The existence of other invariants for perhaps different load cases can be studied. Invariants are important to study since by definition they are the only information one can obtain concerning the pressure loading obtained from displacement data. In the ideal case one could find a complete set of invariants that result in a unique displacement. A different approach concerning such a set is explained in 'Fourier series interaction pressure' recommendation at the end of this chapter.

11.2.6. Plasticity

The described method is used first on a KL plate model and secondly for a continuum model with non-linear elastic material model. In Appendix C it is shown that the plastic linear-elastic and non-linear-elastic models are in good agreement. The plasticity model used and calibrated by TNO is expected as the correct forward model. For large displacements or longer simulations such that unloading occurs the described algorithm will be inaccurate due to an inaccurate forward model. It is recommended to study the algorithm for a forward model that includes plasticity however this requires adjusting the adjoint problem.

11.2.7. Finite difference method

For mine blast models with a small number of degrees of freedom one could use finite difference method to determine a gradient. For such a model the adjoint method is not required such that any forward model can be used. This could be a first approach to test the method using forward models including plasticity.

11.2.8. Validation

The DIC data is noisy and probably not accurate during the start of the loading. Example is the negative plate displacements near the boundary of the DIC data. The IMA converges to strange displacements and corresponding incorrect pressure distributions for this displacement data. Methods such as post processing e.g. smoothing the measurement data such that these effects do not occur should be studied.

When the unconstrained IMA was used negative pressures did occur. Negative pressures are not expected during the mine blast loading hence this behaviour is strange. The benchmark problems contained negative pressures as well, however usually only smaller high frequency oscillations which are known to not influence the response much. One of the reasons could be inaccuracy in forward model. This could be studied toghether with the influence of differences in forward model as discussed earlier.

It is expected that at the start of the loading the boundary conditions will not influence the response. For later stages of the mine blast loading and plate deformations the clamped boundary conditions might be too stiff

compared to the mechanically clamped conditions. This could be the reason that the TNO model deflects less compared to the DIC data in the clamped plate simulation. These effects should be studied.

11.2.9. Jumping height test rig

The advantage of the test rig is that both the local plate displacement and the total impulse applied can be found. This research only focused on the local plate displacement and did not add an error term for the total impulse to the objective function. This extension was is simple and was briefly studied however from the benchmark tests it was found that the IMA accurately determined the resultant force versus time. The integral of this curve will thus also match accurately which is the total impulse applied. For the continuum model the convergence was observed to be less for some simulations, causing the resultant force versus time to be inaccurate. For this situation the total impulse can be added as additional error term.

For a good validation an excellent match between experiment and simulation is required. If the match is not accurate the model used can be very inaccurate in not only pressure but also total force time characteristic. When the displacement match is accurate the resultant force versus time was found to be accurate as well. In that case the total impulse applied is also accurate. It can thus be concluded that when the local displacement is accurately converged the total impulse is also correct, making the jump height information redundant.

11.2.10. Fourier series interaction pressure

The forward problem acts as a low pass filter, both over space and time. Applied pressure distributions with low frequency will have large amplitude displacements and the response for high frequencies will be small. The extreme cases of this makes intuitively sense. Apply a sinusoidal pressure load that has a large number of waves in one plate and the plate will not bend in this shape with large amplitude, this was shown for a static KL plate in appendix F. Similar, pressure loads that oscillated with high frequencies over time will not be followed by the response with large amplitude, simply because the inertia.

Most functions can be approximated by a Fourier series. If the interaction pressure is described using a Fourier series the displacement is mainly caused by the first terms in the series, the lower frequencies. Since the forward problem acts as a low pass filter. For the inverse problem this implies that only the first terms of the Fourier series of the interaction pressure can be determined from displacement measurements.

For mine blast it was recommended to study the defined invariants such as the total force and the radial position as function of time. Ideally one would obtain a set that describes the interaction such that almost the same displacements will result in almost the same invariants (stable set).

The first coefficients of a Fourier series that describes the interaction pressure could be used as such a set. The impact of higher order terms can be studied using only the forward problem, which is cost effective. The coefficients corresponding to frequencies over both space and time that can still be determined should be linked to several parameters such as the measurement accuracy, geometry of the test setup, material used (in this case e.g. plate dimensions, plate thickness, material stiffness, yield characteristics).

The inverse problem of finding the coefficients of the truncated Fourier series describing the interaction pressure can be solved by taking the Fourier series of the pressure obtained using the IMA from this research. Furthermore one could use the method explained in Appendix E using a Fourier series as 'simplified pressure model'. The latter might speedup the IMA convergence by constraining the interaction pressure. It is the author's opinion that this recommended followup research has the potential of answering the research question 'What can we measure with the current test setup'. And thus answering the question; 'What can we validate with the current test setup'. This approach can be combined with radial symmetry further constraining the pressure model and reducing the number of unknowns.

A

Static Kirchhoff Love

The static solution of a Kirchhoff Love (KL) plate can be usefull in understanding the behaviour and some limitations of the Inverse Measurement Problem (IMP). This appendix will show the analytic solution for a KL plate using Navier method. It is known that the derived result is for pined boundary conditions however the conclusions made are qualitative and remain valid. The choice for pined boundary conditions is made to keep the solution simple. The problem to be solved is formulated as follows:

$$\begin{cases} \nabla^4 w(\boldsymbol{x}) = \frac{-q(x)}{D}, & \boldsymbol{x} = (x, y) \in [0, a] \times [0, b] = \Omega \\ w(\boldsymbol{x}) = 0, & \boldsymbol{x} \in \partial\omega \\ \boldsymbol{M}(\boldsymbol{x}) \cdot \boldsymbol{n} = 0 & \boldsymbol{x} \in \partial\Omega \end{cases} \tag{A.1}$$

where $w(\boldsymbol{x})$, $q(\boldsymbol{x})$, $\boldsymbol{M}(\boldsymbol{x})$, D and $\boldsymbol{n}$ are the out off plane plate displacement, distributed load, bending moment, the plate's bending stiffness and the boundary normal vector respectively. One way to solve this problem is by eigenfunction expansion, where the eigenfunctions form a complete basis, that is the Navier method [18]. The set of eigenfunctions are

$$\hat{w}_{nm}(\boldsymbol{x}) = sin(\frac{n\pi x}{a})sin(\frac{m\pi y}{b}). \tag{A.2}$$

Both the solution 'w' and the distributed load 'q' are be written in this basis as follows:

$$w(\boldsymbol{x}) = w(x, y) = \sum_{n=1}^{\infty}\sum_{m=1}^{\infty} sin(\frac{n\pi x}{a})sin(\frac{m\pi y}{b})w_{nm}, \tag{A.3}$$

$$q(\boldsymbol{x}) = w(x, y) = \sum_{n=1}^{\infty}\sum_{m=1}^{\infty} sin(\frac{n\pi x}{a})sin(\frac{m\pi y}{b})q_{nm}, \tag{A.4}$$

here the distributed load coefficients q_{nm} can be found by using Fouriers trick

$$q_{nm} = \frac{4}{ab}\int_{\Omega} q(x)sin(\frac{n\pi x}{a})sin(\frac{m\pi y}{b})\mathrm{d}\Omega. \tag{A.5}$$

Substitution of the eigenfunction expansion for both 'w' and 'q' into the PDE and assuming differentiation and summation may be interchanged the equation can be solved directly for coefficients w_{nm}, that is

$$w_{nm} = \frac{q_{nm}}{\pi^4 D}\frac{1}{((\frac{n}{a})^2 + (\frac{m}{b})^2)^2}. \tag{A.6}$$

The main importance of this derivation is to see that a KL plate works as a low pass filter. High frequency pressure content that is for large n,m in q_{nm} will 'damp' out due to the quick growth of the denominator in equation A.6. For the direct solution to the inverse problem it should then be clear that small error in w_{nm} due to e.g. measurement noise will cause large high frequency content in q, that is large q_{nm}. This illustrates the sensitivity of the IMP to noise for the static KL plate.

B

Benchmark pressure coefficients

In Chapter 3 a benchmark pressure was proposed for testing the IMP algorithm. The parameters 'A', 'w' and v determine the amplitude width and velocity of the localized pressure distribution. The aim of this appendix is to explain how these parameters are chosen based on scaling the results from [40] and TNO experiments.

B.1. Determining A

The variable 'A' is the peak amplitude of the pressure which occurs at (r,t)=(0,0). The value for 'A' is chosen such that the total impulse given by B.1 is consistent with test rig experiments. The value 'A' is given by B.2.

$$I = \int_0^\infty \int_\Omega P(r,t)\, d\Omega \mathrm{d}t \tag{B.1}$$

$$A = \frac{I}{\int_0^\infty \int_\Omega \begin{Bmatrix} e^{-(vt-r)w}(1-(\frac{r}{L})^2), & vt-r>0 \,\mathrm{AND}\, r<L \\ 0, & \text{otherwise} \end{Bmatrix} \mathrm{d}\Omega \mathrm{d}t} \tag{B.2}$$

B.2. Determining w

From [40] results it is seen that the spatial pressure distribution is quite localized. The width of a pressure pulse is approximately 25mm. This width varies over the spatial location, and is a bit arbitrary however for the simulation pressure constant width is used. Note that the experiment was scaled with a factor 'x' w.r.t. the TNO experiments ('x' is confidential). The width parameter 'w' will be chosen such that at (vt-r)=25x the pulse amplitude is 10% of it's peak value nearby (vt-r=0), Equation B.3

$$e^{-0.025xw} = 0.1 \tag{B.3}$$

$$-0.025xw = ln(0.1) \rightarrow w = \frac{-1}{0.025x} ln(0.1)$$

B.3. Determining v

It is assumed that the duration 't_d' for a wave to travel from r=0mm to r=100mm is only a function of dimensions, Soil bubble radius, Soil density, Explosion energy, Soil youngs modulus and Soil failure parameters '$\boldsymbol{d}$',R,ρ, E_t, E_y and $\boldsymbol{\sigma_y}$ respectively, Equation B.4. This can be written implicit as, Equation B.5. All dimensions present are dimensions of mass, length and time [M],[L] and [T] respectively. The implicit relation B.5 can thus be reduced to Equation B.6 for four dimensionless pi-products, B.7, B.8, B.9 and B.10.

$$t_d(\boldsymbol{d}, R, \rho, E_t, E_y, \boldsymbol{\sigma_y}) \tag{B.4}$$
$$f(t_d, \boldsymbol{d}, R, \rho, E_t, E_y, \sigma_y) = 0 \tag{B.5}$$
$$F(\pi_0, \pi_1, \pi_2, \pi_3) \tag{B.6}$$
$$\pi_0 = \frac{\boldsymbol{d}}{R} \tag{B.7}$$
$$\pi_1 = \frac{\boldsymbol{\sigma_y}}{E_y} \tag{B.8}$$
$$\pi_2 = \frac{E_y R^3}{E_t} \tag{B.9}$$
$$\pi_3 = \frac{E_t t^2}{\rho R^5} \tag{B.10}$$

Solving for the duration gives

$$t_d = \sqrt{\frac{\rho R^5}{E_t}} g(\pi_0, \pi_1, \pi_2). \tag{B.11}$$

When scaling the similarity parameters should be kept constant such that 'g' is known. This implies scaling all dimensions $\boldsymbol{d}$ with the same factor. The soil is assumed the same such that π_1 does not change. The scaling of explosive energy can deviate for TNO experiments, however this deviation is ignored for this benchmark problem, note that the deviation if any is confidential. It is thus assumed that 'π_2 remains constant as well. This implies $(\frac{R}{R_{Experiment}})^3 = (\frac{E_t}{E_{t_{Experiment}}})$. The duration is given by B.12

$$\begin{aligned} t_d &= t_{Experiment}(\frac{\rho_d}{\rho_{Experiment}})^{\frac{1}{2}}(\frac{R_d^5}{R_{Experiment}^5})^{\frac{1}{2}}(\frac{E_{t_d}}{E_{t_{Experiment}}})^{-\frac{1}{2}} \\ &= t_{Experiment}(\frac{E_{t_d}}{E_{t_{Experiment}}})^{\frac{5}{6}}(\frac{E_{t_d}}{E_{t_{Experiment}}})^{-\frac{1}{2}} \\ &= t_{Experiment}(\frac{E_{t_d}}{E_{t_{Experiment}}})^{\frac{1}{3}} \\ &= t_{Experiment}(\frac{R_d}{R_{Experiment}}) = x t_{Experiment} \end{aligned} \tag{B.12}$$

The time it takes for the pressure to travel radial outwards over the plate from r=0mm to r=100mm is 0.15ms. For the NATO experiment it will thus take 0.6ms to go from r=0mm to r=400mm. The average velocity thus stays the same. Ofcourse this speed will vary when scaling is performed differently however this is 'just' the benchmark model to test the IMP algorithm. For simplicity a constant velocity is used for the simulation pressure of $v = \frac{0.4}{0.0006} = 666 m/s$.

C

Forward model

It was found in the Chapter 7 that small differences in the displacement can be the cause of largely different interaction pressures. For this reason when the forward model is not accurate incorrect pressure measurements can be the result. It is realized that the non-linear-elastic material model is not correct, especially during unloading. The assumption however is that unloading does (almost) not occur. An often used material model for plasticity is the Johnson-Cook model. The normalized response of such a material in a uniaxial quasi-static isothermal tension test is given in Figure C.1. The figure also includes the response of the calibrated non-linear elastic material.

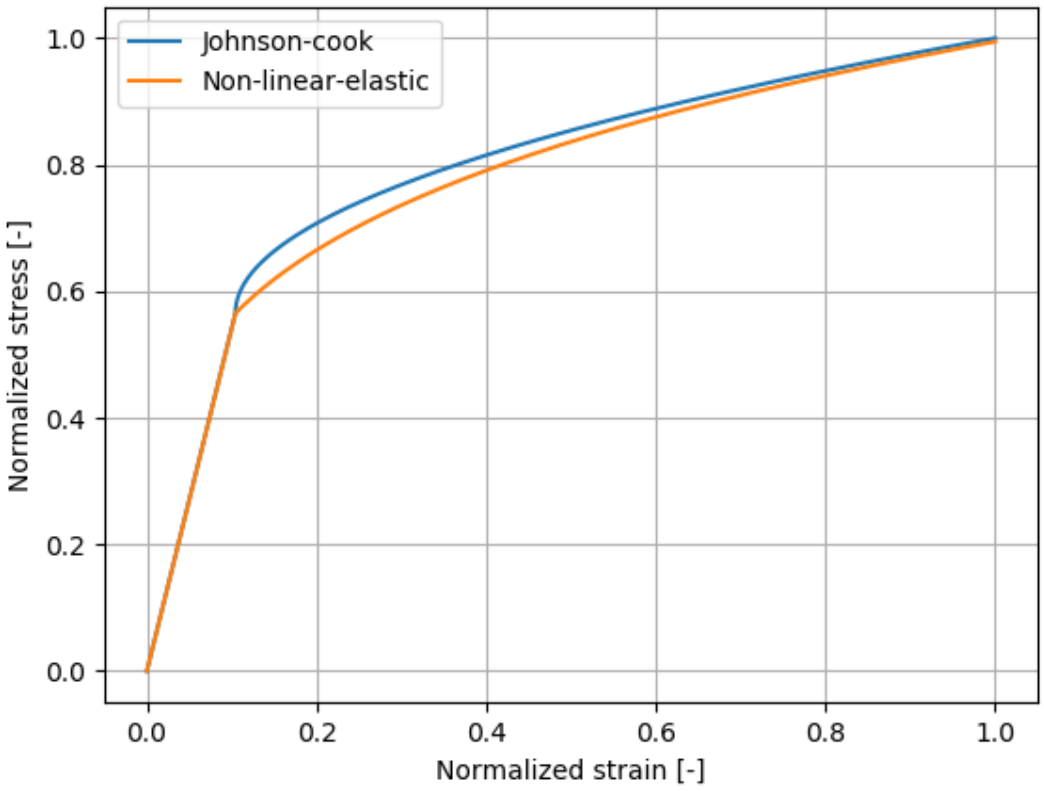

Figure C.1: Calibrated non-linear-elastic model compared to the Johnson-cook material model for a uniaxial tensile test.

It can be seen that both material models are in good agreement for monotonically increasing load in a tension test.

A typical mine blast load from the TNO mine blast model is applied to a plate modeled in LS-Dyna using Johnson-Cook material model. The same loading is applied using the author's FEM solver and the Non-linear elastic material model. The displacements are compared in Figure C.2.

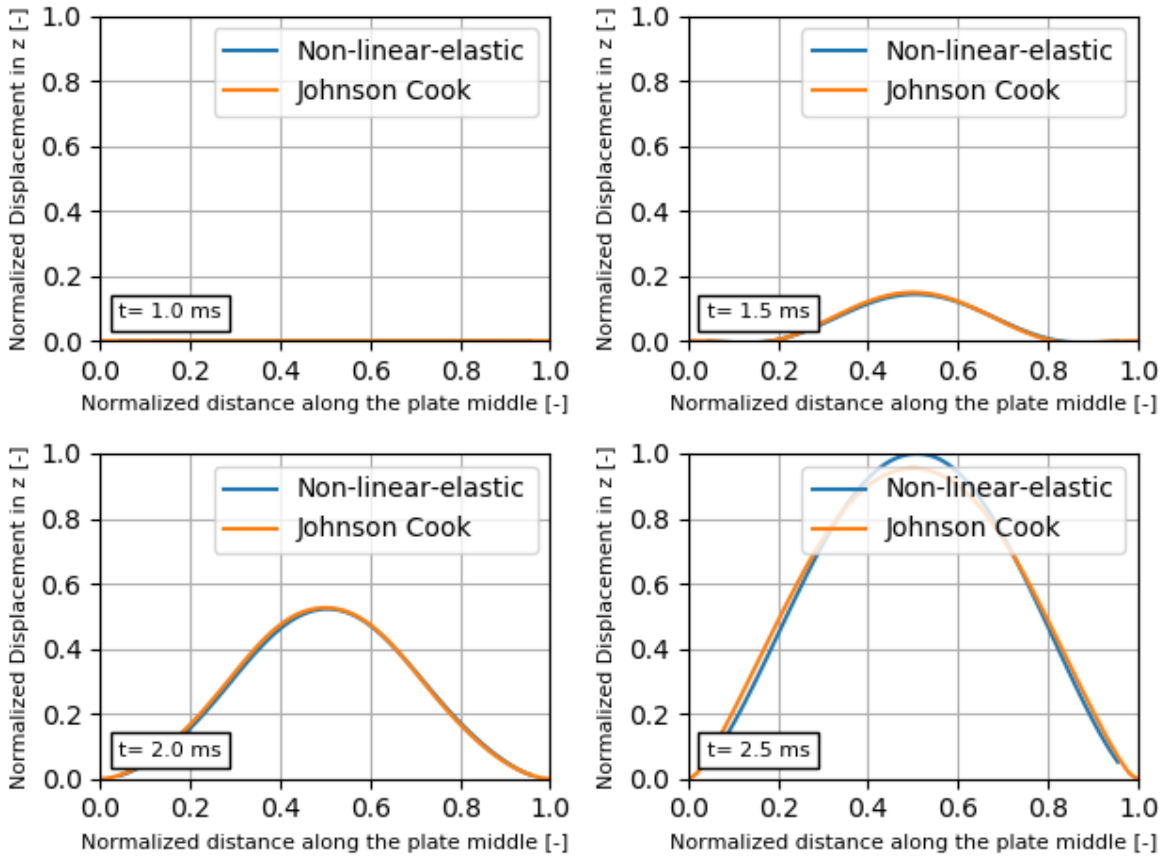

Figure C.2: The response for a mine blast loading for both the Johnson-Cook plasticity model and non-linear-elastic models are shown. It can be seen that for t<1.0ms the displacement is zero, this is due to the arrival time of the pressure loading. For t=1.5 ms and t=2.0 ms both models are in excellent agreement. For t=2.5ms the models slightly deviate however are still in good agreement

It can be seen that both models are in good agreement. This implies that for a mine blast loading, the loading of interest, the response of both models are in good agreement. This motivates the use of the non-linear-elastic material model. No further tests to verify the material model are done.

The Johnson-cook model with the input parameters used (these are confidential and not given) is calibrated by means of other tests that are outside the scope of the current research. Hence the Johnson-Cook model is expected to be the 'correct' forward model.

D

FEM implementation for the continuum

In this appendix the FEM implementation for the continuum problem discussed in Chapter 6 is explained. First the weak formulation will be derived. Secondly the the spatial discretization will be discussed where an 8-node isoparametric hexahedron element is chosen. Then three popular solver algorithms will be discussed which are required for time marching. For the explicit time marching scheme the semi-implicit Euler scheme is used for which the pseudo code is given. This chapter finalizes with a mesh convergence study.

D.1. Weak formulation

Both the adjoint and the forward problem, as derived in Chapter 6 see Table 6.1, can be written as

$$\rho \ddot{\boldsymbol{u}} - \nabla \cdot \boldsymbol{\sigma}(\nabla \boldsymbol{u}) = 0 \tag{D.1}$$

where '$\boldsymbol{u}$'and '$\boldsymbol{\sigma}$' are the displacement field and stress tensor respectively. The corresponding plate is clamped along the edges '$\partial\Omega_u$' that is

$$\boldsymbol{u}(\boldsymbol{x}) = 0 \ \forall \boldsymbol{x} \in \partial\Omega_u. \tag{D.2}$$

For the remaining of the boundary '$\partial\Omega_t$' the traction is prescribed as

$$\boldsymbol{t} = \boldsymbol{\sigma}\boldsymbol{n} = \boldsymbol{f}(\boldsymbol{x}) \ \forall \boldsymbol{x} \in \partial\Omega_t., \tag{D.3}$$

here '$\boldsymbol{n}$' is the unit normal vector and '$\boldsymbol{f}$' the prescribed load. The weak form of Equation D.1 is

$$\int_\Omega \left(\rho \ddot{\boldsymbol{u}} - \nabla \cdot \boldsymbol{\sigma}(\nabla \boldsymbol{u})\right) \cdot \boldsymbol{v} \mathrm{d}\Omega = 0 \forall \boldsymbol{v} \tag{D.4}$$

here the test function '$\boldsymbol{v}$' is zero on '$\partial\Omega_u$'. Integration by parts of the second term in Equation D.4 gives

$$\int_\Omega (\nabla \cdot \boldsymbol{\sigma}) \cdot \boldsymbol{v} \mathrm{d}\Omega = \int_\Omega (\boldsymbol{\sigma} \cdot \nabla \boldsymbol{v}) \, \mathrm{d}\Omega - \int_{\partial\Omega} \left(\boldsymbol{\sigma}^T \boldsymbol{v} \cdot \boldsymbol{n}\right) \mathrm{d}\partial\Omega = \int_\Omega (\boldsymbol{\sigma} \cdot \nabla \boldsymbol{v}) \, d\Omega - \int_{\partial\Omega} (\boldsymbol{t} \cdot \boldsymbol{v}) \, \mathrm{d}\partial\Omega = \int_\Omega (\boldsymbol{\sigma} \cdot \nabla \boldsymbol{v}) \, \mathrm{d}\Omega - \int_{\partial\Omega_t} (\boldsymbol{t} \cdot \boldsymbol{v}) \, \mathrm{d}\partial\Omega \tag{D.5}$$

here the last step uses the zero-condition for the test functions on the displacement constrained boundary. Substitution of D.5 back into D.4 gives

$$\int_\Omega \left(\rho \ddot{\boldsymbol{u}} \cdot \boldsymbol{v} + \boldsymbol{\sigma} \cdot \nabla \boldsymbol{v}\right) \mathrm{d}\Omega = \int_{\partial\Omega_t} \boldsymbol{t} \cdot \boldsymbol{v} \mathrm{d}\partial\Omega \forall \boldsymbol{v}. \tag{D.6}$$

D.2. Discretization

In the previous section the weak formulation is derived. In this section this formulation is discretized in order to derive the mass matrix, the internal force vector and the external force vector. First the displacement field is written as linear combination of shape functions

$$\boldsymbol{u} = u_i = \sum_{k=1}^{N} N_k a_{ki} \tag{D.7}$$

secondly the test functions are written in the same basis

$$\boldsymbol{v} = v_i = \sum_{r=1}^{N} N_r b_{ri} \tag{D.8}$$

where 'N_k' are the shape functions and 'a_{ki}' is the degrees of freedom vector. Substitution of D.8 into D.6, switching summation and integration sign and rearranging gives

$$\sum_{r=1}^{N} \left(\sum_{k=1}^{N} \left(\int_\Omega \rho N_k N_r \mathrm{d}\Omega \ddot{a}_{ki} \right) + \int_\Omega \boldsymbol{\sigma} \cdot \nabla N_r \mathrm{d}\Omega - \int_{\partial\Omega_t} \boldsymbol{t} \cdot N_r \mathrm{d}\partial\Omega \right) b_{ri} = 0 \forall b_{ri}. \tag{D.9}$$

This should hold for any test function '$\boldsymbol{v}$' hence for any 'b_{ri}' such that this can be rewritten to

$$M_{kr} a_{ki} + h_{ri}(a_{lj}) = f_{ri} \tag{D.10}$$

where the mass matrix is given by

$$M_{kr} = \int_\Omega \rho N_k N_r \mathrm{d}\Omega \tag{D.11}$$

the internal force vector is

$$h_{ri} = \int_\Omega \boldsymbol{\sigma}(a_{lj}) \cdot \nabla N_r \mathrm{d}\Omega \tag{D.12}$$

and the external force vector is

$$f_{ri} = \int_{\partial\Omega_t} t_i \cdot N_r \mathrm{d}\partial\Omega \tag{D.13}$$

D.3. Element and implementation

Previous section showed how the weak formulation is used to derive the discretized set of equations. No choice of shape functions was made, in this section the shape functions used are explained. A systematic approach is used such that the method can be applied to arbitrary geometry. First the advantage of localized shape functions will be explained. Then the isoparametric element will be defined. The implementation of the required volume and surface integrals will be explained next. Finally the chosen element, corresponding shape functions and node order will be shown.

D.3.1. Local supported shape functions

The derived discretized weak formulation contains integration of the shape functions over the complete domain. This is a computationally expensive step. To significantly reduce the cost of this step locally supported shape functions are used. Locally supported implies non-zero on only a small part of the complete domain this domain will be called the domain of the shape function given by

$$N_i = \begin{cases} \boldsymbol{x} \in \Omega_{N_i} & N_i(\boldsymbol{x}) \\ \boldsymbol{x} \notin \Omega_{N_i} & 0 \end{cases} \tag{D.14}$$

where N_i are the shape functions and Ω_{N_i} the domain of the corresponding shape function as sketched in D.1. Often the integral of a shape function is required. For a local supported shape function the domain of integration can be reduced such that

$$\int_\Omega N_i(\boldsymbol{x}) \mathrm{d}\Omega = \int_{\Omega_{N_i}} N_i(\boldsymbol{x}) \mathrm{d}\Omega. \tag{D.15}$$

This greatly reduces the computational cost involved with integrating the shape functions. Similar the inner product of two shape functions or their derivatives is required here the integration only needs to be done on the intersection of the domain such that

$$\int_{\Omega} N_i(\boldsymbol{x}) N_j(\boldsymbol{x}) \mathrm{d}\Omega = \int_{\Omega_{N_i} \cup \Omega_{N_j}} N_i(\boldsymbol{x}) N_j(\boldsymbol{x}) \mathrm{d}\Omega. \tag{D.16}$$

of the two shape functions as sketched in Figure D.1.

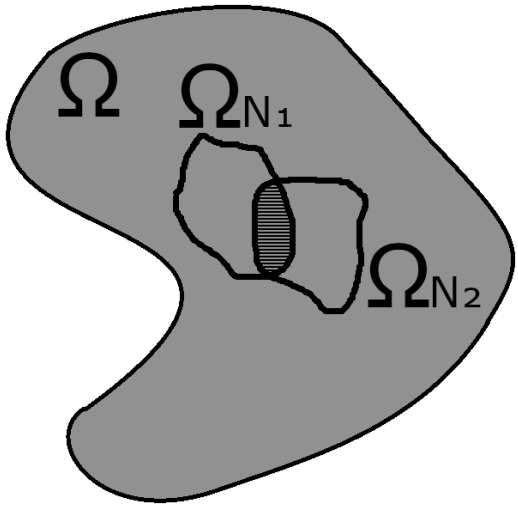

Figure D.1: The discretization uses shape functions which are local supported. The integral of a shape function and the inner product of two shape functions only needs to be calculated on the domain and intersection of the domains respectively.

A systematic way to discretize the computational domain is using local supported shape functions is by the creation of a mesh. The domain is divided into multiple elements as sketched in Figure D.2.

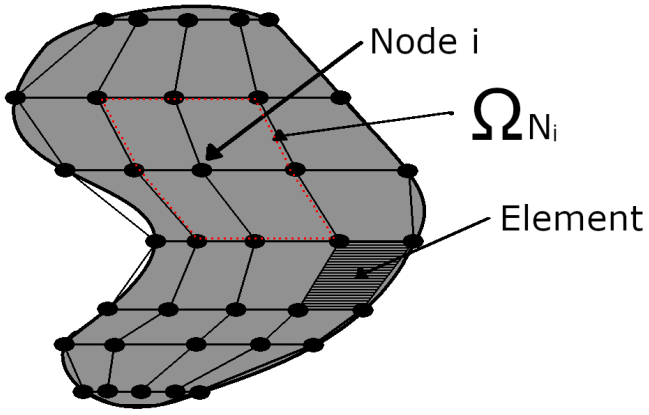

Figure D.2: The computational domain is divided in different non-overlapping elements. Each element contains nodes. Their exists a shape function Corresponding to each node. The domain of the shape function is the union of all adjacent elements.

The mesh contains elements and each element contains nodes. Corresponding each node there exists a shape function whose domain is the union of all adjacent elements. The shape functions are defined for each element in local coordinates. The use of a local coordinate system simplifies the integration and the definition of the shape functions since the shape of the domain is simple and the definition of the shape functions is w.r.t. the local coordinates.

D.3.2. Isoparametric element

The map from local to global coordinates of an element uses the same shape function as for the discretization of a field variable such elements are called 'isoparametric'. A sketch of the global and local definition is given in Figure D.3.

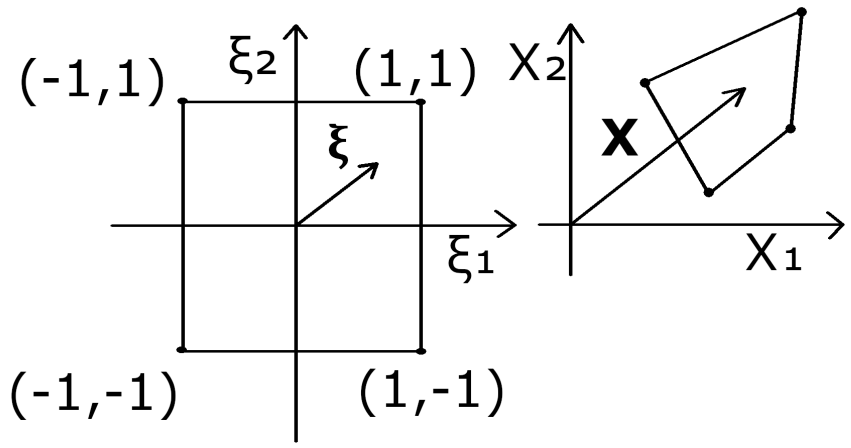

Figure D.3: Left shows the element in local coordinates. The simple shape of the element results in simple shape functions. Right shows a general element in global coordinate frame. A general element is required to discretize a general computational domain. Each coordinate in local coordinate frame $\boldsymbol{\xi}$ corresponds to a coordinate in global coordinate frame $\boldsymbol{x}$. Between both frames a map exists $\boldsymbol{x}(\boldsymbol{\xi})$

The map from the local to the global coordinate system is given by

$$\boldsymbol{x}(\boldsymbol{\xi}) = \boldsymbol{N}(\boldsymbol{\xi})^e_n \boldsymbol{x}_n \tag{D.17}$$

here $\boldsymbol{N}(\boldsymbol{\xi})^e_n$ are the shape functions corresponding to element 'e' on node 'n' and $\boldsymbol{x}_n$ are the global coordinates of the nodes. The same shape functions are used to interpolate a field variable (e.g. displacement) '$\boldsymbol{u}$' given by

$$\boldsymbol{u}^e(\boldsymbol{\xi}) = \boldsymbol{N}(\boldsymbol{\xi})^e_n \boldsymbol{u}_n \tag{D.18}$$

here $\boldsymbol{u}_n$ are the nodal displacements of element 'e' and $\boldsymbol{u}^e(\boldsymbol{\xi})$ is the corresponding continuous displacement field in local coordinates in element 'e'.

D.3.3. Integration

The Jacobi matrix for a 3D case is defined as

$$\boldsymbol{J} = \begin{bmatrix} \frac{\partial x_1}{\partial \xi_1} & \frac{\partial x_1}{\partial \xi_2} & \frac{\partial x_1}{\partial \xi_3} \\ \frac{\partial x_2}{\partial \xi_1} & \frac{\partial x_2}{\partial \xi_2} & \frac{\partial x_2}{\partial \xi_3} \\ \frac{\partial x_3}{\partial \xi_1} & \frac{\partial x_3}{\partial \xi_2} & \frac{\partial x_3}{\partial \xi_3} \end{bmatrix} \tag{D.19}$$

such that

$$\begin{bmatrix} \mathrm{d}x_1 \\ \mathrm{d}x_2 \\ \mathrm{d}x_3 \end{bmatrix} = \boldsymbol{J} \begin{bmatrix} \mathrm{d}\xi_1 \\ \mathrm{d}\xi_2 \\ \mathrm{d}\xi_3 \end{bmatrix}. \tag{D.20}$$

It can be proven that integration over the global domain is related to integration over the local domain such that

$$\int_{\Omega_{Global}} f(\boldsymbol{x}) d\Omega_{Global} = \int_{\Omega_{Local}} f(\boldsymbol{x}(\boldsymbol{\xi}))\, |\boldsymbol{J}|\, d\Omega_{Local}. \tag{D.21}$$

The Jacobi inside an element can be calculated from the nodal coordinates and shape function alone. This relation can be used to integrate the global integrals of the weak formulation Equations D.10, D.11, D.12 and D.13 in the local coordinate frame. The integration over a local element is approximated using Gaussian quadrature

$$\int_{\Omega_{Local}} f(\boldsymbol{\xi}) \mathrm{d}\Omega_{Local} = \sum_{i_1=1}^{N_1} \sum_{i_2=1}^{N_2} \sum_{i_3=1}^{N_3} w_{1_{i_1}} w_{2_{i_2}} w_{3_{i_3}} f(\boldsymbol{\xi}_{i_1,i_2,i_3}) \tag{D.22}$$

where $w_{1_{i_1}}$, $w_{2_{i_2}}$ and $w_{3_{i_3}}$ are the weights corresponding the three axes and $\boldsymbol{\xi}_{i_1,i_2,i_3}$ is the corresponding coordinate. Surface integrals are calculated in a similar manner. Analogous to the volume relation

$$\mathrm{d}\Omega_{Global} = \mathrm{d}x\mathrm{d}y\mathrm{d}z = |\boldsymbol{J}| \mathrm{d}\Omega_{Local} = |\boldsymbol{J}| \mathrm{d}\xi_1 \mathrm{d}\xi_2 \mathrm{d}\xi_3 \tag{D.23}$$

there exists an area relation as sketched in Figure D.4

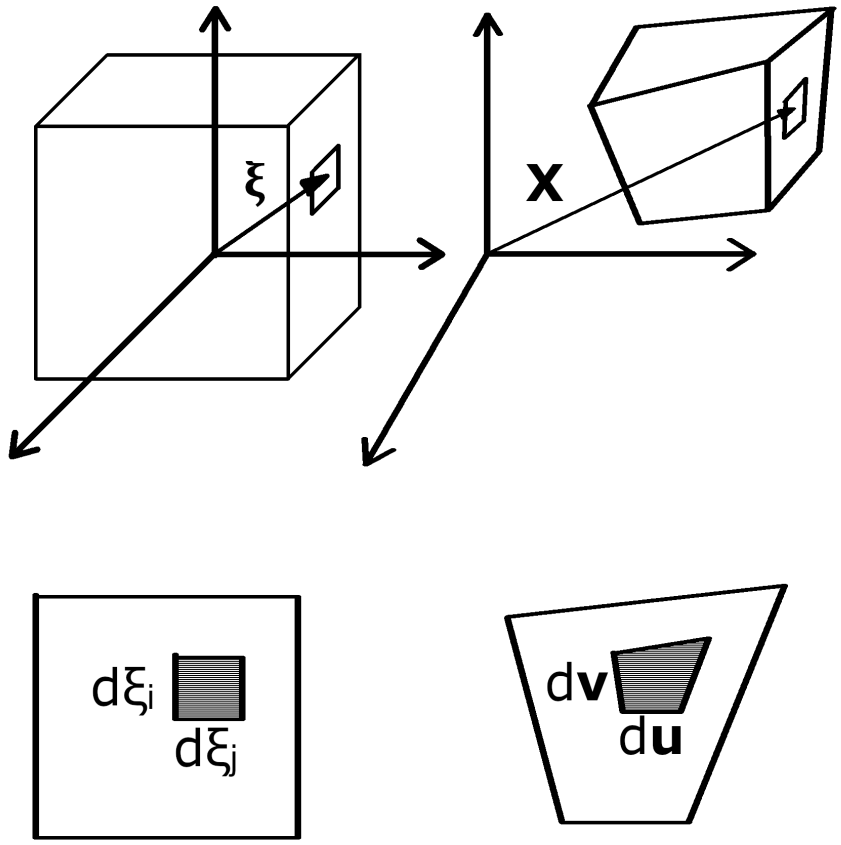

Figure D.4: The surface integration over the face of a general element relates to the surface integration over the face of an element in local coordinates. The advantage of the local coordinates is the simple square domain for the integration.

The integration over the surface of one element will correspond to constant value of one of the local coordinates. Without loss of generality taking $\mathrm{d}\xi_3 = 0$ the integration increments are done in ξ_1 and ξ_2 direction. A step in ξ_1 direction results in a step in the global coordinates of size $\mathrm{d}\boldsymbol{u}$ given by

$$\mathrm{d}\boldsymbol{u} = \begin{bmatrix} \frac{\partial x}{\partial \xi_1} \\ \frac{\partial y}{\partial \xi_1} \\ \frac{\partial z}{\partial \xi_1} \end{bmatrix} \mathrm{d}\xi_1 = \boldsymbol{a} \mathrm{d}\xi_1. \tag{D.24}$$

Similar a step in ξ_2 direction results in a step in global coordinates of size $d\boldsymbol{v}$ given by

$$\mathrm{d}\boldsymbol{v} = \begin{bmatrix} \frac{\partial x}{\partial \xi_2} \\ \frac{\partial y}{\partial \xi_2} \\ \frac{\partial z}{\partial \xi_2} \end{bmatrix} \mathrm{d}\xi_2 = \boldsymbol{b} \mathrm{d}\xi_2. \tag{D.25}$$

The incremental area in global coordinates is then given by

$$\mathrm{d}\partial\Omega_{Global} = |\mathrm{d}\boldsymbol{u} \times \mathrm{d}\boldsymbol{v}| = |\boldsymbol{a} \times \boldsymbol{b}|\,\mathrm{d}\xi_1\mathrm{d}\xi_2 \tag{D.26}$$

The relation between surface integration in local and global coordinates then becomes

$$\int_{\partial\Omega_{Global}} f(\boldsymbol{x})\mathrm{d}\partial\Omega_{Global} = \int_{\partial\Omega_{Local}} f(\boldsymbol{x}(\boldsymbol{\xi}))\,|\boldsymbol{a} \times \boldsymbol{b}|\,\mathrm{d}\partial\Omega_{Local}. \tag{D.27}$$

Similar as for the volume integration the integrals are evaluated in local coordinates using Gaussian quadrature

$$\int_{\partial\Omega_{Local}} f(\boldsymbol{x}(\boldsymbol{\xi}))\mathrm{d}\partial\Omega_{Local} = \sum_{i_1=1}^{N_1}\sum_{i_2=1}^{N_2} w_{1_{i_1}}\, w_{2_{i_2}}\, f(\boldsymbol{\xi}_{i_1,i_2}) \tag{D.28}$$

D.3.4. 8-node isoparametric hexahedron element

The spatial discretization of the FE implementation in this thesis follows the same approach as described in [23]. The geometry (Ω) is discretized using Hexahedron elements. In local coordinates the hexahedron element is shown in Figure D.5.

8-node hexahedron

$$N_1 = \tfrac{1}{8}(1-\xi)(1-\eta)(1-\zeta)$$
$$N_2 = \tfrac{1}{8}(1-\xi)(1-\eta)(1+\zeta)$$
$$N_3 = \tfrac{1}{8}(1+\xi)(1-\eta)(1+\zeta)$$
$$N_4 = \tfrac{1}{8}(1+\xi)(1-\eta)(1-\zeta)$$
$$N_5 = \tfrac{1}{8}(1-\xi)(1+\eta)(1-\zeta)$$
$$N_6 = \tfrac{1}{8}(1-\xi)(1+\eta)(1+\zeta)$$
$$N_7 = \tfrac{1}{8}(1+\xi)(1+\eta)(1+\zeta)$$
$$N_8 = \tfrac{1}{8}(1+\xi)(1+\eta)(1-\zeta)$$

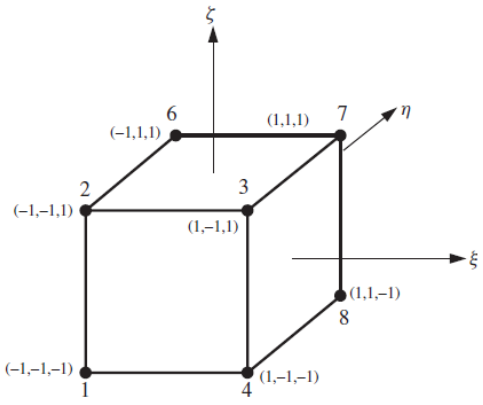

Figure D.5: 8-node Hexahedron element and shape functions from [23] is used in this thesis.

All meshes used in this thesis are created using LS-PrePost [29] which is a pre-and-post-processing tool for LS-Dyna FEM software. Figure D.6 shows four solid elements that can be used in LS-Dyna. It can be seen that the 8-node hexahedron has the same node numbering as the element showed earlier (element is rotated). Hence no changes to the LS-Dyna mesh need to be made when using the element formulation explained earlier (in Figure [23]).

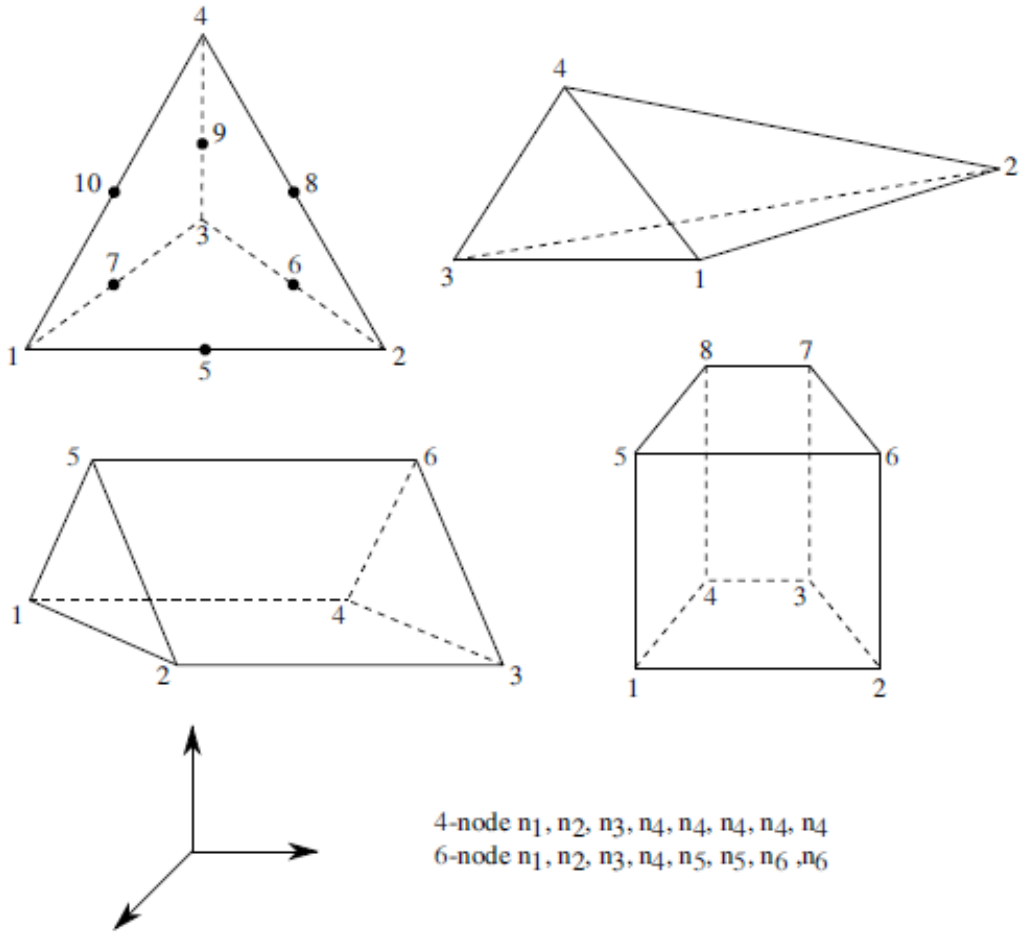

Figure D.6: Four elements used by LS-Dyna for solid modeling from [30]. The 8-node hexahedron element is used for all meshes in this thesis.

D.4. Solver

To determine the second derivative of the dof vector a linear system of equations has to be solved, that is

$$\boldsymbol{Ax} = \boldsymbol{b} \tag{D.29}$$

here the '$\boldsymbol{A}$' matrix is the mass matrix as seen in Section D.5. There are several efficient methods to solve such a system of equations. It is briefly explained why Lumped mass matrix and LU-decomposition methods often employed are not used. Then the iterative Gauss-Seidel method, used for the algorithm, is explained.

D.4.1. Lumped mass matrix

The mass matrix obtained from the weak formulation is called the consistent mass matrix, since it is consistent with the weak formulation. Often in FE-software, especially for explicit algorithms, the mass matrix is made lumped, that is diagonal. Such a matrix is not consistent with the weak formulation, however does yield very similar response. The inversion of such a matrix is trivial, hence such a lumped mass matrix can decrease the computational cost. Several methods to create a lumped mass matrix exist. Two popular methods are taking the row sum which ensures a consistent domain mass, given by

$$M_{\text{lumped}_{ii}} = \sum_{j=1}^{N} M_{ij}. \tag{D.30}$$

The second method is diagonal scaling given by

$$M_{\text{lumped}_{ii}} = cM_{ii} \tag{D.31}$$

where ‘c’ is the scaling factor. One scaling method is ensuring a consistent domain mass given by

$$\sum_{i=1}^{N} cM_{ii} = \sum_{i=1}^{N}\sum_{j=1}^{N} M_{ij},$$
$$c = \frac{\sum_{i=1}^{N}\sum_{j=1}^{N} M_{ij}}{\sum_{i=1}^{N} M_{ii}}. \tag{D.32}$$

A lumped mass matrix was used for all continuum simulations, the benefit is a much faster solver. The influence on the forward problem when using an inconsistent mass matrix (lumped) is studied in the ‘Mesh convergence’ section.

D.4.2. LU decomposition

LU decomposition of a matrix is computationally expensive. When the ‘L’ and ‘U’ matrices are obtained the solution of a system of equations can be directly evaluated in an efficient manner. via forward and backward substitution. Consider the LU decomposition of the matrix ‘$\boldsymbol{A}$’ in the system of Equations D.29

$$\boldsymbol{LUx} = \boldsymbol{b} \tag{D.33}$$

here ‘$\boldsymbol{U}$’ is an upper diagonal matrix and ‘$\boldsymbol{L}$’ is lower diagonal. First the system

$$\boldsymbol{Ly} = \boldsymbol{b} \tag{D.34}$$

is solved for ‘$\boldsymbol{y}$’ by direct forward substitution and then the system

$$\boldsymbol{Ux} = \boldsymbol{y} \tag{D.35}$$

is solved for ‘$\boldsymbol{x}$’ by backwards substitution. LU decomposition is often used since the forward and backward substitution can be done very fast. The problem with LU-decomposition is that the ‘$\boldsymbol{L}$’ and ‘$\boldsymbol{U}$’ matrixes are not necessarily sparse for a sparse matrix ‘$\boldsymbol{A}$’. Sparse LU-decomposition methods exists, however these are approximations of the actual system. To account for possible memory problems LU-decomposition was not used in the continuum problem. The KL-plate implementation used LU-decomposition.

D.4.3. Gauss-Seidel iteration

In Gauss-Seidel iteration the matrix ‘$\boldsymbol{A}$’ is split into the sum of a lower matrix ‘$\boldsymbol{L}$’ and strictly upper matrix ‘$\boldsymbol{U}$’ such that

$$L_{ij} = \begin{cases} A_{ij}, & i \geq j \\ 0, & \text{else} \end{cases} \tag{D.36}$$

$$U_{ij} = \begin{cases} A_{ij}, & i < j \\ 0, & \text{else} \end{cases} \tag{D.37}$$

$$A_{ij} = L_{ij} + U_{ij}. \tag{D.38}$$

Substitution of D.38 into D.29 gives

$$\boldsymbol{Lx} = \boldsymbol{b} - \boldsymbol{Ux}. \tag{D.39}$$

This equation is rewritten as iterative scheme for iteration ‘n’ by

$$\boldsymbol{Lx}^{n+1} = \boldsymbol{b} - \boldsymbol{Ux}^{n} \tag{D.40}$$

here the right hand side is known and the left hand side can be directly calculated by forward substitution. The use of Gauss-Seidel iteration offers several advantages;

- Can be implemented for sparse matrices and for that case will save computational costs. In that case the forward substitution scales linear with size.

- For the initial guess '$\boldsymbol{x}^0$' the previous time step can be used such that little iterations are required.
- Efficient for storage since the new vector '$\boldsymbol{x}^{n+1}$' can overwrite the old vector '$\boldsymbol{x}^n$' during the forward substitution because matrix '$\boldsymbol{U}$' is strictly upper diagonal
- Method is simple to implement.

The disadvantage of this algorithm is that it cannot be done in parallel. Since the size of the system is moderately small this is not a big problem. For developing of the algorithm Gauss-Seidel iteration was used, most importantly to show that lumped mass gives accurate results. Later lumped mass approach was adopted for speeding up the algorithm. It is realized that more efficient iterative methods exists however these were more difficult to implement and hence outside the current scope.

D.5. Time marching

For the current implementation a simple explicit time marching scheme was chosen. It is realized that more efficient methods exists however the study and implementation of such methods is outside the scope of this thesis. The pseudo Code for of the time marching scheme used for the continuum model is given below 2. Here the boundary condition of the clamped nodes are explicitly updated each time step.

Algorithm 2: Semi-implicit Euler time integration

n=0;
//set initial conditions
$\boldsymbol{v}_n = \boldsymbol{v}_0$;
$\boldsymbol{x}_n = \boldsymbol{x}_0$;
Δt = ...;
N = ...;

while n<N **do**
  $\boldsymbol{a}_n = \boldsymbol{M}^{-1}\left(\boldsymbol{f}_n - \boldsymbol{h}(\boldsymbol{x}_n)\right)$;
  $\boldsymbol{v}_{n+1} = \boldsymbol{v}_n + \boldsymbol{a}_n \Delta t$;
  $\boldsymbol{x}_{n+1} = \boldsymbol{x}_n + \boldsymbol{v}_{n+1} \Delta t$;
  $BC(\boldsymbol{x}_{n+1})$;
  n++;
end

void BC($\boldsymbol{x}$){
for *i in boundary nodes* **do**
  $\boldsymbol{x}$[i]=0;
end
}

D.6. Mesh convergence

This section shows the mesh convergence study for a continuum model of a plate. For the convergence study the 2d sine distributed load is used. The plate mesh is NxNxm elements where N are the longer dimensions and m are the number of elements through the thickness. First the convergence for N is studied using m=3 later it is proven that three elements through the thickness (m=3) is enough for accurately modeling the plate.

D.6.1. Discretization of the plate area

For the discretization of the longer dimensions of the plate (the plate area) a mesh of NxN is used. Mesh values of N={5, 10, 20, 40, 80, 160} are chosen. The Convergence study is done for both an exact solver and lumped mass approach. In Figure D.7 response of the plate plotted along the diagonal is shown using the exact solver and in Figure D.8 for the lumped mass approach. It can be seen that for N=80 the solution is converged for both the exact and lumped mass solver. In Figure D.9 several exact solver and lumped mass matrix results are compared in the same plot. It can be seen that lumped mass approaches the exact solver results for decreasing mesh size.

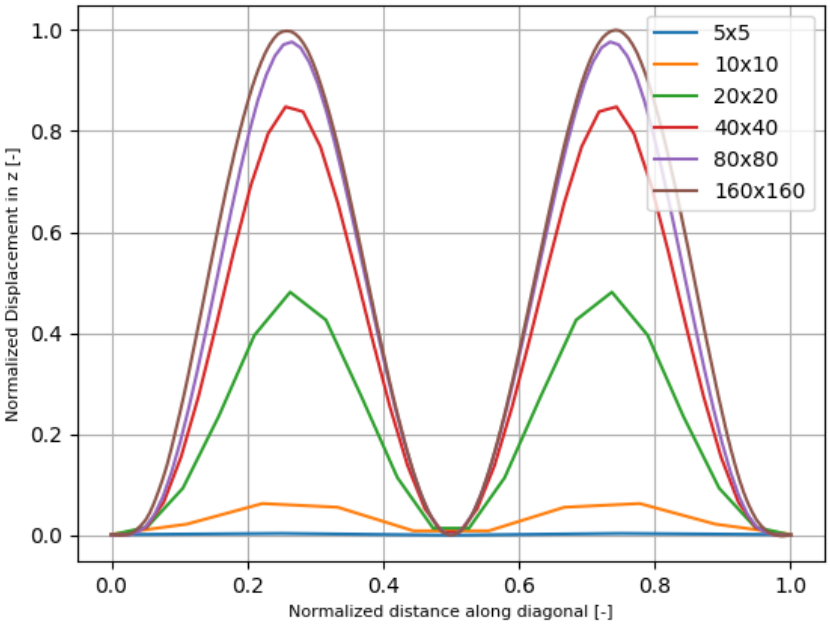

Figure D.7: Displacement of the plate plotted over the diagonal for different meshes using the exact solver. For N=80 the solution is close to N=160.

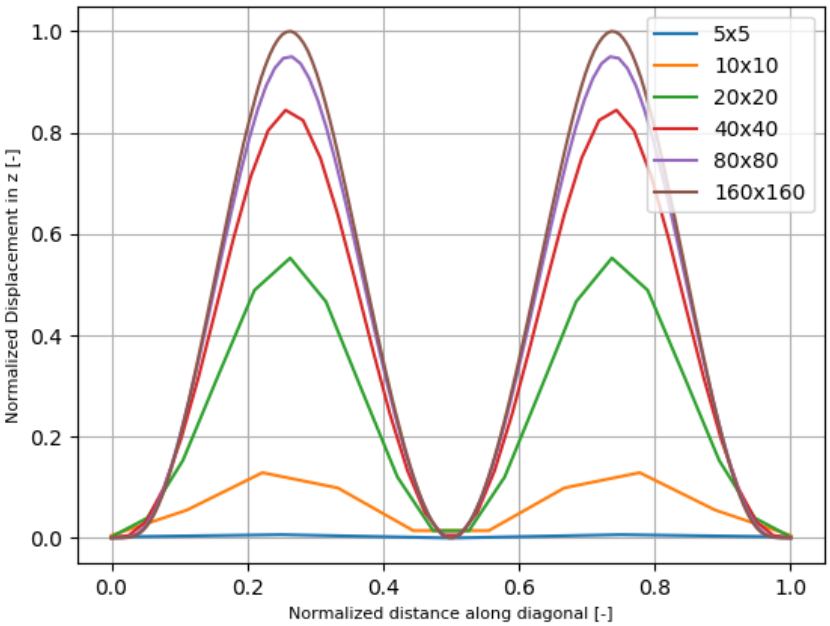

Figure D.8: Displacement of the plate plotted over the diagonal for different meshes using the lumped mass approach. For N=80 the solution is close to N=160.

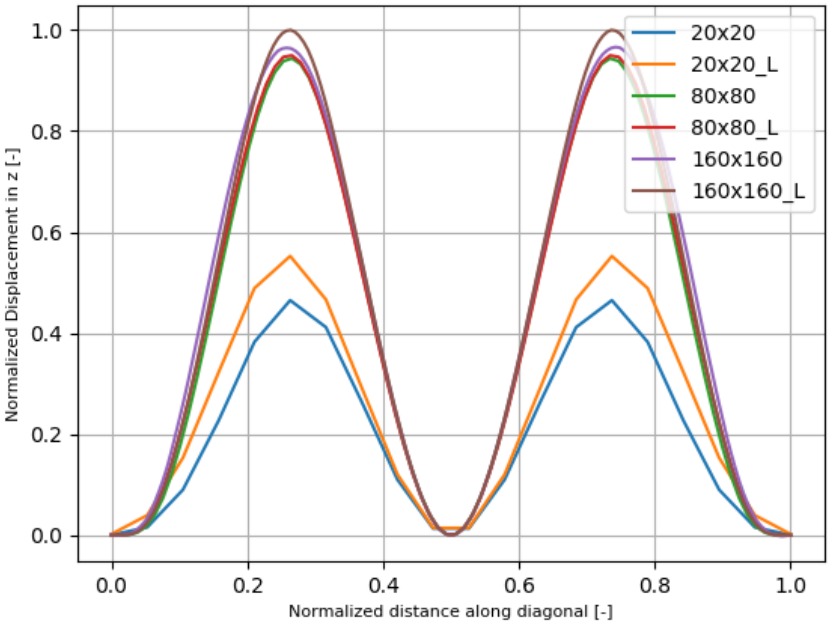

Figure D.9: Displacement of the plate plotted over the diagonal for different meshes comparing the exact solver and lumped mass approach. It can be seen that the exact solver and lumped mass approach converge to the same solution. For N=80 the lumped and exact are in very good agreement. It is however observed that for N=160 the match between lumped and exact is less, however still good.

D.6.2. Discretizations through thickness

Using the 80x80xm mesh the convergence for m is studied using m in $\{1,2,3,4\}$. In Figure D.10 it can be seen that the difference between m=3 and m=4 is small, for that reason m=3 used for the remaining simulations.

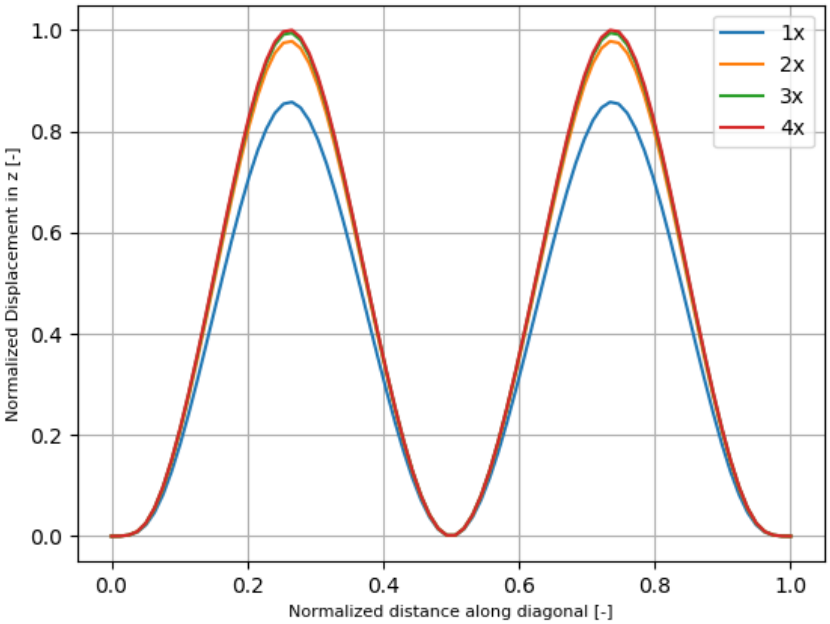

Figure D.10: Displacement of the plate plotted over the diagonal for different number of elements in thickness direction. It can be seen that less elements through the thickness results in a stiffer plate (less deformation). The results for 3 and 4 elements are almost identical hence 3 elements over the thickness will be used for all the simulations

D.6.3. Final Mesh

The mesh used for the continuum plate simulations is 80x80x3 as shown in Figures D.11, D.12 and D.13.

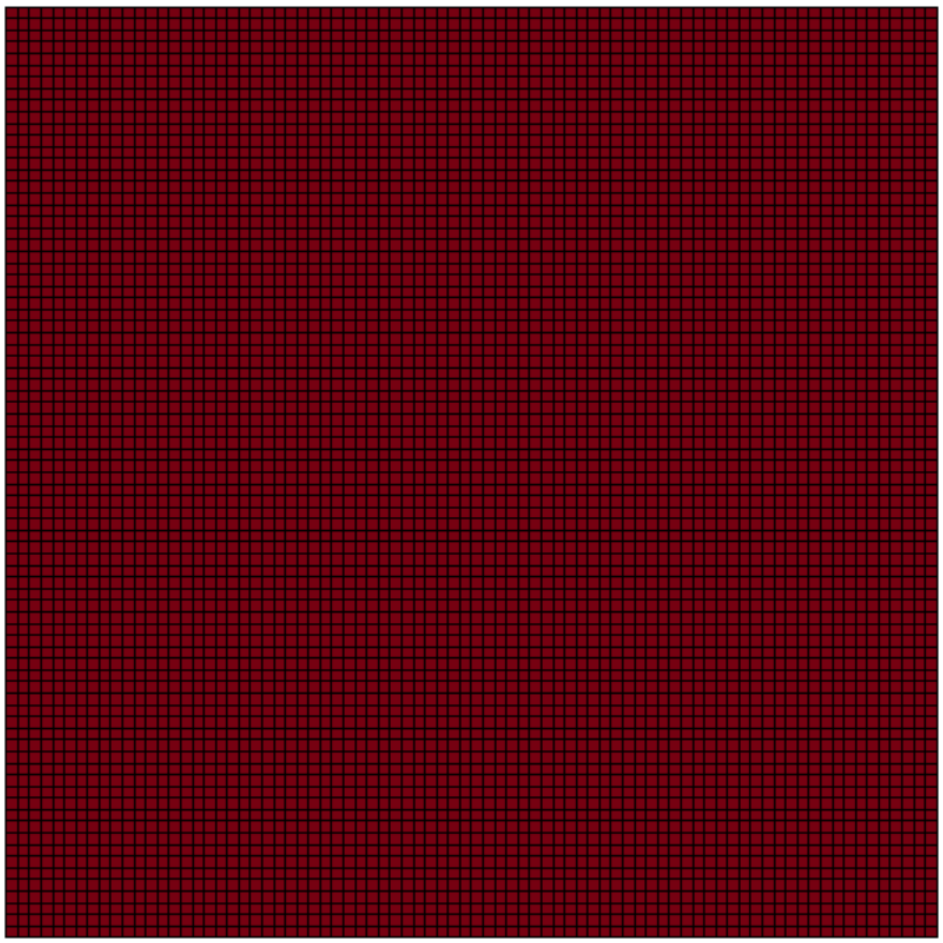

Figure D.11: Figure shows the top view of the mesh as visualized by LS-Prepost [29]. The mesh contains 80x80 elements over the plate area.

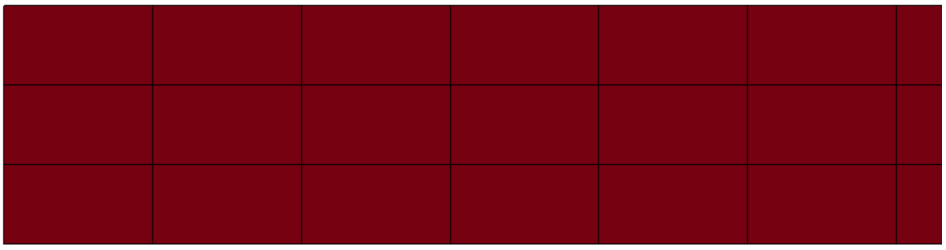

Figure D.12: Figure shows a small section of the side view of the mesh as visualized by LS-Prepost [29]. The aspect ratio is 1.875.

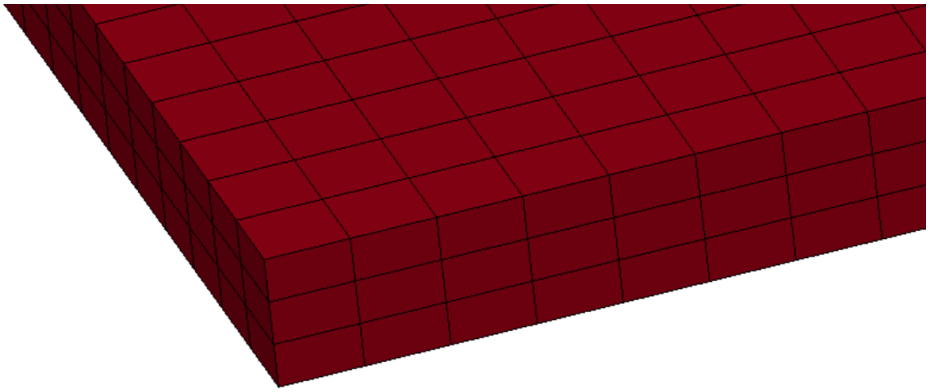

Figure D.13: Figure shows a zoomed in isoparametric view of the mesh as visualized by LS-Prepost [29].

E

Simplified pressure model

The current approach assumes no prior knowledge of any kind concerning the traction on the loaded surface of the continuum. Using prior knowledge one can constrain the traction, for example to be radial symmetric. In this appendix the variation of the error for a non-generic pressure model will be discussed. First starting with the variation derived earlier 6.28 and repeated here

$$\delta \tilde{J} = \int_0^T \int_{\partial\Omega_2} \delta t_i \phi_i \mathrm{d}\partial\Omega \mathrm{d}t. \tag{E.1}$$

The variation of the traction is the only part that will change for this discussion. the traction may for example be written similar to the 'localized smooth distribution' given by

$$t_3 = (h(t))^2 e^{-(x-r(t))^2 B(t)} \tag{E.2}$$

with the other components t_1 and t_2 are zero. This is a radial symmetric pressure distribution with a strictly positive pressure distribution peaking at a height of $\sqrt{h(t)}$, maximum value at r(t) and width controlled by function B(t). Such a model may be assumed generic enough to accurately describe mine blast models, yet significantly reduces the freedom since now only three time dependent functions need to be determined. The variation for this case is given by

$$\delta t_3 = \frac{\partial t_3}{\partial h}\delta h + \frac{\partial t_3}{\partial r}\delta r + \frac{\partial t_3}{\partial B}\delta B. \tag{E.3}$$

The derivative of J w.r.t h(t), r(t) and B(t) are then

$$\begin{aligned} \frac{\delta J}{\delta h} &= \phi_3 \frac{\partial t_3}{\partial h} \\ \frac{\delta J}{\delta r} &= \phi_3 \frac{\partial t_3}{\partial r} \\ \frac{\delta J}{\delta B} &= \phi_3 \frac{\partial t_3}{\partial B}. \end{aligned} \tag{E.4}$$

With these functional derivatives an optimization algorithm such as gradient of descent can be applied to solve for h(t), r(t) and B(t). in general one could construct a pressure model $\boldsymbol{t}(x,t;\boldsymbol{f}_1(x,t),\boldsymbol{f}_2(x,t),...\boldsymbol{f}_n(x,t))$ where $\boldsymbol{f}_1(x,t),\boldsymbol{f}_2(x,t),...\boldsymbol{f}_n(x,t)$ need to be determined. in such a case the derivatives are found by

$$\frac{\delta J}{\delta \boldsymbol{f}_i} = \boldsymbol{\phi} \cdot \frac{\partial \boldsymbol{t}}{\partial \boldsymbol{f}_i}. \tag{E.5}$$

One could parameterize functions $\boldsymbol{f}_i$ using coefficients a_{ij} to obtain the gradient $\frac{\partial J}{\partial a_{ij}}$. Ofcourse when the number of coefficients is small one could simpy use finite difference to estimate $\frac{\partial J}{\partial a_{ij}}$. The above described approach is not applied in this thesis however is recommended for future research in an effort stabilize the inverse problem.

F

Gradient descent

Gradient of descent optimization algorithm is used in this thesis. It is based on the idea that the steepest descent direction is parallel to the gradient direction, hence also named steepest descent method. This important property is however not proven yet. This appendix will provide such a proof for the discrete case.

The problem

The directional derivative of a function $J(x_1, x_2, ...x_n)$ in direction $\boldsymbol{u}$ is given by

$$D_{\boldsymbol{u}} J = \nabla J \cdot \boldsymbol{u}. \tag{F.1}$$

The linearization of $J(x_1, x_2, ...x_n)$ at point $x_1, x_2, ...x_n$ is then

$$\hat{J}(\boldsymbol{x} + \boldsymbol{u}) = J(\boldsymbol{x}) + \nabla J \cdot \boldsymbol{u}. \tag{F.2}$$

We want to find the vector $\boldsymbol{v}$ such that

$$\hat{J}(\boldsymbol{x} + \boldsymbol{v}) \leq \hat{J}(\boldsymbol{x} + \boldsymbol{u}) \;\; \forall \boldsymbol{u}, \boldsymbol{v} \in U = \{\boldsymbol{r} : |\boldsymbol{r}| = 1\}. \tag{F.3}$$

Using Lagrange multipliers we may write the auxiliary Lagrangian to be minimized as

$$L(\boldsymbol{u}, \lambda) = J(\boldsymbol{x}) + \nabla J \cdot \boldsymbol{u} - \lambda(|\boldsymbol{u}| - 1) \tag{F.4}$$

In order to be at a critical point the following relations have to be satisfied:

$$\begin{aligned} \frac{\partial L}{\partial \boldsymbol{u}} &= 0 \\ \frac{\partial L}{\partial \lambda} &= 0. \end{aligned} \tag{F.5}$$

The first relation in F.5 gives

$$\nabla J = \lambda \frac{\boldsymbol{u}}{|\boldsymbol{u}|}. \tag{F.6}$$

The second relation in F.5 gives

$$|\boldsymbol{u}| = 1. \tag{F.7}$$

Hence the unit vector in steepest descent direction is parallel to the gradient. it is important to note that if the relation $\boldsymbol{u} = \nabla J$ is substituted into the linearization of 'J' the function increases. Hence steepest descent for minimization problems is in opposite direction of the gradient.

G

Direct solution of the inverse problem

This appendix demonstrates, for a static beam, that the direct solution of the inverse problems is unstable. It shows that the 'real' optimum of the problem will fit the noise of the measurement data too much causing large pressure fluctuations. The effect of regularization on pressure is shown. Finally it is shown that including a discontinuity in the regularized solution can greatly increase the accuracy.

G.1. Direct solution

The Euler Bernouli beam model is given by

$$EI\frac{\mathrm{d}^4 w}{\mathrm{d}x^4}(x) = q(x) \tag{G.1}$$

were w(x) is the out of plane displacement, q(x) is the distributed load and EI the bending stiffness of the beam. Instead of solving this model exactly the ODE is discredited using finite difference scheme to obtain

$$\boldsymbol{K}\boldsymbol{u} = \boldsymbol{p} \tag{G.2}$$

here $\boldsymbol{K}$, $\boldsymbol{u}$ and $\boldsymbol{p}$ are the stiffness matrix nodal displacement and nodal force respectively. For a measured DIC displacement the nodal displacement can be calculated or interpolated to obtain the nodal displacement '$\boldsymbol{u}$'. The nodal force can then directly be computed using Equation G.2. A benchmark pressure distribution and displacement is shown in Figure G.1 here the beam is clamped at both ends.

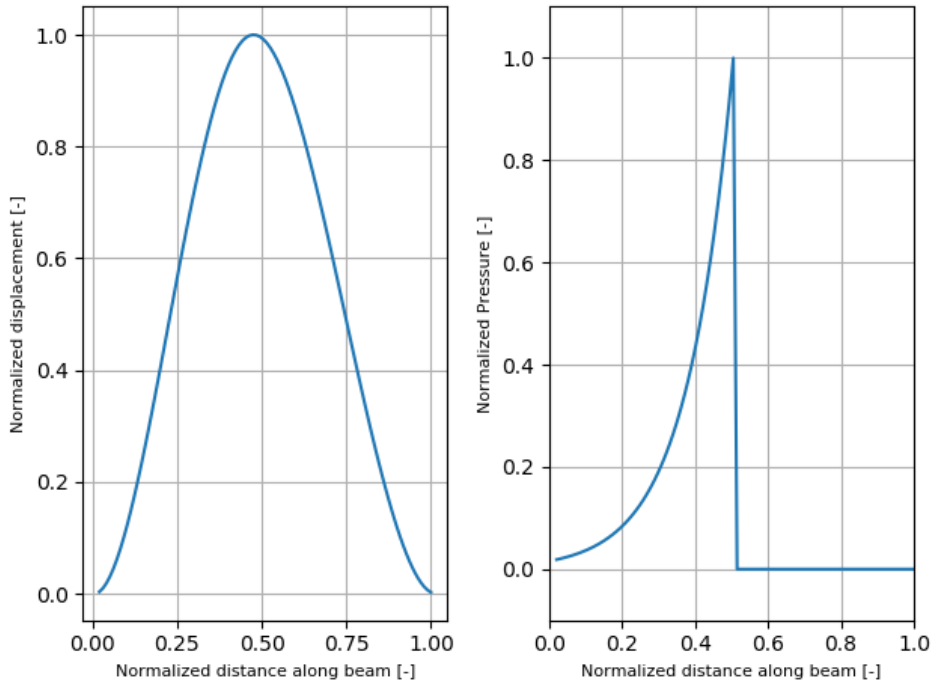

Figure G.1: Left the normalized displacement of a beam and right the normalized distributed load.

Adding 0.1% noise $\boldsymbol{\eta}$ to the nodal displacement $\boldsymbol{u}$ gives

$$\boldsymbol{u}_{\text{DIC}} = \boldsymbol{u} + \boldsymbol{\eta}. \tag{G.3}$$

This new nodal displacement vector $\boldsymbol{u}_{\text{DIC}}$ representing measurement data is used to calculate the distributed load using Equation G.2. In Figure G.2 the results are shown. The noise level applied is small such that both displacement curves are almost the same however the difference in distributed load is huge. The direct solution fits a beam displacement through each measurement point for which an oscillating distributed load with large amplitude is required. This method results in a direct solution for the distributed load that is a couple of orders of magnitude off.

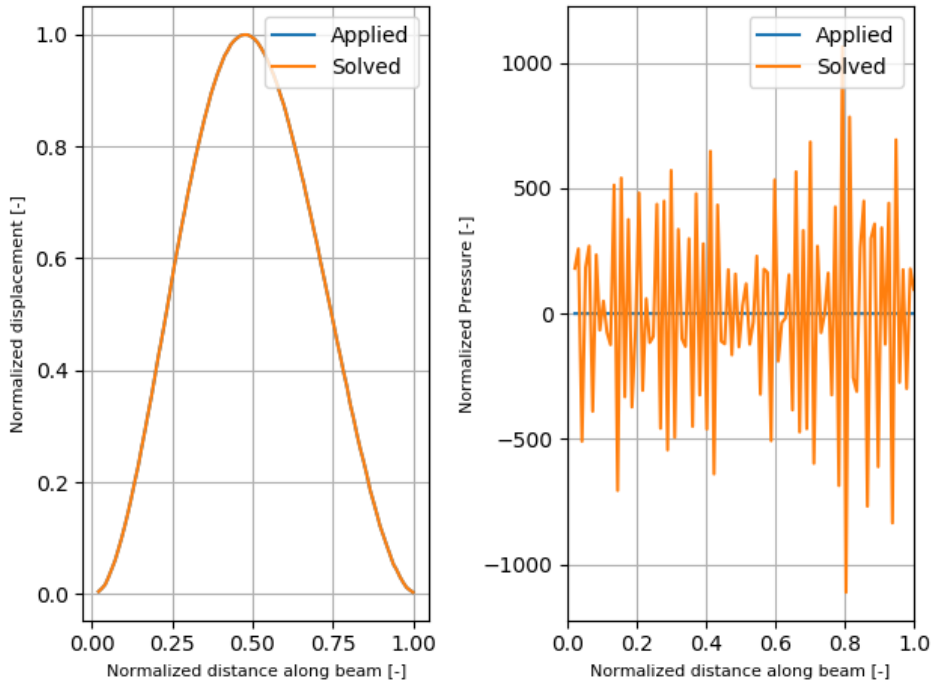

Figure G.2: Left the displacement of the forward model and the corresponding simulated measurement data. Right plot shows the direct solution, which has large oscillations in order to fit the noise in the displacement data exactly.

G.2. Regularization

The direct solution discussed in previous section is the exact solution of the functional

$$J[\boldsymbol{p}] = \left|\boldsymbol{K}^{-1}\boldsymbol{p} - \boldsymbol{u}_{\text{DIC}}\right|^2. \tag{G.4}$$

It was observed that the direct solution fits the measurement data exactly such that J=0 for which a high frequency oscillating pressure with large amplitude is required. This pressure does not match the actually applied pressure. It is a priori known that the pressure does not contain such oscillations. In that case regularization can be used, changing the problem slightly by penalizing unwanted characteristics of the pressure in functional J. In this case one could penalize non-smooth distributed load by adding

$$J_{\text{reg}}[q] = \alpha \int_0^L \left(\frac{\mathrm{d}^2 q}{\mathrm{d}x^2}\right)^2 \mathrm{d}x \tag{G.5}$$

to the objective functional J which penalized the presence of large curvature. In discrete form this given by

$$J_{\text{reg}}[\boldsymbol{p}] = \alpha \left|\boldsymbol{D}\boldsymbol{p}\right|^2 \tag{G.6}$$

such that the new objective function becomes

$$J[\boldsymbol{p}] = \left|\boldsymbol{K}^{-1}\boldsymbol{p} - \boldsymbol{u}_{\text{DIC}}\right|^2 + \alpha \left|\boldsymbol{D}\boldsymbol{p}\right|^2 \tag{G.7}$$

were $\boldsymbol{D}$ is the regularization matrix. More general regularization can be written as

$$J[\boldsymbol{p}] = \left|\boldsymbol{K}^{-1}\boldsymbol{p} - \boldsymbol{u}_{\text{DIC}}\right|^2 + \left|\boldsymbol{\Gamma}\boldsymbol{p}\right|^2 \tag{G.8}$$

were $\boldsymbol{\Gamma}$ is known as the Tikhonov matrix. This method of regularization (Tikhonov regularization) has the exact solution

$$\boldsymbol{p} = (\boldsymbol{K}^{-T}\boldsymbol{K}^{-1} + \boldsymbol{\Gamma}^T\boldsymbol{\Gamma})^{-1}\boldsymbol{K}^{-T}\boldsymbol{u}_{\text{DIC}} \tag{G.9}$$

The results for regularization on slope in accordance with Equation G.10 for increasing values of α are given in Figures G.3, G.4, G.5, G.6.

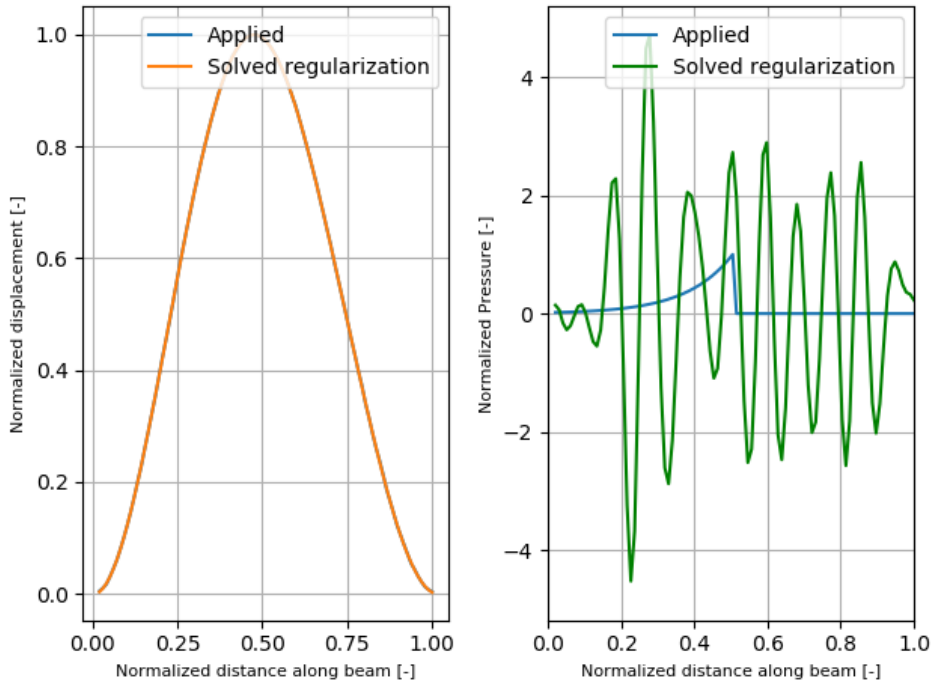

Figure G.3: It can be seen that with little regularization (small value for α) the oscillations are greatly reduced. The oscillations are still present however the amplitude of the pressure signal is now of the same order as the actually applied one

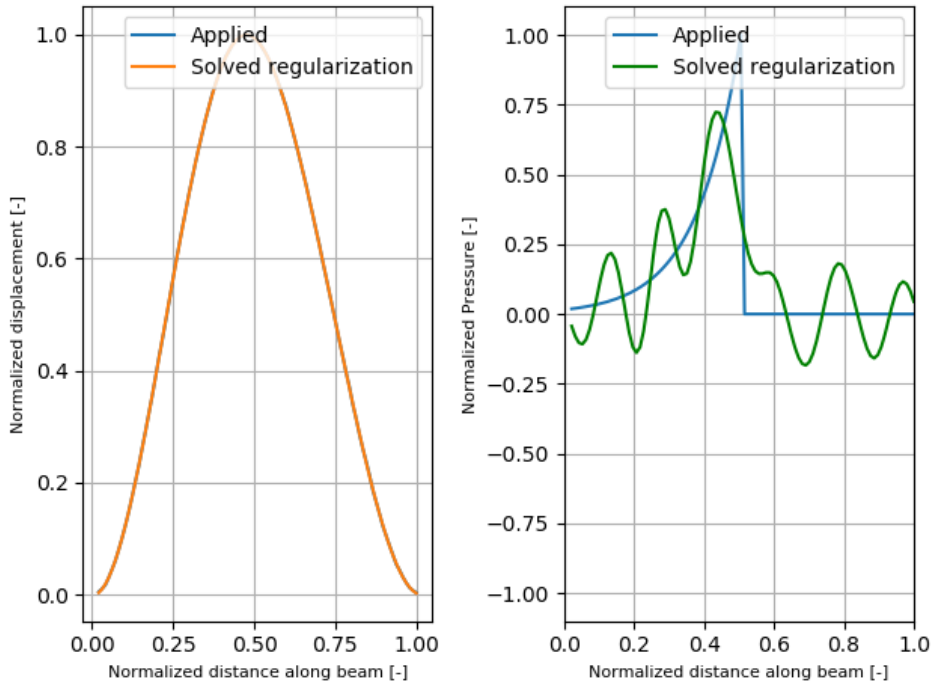

Figure G.4: Increasing the amount of regularization (medium value of α) shows a reduction in oscillations and the signal starts to better match the applied one.

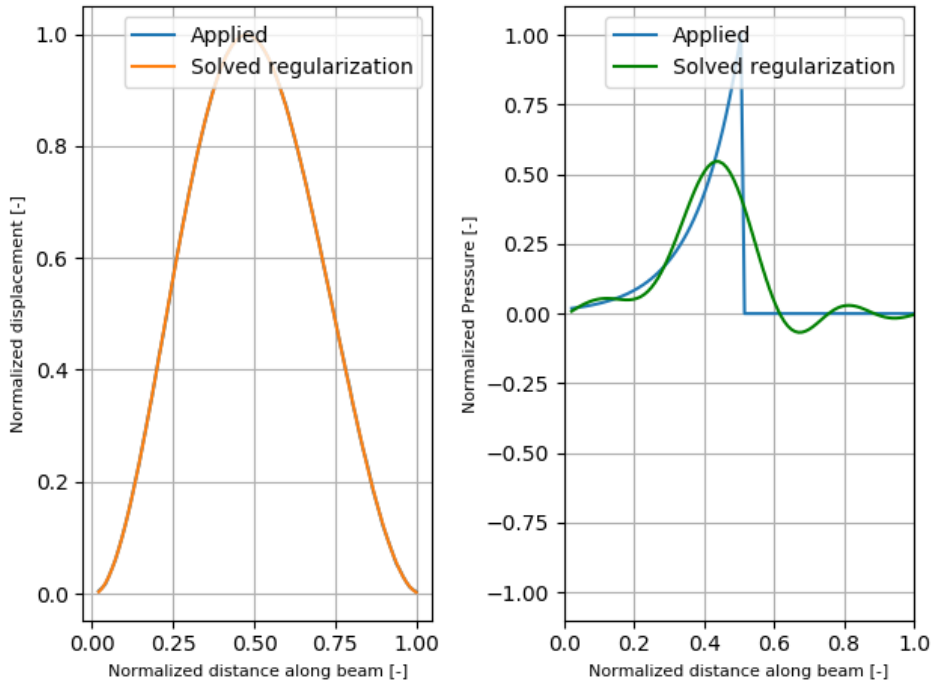

Figure G.5: Here enough regularization is used such that almost all oscillations are removed from the distributed load.

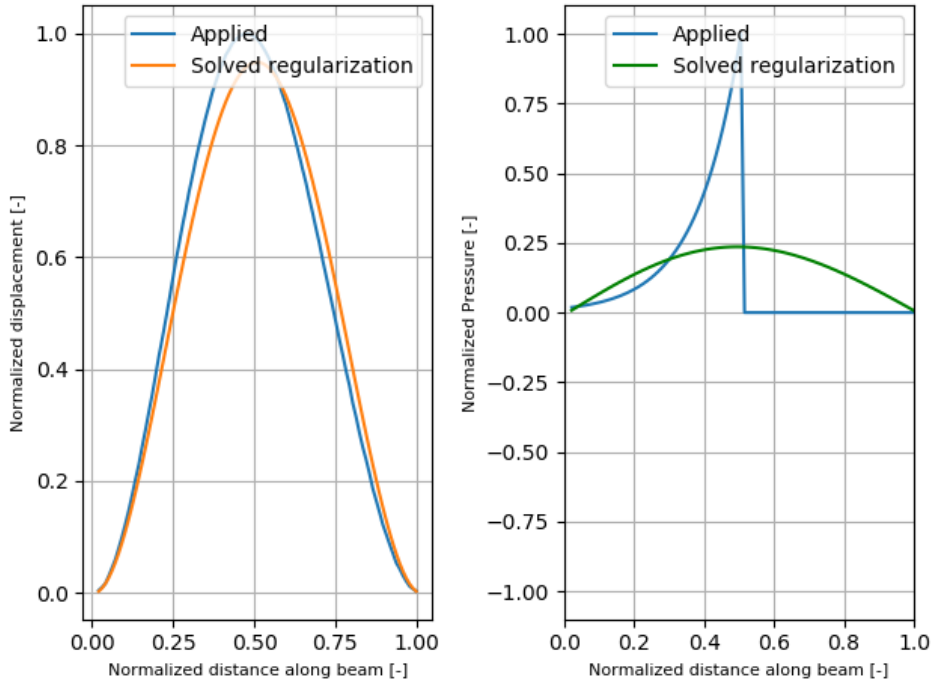

Figure G.6: Increasing the amount of regularization to much will result in a highly smoothed distributed load. This results in a less accurate displacement and therefore incorrect distributed load.

from the results in Figures G.3, G.4, G.5, G.6 it is clear that regularization stabilizes the inverse problem. Furthermore when little regularization is used the the displacements remain an accurate match. Too much regularization will shift the solution to enforce smoothness more then the actual displacement. When regularization is used one has to determine the amount used as function of the noise.

G.3. Regularization including a discontinuity

from the results in Figures G.3, G.4, G.5, G.6 it is clear that regularization stabilizes the inverse problem. Furthermore when little regularization is used the the displacements remain an accurate match. Too much regularization will shift the solution to enforce smoothness more then the actual displacement. When regularization is used one has to determine the amount used as function of the noise. The benchmark pressure contains a discontinuity which contradicts the smoothness requirement to be satisfied. For that reason non of the regularized solved distributed loads matches the applied load. Allowing one discontinuity in the distributed load can result in a much better match. One way to allow for such a discontinuity is by modifying the regularization term

$$J_{\text{reg}}[q] = \alpha \int_0^{x_0 - \frac{\delta}{2}} \left(\frac{\mathrm{d}^2 q}{\mathrm{d}x^2} \right)^2 \mathrm{d}x + \alpha \int_{x_0 + \frac{\delta}{2}}^{L} \left(\frac{\mathrm{d}^2 q}{\mathrm{d}x^2} \right)^2 \mathrm{d}x \tag{G.10}$$

here x_0 is the location where the discontinuity is allowed and δ is the size of the unregularized distributed load section. For the discrete case this can be implemented by setting some row vectors in the '$\boldsymbol{d}$' matrix to zero at the location corresponding to '$\boldsymbol{x}_0$'. The amount of rows to be removed depends on the discretization used, the aim is to decouple the the regularization matrix in two smaller independent regularization matrices given by

$$\boldsymbol{D} = \begin{bmatrix} \boldsymbol{D}_1 & \boldsymbol{0} \\ \boldsymbol{0} & \boldsymbol{D}_2 \end{bmatrix}. \tag{G.11}$$

For the correct value of '$\boldsymbol{x}_0$' the solution is given in Figure G.7.

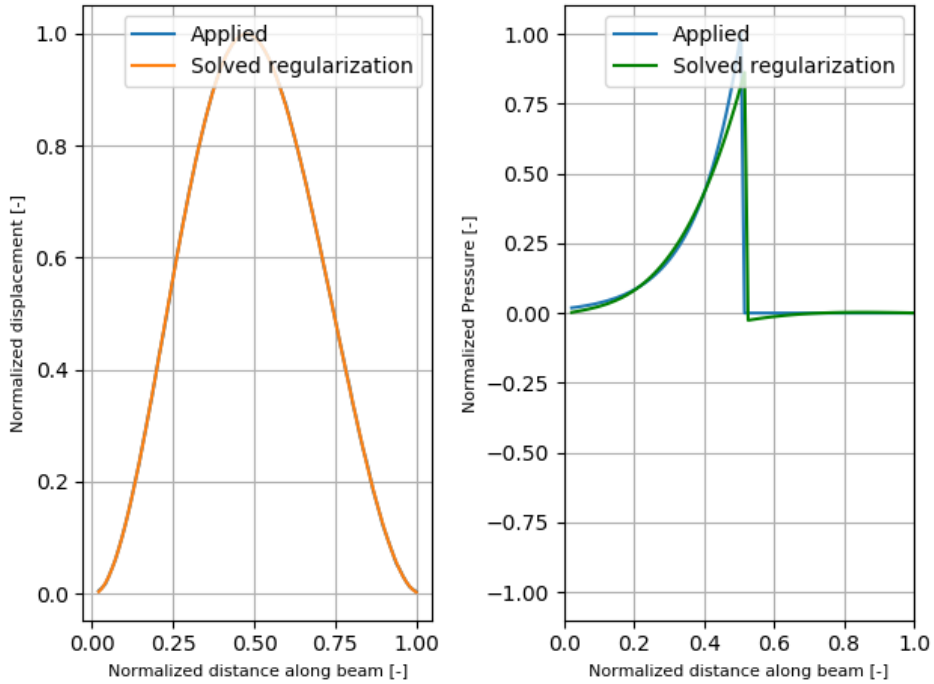

Figure G.7: Regularization on distributed load allowing for one discontinuety at the correct location results is very accurate distributed load obtained by the direct solution.

When the location of the discontinuity is incorrect the spectacular increase in accuracy is not possible as shown in Figure G.8

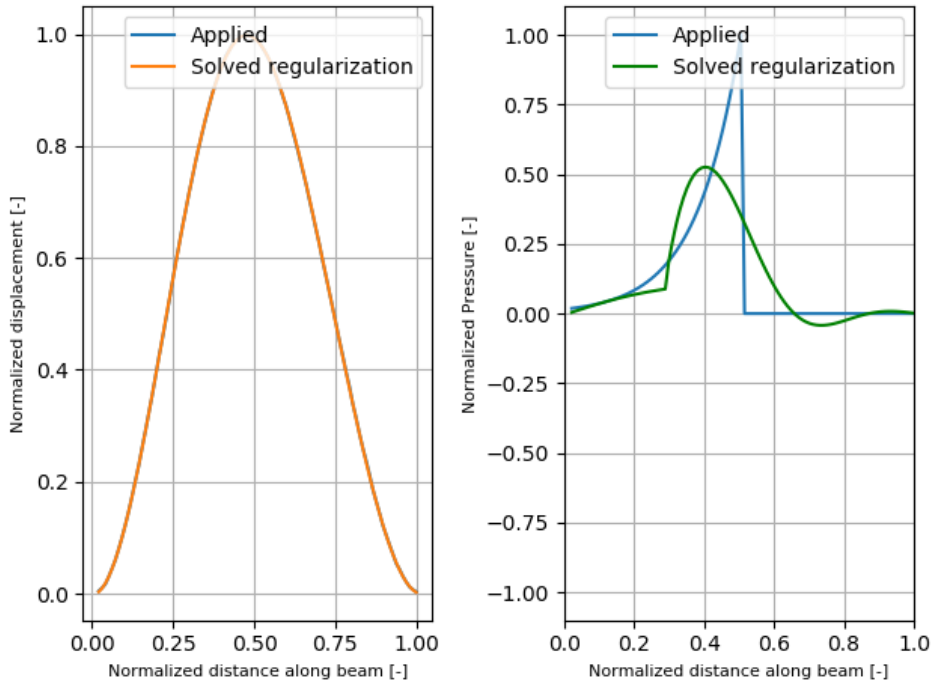

Figure G.8: Regularization on distributed load allowing for one discontinuety at an incorrect location does not result in much better accuracy in distributed load obtained by the direct solution.

In order to accurately capture distributed loads that contain a discontinuity it is clear that the new variable '$\boldsymbol{x}_0$' has to be known. This variable could be solved iterative however that greatly increases the computational cost. For indirect methods the aim is to minimize the objective function in an iterative way hence the extra variable is not expected to increase the computational cost by much.

It was illustrated that the sensitivity to noise becomes less when more regularization is used. To much regularization will result in inaccurate solved displacement. When the signal is expected to be relatively smooth except for one discontinuity, such as the benchmark problem, then large amount of regularization can be used. In Figure G.10 the results for large amount of noise and large amount of regularization are shown. The accuracy of the solved distributed load is remarkable however a direct result of the regularization used. For the same noise and discontinuity location using less regularization results in completely incorrect distributed load which per definition fits the data better (less regularization hence more focus on fitting the data).

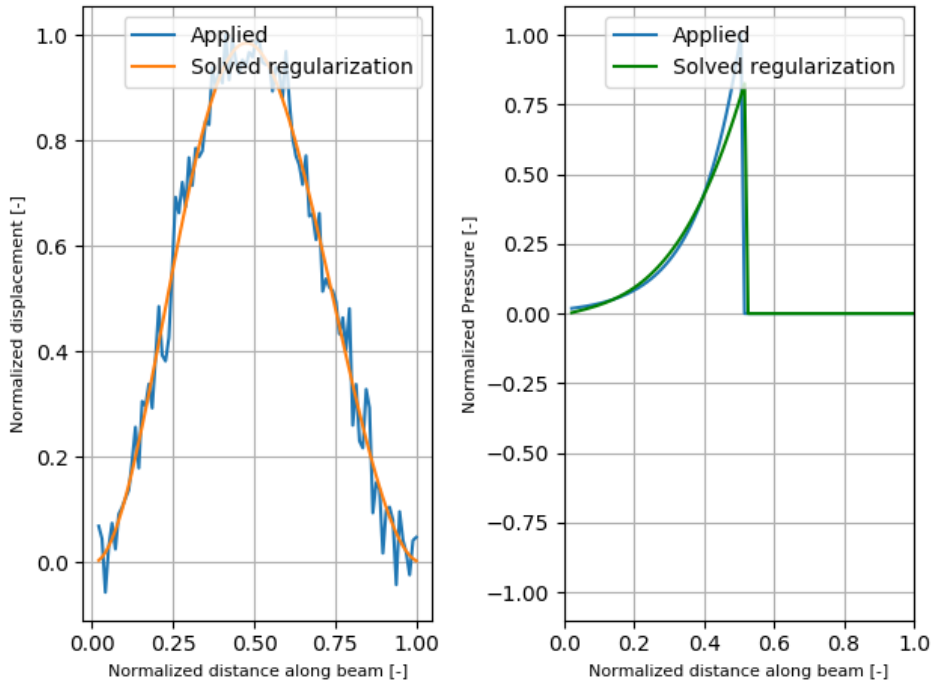

Figure G.9: Applied displacement that contains large amount of noise and large amount of regularization on distributed load allowing for one discontinuity at the correct location. The solved distributed load very accurate.

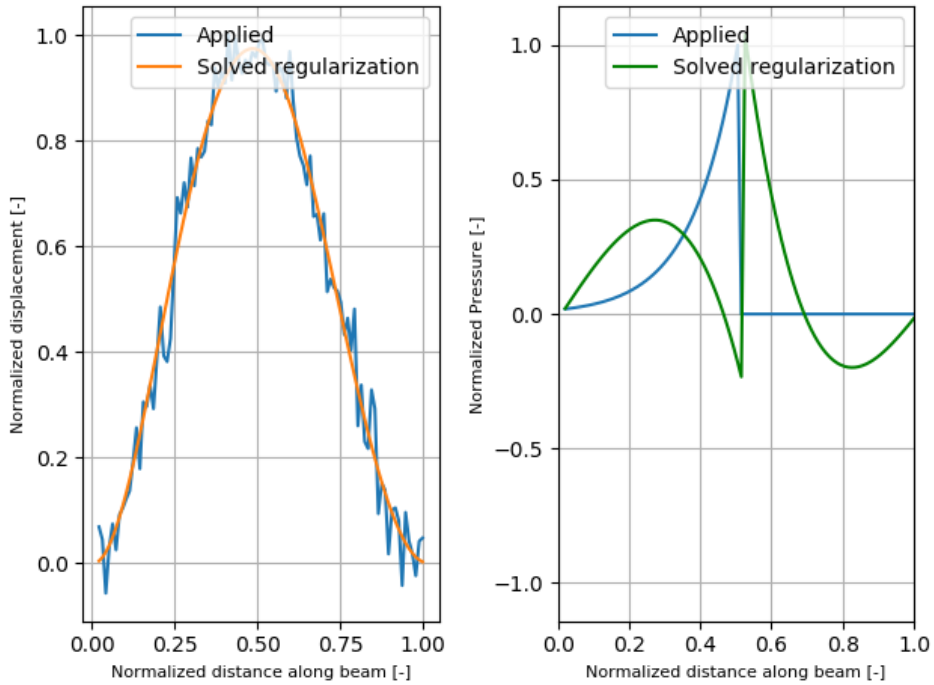

Figure G.10: Applied displacement that contains large amount of noise and allowing for one discontinuity at the correct location. Less regularization on distributed load as compared to Figure G.10 is used. The solved distributed load very inaccurate.

G.4. Landweber regularization

Previous sections discussed the direct or exact solution that minimizes the objective function. Often iterative methods are used to obtain approximate the solution that minimizes the objective function. Gradient of decent the iterative method used in this report. Gradient of decent algorithm is the same as landweber iteration when solving a linear system of equations. It is known that landweber iteration has regularization properties. Where the exact solution would be noisy the iterative solution obtained is often smooth. Landweber iteration is stopped and assumed converged when the error is similar to the noise level (convergence critera). In this report is was shown that the gradient of the objective function is a solution of a PDE similar as the forward problem. The solution of such a problem is known to be smooth. Solutions of gradient of decent algorithms are thus the sum of smooth solutions, hence the final solution is expected to be smooth. This explains the regularization properties of Landweber iteration or gradient of decent algorithms.

G.5. Direct solution dynamic problem

The discretized dynamic model of both a beam and a plate can be written as

$$\boldsymbol{M}\ddot{\boldsymbol{u}} + \boldsymbol{K}\boldsymbol{u} = \boldsymbol{f} \tag{G.12}$$

where $\boldsymbol{M}$, $\ddot{\boldsymbol{u}}$, $\boldsymbol{K}$ and $\boldsymbol{f}$ are the mass matrix, the nodal displacements, the stiffness matrix and the external force vector respectively. Such a system may be discretized in time, resulting in unkown vecotors $\boldsymbol{u}_n \, n \in [0, 1, ...N]$, and solved using time marching. On the other hand one could construct vectors with all knowns and unknowns in e.g. lexiographic order given by

$$\boldsymbol{F} = \langle \boldsymbol{f}_1, \boldsymbol{f}_2, ... \boldsymbol{f}_N \rangle^T \tag{G.13}$$

and

$$\boldsymbol{U} = \langle \boldsymbol{u}_1, \boldsymbol{u}_2, ... \boldsymbol{u}_N \rangle^T \tag{G.14}$$

The spatial and time discretized system of equation can be written as

$$\hat{\boldsymbol{K}}\boldsymbol{U} = \boldsymbol{F} \tag{G.15}$$

which has the same form as the static case. This proves that their exists one optimum that minimizes the objective function for linear dynamic problems. This solution has the same stability problem as the described for the static case. When regularization is used for the dynamic problem a large system of equation has to be solved since the dof now contain both spatial and time discretized variables. Since the system studied mostly for this report was non-linear the direct method is not used. The behaviour of the inverse problem for the non-linear and linear models are however expected to be similar. For that reason the exact optimum for non-linear problems is expected to contain large pressure oscillations to fit the noise in the data. Hence regularization would be required however gradient of decent has regularization properties. The disadvantage is that the amount of regularization in gradient of decent algorithm can only be indirectly controlled by the convergence criteria.

Bibliography

[1] 3d software: Gom inspect. `https://www.gom.com`.

[2] A. Antoniou & W.S Lu. *Practical Optimization*. Springer, 2007.

[3] A. Bouamoul. Comparison of ale and sph methods for simulating mine blast effects on structures. *Defence research and development Canada*, 2010.

[4] A. Bouamoul et. al. An empirical model for mine-blast loading. *Defence Research and Development Canada*, pages 1–4, 2014.

[5] A. Iluk. Modeling and evaluation of loads in vehicles subjected to mine blast. *University of Technology Lukasiewicza*, 2015.

[6] A. Kozma, C. Conte & M. Diehl. Benchmarking large-scale distributed convex quadratic programming algorithms. *Optimization methods and software*, 2005.

[7] A.D. Stelzner & D.C. Kammer. Input force estimation using an inverse structural filter. *presented at 17th International Modal Analysis Conference (IMAC XXVII), Kissimmee, Florida, 1999.*, 1971.

[8] Ahrens, James, Geveci, Berk, Law, Charles. Paraview: An end-user tool for large data visualization, visualization handbook. *Elsevier*, 2005.

[9] A.I. Khuri & S. Mukhopadhyay. Response surface methodology. *WIREs Computational Statistics*, 2010.

[10] C. Xu & J. Zhang. A survey of quasi-newton equations and quasi-newton methods for optimization. *Annals of Operations Research*, 2001.

[11] Charles E. Anderson Jr., T. Behner & C.E. Weiss. Mine blast loading experiments. *Elsevier, International Journal of Impact Engineering*, 6 2010.

[12] Christopher T. Mann, Hannah Fischer . Recent trends in active-duty military deaths. *Congressional Research service*, 2018.

[13] D. Bergeron, R. Walker & C. Coffey. Detonation of 100-gram anti-personnel mine surrogate charges in sand - a test case for computer code validation. *Defence Research Establishment Suffield, Ralston ALTA (CAN)*, 10 1998.

[14] D. Bonorchis & G.N. Nurick. The influence of boundary conditions on the loading of rectangular plates subjected to localised blast loading – importance in numerical simulations. *International Journal of Impact Engineering*, 2008.

[15] D. Calvetti, S. Morigi, L.Reichel & F.Sgallari. Tikhonov regularization and the l-curve for large discrete ill-posed problems. *Computational and applied mathematics*, 2000.

[16] D.M. Fox X. Huang, D. Jung, W.L. Fourney, U. Leiste & J.S. Lee. The response of small scale rigid targets to shallow buried explosive detonations. *Elsevier, International Journal of Impact Engineering*, 2010.

[17] D.P. Bertsekas. Constrained optimization and lagrange multiplier methods. *Elsevier: Mathematics (General)*, 1982.

[18] Dym, Clive L., Shames, Irving H. *Solid Mechanics*. Springer, 2013.

[19] E. Lazarson H. Raz & Z. Asaf. Applying buried mine blast loads to a structure utilizing the user module capability. *LS-DYNA conference 2017*, 2017.

[20] Edan Lazarson et. al. Applying buried mine blast loads to a structure utilizing the user module capability. *LS-Dyna Conference Salzburg Austria*, pages 1–4, 2017.

[21] E.G. Pickering S. Chung Kim Yuen, G.N. Nurick & P. Haw. The response of quadrangular plates to buried charges. *Elsevier, International Journal of Impact Engineering*, 2012.

[22] G. Venter. Review of optimization techniques. *In Encyclopedia of Aerospace Engineering (Blockley R and Shyy W (eds)). Wiley, New York, NY, USA, vol. 8,part 42*, 2010.

[23] I.M. Smith, D.V. Griffiths and L. Margetts. *Programming the finite element method*. Wiley, 2014.

[24] J.A. Ford & I.A. Moghrabi. Multi-step quasi-newton methods for optimization. *Computational and Applied Mathematics*, 1994.

[25] J.F. Doyle. A wavelet deconvolution method for impact force identification. *Experimental Mechanics (1997) 37: 403.*, 1997.

[26] J.R. Shewchuk. An introduction to the conjugate gradient method without the agonizing pain. *School of computer science Carnegie Mellon University*, 1994.

[27] J.S. Arora, O.A. Elwakeil & A.I. Chahande . Global optimization methods for engineering applications: review. *Springer: Structural Optimization*, 1995.

[28] Len Schwer, Samuel Rigby. Buried charges: The challenge of computing target pressure distributions. *ScienceDirect*, pages 6–7, 2017.

[29] LSTC. *LS-Prepost online documentation*. `http://www.lstc.com/lspp/content/tutorials.shtml`.

[30] (LSTC). LS-DYNA keyword user's manual volume I. *Livermore Software Technology Corporation*, 2014.

[31] M. Gong, X. Jiang & H. Li. Optimization methods for regularization-based ill-posed problems: a survey and a multi-objective framework. *Frontiers of Computer Science*, 2017.

[32] M. Saleh & L. Edwards. Evaluation of soil and fluid structure interaction in blast modelling of the flying plate test. *International Journal of Computers and Structures*, 2010.

[33] Matheus J. Lazo, Delfim F. M. Torres. The dubois-reymond fundamental lemma of the fractional calculus of variations and an euler-lagrange equation involving only derivatives of caputo. *Cornell University*, 2012.

[34] M.R. Hestenes & E. Stiefel. Methods of conjugate gradients for solving linear systems. *Journal of Research of the National Bureau of Standards*, 1952.

[35] M.S. Bazaraa, H.D. Sherali & C.M. Shelly. *NonLinear Programming*. Wiley Online Library, 2005.

[36] N. Chandra, S. Ganpule, N. N. Kleinschmit, R. Feng, A. D. Holmberg, A. Sundaramurthy, V. Selvan, A. Alais. Evolution of blast wave profiles in simulated air blasts: experiment and computational modeling. *Springer: Shock waves*, 2012.

[37] NATO Standarisation Agency. Protection levels for occupants of armoured vehicles. *STANAG 4569*, 2011.

[38] R. Fletcher & C.M. Reeves. Function minimization by conjugate gradients. *The computer journal*, 1964.

[39] S. Xu, V. Tiwari, X. Deng, M.A. Sutton & W.L. Fourney. Identification of interaction pressure between structure and explosive with inverse approach. *International Journal of Impact Engineering*, 2009.

[40] S.D. Clarke, S.D. Fay, J.A. Waren, A. Tyas, S.E. Rigby & I. Elgy. A large scale experimental approach to the measurement of spatially and temporally localised loading from the detonation of shallow-buried explosives. *Measurement Science and Technology*, 2015.

[41] S.E. Rigby . Influence of particle size distribution on the blast pressure profile from explosives buried in saturated soils. *University of Sheffield*, 2017.

[42] S.E. Rigby, S.D. Fay, S.D. Clarke, A. Tyas, J.J. Reay, J.A. Warren, M. Gant & I. Elgy. Measuring spatial pressure distribution from explosives buried in dry leighton buzzard sand. *Elsevier, International Journal of Impact Engineering*, 2016.

[43] Sergio Turteltaub. Continuum mechanics. 2015.

[44] Shaowen Xu, Xiaomin Deng, Vikrant Tiwari, Michael A. Sutton, William L. Fourney & Damien Bretall. An inverse approach for pressure load identification. *International Journal of Impact Engineering*, 2008.

[45] Janusz Sliwinski. Protection of vehicles against mines, 2015.

[46] T.J. Kreittinger. Force identification from structural response. *PHD thesis: The University of New Mexico Albuquerque,*, 1971.

[47] J.E. Tremblay. Impulse on blast deflectors from a landmine explosion. *Defence Research Establishment*, pages 2–5, 1998.

[48] U. Leiste. Experimental studies to investigate pressure loading on target plates. *Digital repository at the university of Maryland*, 2012.

[49] V. Denefeld N. Heider & A. Holzwarth. Measurement of the spatial specific impulse distribution due to buried high explosive charge detonation. *Elsevier, Defence Technology*, 2017.

[50] V. Radonic et al. Injuries from antitank mines in southern croatia, 2004.

[51] W. Hare,J. Nutini & S. Tesfamariam. A survey of non-gradient optimization methods in structural engineering. *Advances in Engineering Software*, 2012.

[52] W.L. Fourney U. Leiste, R. Bonenberger & D. Goodings. Explosive impulse on plates. *International Journal for Blasting and Fragmentation*, 2008.

[53] Y. Liu & C. Storey. Efficient generalized conjugate gradient algorithms, part1: Theory. *Journal of Optimization Theory and Applications*, 1991.